

Mechanistic Insights and Theory-Assisted Catalyst Development toward Kinetically E-Selective Olefin Metathesis

Immanuel Albrecht Manfred Reim

Thesis for the degree of Philosophiae Doctor (PhD)
University of Bergen, Norway
2024

UNIVERSITY OF BERGEN



Mechanistic Insights and Theory-Assisted Catalyst Development toward Kinetically E-Selective Olefin Metathesis

Immanuel Albrecht Manfred Reim



Thesis for the degree of Philosophiae Doctor (PhD)
at the University of Bergen

Date of defense: 24.05.2024

© Copyright Immanuel Albrecht Manfred Reim

The material in this publication is covered by the provisions of the Copyright Act.

Year: 2024

Title: Mechanistic Insights and Theory-Assisted Catalyst Development toward Kinetically E-Selective Olefin Metathesis

Name: Immanuel Albrecht Manfred Reim

Print: Skipnes Kommunikasjon / University of Bergen

Scientific Environment

I completed my Doctor of Philosophy at the University of Bergen (UiB) in Bergen, Norway, in collaboration with the University of Ottawa (UO) in Ottawa, Canada. During my doctoral studies, I had the privilege of being a member of Vidar R. Jensen's research group, where I focused on the development of *E*-selective olefin metathesis catalysts.

Prof. Vidar R. Jensen served as my principal supervisor at UiB, while I was also fortunate to receive guidance from Dr. Giovanni Occhipinti at UiB and Prof. Deryn E. Fogg at UO, who co-supervised my research.



This PhD received financial support from the Research Council of Norway (RCN) via the FRIPRO program (grant number 262370) and the Norwegian NMR Platform, NNP (226244). The RCN is also thanked for CPU (NN2506K) and storage resources (NS2506K).

Acknowledgements

I want to take a moment to acknowledge all the incredible people who have helped me along the way in achieving my PhD. They have played a crucial role in making this journey possible, and I am truly grateful for their support.

First and foremost, a big thank you to Prof. Vidar R. Jensen for allowing me to be a part of his group and work on such an exciting topic. I would also like to express my gratitude to Dr. Giovanni Occhipinti for stimulating discussions and brainstorming sessions, as well as his guidance and supervision. And Dr. Marco Foscatto, who was there when I needed help with computational chemistry.

I am also indebted to Assoc. Prof. Erwan Le Roux for always being open and approachable. A special shout-out to Prof. Pascal D.C. Dietzel for supporting the good old German teaching style. I would also like to extend my thanks to Prof. Deryn E. Fogg for giving me the opportunity to spend time in her group in Ottawa. It was an amazing experience, and I learned a lot from it.

A heartfelt thank you to the research staff who have been involved in this thesis. Dr. Bjarte Holmelid, your help with measuring and understanding mass spectra has been invaluable. Jose Carlos Reyes Guerrero, Assoc. Prof. Jarl Underhaug, and Assoc. Prof. Nils Åge Frøystein, your assistance with NMR experiments was truly instrumental. Prof. Karl W. Törnroos, thank you for your expertise in measuring and solving the single-crystal X-ray diffractions. And thanks to Inger Johanne Fjellanger for your help with elemental analysis. Your collective support and expertise have been indispensable.

I would like to acknowledge my research group: Christian S. Gjermestad, Morten Tysse, Jonas Himmelstrup, Jonas Ekeli, Marcello Costamagna, Leif Hertwig, Sven Nappen, and Fredrik Nesse. Whether we were working together or enjoying some board games and beer, the time spent with you all was truly memorable.

I also want to thank my colleagues at the department who have made the past few years more enjoyable. Sara Suito, Julia Schmidt, Beate Halsvik, Gabriel Jeantelot, and Tamal Roy, thank you for the camaraderie and fun times.

A special thanks to Christian, Jonas, Julia, Leif, Tamal, and Martin for proofreading this thesis.

And now, to my parents, Elvira and Albrecht, thank you for your support throughout my journey to become a chemist. To my sisters, Franziska, Dorothea, and Magdalena, thank you for always being there for me.

Last but not least, a special thanks to my partner, Alice Refosco, for standing by my side and supporting me as I completed this thesis. Your love and patience mean the world to me.

To all those mentioned and to those who may have been inadvertently overlooked, please know that your help, encouragement, and support have made a significant impact on my success. Thank you.

Abstract in English

Olefin metathesis, a C=C bond rearrangement, has become a versatile methodology for building molecular carbon frameworks over the last 30 years. Most catalysts focus on converting readily available 1-alkenes into disubstituted, internal olefins, encompassing both *cis* (*Z*) and *trans* (*E*) isomers. Selective *Z*-alkene catalysts emerged only a decade ago, with no reported *E*-selective catalysts yet. Instead, the desired *E*-olefins have been synthesized via indirect approaches, e.g., semireduction of alkynes or stereoretentive olefin metathesis. Thus, this doctoral project explores the development of kinetically *E*-selective ruthenium-based olefin metathesis catalysts for a direct route to *E*-olefins.

Catalysts of the RuXX'(NHC)(py)(=CHR) type, where XX' is a S⁰N bidentate, dianionic thioindolate ligand, NHC is a N-heterocyclic carbene, and py is pyridine, were initially predicted, via density functional theory (DFT) calculations, to be *E*-selective by favoring anti-positioning of substituents in the expected rate-determining transition state: the cycloreversion of the metallacyclobutane intermediate (MCB). Three pyridine-stabilized catalysts (**52a-c**) with different substituents (H, Me, or Ph) in the C2 position of the thioindolate ligand were synthesized, all employing the unsaturated 1,3-dimesityl-4,5-dimethyl-imidazoline-2-ylidene **C1** as the NHC ligand. Single-crystal X-ray diffraction analysis of catalysts **52a** and **52c** confirmed the ligand orientation needed for *E*-selective metathesis, with the thioindolate sulfur atom binding *cis*, and the indolate nitrogen atom *trans*, to the NHC. Whereas these newly synthesized complexes exhibited metathetic exchange of their 2-thienylmethylidene ligands with 1-alkenes, no corresponding self-metathesis products were obtained. Only small quantities of 2-butene (0.35 turnover, 73% *Z*-isomer) were produced during the self-metathesis of propene using thioindolate catalyst **52a**. In contrast to the original expectation, detailed DFT analysis revealed that slow product release, not cycloreversion, limited the reaction, explaining the low metathesis activity and unexpected *Z*-selectivity of the S⁰N-catalyst **52a**.

To lower the dissociation barrier, NHCs less bulky than **C1** were investigated, along with an S[⊖]N ligand containing a more acidic nitrogen atom than that of indole to improve catalyst stability. However, catalyst **57**, bearing a mercaptophenyltrifluoromethanesulfonamide ligand **55**, did not show significant improvement in productivity or *E*-selectivity compared with **52a**. Furthermore, Ru nanoparticles were formed upon the addition of the S[⊖]N ligand **55** to Ru complexes containing less bulky NHCs. Thioindolate ligand **49a** was found to be compatible with these NHCs. However, due to the activation of the o-C–H bonds of N-bound NHC phenyls, only the fluorinated 1,3-bis(2,6-difluorophenyl)-4,4-dimethyl-5,5-dihydro-imidazol-2-ylidene **C5** led to a stable thioindolate-coordinated catalyst **65**. Unexpectedly, in **65**, the thioindolate **49a** bonds with the indolate positioned trans to pyridine, resulting in low catalytic activity and *E*-selectivity in 1-alkene self-metathesis. DFT calculations indicate that the low activity can be attributed to the weak trans influence and significant π donation of the indolate. In contrast, the initially intended isomer **65'**, with the thiolate positioned trans to pyridine, is predicted to be more active and *E*-selective with cycloreversion as the rate-limiting step.

The above results prompted a reevaluation of the dianionic X[⊖]Y ligand, highlighting the importance of having an X fragment with a strong trans influence and a Y fragment with a weak trans influence, which exerts selective steric pressure on the β -position of the MCB.

Following these considerations, anionic carbon-based C[⊖]N ligands, e.g., derived from phenylimidazole, were identified as promising. These ligands were expected to possess favorable properties for both activity and selectivity, leveraging the carbon-based moiety for increased activity and the N-based fragment for promoting *E*-selectivity. Unfortunately, challenges were encountered while attempting to install various C[⊖]N ligands on Ru alkylidene precursors via C–H activation or transmetalation, and the desired C[⊖]N-coordinated ruthenium alkylidenes could not be realized.

In addition to offering a new class of ligands and a range of new organometallic complexes, this thesis offers insight into the fundamental requirements of *Z*- and *E*-

selective metathesis catalysts. The thesis also demonstrates the magnitude and multifaceted nature of the challenge posed by *E*-selective olefin metathesis: addressing one aspect, such as introducing selectivity-inducing steric pressure, may generate new challenges, such as a change in the rate- and selectivity-determining step. To navigate this complicated chemical landscape, DFT calculations were used to both guide the experimental work by predicting catalyst candidates and subsequently, identify and analyze the factors responsible for the lower-than-expected activity and selectivity of the synthesized complexes. Thus, whereas the challenge of ruthenium-catalyzed *E*-selective metathesis of terminal alkenes remains, the insight into factors governing catalyst stability, activity, and selectivity offered in this thesis may inform future catalyst redesign and thus, indirectly, contribute to achieving the ambitious goal of selective metathetic synthesis of *E*-olefins from 1-alkenes.

Abstract in Norwegian

Olefinmetatase, en omordning av C=C-bindinger, har blitt en allsidig metodologi for å konstruere molekylære karbonrammer de siste 30 årene. De fleste katalysatorene fokuserer på å konvertere lett tilgjengelige 1-alkener til disubstituerte, interne olefiner, inkludert både *cis* (*Z*) og *trans* (*E*) isomerer. Selektive *Z*-alkenkatalysatorer dukket opp for bare et tiår siden, uten rapporterte *E*-selektive katalysatorer så langt. I stedet er de ønskede *E*-olefinene laget via indirekte tilnærminger, f.eks. semireduksjon av alkyner eller stereoretentiv olefinmetatase. Derfor utforsker dette doktorprosjektet utviklingen av kinetisk *E*-selektive rutheniumbaserte olefinmetatesekatalysatorer for en direkte rute til *E*-olefiner.

Katalysatorer av typen RuXX'(NHC)(py)(=CHR), der NHC er en N-heterosyklisk karben, py er pyridin, og XX' er en S^ηN-bidentat, dianionisk tioindolatligand, ble først forutsagt, via densitetsfunksjonsteori (DFT)-beregninger, å være *E*-selektive ved å favorisere anti-posisjonering av substituenten i forventet ratebestemmende overgangstilstand: sykloreversjonen av metallasyklobutanintermediatet (MCB). Tre pyridin-stabiliserte katalysatorer (**52a-c**) med forskjellige substituenten (H, Me eller Ph) i C2-posisjonen til tioindolatliganden ble syntetisert, alle ved bruk av den umettede 1,3-dimesityl-4,5-dimetyl-imidazolin-2-yliden **C1** som NHC-ligand. Single-krystall røntgendiffraksjonsanalyse av katalysatorer **52a** og **52c** bekreftet ligandorienteringen som trengs for *E*-selektiv metatase, med tioindolatsvovelatomet som binder *cis*, og indolat-nitrogenatomet som binder *trans*, til NHC. Mens disse nylig syntetiserte kompleksene viste metataseutveksling av deres 2-tienylmetylidengigand med 1-alkener, ble ingen tilsvarende selvmetataseprodukter oppnådd. Bare små mengder 2-butene (0,35 omdreining, 73% *Z*-isomer) ble produsert under selvmetatase av propen ved bruk av tioindolat-katalysator **52a**. I motsetning til den opprinnelige forventningen, avslørte detaljert DFT-analyse at treg produktfrigjøring, ikke sykloreversjon, begrenset reaksjonen, noe som forklarer den lave metataseaktiviteten og den uventede *Z*-selektiviteten til S^ηN-katalysator **52a**.

For å senke dissosiasjonsbarrieren ble mindre klumpete NHC enn **C1** undersøkt, sammen med en $S^{\cap}N$ -ligand som inneholdt et mer surt nitrogenatom enn indol for å forbedre katalystabiliteten. Imidlertid viste katalysator **57**, med mercaptophenyltriflourometansulfonamid **55**, ingen betydelig forbedring i produktivitet av *E*-selektivitet sammenlignet med **52a**. Videre ble Ru-nanopartikler dannet ved tilsetning av $S^{\cap}N$ -ligand **55** til Ru-komplekser som inneholder mindre klumpete NHC. Tioindolatligand **49a** viste seg å være kompatibel med disse NHC-ene. Imidlertid, på grunn av aktivering av o-C–H-bindinger til N-bundne NHC-fenyl, førte bare den fluorerte 1,3-bis(2,6-difluorofenyl)-4,4-dimetyl-5,5-dihydro-imidazol-2-yliden **C5** til en stabil tioindolat-koordinert katalysator **65**. Overraskende, i **65** bundet **49a** med indolaten posisjonert trans til pyridin, noe som førte til lav katalytisk aktivitet og *E*-selektivitet i selvmetatesen av 1-alkener. DFT-beregninger viser at den lave aktiviteten stammer fra den svake trans-innflytelsen og betydelig π -donasjon av indolaten. I motsetning til dette forventede isomeren **65'**, der tioletatet er plassert trans til pyridin, forutsies å være mye mer aktiv og *E*-selektiv med syklereversjon som hastighetsbegrensende trinn.

Disse resultatene førte til en reevaluering av den dianioniske $X^{\cap}Y$ -liganden, og understreket viktigheten av å ha et X-fragment med sterk trans påvirkning og et Y-fragment med svak trans påvirkning, som utøver selektiv sterk trykk på β -posisjonen av MCB. Etter disse betraktningene ble anioniske karbonbaserte $C^{\cap}N$ -ligander, f.eks. derivert fra fenylimidazol, identifisert som lovende. Disse ligandene ble forventet å ha gunstige egenskaper for både aktivitet og selektivitet, utnytte karbonbasert del for økt aktivitet og N-basert del for å fremme *E*-selektivitet. Dessverre oppsto utfordringer ved forsøk på å installere ulike $C^{\cap}N$ -ligander på Ru-alkylidenforløpere via C–H-aktivering eller transmetallasjon, og de ønskede $C^{\cap}N$ -koordinerte ruthenium-alkylidenene kunne ikke realiseres.

I tillegg til å tilby en ny klasse ligander og et utvalg av nye organometalliske komplekser, gir denne avhandlingen innsikt i de grunnleggende kravene til *Z*- og *E*-selektive metatesekatalysatorer. Avhandlingen demonstrerer også omfanget og mangfoldet av utfordringene som *E*-selektiv olefinmetatase utgjør: Å håndtere ett

aspekt, som å introdusere selektivitetsinduserende sterk trykk, kan generere nye utfordringer, som en endring i rate- og selektivitetsbestemmende trinn. For å navigere i dette kompliserte kjemiske landskapet, ble DFT-beregninger brukt både til å veilede eksperimentelt arbeid ved å forutsi katalysatorkandidater og deretter identifisere og analysere faktorene som er ansvarlige for den lavere enn forventede aktiviteten og selektiviteten til syntetiserte komplekser. Således, mens utfordringen med ruthenium-katalysert *E*-selektiv metatase av terminale alken forblir, kan innsikten i faktorer som styrer katalyststabilitet, aktivitet og selektivitet som tilbys i denne avhandlingen, informere fremtidig katalystomforming og dermed indirekte bidra til å oppnå det ambisiøse målet om selektiv metatesesyntese av *E*-olefiner fra 1-alkener.

List of Publications

Paper I:

Reim, I.; Occhipinti, G.; Nappen, S. T.; Fogg, D. E.; Jensen, V. R. Stereocontrol in Ruthenium-Catalyzed Olefin Metathesis: Mechanisms and Catalyst Design Strategies. Manuscript in preparation.

Paper II:

Reim, I.; Occhipinti, G.; Törnroos, K. W.; Fogg, D. E.; Jensen, V. R. Toward *E*-Selective Olefin Metathesis: Computational Design and Experimental Realization of Ruthenium Thio-Indolate Catalysts. *Top Catal* **2022**, *65* (1–4), 448–461. <https://doi.org/10.1007/s11244-021-01468-3>.

Paper III:

Reim, I.; Occhipinti, G.; Törnroos, K. W.; Jensen, V. R. Pursuing *E*-Selective Olefin Metathesis: Tuning Steric and Electronic Properties of S,N-Chelated Ruthenium Alkylidenes. *Organometallics* **2024**, *43* (7) 726–736. <https://doi.org/10.1021/acs.organomet.3c00522>.

Additional Work during the PhD:

Nascimento, D. L.; Reim, I.; Foscatto, M.; Jensen, V. R.; Fogg, D. E. Challenging Metathesis Catalysts with Nucleophiles and Brønsted Base: Examining the Stability of State-of-the-Art Ruthenium Carbene Catalysts to Attack by Amines. *ACS Catal.* **2020**, *10* (19), 11623–11633. <https://doi.org/10.1021/acscatal.0c02760>.

The published paper is reprinted with permission from Springer (Paper II). All rights reserved.

Abbreviations

ADMET	Acyclic Diene Metathesis
Bn	Benzyl
CAAC	Cyclic(alkyl)(amino)carbenes
Cat	Catalyst
CM	Cross-metathesis
Cy	Cyclohexyl
DBU	1,8-Diazabicyclo(5.4.0)undec-7-ene
DCM	Dichloromethane
Dipp	2,6-Diisopropylphenyl
DFT	Density functional theory
H ₂ IMes	1,3-Dimesityl-4,5,-dihydro-imidazol-2-ylidene
HRMS	High-resolution mass spectrometry
IMes	1,3-Dimesityl-imidazol-2-ylidene
<i>i</i> -Pr	isopropyl
KHMDS	Potassium bis(trimethylsilyl)amide
MCB	Metallacyclobutane
Mes	Mesityl, 2,4,6-trimethylphenyl
MW	Microwave reactor
NHC	N-heterocyclic carbene
NMR	Nuclear magnetic resonance
Ph	Phenyl
Py	Pyridine
RCM	Ring-closing Metathesis
ROCM	Ring-opening cross-metathesis
ROMP	Ring-opening metathesis polymerization
RT	Room temperature
THF	Tetrahydrofuran
TON	Turnover number
X ⁿ Y	Chelating bidentate ligand

Contents

Scientific Environment	3
Acknowledgements	4
Abstract in English	6
Abstract in Norwegian	9
List of Publications	12
Abbreviations	13
Contents	14
1. Introduction	16
2. Aim of the Thesis	19
3. Discovery and Development of Olefin Metathesis	20
3.1. Discovery of Olefin Metathesis	20
3.2. The Mechanism Proposed by Chauvin and Hérisson	21
3.3. Schrock-type Olefin Metathesis Catalysts.....	22
3.4. Grubbs-type Olefin Metathesis Catalysts	24
4. Decomposition and Stability of Ru-Based Catalysts	27
5. Selectivity in Ruthenium-Based Olefin Metathesis	30
5.1. Z-Selectivity in Ruthenium-Based Olefin Metathesis	30
5.1.1 Monothiolate Catalysts	31
5.1.2 Cyclometalated Catalysts.....	32
5.2. Stereoretention in Olefin Metathesis	34
5.3. Current Progress in <i>E</i> -Selectivity	38

6. Methods	40
6.1. Experimental Methods	40
6.1.1 Handling and Synthesis of Compounds	40
6.1.2 Analysis of Synthesized Compounds.....	40
6.2. Computational Methods	41
6.2.1 Geometry Optimization.....	41
6.2.2 Single-point Energy Calculations	42
6.2.3 Calculation of Standard State-Corrected Free Energies	42
7. Results and Discussion	43
7.1. Application of S ^η N-Ligands in <i>E</i> -Selective Olefin Metathesis	43
7.1.1 Thioindolate as a Selectivity-Inducing Ligand	43
7.1.2 Triflouromethanesulfonyl Group for Higher Stability.....	47
7.2. Utilizing Smaller NHCs for Higher Activity	49
7.3. Revision of S ^η S and S ^η N Ligands for <i>E</i> -Selectivity.....	60
7.4. A New Design Approach for Bidentate Ligands	62
7.5. Anionic Carbon-Based Ligands for Olefin Metathesis.....	63
7.5.1 Background: Studies on Biphenyl Ru Complexes.....	63
7.6. Aryl-Based Ru Olefin Metathesis Alkylidenes.....	66
7.6.1 Application of C ^η N-Based Ligands in Olefin Metathesis	68
8. Conclusions	74
9. Future Directions	74
10. References	78

1. Introduction

In recent years olefin metathesis has seen expanding usage in the pharmaceutical,¹ organic, and polymer industries.² It is the most versatile method for the reorganization of carbon-carbon double bonds. Although at first glance it may seem trivial, selective scission and regeneration of olefinic bonds enables the synthesis of complex and valuable compounds from abundant starting materials. Therefore, it has been widely adopted for the synthesis of complex organic molecules,^{3–6} including pharmaceuticals,^{7–10} and soft materials.^{11–20}

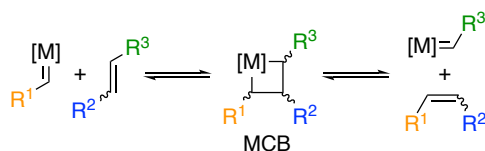
Before the development of olefin metathesis catalysts, selective formation of olefins was performed using Wittig,²¹ Horner-Wadsworth-Emmons,²² and Julia²³ olefination reactions. The disadvantages are the prerequisite for specific functional groups and their terrible atom efficiency. For example, the Wittig reaction produces an equal amount of triphenylphosphine oxide as an undesired side product. In contrast, olefin metathesis allows the formation of carbon-carbon double bonds catalytically and is highly atom-efficient by releasing only ethene or other olefins.^{24–26} Alternatively, *E*- or *Z*-olefins can be obtained via alkyne metathesis followed by selective semireduction to *E*- or *Z*-alkene, however, the availability of substrates and functional group tolerance of alkyne metathesis catalysts are limiting factors for widespread application.²⁷

Over the past decades, olefin metathesis catalysts have evolved from ill-defined mixtures²⁸ to well-defined, fully characterized organometallic complexes based on ruthenium, molybdenum, tungsten, vanadium, niobium, rhenium, osmium, and iron.^{29–42} The different metal-based catalysts have complementary properties. For instance, ruthenium-based catalysts possess high tolerance toward functional groups, moderate air and water stability, and ease of handling,^{43–46} whereas molybdenum-based catalysts are practically immune against the internal β -hydride elimination.⁴⁷

The mechanism, proposed by Chauvin and Hérisson for olefin metathesis involves a [2+2] cycloaddition between the substrate olefin and a metal alkylidene (Scheme 1, left), forming a metallacyclobutane (MCB) intermediate (Scheme 1, middle).⁴⁸ The MCB then undergoes cycloreversion to release the product olefin and regenerate a new

metal alkylidene (Scheme 1, right).^{48,49} Most olefin metathesis catalysts generally exert limited control over the stereoisomer distribution of the product, and the *E/Z* ratio is primarily determined by thermodynamic factors generally favoring the *E*-isomer. However, it is important to consider that the ratio of *E/Z* isomers can be influenced by the steric and electronic properties of the substituents present on the olefinic substrates. Additionally, there are catalysts available that operate under kinetic control and can alter the stereoisomer distribution.⁵⁰

Scheme 1. Metathetic Rearrangement of Pairs of Double Bonds via the Metallacyclobutane (MCB) Intermediate.



Controlling the stereochemical outcome of reactions is crucial in the synthesis of fine chemicals such as pharmaceuticals, natural products, and polymers with tailored physical properties.^{51–59} Consequently, significant research efforts have been focused on the development of catalysts for stereocontrolled olefin metathesis. Although there have been notable advancements in *Z*-selective olefin metathesis catalysts,⁶⁰ challenges still need to be overcome.

One significant challenge is the inability of current catalysts to improve the production of *E*-olefin products from 1-alkenes beyond their thermodynamic distribution. Instead, the synthesis of *E*-alkenes often relies on starting with *E*-configured substrates via stereoretentive metathesis.^{61,62} This approach requires expensive, isomerically pure starting materials, which limits its practicality. Therefore, there is a need for catalysts that can selectively generate *E*-olefins from more readily available and cost-effective 1-alkene starting materials.

A second major challenge is the instability of catalytic intermediates in stereocontrolled metathesis.^{63–73} Ruthenium-based metathesis catalysts typically decompose after only a few thousand turnovers,^{67,74–77} which is insufficient for many industrial applications.⁷⁸ Catalyst decomposition leads to unwanted side reactions, such as olefin

isomerization,⁶⁷ double-bond migration,⁶⁵ and *Z*-to-*E* isomerization,⁷⁹ compromising product yields and selectivities.⁶⁷ Stereocontrol-wielding catalysts have shown reduced stability and functional group tolerance compared with their unselective counterparts, limiting their substrate scope, and practical utility.⁵⁵

2. Aim of the Thesis

This thesis aims to develop the first *E*-selective olefin metathesis catalyst, specifically targeting the transformation of 1-alkenes into *E*-configured products. While recent years have seen advancements in the development of kinetically *Z*-selective catalysts for 1-alkene metathesis, there is currently a lack of catalysts that can selectively produce *E*-alkenes. As a result, the synthesis of *E*-alkenes typically involves either isolating the *E*-olefin from the thermodynamically driven product distribution using unselective catalysts or relying on *E*-configured substrates through stereoretentive metathesis.^{61,62}

These approaches have drawbacks, such as the generation of significant side-products or the requirement for isomerically pure starting materials. Therefore, the development of a catalyst that enables the kinetically selective transformation of 1-alkenes into *E*-configured products would offer a more sustainable and efficient approach. Furthermore, such a catalyst could provide access to new biologically active compounds, expanding the possibilities in drug discovery and development.⁷

3. Discovery and Development of Olefin Metathesis

3.1. Discovery of Olefin Metathesis

The discovery of olefin metathesis began in the early 1950s by Ziegler and co-workers when they attempted to synthesize polyethylene from available ethene but encountered 1-butene almost exclusively. Further investigation revealed that the presence of nickel salts was responsible for this undesired elimination reaction.⁸⁰

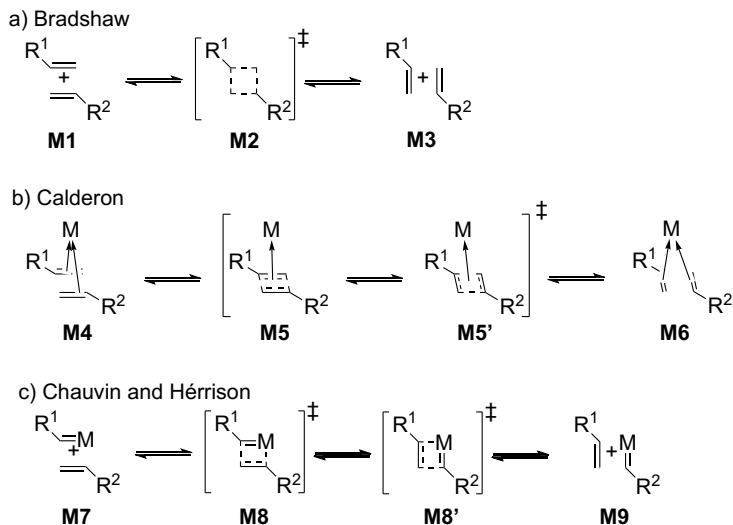
In subsequent studies, the Ziegler-Natta catalyst was applied to the cyclic olefin 2-norbornene, resulting in the first example of ring-opening metathesis polymerization. Instead of the intended saturated polymer, an unsaturated polymer with opened rings was formed.⁸¹ Similarly, ring-opening metathesis polymerization was observed with cyclopentene using tungsten and molybdenum halides.³⁰

In the 1960s, the disproportionation reaction of propene to ethene and 2-butene over a molybdena-alumina catalyst found industrial application at Philipps Petroleum Co.⁸² This reaction was named "olefin metathesis" by Calderon and co-workers, referring to the transfer of substituents through the scission of carbon-carbon double bonds.⁸³

Initially, several different mechanisms were proposed by various research groups: Bradshaw suggested the formation of a "quasi-cyclobutane" intermediate **M2** (Scheme 2a), although he admitted that detailed knowledge supporting this intermediate was missing.⁸⁴ Additionally, the formation of a cyclobutane intermediate contradicted the Woodward-Hoffman rules.⁸⁵ However, theoretical studies by Mango and colleagues suggested that forbidden cycloaddition reactions could be allowed if metal systems were involved.⁸⁶ Thus, Calderon proposed the formation of a bisolefin-metal complex **M4** instead (Scheme 2b).^{83,87} Shortly thereafter, Chauvin and Hérisson discovered inconsistencies in this mechanism, particularly in explaining the kinetic distribution of the ring-closing metathesis of 1,7-octadiene. They proposed the formation of a one-carbon metal alkylidene complex **M7** and metallacyclobutanes **M8** (Scheme 2c).⁴⁸ Subsequent studies by Grubbs and Katz supported the mechanism proposed by Chauvin and Hérisson.⁸⁸⁻⁹¹ The determination of the key intermediates and active

species allowed for the rational design of catalysts, moving away from ill-defined systems.

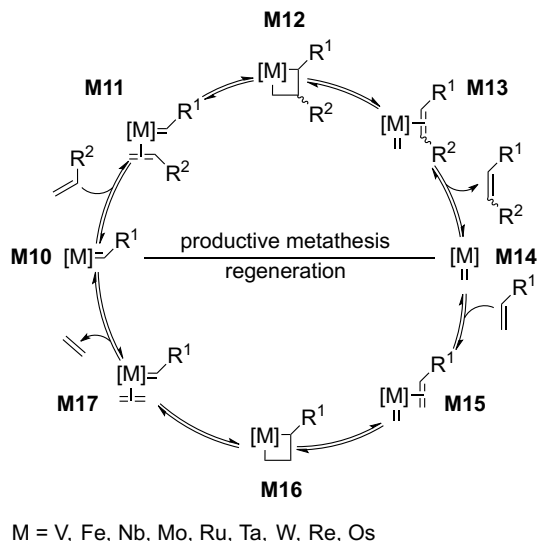
Scheme 2. Proposed Mechanism by (a) Bradshaw, (b) Calderon, and (c) Chauvin and Hérisson and Hérisson.



3.2. The Mechanism Proposed by Chauvin and Hérisson

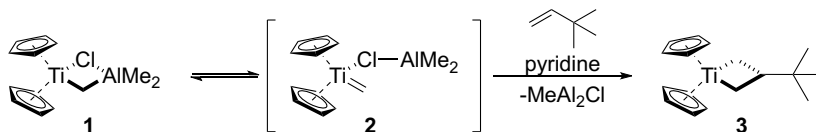
The proposed mechanism by Chauvin and Hérisson is based on the [2+2] cycloaddition of an alkene and a metal alkylidene.^{48,92} The initiation of the precatalyst, often via the dissociation of a dative ligand, results in the active species **M10** (Scheme 3). The catalytic cycle begins with the coordination of a terminal olefin forming the π -complex **M11**. Subsequent cycloaddition leads to the metallacyclobutane intermediate **M12** which, through cycloreversion, forms the product π -complex **M13**. There, the desired product can dissociate, forming the methylidene species **M14**, which can reform the initial 14 electron species **M10** through a regenerative half-cycle (**M15-17**).

Scheme 3. Hérisson-Chauvin Mechanism for Olefin Metathesis Depicting the Full Catalytic Cycle of Terminal Olefins.



One of the first well-defined metathesis catalysts was developed by Fred Tebbe at DuPont. The Tebbe reagent **1** can form the metal alkylidene **2**, which can perform olefin metathesis (Scheme 4).^{93,94} Additionally, the reaction of **1** with pyridine removed Me_2AlCl and formed a free alkylidene intermediate, which was then trapped with 3,3-dimethylbutene resulting in the metallacyclobutane **3** (Scheme 4), further affirming the Hérisson-Chauvin mechanism.⁹⁵

Scheme 4. Tebbe Reagent 1 Allows the Formation of the Alkylidene Species 2 which is Active in Ring-Opening Metathesis Polymerization.

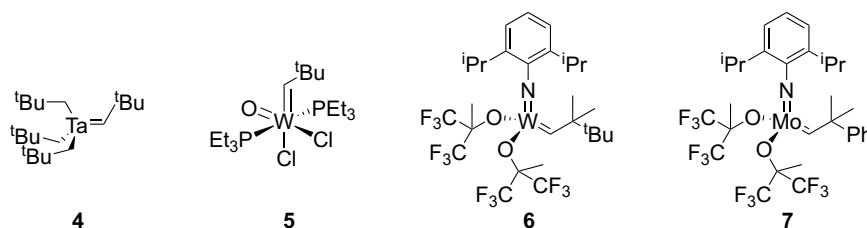


3.3. Schrock-type Olefin Metathesis Catalysts

Subsequent research conducted by Richard R. Schrock and his team resulted in the development of the first stable metal alkylidene complex **4** (Chart 1), through α -hydrogen activation from a $\text{Ta}(\text{CH}_2^t\text{Bu})_5$ intermediate, marking a significant milestone

in olefin metathesis research.⁹⁶ Complex **4**, however, exhibited low activity in olefin metathesis reactions.⁹⁷ As a result, the focus of the research shifted toward tungsten and molybdenum systems, which had demonstrated promising activity in ill-defined systems.^{98,99} This led to the discovery of the tungsten complex **5**, which displayed catalytic activity but required the presence of AlCl_3 as a co-catalyst.¹⁰⁰ Five years later, catalyst **6** was discovered, which exhibited remarkable catalytic activity, achieving 1000 turnovers per minute without the need for a Lewis acid co-catalyst.^{101,102} Afterwards, the molybdenum analog **7** was developed. It possessed higher functional group tolerance and allowed for the successful metathesis of various substrates such as enol ethers, acrylates, acrylonitrile, and tri- and tetrasubstituted olefins.^{24,103} This broad substrate scope expanded the versatility of olefin metathesis reactions.

Chart 1. Olefin Metathesis Catalysts Developed by Schrock and Co-workers.

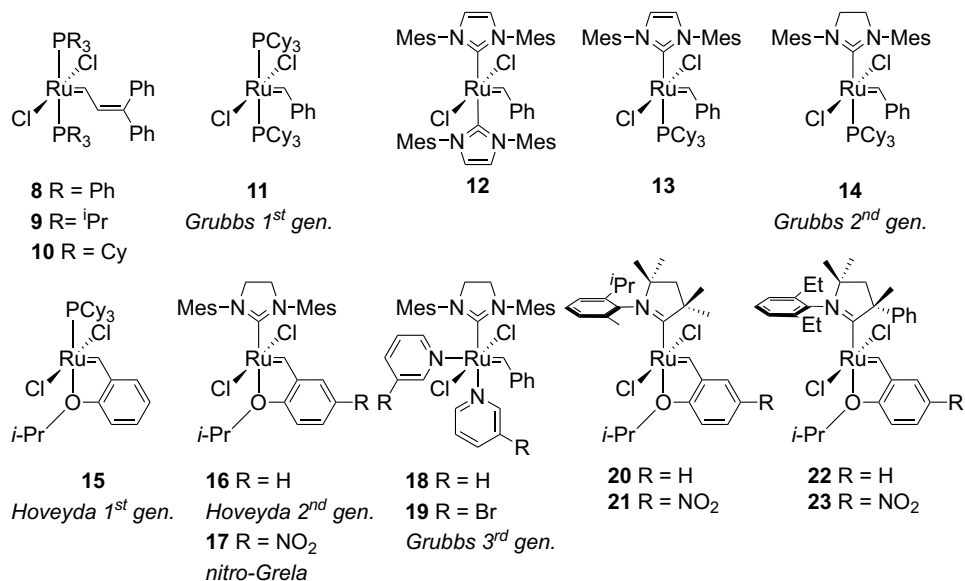


It is worth noting that most tungsten- and molybdenum-based olefin metathesis catalysts are highly oxophilic, making their handling, manipulation, and application challenging. Significant advancements have been made in addressing this limitation and improving the usability of these catalysts. The development of new ligands has increased the variety of ligand frameworks available for catalyst design, enabling the optimization of catalyst stability, reactivity, and functional group tolerance. Additionally, efforts have been made to produce air-stable tungsten and molybdenum precatalysts, which are commercially available as paraffin tablets. Furthermore, recent studies have focused on achieving *E*- and *Z*-selective metathesis using tungsten- and molybdenum-based catalysts.^{26,50,104–115}

3.4. Grubbs-type Olefin Metathesis Catalysts

Early experiments using ruthenium salts showed promising results with highly strained substrates, even maintaining their activity in aqueous medium, promising greater functional group tolerance compared with tungsten and molybdenum complexes. The in situ generation of the ruthenium alkylidene precursor addressed the issue of slow initiation and enabled ring-opening metathesis polymerization with less reactive monomers. A milestone was reached when Grubbs and co-workers synthesized the first well-defined ruthenium-based alkylidene catalyst **8** (Chart 2), although it suffered from low catalytic activity and a slow initiation rate.^{116,117} The catalytic activity was found to correlate with the electronic donation and size of the phosphine ligand, leading to the development of more active catalysts, such as catalysts **9** and **10**, by exchanging PPh₃ with P(*i*-Pr)₃ and PCy₃, respectively.¹¹⁸ The initiation rate was improved by replacing the alkylidene moiety in **10** with a benzylidene, yielding catalyst **11**, also known as Grubbs 1st generation.¹¹⁹ Catalyst **11** became the most economical and commercially available ruthenium catalyst, finding numerous applications in organic and organometallic synthesis.¹²⁰

Chart 2. Selected Non-selective Ru-based Olefin Metathesis Catalysts.



Efforts were made to further improve the catalytic system $[L_2Cl_2Ru=CHPh]$ by modifying the donor ligand L , but these attempts were unsuccessful.^{121–123} A breakthrough was achieved with the implementation of N-heterocyclic carbenes (NHC). NHCs exhibit stronger σ -donation than phosphine-based ligands and should thereby improve the catalytic activity. While the bis-NHC complex **12** showed promising air and moisture stability, it lacked catalytic activity.¹²⁴ A subsequent DFT study revealed that the formation of the active species was impeded by the high dissociation energy of the NHC. It was postulated that the combination of an NHC and a coordinatively labile ligand should possess a synergetic effect, leading to more stable and active catalysts.¹²⁵ Indeed, the mixed complex **13** with 1,3-dimesitylimidazol-2-ylidene (IMes) and PCy_3 showed improved catalytic activity.^{126–128} Grubbs further postulated that the saturated NHC analog 1,3-bis(mesityl)-4,5-dihydro-imidazol-2-ylidene (H_2IMes) should exhibit even better donation due to the absence of π -interactions. This was confirmed as complex **14**, known as Grubbs 2nd generation, outperformed catalyst **13**.¹²⁹

Hoveyda and co-workers discovered during their investigation of the reaction between catalyst **11** and 2-isopropoxystyrene the formation of catalyst **15**, in which one PCy_3 was replaced by the ether moiety.¹³⁰ Catalyst **15**, known as Hoveyda 1st generation, exhibited tremendous stability in air and could be recovered and recycled via column chromatography. Similarly, by reacting 2-isopropoxystyrene with catalyst **14**, they obtained the phosphine-free complex **16**, referred to as Hoveyda 2nd generation.^{131,132} This opened up new possibilities for tuning the properties of the catalytic system by modifying the NHC or styrene ether. For example, Grela and co-workers introduced an electron-withdrawing nitro group in complex **17**, increasing the initiation rate and enabling efficient olefin metathesis even at low temperatures.^{133,134}

Through the reaction of **14** with pyridine, Grubbs and co-workers obtained the bispyridine complex **18**, which possesses a high initiation rate.¹³⁵ The application of 3-bromopyridine further increased the lability of the dissociation ligand, leading to an even higher initiation rate for the resulting catalyst **19**, also known as Grubbs 3rd

generation.¹³⁶ This allowed for a controlled living ring-opening-metathesis polymerization of 2-norbornene derivatives.¹¹

While the Grubbs-type catalysts demonstrated superior functional group tolerance and allowed the performance of olefin metathesis in water, they lacked the high efficiency observed with Schrock-type catalysts, partly due to internal β -hydride elimination.^{43-46,73} The implantation of cyclic(alkyl)(amino)carbenes (CAAC) in ruthenium-based catalysis (complex **20-23**, Chart 2) allowed for turnovers exceeding 300 000, making them viable for industrial applications, as the β -hydride elimination pathway is essentially shut down.^{137,138}

Z-selective ruthenium-based catalysts for 1-alkene metathesis and stereoretentive catalysts have been achieved only in the two decades and will be discussed in detail in Chapters 5.1 and 0.

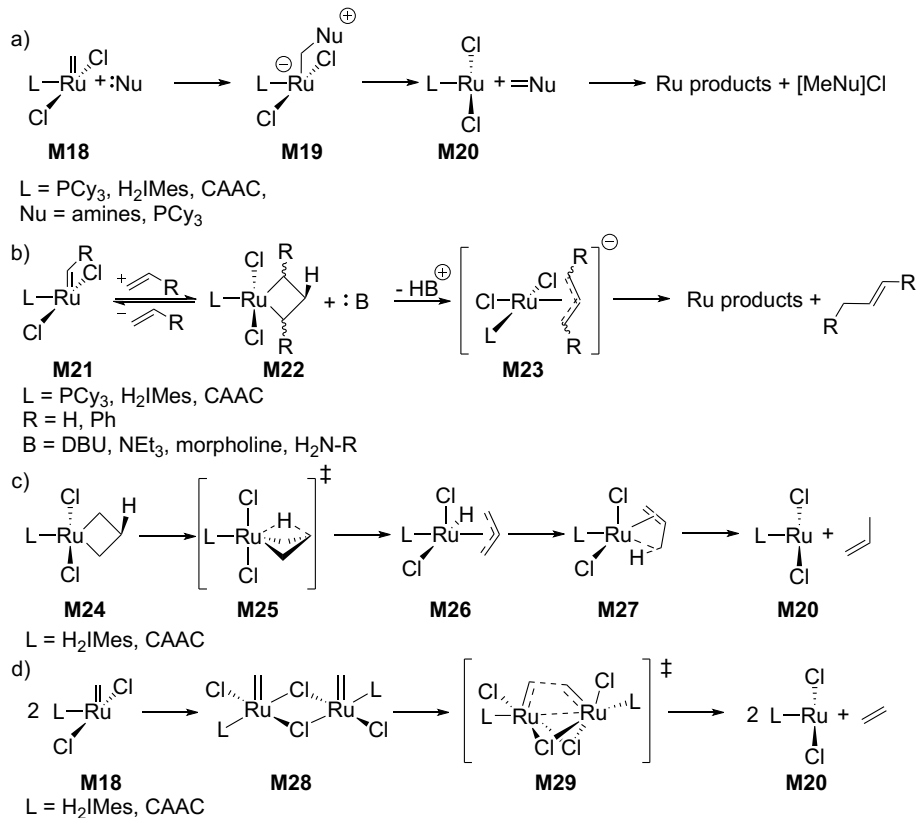
4. Decomposition and Stability of Ru-Based Catalysts

Ru-based olefin metathesis catalysts have undergone significant developments to enhance their activity, selectivity, stability, and resistance to decomposition. Catalyst stability is crucial for maintaining catalytic activity and facilitating catalyst recyclability. Deactivation of catalysts into inactive species diminishes their efficiency, whereas decomposition into isomerization-active species leads to product degradation through *E/Z* isomerization or double bond migration.^{71,139,140} As a result, their application in industrial settings is often limited due to the high cost and challenges associated with product purification and high catalyst loading. Consequently, extensive research has been conducted to understand the decomposition modes and their origins (Scheme 5).^{72,141}

Impurities, such as amines, can induce decomposition by nucleophilic attack on the methyldiene species (**M18**, Scheme 5a),^{68,69,142–144} or deprotonation of the metallacyclobutane (**M22**, Scheme 5b).^{66,144} Intrinsic decomposition modes, such as β -hydride elimination^{73,137,138} (**M25**, Scheme 5c), and bimolecular coupling^{64,138,145} (**M28**, Scheme 5d), can be addressed in the catalyst design. Therefore, numerous catalysts have been synthesized to reduce decomposition modes through catalyst design strategies.

For instance, phosphine-free catalysts mitigate donor-induced decomposition (Scheme 5a). The incorporation of CAACs in olefin metathesis has significantly improved turnover numbers (TONs), which is particularly evident in the ethenolysis of methyl oleate. For example, CAAC-based catalyst **20** achieved a TON of 330 000, whereas typical NHC-based Ru catalysts exhibited TONs of 2 000 – 5 000 in the same reaction.¹⁴⁶ This low activity stands in strong contrast to the performance of Hoveyda 2nd generation catalyst **16** in the butenolysis of methyl oleate, reaching 470 000 TONs.¹⁴⁷ The difference in activity between ethenolysis and butenolysis arises due to the formation of the methyldiene species **M18** and subsequently, the unsubstituted metallacyclobutane **M24**.

Scheme 5. Decomposition Pathways of Ru Olefin Metathesis Catalysts: (a) Nucleophilic Attack on the Methylidene Species M18, (b) MCB Deprotonation, (c) β -Hydride Elimination via M25, and (d) Bimolecular Coupling via M28.

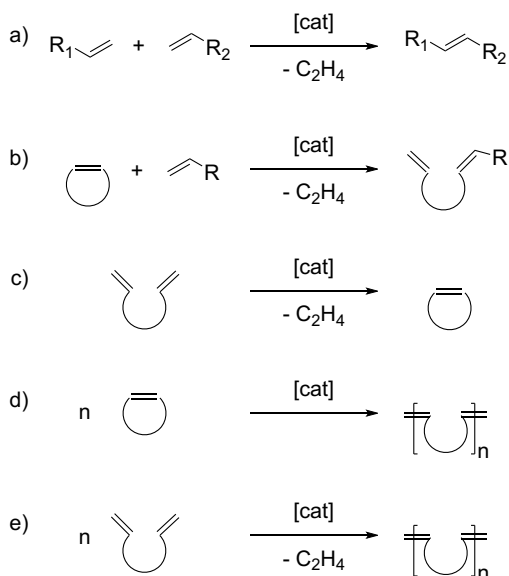


Recent studies have demonstrated that catalyst **20** is practically immune to β -hydride elimination due to the strong trans influence of CAAC compared with NHC in catalyst **16**.^{137,138} However, this benefit also renders catalyst **20** more susceptible to bimolecular coupling, which can be mitigated through high dilution. Nevertheless, high dilution increases the vulnerability of both catalysts to impurities.^{138,145} For instance, the TON of 470 000 for catalyst **16** in butenolysis requires triple distillation of methyl oleate and drops to 1 800 TONs when using commercially available substrates.¹⁴⁷ Surprisingly, CAAC-based catalysts do not exhibit superior stability against exogenous agents, particularly amines, as both CAAC- and NHC-based catalysts are susceptible to β -proton abstraction by bases. This susceptibility is likely due to the comparable net

electron donation of these ligands, resulting in similarly electron-rich Ru centers in the metallacyclobutane intermediates.¹⁴⁴

Furthermore, the intricate relationship between the catalyst, the substrate, and the specific type of olefin metathesis reaction (e.g., cross-metathesis, ring-closing metathesis, ring-opening polymerization, etc.; see Scheme 6) contributes to the ongoing development of olefin metathesis catalysts.⁴⁴ No single catalyst is suitable or optimal for all types of olefin metathesis reactions, necessitating the screening of multiple catalysts to identify the most suitable candidate for a specific process. Therefore, expanding the repertoire of available catalysts is crucial in addressing the diverse needs of various applications in this field.

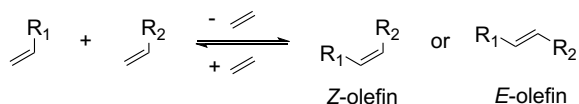
Scheme 6. Overview of Olefin Metathesis Reactions: (a) Cross-metathesis (CM), (b) Ring-opening Cross-metathesis (ROCM), (c) Ring-closing Metathesis (RCM), (c) Ring-opening Metathesis Polymerization (ROMP) and (e) Acyclic Diene Metathesis (ADMET).



5. Selectivity in Ruthenium-Based Olefin Metathesis

In olefin metathesis, two terminal olefins can form two stereoisomers: *E*- and *Z*-olefin (Scheme 7). For non-selective catalysts, the *Z*-olefin is often kinetically favored, while the *E*-olefin is the thermodynamic product, leading to a time-dependent product distribution due to the reversibility of the reaction.¹⁴⁸ Thus, the lack of kinetic stereocontrol leads to a product distribution representing the thermodynamic stability of the *E/Z* isomers.⁵⁰

Scheme 7. The Reaction of Two Terminal Olefins Can Form either a *Z*- or *E*-Olefin.



Selectivity in a reversible catalytic system is determined by the selectivity in the rate-determining transition state of its mechanism. Thus, establishing the mechanism, determining the rate-determining step, and controlling the steric environment of the latter are fundamental requirements for designing a stereoselective catalyst. Mapping and understanding these requirements have thus been critical for the present work, especially during the early phase of the doctoral project. Whereas a summary of the fundamental requirements is presented in Chapter 5 below, a more complete description, including a comprehensive review of the literature on ruthenium-catalyzed stereoselective olefin metathesis (including Paper II of this thesis), is available as Paper I.

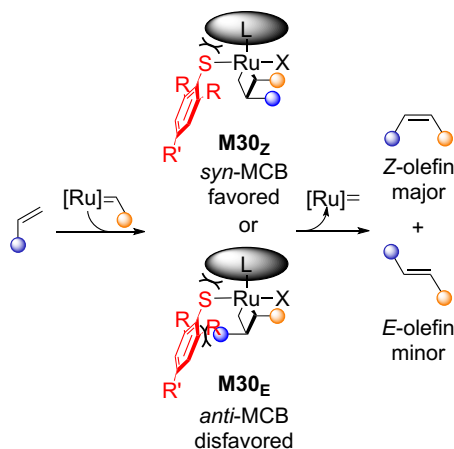
5.1. *Z*-Selectivity in Ruthenium-Based Olefin Metathesis

Kinetically *Z*-selective catalysts for 1-alkene metathesis have been achieved only in the last two decades, and only two such classes of catalyst exist: monothiolate^{55,79,149–153} and cyclometalated catalysts.^{154–160}

5.1.1 Monothiolate Catalysts

Early attempts to generate *Z*-selective Ru-based catalysts were based on the substitution of one chloride with a more sterically demanding anionic ligand, for instance, aryloxides,¹⁶¹ arylsulfates,^{162,163} and arylphosphates.¹⁶³ The break in symmetry and the larger steric pressure should enforce a *syn*-arrangement of the substituents on the MCB (Scheme 8). However, the obtained complexes showed only moderate *Z*-selectivity (up to ca. 30%) due to complex instability and wide Ru–O–R angles, which limited the steric pressure applied to the MCB. Using DFT, Jensen and co-workers predicted that the use of arylthiolates should lead to sharper angles and stronger Ru–SR bonds compared with the corresponding Ru–OR, and thus, enabling *Z*-selectivity.^{149,164}

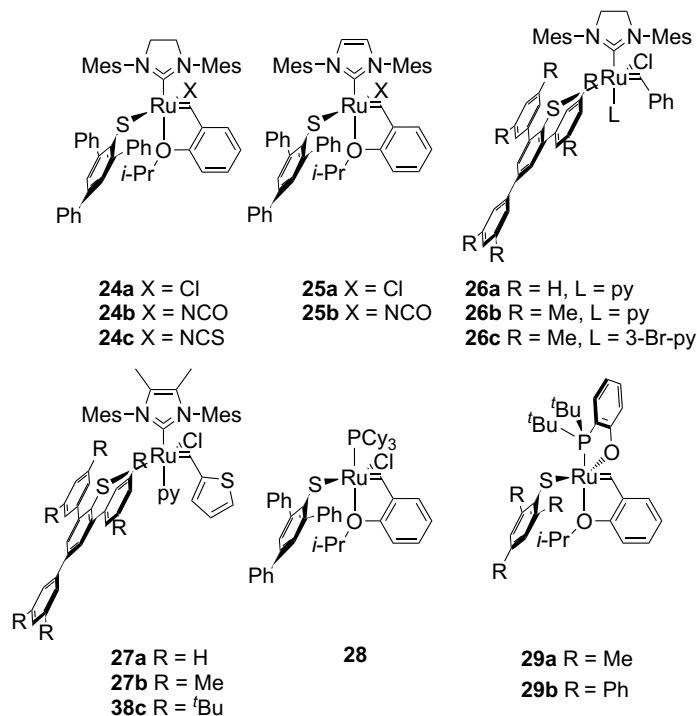
Scheme 8. Trans-Anionic Pathway of the *Z*-Selective Monothiolate-Based Catalysts. Steric Pressure from both the Dative (L) and the Arylthiolate Ligand Favors a *Syn*-Disubstituted MCB and hence, the *Z*-Alkene Product.



The one-step synthesis from non-selective Grubbs-type catalysts resulted in a large diversity of arylthiolate-substituted catalysts (Chart 3). Beneficial traits found in the parent Grubbs-type catalysts are often inherited by the respective monothiolate catalysts. Furthermore, DFT-guided development led to the implementation of isocyanate in complexes **24b** and **25b**, increasing their stability and enabling metathesis in air.¹⁴⁹ The low force constant of the Ru–S–R valence angle limits the *Z*-selectivity

of monothiolate catalysts. Thus, restraining the thiolate and preventing bending and rotation should increase *Z*-selectivity.

Chart 3. Various *Z*-selective Monothiolate Catalysts.



Hoveyda-Grubbs 2nd gen. type based on large monothiolates **24-25**, including the air-stable, **24b**, **24c**, and **25b** congeners.^{35,79,149,164,165} The pyridine and 3-bromo-pyridine fast-initiating versions **26-27**.^{35,55,152,165} The phosphine-based versions **28-29**.¹⁵¹

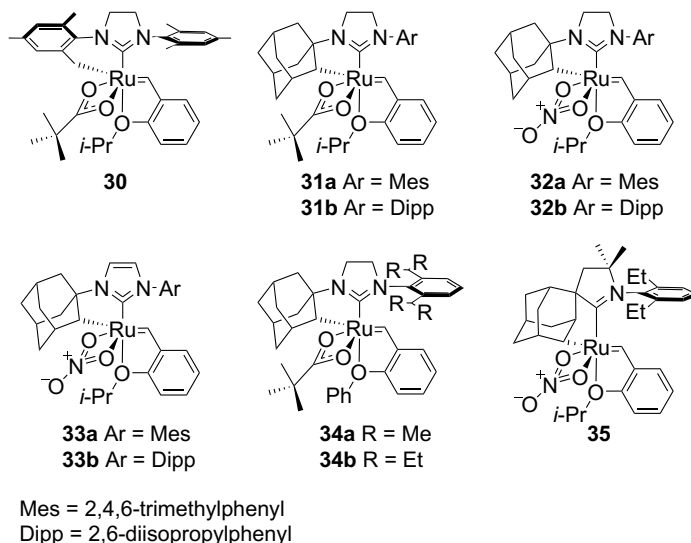
Monothiolate catalysts exhibit notable *Z*-selectivity along with high activity and remarkable tolerance toward air and acidic functional groups. However, maintaining this *Z*-selectivity becomes challenging as the catalyst decomposes, necessitating fast initiation and shorter reaction times. Consequently, there is a need for further enhancements in catalyst stability to address this challenge.^{55,79,151,152,164,165}

5.1.2 Cyclometalated Catalysts

The Grubbs-type *Z*-selective catalysts were discovered by chance in 2011.^{60,158,166} The addition of silver pivalate to **16** substituted not only both chlorides but resulted in the six-membered chelate complex **30** (Chart 4), via a carboxylate-assisted intramolecular

C–H bond insertion at the ortho methyl position of the mesityl group (cyclometalation).¹⁵⁸ Interestingly, **30** was both active and moderately *Z*-selective in olefin metathesis. Previously, cyclometalated complexes, lacking the alkylidene moiety, were reported as catalyst decomposition products.¹⁶⁷ The pivalate-assisted cyclometalation occurred even faster and cleaner with the CH₂-group on the N-1-adamantyl substituent, resulting in the five-membered chelate complex **31a**, which was a highly *Z*-selective catalyst.^{158,168–170}

Chart 4. Selected Cyclometalated Catalysts.

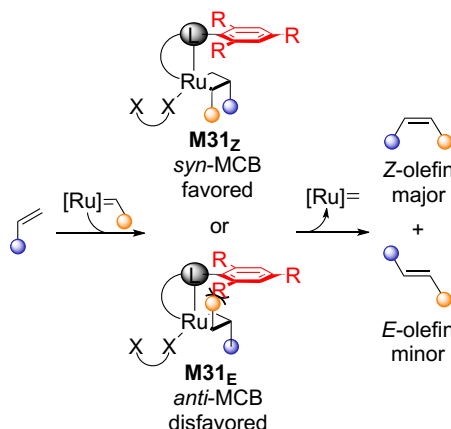


The 6-membered mesityl chelated version **30**.^{158,171} The 5-membered adamantly chelated version **31**.^{158,172–174} The improved nitrate version with various N-aryls **32–33**.^{155,156,159,160,172,174} The 5-membered adamantly chelated version with bulky N-Ar substituents **34**.^{160,175} CAAC-based complex **35**.¹⁵⁵

Experimental^{171,172} and theoretical^{154,176} studies reveal that two major structural features are required for achieving catalytic activity and *Z*-selectivity: a cyclometalated NHC (L) and a hemilabile η^2 -bound anionic ligand ($X^{\ominus}X$). The cyclometalation prevents the rotation of the NHC and forces the sterically demanding N-aryl group above the MCB, promoting the *Z*-selectivity (Scheme 9).¹⁷¹ An anionic ligand that can change from bidentate (η^2 -bound) to monodentate (η^1 -bound), stabilizes reaction intermediates and transition states, and is central to the catalytic activity.^{154,176} Catalysts

based on monodentate (η^1) anionic ligands, such as chloride, iodide, and phenolate, are essentially inactive.^{171,172,176}

Scheme 9. Cis-anionic Pathway of the *Z*-Selective Cyclometalates. Steric Repulsion Favors the Syn-MCB Configuration M31_Z, which Results in the *Z*-Olefin Product.



Five key elements have been identified, leading to a variation in the cyclometalated design (Chart 4): (i) the N-alkyl chelating group,^{156,171,177} (ii) the hemilabile η^2 -bound anionic ligand ($X^\cap X$),^{172,173} (iii) the N-aryl group,^{160,174} (iv) the carbene ligand (L),^{155,159,178} and (v) the chelating alkylidene ligand.^{160,175}

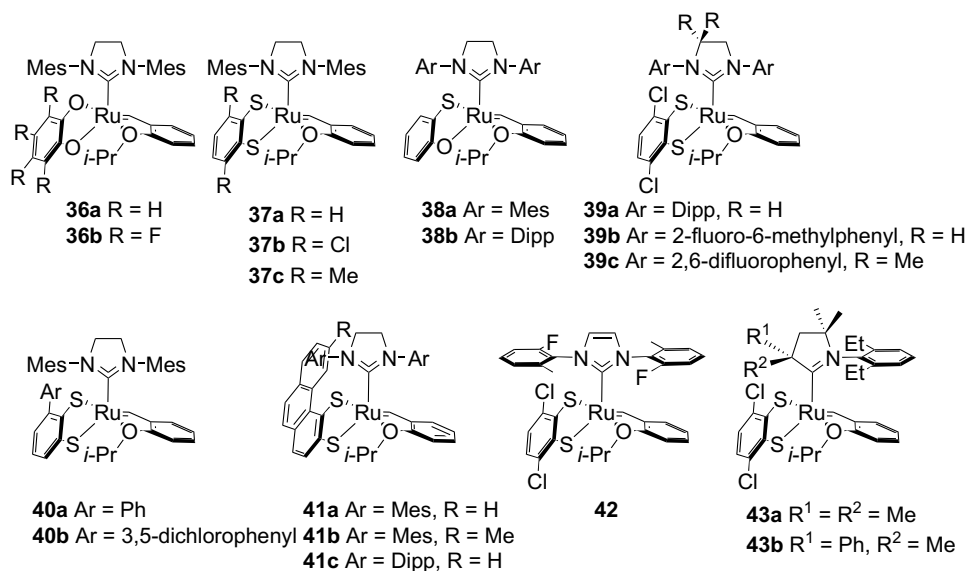
The cyclometalated catalysts display exceptional activity, efficiency, and *Z*-selectivity in a broad range of olefin metathesis applications, including cross-metathesis, ring-closing metathesis, ring-opening metathesis polymerization, asymmetric ring-opening cross-metathesis, and ethenolysis. The substrate scope is excellent, with important exceptions being sterically hindered and acidic substrates. Cyclometalated catalysts are greatly modifiable with respect to the carbene ligand, the N-alkyl chelating group, the N-aryl group, and the hemilabile η^2 -bound anionic ligand ($X^\cap X$).

5.2. Stereoretention in Olefin Metathesis

Hoveyda and co-workers demonstrated that by using a bidentate dithiolate ligand, leading to complex **37a** (Chart 5), high *Z*-selectivity (>98%) was obtained in ring-opening cross-metathesis and ring-opening metathesis polymerization.¹⁷⁹ Similar to the cyclometalated complexes (Chart 4), the bidentate ligand enforces metathesis via a

side-bound MCB. Yet, the NHC is not restricted and positions itself above the MCB covering both α -positions of the MCB with its aryls while the space above the β -position remains available (Scheme 10).¹⁸⁰ Nevertheless, the steric pressure of the NHC favors the formation of an all *syn*-MCB, leading to a highly *Z*-selective polymer.¹⁷⁹ This is in contrast to the catechol complex **36a**, where an unselective polymer was obtained.¹⁷⁹

Chart 5. Overview of Selected Stereoretentive Catalysts.

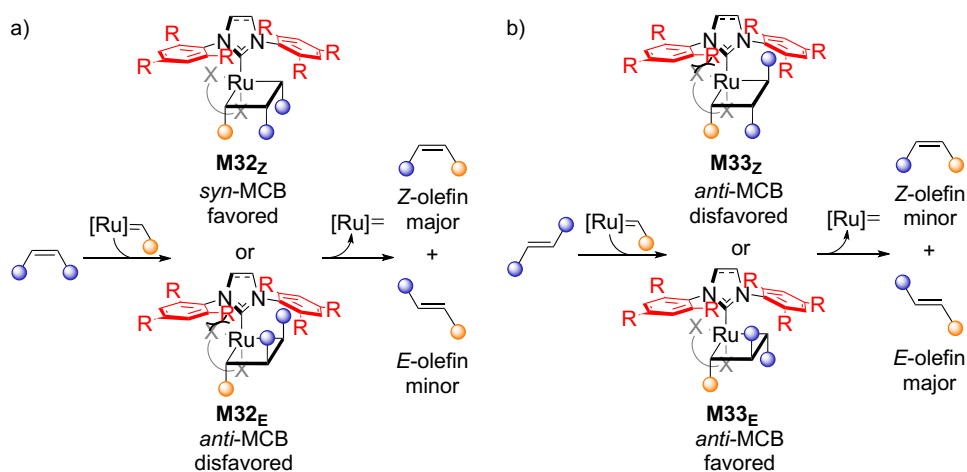


Catechthiolates with various N-aryls **37** and **39**.^{54,179,181} Mercaptophenolates with chelated benzylidene **38**.¹⁸² Sterically more demanding catechthiolates **40** and **41**.¹⁸³ The unsaturated NHC version **42**.¹⁸⁴ Finally, CAAC-based catalysts **43**.^{185,186}

The stronger σ -donation (disfavoring of olefin complex formation) and trans influence (repulsive interaction between NHC and trans sulfide moiety) of the catechthiolate ligand in **37a** shifts the rate-limiting transition step to cycloaddition (irreversible) from alkene association (reversible) in the catechol system **36a**. The weakened steric pressure of the NHC during the alkene association diminishes the selectivity.¹⁸⁷ The mercaptophenolate complexes **38a** and **38b** were all isolated with oxygen trans to the NHC. This arrangement is favored because of the lower trans influence of O versus S. Surprisingly, ring-opening metathesis polymerization of 2-norbornene with **38a**

revealed low *Z*-stereoretention (61%). DFT calculations of the reaction profile indicate that the mercaptophenolate system **38a** resembles the catechol (**36a**) system more than the dithiolate (**37a**) system with the alkene association as the rate-limiting step.¹⁸² The addition of chlorides in **37b** improved the stability by reducing the electron density at the sulfide site and consequently the trans influence of the ligand. In addition, the nucleophilicity of the thiolates is reduced, which decelerates the decomposition via intramolecular nucleophilic attack on the alkylidene.⁵⁴ In agreement with this observation, complex **37c** with two additional methyl substituents showed reduced stability due to the larger trans influence and nucleophilicity of the ligand.⁵⁴ Complex **37b** has found application in ring-opening cross-metathesis,¹⁷⁹ cross-metathesis,^{54,56,188,189} self-metathesis,¹⁸⁸ as well as ring-closing metathesis⁵⁷ tolerating hydroxyl, ketone, aldehyde, carboxyl acid, sterically hindered, and diene functionalities.^{54,56} Intrigued by these experimental results, Grubbs and co-workers investigated complex **37b** with the *E*- and *Z*-isomer of 5-tetradecene. In both cases, a near-equilibrium distribution of the products was reached after a 2 h reaction time while retaining the stereochemistry of the substrate.¹⁸¹ Based on these findings, they proposed the now accepted mechanism for stereoretention of catecholthiolate catalysts, which was further analyzed and confirmed using DFT (Scheme 10).^{181,190}

Scheme 10. Illustration of the Favored and Unfavored MCB Intermediates Formed in Stereoretentive Olefin Metathesis of (a) *Z*- and (b) *E*-Olefins.



Further experiments of **37b** with methyl oleate and methyl elaidate showed significantly lower activity with the trans isomer. Hence, three new complexes **39a-c** were synthesized with varying N-aryl sizes to facilitate the metathesis of either *Z*- or *E*-olefin (Chart 5). Indeed, testing the complexes **39a-c** in the cross-metathesis of 1-decene and 4-octene to 4-tridecene shows significant differences in their activity depending on the stereochemistry of the 4-octene.¹⁸¹ The substitution of a single methyl group with fluorine in **39b** improved the yield with the *E*-4-octene fourfold.¹⁸¹ By reducing the size of the ortho substituent (*i*-Pr > Me > F), the space between both N-aryl increases, which leads to a higher activity with *E*-olefins (**39a** < **37b** < **39b** < **39c**), presumably due to reduced steric interaction of the β -substituent of the MCB with the ortho substituent of the NHC-aryls (Scheme 10). The larger Dipp-moiety in **39a** improved the stability and allowed to lower the catalyst loading to 0.01 mol% for the self-metathesis of methyl oleate.¹⁸¹ For improving the *E*-stereoretentivity, Grubbs and co-workers intended that the phenanthrene-dithiolate in complexes **40a-c** increases the pressure on the H β of the MCB and subsequently enables *E*-selective olefin metathesis. However, the isomer with the phenanthrene moiety pointing toward the NHC is favored, diminishing any selectivity-inducing effect.¹⁸³

The unsaturated NHC in catalyst **42** enabled the stereoretentive metathesis of electron-deficient substrates. The unsaturated backbone of the NHC reduces the barrier to productive metathesis and increases the barrier to β -hydride elimination decomposition.¹⁸⁴ The CAAC-derivates **43a** and **43b** showed lower conversion due to slow initiation but produced a highly syndiotactic polymer in ring-opening metathesis polymerization of 2-norbornene.^{185,186}

Recent developments have proven stereoretentive catalysts to have complementary applications to *Z*-selective catalysts. The ability to produce *E*-olefins with high selectivity presents new opportunities and possibilities. Moreover, the substrate scope is broadened, enabling the transformation of trisubstituted olefins⁵⁶ and olefins containing a variety of functional groups, including electron-withdrawing groups (ketone, aldehyde, carboxyl acids) and other groups, located near the alkene functionality.^{54,181,184,189} A major drawback for the commercialization of these catalysts

is their general instability toward air, even in their solid form.^{191,192} Nevertheless, methods have been developed and examples have shown circumstances that partly overcome this. The catalyst design was improved by increasing the acidity of the catecholthiolate (reduction of the electron density on the S atom) and lowering the trans influence of the NHC.^{54,184} Furthermore, both cyclometalated and stereoretentive catalysts could benefit from advances in either design strategy because they follow similar mechanisms. However, the utility of stereoretentive metathesis is limited by the cost and accessibility of the isomerically pure starting materials.

5.3. Current Progress in *E*-Selectivity

Despite extensive study of ruthenium-based olefin metathesis selectivity, achieving *E*-selective metathesis of 1-alkenes remains challenging due to more complex steric requirements. The *Z*-selective pathway is favored by sterically hindering one plane of the MCB, as described in Chapter 5.1, either via a bulky thiolate or an NHC-aryl substituent. *E*-selectivity necessitates to sterically hinder both the α - and β -positions of the MCB from opposing sites, enforcing the *anti*-MCB. This constraint demands careful design to minimize steric requirements and uphold a catalytically active system.

Grubbs and co-workers pursued this goal with two different approaches: (i) modification of the NHC¹⁹³ and (ii) modification of the catecholthiolate.¹⁸³ The former led to catalyst **44** as a possible *E*-selective candidate (Figure 1a), although the cross-metathesis reaction of 5-decene and 1,4-dibenzoyloxy-2-butene revealed only a negligible improvement in *E*-selectivity compared with **16** (87 vs 86%, respectively).¹⁹³ The latter resulted in catalyst **41b** (Figure 1b), which favors the undesired isomer **M34** (with the phenanthrene ring system oriented away from the MCB, Figure 1c) during metathesis, thus causing no steric impact on the β -position. Furthermore, DFT calculations on the unsubstituted MCB predicted a 5 Å separation between H $_{\beta}$ and the phenanthrene ring when oriented toward the MCB. Consequently, the catecholthiolate ligand appears too distant to influence the orientation of the β -substituent to any great extent.¹⁸³

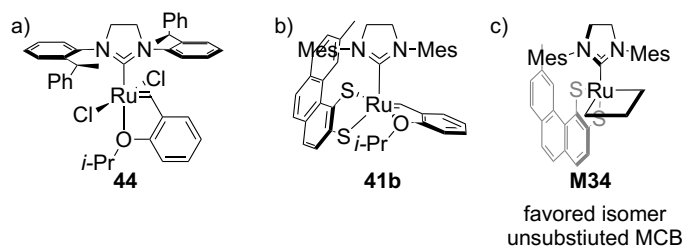


Figure 1. Proposed *E*-selective catalysts with (a) *N*-2-(1-phenylethyl)phenyl and (b) sterically demanding dithiolate with (c) its favored isomer in the key MCB intermediate.

6. Methods

6.1. Experimental Methods

6.1.1 Handling and Synthesis of Compounds

The reactions in this study were conducted in an argon-filled glovebox to ensure the exclusion of air and moisture and were performed at room temperature (25 ± 2 °C), unless stated otherwise. Solvents were dried and degassed using a glass contour solvent purification system. Subsequently, they were stored under argon in a glovebox over 4 Å molecular sieves for a minimum of 16 h prior to use. Liquid reagents underwent a degassing process involving five consecutive freeze/pump/thaw cycles. Following the degassing procedure, they were stored under argon in a glovebox freezer at -35 °C. Dry reagents were imported with an open lid directly to remove air and moisture.

6.1.2 Analysis of Synthesized Compounds

NMR spectra were obtained using Bruker Biospin AV500 and 850 Ascend spectrometers at a temperature of 298 K and were referenced against the residual proton signals of the deuterated solvents (^1H NMR).¹⁹⁴ High-resolution mass spectra (HRMS) were recorded using an orthogonal electrospray ionization (ESI) ion source connected either to a JMS-T100LC AccuTOF mass spectrometer from JEOL USA or a 6546 LC/Q-TOF mass spectrometer from Agilent. The ions were guided into the orthogonal accelerating time-of-flight (TOF) single-stage reflectron mass analyzer using a high-frequency and high-voltage quadrupole ion guide. Detection was achieved using a dual microchannel plate detector. Elemental analyses were performed using an Elementar Vario EL III analyzer to determine the elemental composition of the compounds. GC quantifications were performed on an Agilent 7890A series GC system equipped with a flame ionization detector (FID), an Agilent 7683B series autosampler, and an Agilent HP-5 polysiloxane column (30 m length, 320 µm diameter). Prior to analysis, GC samples were quenched using approximately 10 equivalents of ethyl vinyl ether in THF. For diffraction experiments, suitable crystals were immersed in Paratone-N (Hampton Research) in a nylon loop. Data collection was performed on a Bruker AXS

TXS rotating anode system using an APEXII Pt135 CCD detector with graphite-monochromated Mo K α radiation ($\lambda = 0.71073 \text{ \AA}$) and at the Swiss-Norwegian beamlines at the ESRF synchrotron in Grenoble, France, using Si double-mirror monochromated radiation ($\lambda = 0.62379 \text{ \AA}$) in conjunction with a 360-degree phi-scan and a Pilatus2M detector.

6.2. Computational Methods

Density Functional Theory (DFT) calculations were performed using Gaussian 16 with revisions C.01¹⁹⁵ utilizing the built-in ultrafine grid for numerical integrations.

6.2.1 Geometry Optimization

Based on a brief validation against experimentally determined stereoselectivity in Paper II,¹⁹⁶ ω B97XD was selected as the functional for geometry optimization. The Stuttgart/Cologne 28-electron relativistic effective core potentials (ECP28MDF)¹⁹⁷ were used for Ru atoms, in conjunction with the corresponding correlation-consistent valence double- ζ plus polarization basis set augmented by diffuse functions (aug-cc-pVDZ-PP),¹⁹⁷ as obtained from the Stuttgart/Cologne basis set repository.¹⁹⁸ Correlation-consistent, valence double- ζ plus polarization basis sets (cc-pVDZ¹⁹⁹ from the EMSL basis set exchange website)²⁰⁰ were used for all other atoms.

Geometries were optimized using tight convergence criteria (max. force $1.5 \cdot 10^{-5}$ a.u., RMS force $1.0 \cdot 10^{-5}$ a.u., max. displacement $6.0 \cdot 10^{-5}$ a.u., RMS displacement $4.0 \cdot 10^{-5}$ a.u.), without symmetry constraints, using tighter convergence criteria for the self-consistent field (SCF) optimization procedure (RMS change in density matrix $< 1.0 \cdot 10^{-9}$, max. change in density matrix = $1.0 \cdot 10^{-7}$), and with a spin multiplicity of 1. All stationary points were confirmed to be either minima (all-positive Hessian eigenvalues) or transition states (a single negative Hessian eigenvalue) by analytical calculation of the second derivatives, i.e., the Hessian matrix. Textbook procedures were used to calculate the translational, rotational, and vibrational components of the thermal corrections to enthalpies and Gibbs free energies within the ideal-gas, rigid-rotor, and harmonic oscillator approximations, with one exception: all frequencies

below 100 cm^{-1} were shifted to 100 cm^{-1} when calculating the vibrational component of the entropy, which is often referred to as the quasi-harmonic oscillator approximation.^{201,202} This approach is aimed at preventing breakdown (i.e., the asymptote corresponding to infinite entropy) of the harmonic approximation for low-frequency modes.²⁰³

6.2.2 Single-point Energy Calculations

The geometries obtained as described above were adopted in single-point energy calculations using the PBE functional in conjunction with the PCM polarizable continuum solvent model, with default parameters for benzene as solvent. All PBE calculations included Grimme's empirical D3 dispersion corrections,²⁰³ with revised Becke–Johnson damping parameters (labeled D3M(BJ) for brevity).²⁰⁴ In all single-point calculations, the above basis sets were extended to the valence quadruple- ζ level. Specifically, Ru was described by combining the 28-electron relativistic effective core potential (ECP28MDF)¹⁹⁷ with the corresponding correlation-consistent valence quadruple- ζ plus polarization basis set augmented by diffuse functions (aug-cc-pVQZ-PP)¹⁹⁷ from the Stuttgart/Cologne basis set repository.²⁰⁰ The other atoms were described by correlation-consistent, valence quadruple- ζ plus polarization basis sets (cc-pVQZ¹⁹⁹ from the EMSL repository).²⁰⁰ The convergence criteria for the SCF procedure were relaxed in single-point calculations (RMS change in density matrix $< 1.0 \cdot 10^{-5}$, max. change in density matrix $< 1.0 \cdot 10^{-3}$).

6.2.3 Calculation of Standard State-Corrected Free Energies

Free energies in solution were calculated using the following equation:

$$G_{\text{PBE-D3M(BJ)-PCM(Benzene)}}^{\text{T}=298.15\text{ K}} = E_{\text{PBE-D3M(BJ)-PCM(Benzene)}} + \Delta G_{\omega\text{B97XD,qh}}^{\text{T}=298.15\text{ K}} + \Delta G_{1\text{atm} \rightarrow 1\text{M}}^{\text{T}=298.15\text{ K}},$$

where $E_{\text{PBE-D3M(BJ)-PCM(Benzene)}}$ is the SP energy calculated with the computational model, $\Delta G_{\omega\text{B97XD,qh}}^{\text{T}=298.15\text{ K}}$ is the thermal correction to the Gibbs free energy calculated at the geometry-optimization level with the quasi-harmonic oscillator approximation as described above, and $\Delta G_{1\text{atm} \rightarrow 1\text{M}}^{\text{T}=298.15\text{ K}}$ is the standard state correction from the ideal gas at 1 atm to a 1 M solution (but exhibiting infinite-dilution, ideal-gas-like behavior), which is equal to $1.89\text{ kcal mol}^{-1}$ at RT.²⁰⁵

7. Results and Discussion

7.1. Application of S[∩]N-Ligands in *E*-Selective Olefin Metathesis

7.1.1 Thioindolate as a Selectivity-Inducing Ligand

The *E*-stereoretention presented by the catecholthiolate catalysts is seemingly the best starting point for *E*-selectivity.¹⁸¹ The approach by Grubbs and co-workers did not succeed because of the ineffectiveness of their steric demand.¹⁸³ Therefore, the introduction of a nitrogen center bearing a substituent to reduce the distance while maintaining a neutral Ru complex was considered. Furthermore, a planar, rigid, and bicyclic κ^2 -S[∩]N ligand should maximize the steric pressure on the MCB β -position. These requirements led to thioindolate as a selectivity-inducing ligand, and the results are presented in Paper II.¹⁹⁶

An initial computational study of **45a** revealed high *E*-selectivity for cycloreversion during the self-metathesis of propene, as the distance from ligand to H $_{\beta}$ was reduced to 2.35 Å (Table 1, entry 1). Moreover, the activation barrier for cycloreversion was in line with the previously published dithiolate catalyst **37b** (Table 1, entry 5).⁵⁴ The *E*-selectivity of the thioindolate system can be further improved by substituting position 2 of the ligand albeit at the expense of increased catalysis cost (Table 1, entries 2 and 3).

Table 1. Predicted Barriers to Propene Self-Metathesis, and Computed *E/Z* Selectivity for Catalysts **46 and the Proposed Catalysts **45a-c**.**

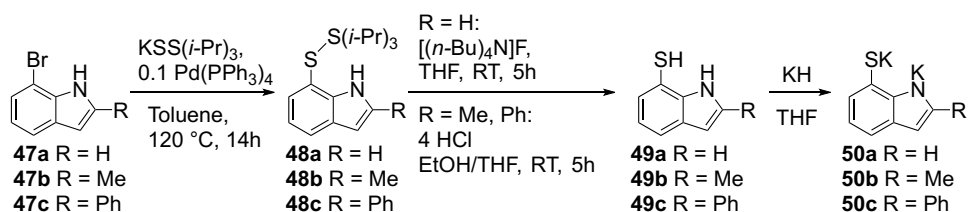
Entry	Cat.	R	ΔG^{\ddagger}_E ^a	ΔG^{\ddagger}_Z ^a	$\Delta\Delta G^{\ddagger}_{E/Z}$ ^b
1	45a	H	17.9	21.3	3.4
2	45b	Me	19.0	23.2	4.0
3	45c	Ph	24.1	35.5	11.5
4	46	Me	22.7	21.5	-1.2
5	37b	<i>i</i> -Pr	22.2	21.0	-1.2

in kcal mol⁻¹. ^avs precursor. ^b $\Delta\Delta G^{\ddagger}_{E/Z} = \Delta G^{\ddagger}_E - \Delta G^{\ddagger}_Z$.

Thus, I proceeded to synthesize ruthenium alkylidenes bearing such ligands. The thioindolate ligands were synthesized from commercially available 7-bromoindole

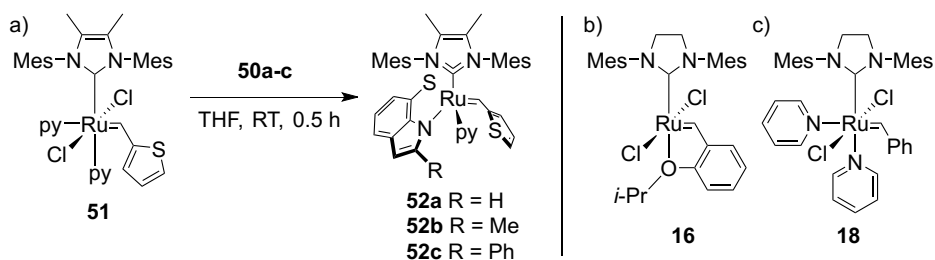
47a-c via a two-step procedure: Pd-catalyzed exchange of the bromine atom with a silylthioester forming **48a-c**, followed by deprotection using hydrochloric acid or $[(n\text{-Bu})_4\text{N}]\text{F}$ yielding the thioindole ligand **49a-c**. Subsequent treatment with KH in THF afforded the dipotassium salt **50a-c** (Scheme 11).

Scheme 11. Synthesis of Thioindolate Ligand 49a-c.



Salt metathesis with Hoveyda 2nd generation complex **16** failed in contrast to the reported sterically demanding dithiolates (**41a-c**), probably due to the steric clash between the isopropyl moiety and the ligand. While the reaction with the pyridine-stabilized complex **18** initially succeeded, the newly formed complex decomposed prior to isolation. Success was achieved using catalyst **51**, possibly due to the decreased steric demand of the 2-thienylmethylidene and the unsaturated NHC (Scheme 12a). Additionally, catalyst **51** has been successfully used as a precursor in Z-selective metathesis yielding the monothiolate complexes **27a-c**.⁵⁵

Scheme 12. Installation of Ligands 50a-c on (a) Catalyst 51 while Installation on (b) Catalyst 16 or (c) 18 Failed.



The three new complexes **52a-c** were synthesized in good yield (60-65%) and characterized by NMR and MS analysis, and in the case of **52a** and **52c** by single-crystal X-ray diffraction (Figure 2), although the quality of the crystal of **52a** only

permitted proof of connectivity. To the best of my knowledge, these represent the first set of transition-metal complexes bearing thioindolate chelate ligands.

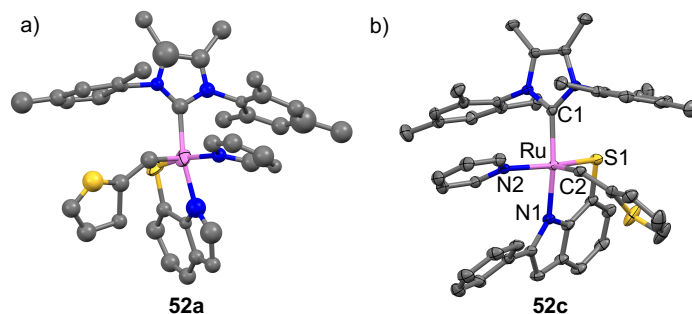
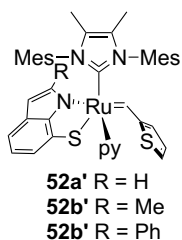


Figure 2. X-ray crystal structure of **52a** and **52c**, with displacement ellipsoids drawn at 50% probability for **52c**. For **52a**, the quality of the obtained crystals was good for proof of connectivity, but not for qualitative comparison. Ruthenium is shown in magenta, sulfur in yellow, nitrogen in blue, and carbon in gray. Hydrogen atoms have been omitted for clarity. Selected geometrical parameters for **52c** (bond distances in Å and angles in deg.): Ru–C1: 2.0704(17), Ru–N1: 2.1295(15), Ru–S1: 2.3031(5), Ru–N2: 2.1316(16), Ru–C2: 1.8490(18); N1–Ru–S1: 85.11(4), S1–Ru–C1: 87.27(5), N1–Ru–C1: 162.78(6).

The X-ray structures confirm the binding of the thioindolate fragment as an $S^{\eta}N$ -chelate. Crucially, and as predicted by the DFT calculations, the dianionic ligand adopts the orientation required for *E*-selective metathesis, with the thiolate sulfur cis, and the indolate nitrogen trans, to the NHC. In addition, DFT calculations predict that the unintended isomer **52a'**, with the thiolate sulfur trans, and the indolate nitrogen cis, to the NHC, is only 1.9 kcal mol⁻¹ less stable, and may also be present (Table 2, entry 1). Indeed, ¹H NMR spectra of catalyst **52a** consistently exhibit a minor alkylidene singlet (5%) at $\delta = 15.4$ ppm, with the main alkylidene signal located at $\delta = 16.2$ ppm. A NOESY experiment confirmed the existence of an exchange equilibrium between these two alkylidene singlets, with the minor alkylidene species being 1.8 kcal mol⁻¹ less stable than the dominant species. From the agreement between the NMR experiment and the DFT calculations, the minor species is presumed to be **52a'**. Such minor alkylidene species are not observed for complexes **52b** and **52c** containing larger thioindolates, and calculations also indicate that the isomers **52b'** and **52c'** with rotated $S^{\eta}N$ ligands are energetically unfavorable (Table 2, entry 2 and 3).

Table 2: Predict vs Experimental Relative Stability of the Isomers 52a'-c'.

Entry	Cat.	$\Delta G_{\text{DFT}}^{\text{a}}$	$\Delta G_{\text{Exp}}^{\text{b}}$
1	52a'	1.9	1.8
2	52b'	4.0	-
3	52c'	11.3	-

in kcal mol⁻¹. ^avs respective isomer **52a-c**.
^bRelative abundance in ¹H NMR.

The metathesis activity of **52a** and **52b** was initially assessed by reaction with styrene at room temperature. Unexpectedly, ¹H NMR analysis showed no evidence of the stilbene (self-metathesis product). Instead, a new alkyldiene singlet along with vinylthiophene was observed. The new alkyldiene species, identified as the benzyldiene analogs of **52a** and **52b**, resulted from unproductive metathesis with styrene. Complex **52a** reaches equilibrium within 15 min, versus nearly an hour for catalyst **52b**. The slower reaction of **52b** is consistent with the higher barrier to metathesis calculated for the bulkier thioindolate in the H₂IMes analogs **45a-c** (see Table 1). Increasing the reaction temperature or time resulted in the loss of the alkyldiene signals as well as a black precipitate, indicating catalyst decomposition and formation of Ru nanoparticles.⁶⁷ The reaction with allylbenzene was examined to test whether the reduced steric bulk at C_β would enable productive metathesis, but again, no metathesis products were observed. In the case of **52a**, 35% 2-vinylthiophene was detected by ¹H NMR analysis with full conversion of the starting catalyst. In comparison, 17% of **52b** remained even after a 12 h reaction time, indicating slow initiation and a relatively stable precatalyst. Isomerization of allylbenzene was also observed, presumably by decomposed Ru species.^{67,71} Surprisingly, catalyst **52a** showed low activity in propene self-metathesis (0.35 turnover), although the calculated barrier for cycloreversion was similar to complex **37b**. Moreover, the major product was *Z*-2-butene (73%), instead of *E*-2-butene, as initially predicted. Further DFT calculations identified 2-butene dissociation as the rate-limiting step favoring the dissociation of *Z*-2-butene (see Figure 3). The higher barrier for dissociation likely originates from the increased steric congestion of the system.¹⁹⁶

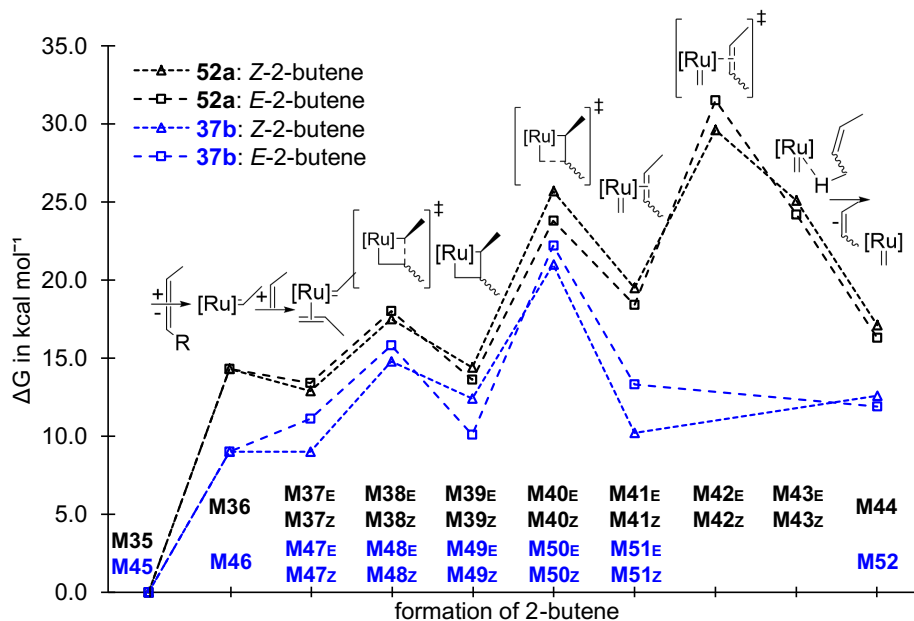


Figure 3. Gibbs free energies calculated for intermediates and transition states of propene self-metathesis for catalysts **52a** (=M35, black) and **37b** (=M45, blue). The Z-2-butene pathways are indicated by triangles and those of E-2-butene by squares. A standard state corresponding to an ideal 1 mol L⁻¹ solution (benzene) is assumed for all species, and free energies are given relative to the respective precursors.

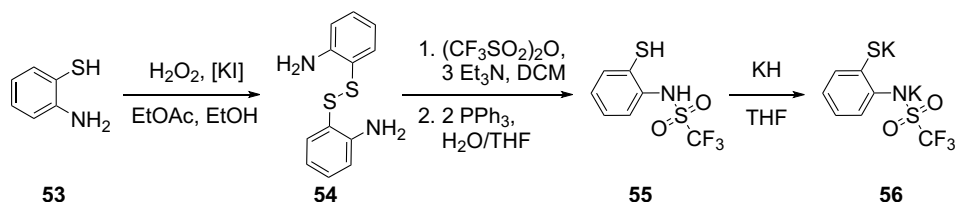
Based on these results, the development of an *E*-selective catalyst necessitates two key factors: (i) applying opposing steric pressure from different directions, and (ii) maintaining low net steric congestion to enable productive metathesis, particularly during the dissociation of the olefin product from the metal.

7.1.2 Trifluoromethanesulfonyl Group for Higher Stability

Reducing the electron density of **37a** by the addition of two chlorides resulted in the more stable and active complex **37b**. Therefore, the question arose as to whether reducing the electron density on N would enable more catalytic activity of the S⁰N system as well. This led to the investigation of the mercaptophenyltrifluoromethanesulfonamide ligand precursor **55**. The neighboring trifluoromethanesulfonyl moiety should increase the acidity and drastically decrease electron density at the N. The results are presented in Paper III.

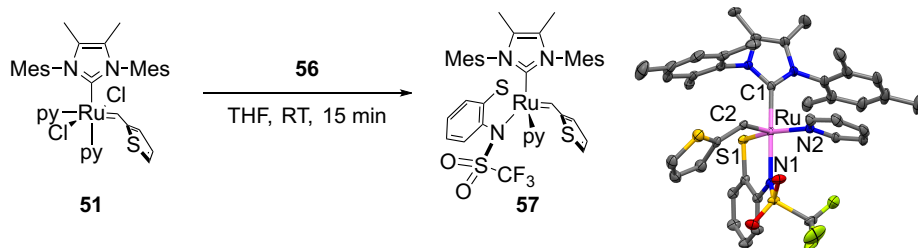
The ligand **55** was prepared by adapting a protocol from the literature (Scheme 13).^{206,207} Commercially available 2-aminothiophenol **53** was oxidized into bis(2-aminophenyl) disulfide **54**. Subsequently, disulfide **54** was reacted with trifluoromethanesulfonic anhydride at low temperature to yield the corresponding sulfonamide derivate, where the disulfide bond was cleaved using triphenylphosphine and water, resulting in the ligand **55**. The latter was transformed into the required dipotassium salt **56** for installation on Ru complexes.

Scheme 13. Synthesis of Mercaptophenyltrifluoromethanesulfonamide Ligand **55**.



Similar to the thioindolate, the salt metathesis of dipotassium salt **56** and Ru alkylidene complex **51** worked well with 90% isolated yield (Scheme 14). Complex **57** was characterized using NMR, MS, and single-crystal X-ray diffraction, revealing the expected isomer with N trans to the NHC.

Scheme 14. Installation of **56** on Ru Complex **51**.



X-ray crystal structure of **57**, with displacement ellipsoids drawn at 50% probability. Ruthenium is shown in magenta, sulfur in yellow, nitrogen in blue, fluorine in green, and carbon in gray. Hydrogen atoms have been omitted for clarity. Selected geometrical parameters (bond distances in Å and angles in deg.): $\text{Ru}-\text{C}1 = 2.056(2)$, $\text{Ru}-\text{N}1 = 2.207(19)$, $\text{Ru}-\text{S}1 = 2.264(7)$, $\text{Ru}-\text{N}2 = 2.134(19)$, $\text{Ru}-\text{C}2 = 1.850(2)$, $\text{N}1-\text{Ru}-\text{S}1 = 83.03(5)$, $\text{S}1-\text{Ru}-\text{C}1 = 86.49(6)$, $\text{N}1-\text{Ru}-\text{C}1 = 167.30(8)$.

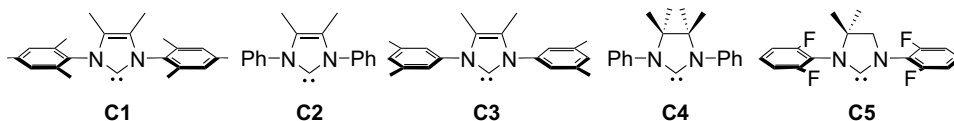
Complex **57** exhibited slightly better activity in the self-metathesis of propene than complex **52a** (0.95 vs 0.35 turnovers) and increased *E*-2-butene formation (37% vs 27% with **52a**). However, the observed *Z*-selectivity again indicates a high barrier to

dissociation, as during the cycloreversion step the *E*-pathway is favored by 3.5 kcal mol⁻¹. Therefore, it is hypothesized that reducing the steric demand of the NHC should be beneficial for product dissociation, which will be discussed in the next chapter.

7.2. Utilizing Smaller NHCs for Higher Activity

In the previous chapters, it was determined that the rate-determining step shifted from cycloreversion to product dissociation due to the steric bulk of the system, altering the predicted selectivity from *E* to *Z* and decreasing the overall activity of the catalytic system. Thus, reducing the steric demand of the NHC **C1** by minimizing the ortho substituents on the aryl moiety should facilitate easier product dissociation. Additionally, the diminished steric size of the NHC-aryls would create more space above the β -position of the MCB, enhancing the *E*-selectivity of the catalyst. The selected NHCs **C2-5** are shown in Chart 6. This work is presented in Paper III.

Chart 6. Selected N-Heterocyclic Carbenes C2-5 with Smaller Ortho Substituents.

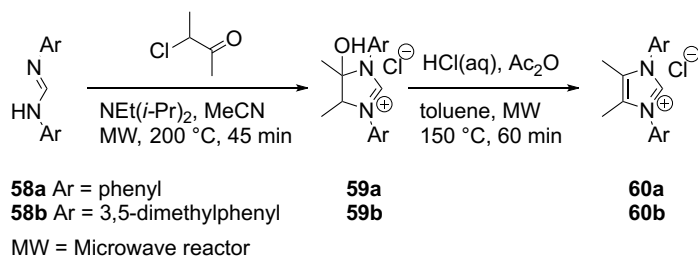


C2 and **C3** were specifically chosen to evaluate the impact of steric hindrance near the ruthenium center, while maintaining similar electronic properties as **C1**. NHC **C4**, in particular, was selected because Grubbs and co-workers reported that a tetramethyl-substituted backbone should restrict the rotation of the NHC aryl groups, preventing potential decomposition pathways such as C–H activation, which is a concern with phenyl-based NHCs.^{208,209} Despite having larger ortho fluorine substituents compared with the ortho hydrogens in **C2-4**, NHC **C5** was selected because it has been successfully applied for *E*-stereoretentive metathesis in catalyst **39c** and is immune to C–H activation.

The synthesis of imidazolium salts **60a** and **60b**, precursors to the NHC **C2** and **C3**, respectively, proved to be unexpectedly challenging (Scheme 15). By adapting the protocol for highly substituted imidazolium salts developed by Glorius and co-workers,

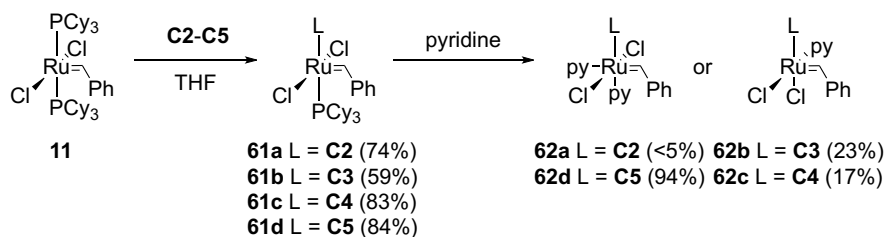
the synthesis was improved by performing the reaction in a microwave reactor (MW).^{210,211} The amidines **58a** and **58b**²¹² were reacted with 3-chloro-2-butanone to yield the imidazolium salt **59a** and **59b**. These intermediate salts were then dehydrated using acetic anhydride and hydrochloric acid, resulting in the formation of the unsaturated imidazolium salt **60a** and **60b**. The use of a microwave reactor significantly reduced the reaction time compared with the original protocol developed by Glorius and co-workers, which relied on standard heating techniques. In the microwave reactor, each reaction was completed within 1 h, whereas it took several days using traditional heating methods. The imidazolium salts of **C4** and **C5** were synthesized according to their respective reported synthesis.^{181,208}

Scheme 15. Microwave-Assisted Synthesis of Imidazolium Salts **60a** and **60b**.



The synthesis of the desired pyridine-stabilized precatalysts **62a-d** involved the reaction of Grubbs 1st generation **11** with the in situ generated carbenes **C2-5** derived from the respective imidazolium salts and potassium bis(trimethylsilyl)amide (KHMDS) with subsequent exchange of tricyclohexylphosphine with pyridine (Scheme 16). However, the synthesis of phenyl-based complexes **62a-c** proved to be challenging because they exhibited general instability and were prone to decomposition, presumably resulting from C–H activation of the NHC ligand.^{167,213,214}

Scheme 16. Synthesis of the Pyridine-Stabilized Precatalysts **62a-d**.



For **62a**, the stability problems resulted in yields insufficient for product isolation. Complex **62b**, containing a more substituted NHC, was isolated in 23% yield, and single-crystal X-ray diffraction analysis revealed a cis-configuration of the two chloride ligands (Figure 4). During attempts to grow crystals of **62b** in a glovebox freezer (-35 °C), a partial color change of the microcrystalline solid from green to blue was observed over time. The ¹H NMR analysis of the blue microcrystalline compound showed decomposition through the lack of an alkylidene signal, presumably via C–H activation enabled through the vacant coordination site at Ru in the monopyridine complex.^{167,213}

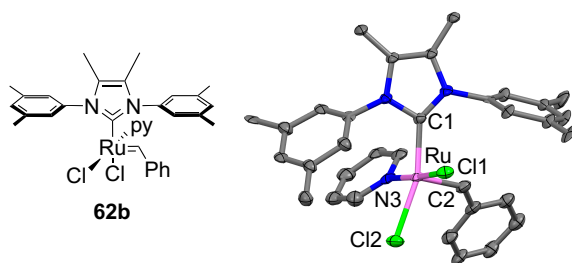


Figure 4. X-ray crystal structure of **62b** with displacement ellipsoids drawn at 50% probability. Ruthenium is shown in magenta, chloride in green, nitrogen in blue, and carbon in gray. Hydrogen atoms have been omitted for clarity. Selected geometrical parameters (bond distances in Å and angles in deg.): Ru–C1 = 2.03(2), Ru–N1 = 2.071(17), Ru–C11 = 2.402(5), Ru–Cl2 = 2.416(6), Ru–C2 = 1.84(2), C11–Ru–Cl2 = 88.09(19), C11–Ru–C1 = 89.6(5), Cl2–Ru–C1 = 160.9(6), C11–Ru–N1 = 173.2(6), C2–Ru–C1 = 96.1(9).

The expectation that the tetramethyl-substituted backbone in **62c** would restrict the rotation of the NHC aryls, thereby preventing C–H activation and increasing stability, did not hold true.^{208,209} While I was able to improve the yield of the phosphine-stabilized complex **61c** from 55% to 83%,²⁰⁸ attempts to improve the exchange of the PCy₃ ligand with pyridine to obtain **62c** were disappointing, resulting in only 17% yield of the desired pyridine-stabilized complex. Various strategies, such as reducing reaction time, using lower temperatures, or adding hexane, did not improve the yield. In addition, the initial green solution of **62c** turned red even at -35 °C, indicating decomposition of the target complex. Efforts to obtain suitable crystals for X-ray diffraction analysis resulted in the formation of complex **63** instead of **62c** (see Figure 5). Previous reports by Grubbs and co-workers described similar complexes stabilized

by two PCy₃ ligands, featuring double C–H activation.²¹⁵ Furthermore, stability problems were also encountered with the phosphine-stabilized precursor **61c**.²⁰⁸ The pyridine exchange process may contribute to the decomposition due to the formation of pyridinium chloride. The attempt to prevent the formation of **63** by washing complex **62c** with hexane after the pyridine exchange, aiming to remove free PCy₃ and excess pyridine, unfortunately led to product loss due to decomposition. This was evident as the filtrate remained red and the green filter cake disappeared.

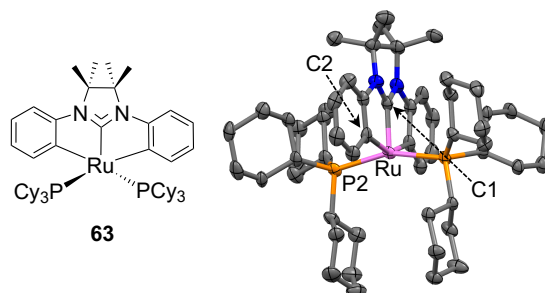
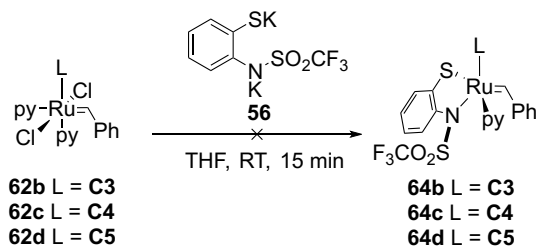


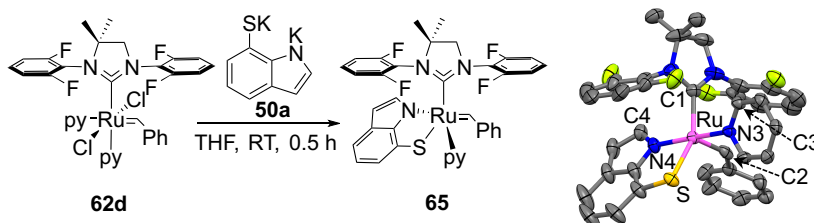
Figure 5. X-ray crystal structure **63**, with displacement ellipsoids drawn at 50% probability. Ruthenium is shown in magenta, phosphine in orange, nitrogen in blue, and carbon in gray. Hydrogen atoms have been omitted for clarity. Selected geometrical parameters (bond distances in Å and angles in deg.): Ru–C1: 1.915(4), Ru–C2 = 2.150(4), Ru–P2 = 2.372(15), C1–Ru–C2 = 76.07(16), C1–Ru–P2 = 101.79(16), C2–Ru–P2 = 92.32(14).

These observations indicate that the rotation of the NHC aryl groups cannot be prevented by simple means, for instance, by using an extensive backbone. Therefore, the introduction of the ortho fluorinated NHC **C5**, which reduces the steric environment around the Ru center while being resistant to decomposition, was pursued.^{181,215} In comparison to complexes **62a-c**, the 2,6-difluorophenyl-based complex **62d** was successfully isolated in high yield (94%, see Scheme 16), and only 30% decomposed after 12 h in a NMR tube. The high stability of **62d** suggests that the decomposition observed earlier was indeed a result of the rotation and subsequent C–H activation of the NHC aryl groups.

The reaction of the phenyl-based complexes **62b** and **62c** with the sulfonamide ligand **56** resulted in the disappearance of the alkylidene signal, indicating decomposition of the complexes. Even salt metathesis with the more stable precursor **62d** led to decomposition through the formation of nanoparticles (Scheme 17).

Scheme 17. Attempted Installation of Sulfonamide 56 on Ru Complex 62b-d.


Considering the unsuccessful installation of **56**, the investigation shifted toward the installation of thioindolate ligand **50a** on **62b-d**. Once again, the reaction with **62b** and **62c** led to unstable Ru alkylidene complexes that decomposed during purification. In contrast, the reaction with **62d** resulted in the formation of the stable complex **65**. Contrary to the previous study on **52a**, single-crystal X-ray diffraction analysis of **65** revealed that the isomer with N in a cis orientation to the NHC is more favorable, as shown in Scheme 18.

Scheme 18. Installation of Thioindolate 50a on 62d.


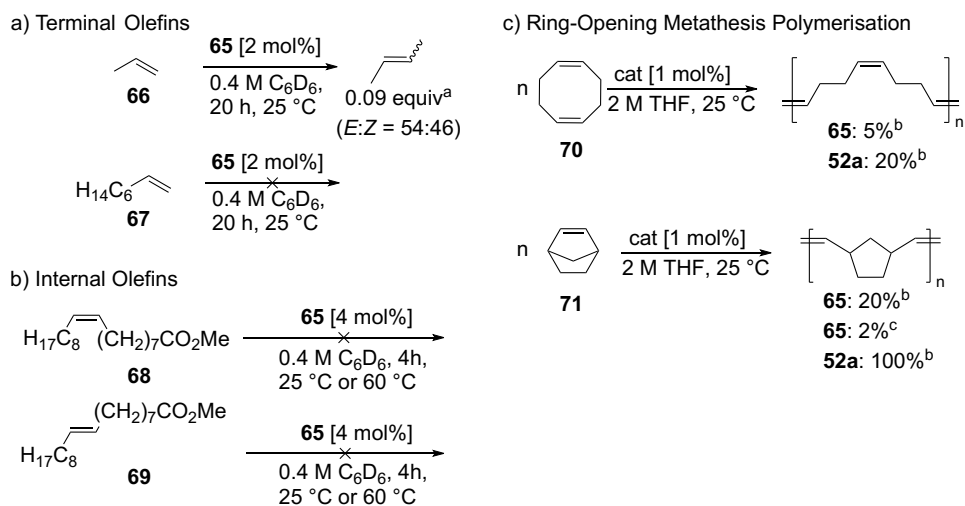
X-ray crystal structure of **65**, with displacement ellipsoids drawn at 50% probability. Ruthenium is shown in magenta, sulfur in yellow, nitrogen in blue, fluorine in green, and carbon in gray. Hydrogen atoms have been omitted for clarity. Selected geometrical parameters (bond distances in Å and angles in deg.): Ru–C1 = 2.034(5), Ru–N4 = 2.056(4), Ru–S = 2.3627(13), Ru–N3 = 2.144(4), Ru–C2 = 1.810(6), N1–Ru–S = 88.59(10), S–Ru–C1 = 149.93(17), N3–Ru–C1 = 93.97(17), C4–N4–N3–C3 = 43.05.

This preference is likely due to the reduced steric hindrance and weaker trans influence of the NHC allowing stabilization of the isomer (**65**) in which the bulkier indolate part of the S¹N ligand is placed near the smaller, fluorine-substituted NHC.

Catalyst **65** displays low catalytic activity in the self-metathesis of propene **66**. After complete loss of starting complex **66** in the propene self-metathesis experiment, only 23% of free styrene was observed in the ¹H NMR spectrum, suggesting that 77% of the

catalyst decomposes before completing the initiation. The initiated complex manages to produce a low amount of 2-butene (0.09 turnovers), slightly favoring the *E*-isomer (54% vs 46% *Z*-isomer). The application of larger terminal olefins, such as 1-octene **67**, or internal olefins, such as methyl oleate **68** and methyl elaidate **69** (Scheme 19, parts a and b), showed no productive metathesis. In contrast, low catalytic activity was recorded in the ring-opening metathesis polymerization (ROMP) of cyclooctadiene **70** and 2-norbornene **71** (Scheme 19, part c).

Scheme 19. Tested Olefin Metathesis Reactions of Catalyst **65**.



^aEquivalents vs **65** determined by ¹H NMR analysis. ^bYield determined by ¹H NMR analysis. ^cIsolated yield using 0.1 mol% catalyst loading.

The stereochemistry of the resulting polynorbornene was highly dependent on the catalyst. While catalyst **52a** was highly *Z*-selective (89%), catalyst **65** only achieved a moderate *Z*-selectivity (50%) similar to the mercaptophenonlate complexes **38a** and **38b**.¹⁸² The lower *Z*-selectivity of **65** presumably originates (i) from the lower Lewis base character of N versus S or (ii) from the sterically more accessible NHC. While the former would result in alkene coordination as rate-determining step where steric factors play a minor role, the latter with a diminished steric effect of the smaller NHC-aryls would lead to an increased *E*-selectivity.^{181,182}

Still, this unexpectedly low activity of the catalyst is surprising considering that the smaller NHC in catalyst **65** was expected to enhance product dissociation, which was identified as the limiting factor in catalyst **52a**. Thus, further DFT calculations on catalyst **65** were initiated to explain the low activity.

They indicate that catalyst **65** is approximately 6 kcal mol⁻¹ lower in energy than isomer **65'** (where the thioindolate ligand is oriented with S cis, and N trans, to the NHC), suggesting that the two observed alkylidene signals in the ¹H NMR (at 14.6 and 15.0 ppm) belong to catalyst **65** due to the presence of the asymmetric NHC ligand.^{181,196} Additionally, whereas a NOESY experiment indicated dynamic exchange between the corresponding two isomers (the indolate cis and trans to the NHC, respectively) of **52a**,¹⁹⁶ no signs of a corresponding exchange between the 14.6 ppm and 15.0 ppm signals were observed for **65**.

Next, the initiation of catalyst **65** was investigated. Surprisingly, pyridine dissociation from **65** is costly, with a barrier of 26.6 kcal mol⁻¹ via transition state **M54** (Figure 6), due to the weak trans influence of the indolate amide nitrogen atom and the significant through-complex N(amide)–Ru–N(pyridine) π interaction (the thioindolate–pyridine dihedral angle is ca. 43° in **65**; see Scheme 18).

Further calculations at successively longer Ru–py distances resulted in monotonically increasing potential energies, and the complete loss of pyridine from **M55** does not seem to involve a transition state on the potential energy surface (PES). Therefore, it can be assumed that dissociation from the second coordination sphere proceeds at a rate close to the diffusion limit. In conclusion, the estimated barrier for pyridine loss from **M53 (65)**, including the dissociation of pyridine from the second coordination sphere, is 26.6 kcal mol⁻¹.

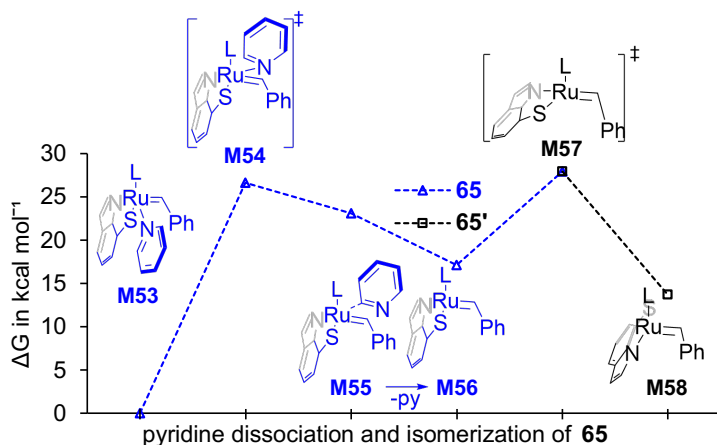


Figure 6. Gibbs free energies calculated for the initiation of **65** (the model of which is **M53**) via pyridine dissociation and isomerization to the **65'**-derived **M58**. Complexes with the thiolate sulfur atom trans to the L-ligand (as in the **65** precursor) are indicated by blue triangles and those with a corresponding cis-configuration by black squares. A standard state corresponding to an ideal 1 mol L⁻¹ solution (benzene) is assumed for all species, and free energies are given relative to the most stable rotamer of the **65** precursor.

Subsequent isomerization of the four-coordinate complex **M56** to **M58** by rotating the S⁰N ligand around an axis nearly parallel to the Ru alkylidene bond,¹⁸² would result in the thiolate S atom cis to the NHC ligand. The stronger σ donation and trans influence of the thiolate S atom, positioned trans to the evolving MCB, should facilitate the metathetic bond-rupture and bond-formation steps. Indeed, the cycloreversion step of **65'** is 4.7 kcal mol⁻¹ lower in energy than that of **65** (see Figure 7). This S⁰N ligand isomerization was assumed to be fast because of the dynamic equilibrium between the two corresponding isomers of **52a** observed in a NOESY experiment⁵⁶ and the low barrier calculated for the catecholthiolate rotation in the 14-electron complex of the stereoretentive catalyst **37b**.^{182,216} However, the predicted barrier to S⁰N ligand rotation (27.9 kcal mol⁻¹ via **M57**) is surprisingly high and comparable to that of the pyridine dissociation. The faster isomerization observed for **52a** presumably originates from the larger **C1** ligand, as calculations on the bidentate catecholthiolate ligand in stereoretentive catalysts identified a correlation between steric bulk and ease of rotation.²¹⁶

Continued initiation requires the coordination of the substrate (here: propene) to yield the π -complex **M59** or **M67**, cycloaddition and cycloreversion to yield the

corresponding styrene π -complexes **M63** or **M71**, and styrene dissociation to form the 14-electron ethylidene species **M66** or **M74**. The free energies calculated for these intermediates and transition states reveal that both the key metathetic bond rupture and formation steps are clearly disfavored by the amide moiety of the $S^{\wedge}N$ ligand being situated trans to the evolving MCB. Metathesis activity is known to benefit from ligand-to-metal σ donation from the trans-disposed ligand.²¹⁷ The amide unit is a poor σ donor, compared with the thiolate of **52a** and **65'**. Surprisingly, the low trans influence of the amide moiety did not increase the barrier to styrene dissociation (24.6 kcal mol⁻¹, via **M64**) for **65** compared with **65'** (24.3 kcal mol⁻¹, via **M72**). The subsequent styrene dissociation from the weakly bound complexes **M65** and **M73** is linked to significant stabilization, not involving transition states on the PES, and can be assumed to be fast. Contrary to initial assumptions, the initiation of **65** does not involve $S^{\wedge}N$ ligand rotation (via **M57**) for metathesis to proceed via the intermediates and transition states of the catalytically more active **65'**. Even subsequent isomerization of the ethylidene species **M66** to **M74** is unlikely (31.6 kcal mol⁻¹).

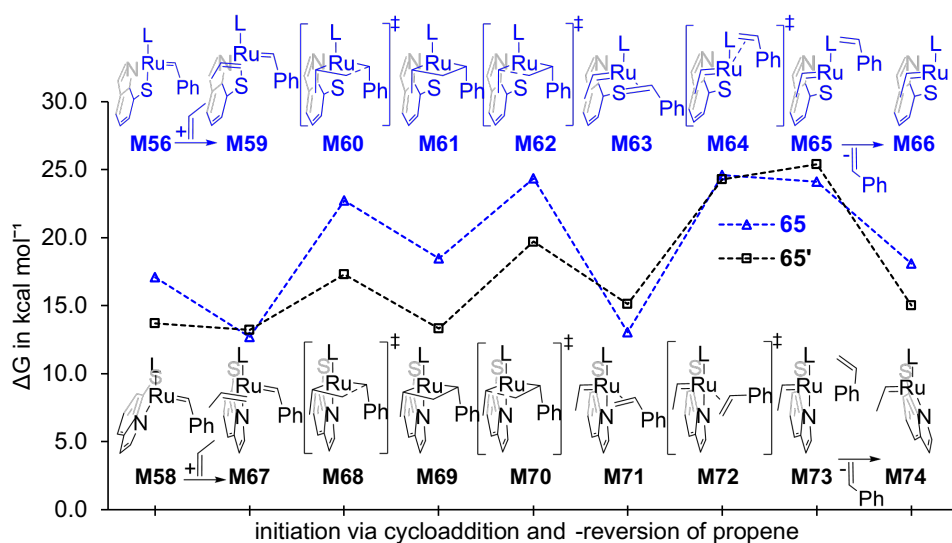


Figure 7. Gibbs free energies calculated for propene coordination, cycloaddition, cycloreversion, and styrene dissociation for the 14-electron, pyridine-free complexes **M58** and **M67** of catalyst isomers **65** and **65'**, respectively. See Figure 6 for pyridine dissociation from catalyst precursor **65** and its isomerization to **65'**. Intermediates and transition states with the thiolate sulfur atom trans to the L-ligand (as in the **65** precursor) are indicated by blue triangles

and those with a corresponding *cis*-configuration by black squares. A standard state corresponding to an ideal 1 mol L⁻¹ solution (benzene) is assumed for all species, and free energies are given relative to the most stable rotamer of the **65** precursor.

In conclusion, the initiation is limited by the dissociation of pyridine and is estimated to be in the range 26–28 kcal mol⁻¹. This barrier suggests a very slow reaction (perhaps taking days to complete at room temperature), which could easily be outcompeted by catalyst decomposition reactions such as nucleophilic attack of the thiolate on the benzylidene, a prominent decomposition reaction for the closely related **37b**.^{54,196} These results are thus consistent with the small amount (23%) of free styrene and the significant catalyst loss observed in the propene self-metathesis experiment (see above).

The calculated relative free energies for **65**-catalyzed propene self-metathesis (Figure 8) are qualitatively consistent with the observed product formation, showing high barriers and marginal predicted *E*-selectivity (0.3 kcal mol⁻¹, via **M80E**). Considering the catalyst isomer configuration, with the indolate positioned *trans* to the evolving MCB and 2-butene, a low metathesis activity is expected. However, the observed activity (0.09 equivalents vs **65** in 20 h) appears surprisingly high, especially considering the rate-determining barriers exceeding 30 kcal mol⁻¹. Assuming reversibility, the barriers could imply that the observed 2-butene might stem from catalyst isomerization through **M57** (27.9 kcal mol⁻¹) with subsequent **65'**-catalyzed propene self-metathesis, as depicted in Figure 9. However, the reported free energies assume standard state corresponding to an ideal 1 mol L⁻¹ solution (benzene) for all species. Accounting for the experimental catalyst concentration (0.01 M) and considering that only 23% of the catalyst was initiated, the product dissociation barriers of **65** (23.4 kcal mol⁻¹ for *E*-2-butene and 23.7 kcal mol⁻¹ for *Z*-2-butene) are indeed lower than that of catalyst isomerization (23.8 kcal mol⁻¹).

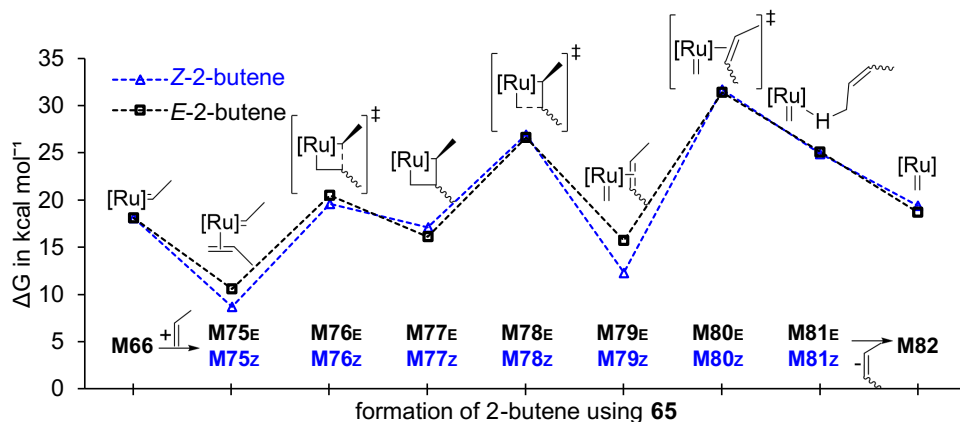


Figure 8. Gibbs free energies calculated for intermediates and transition states of propene self-metathesis for catalyst **65**. The *Z*-2-butene pathway is indicated by blue triangles and that of *E*-2-butene by black squares. A standard state corresponding to an ideal 1 mol L⁻¹ solution (benzene) is assumed for all species, and free energies are given relative to the most stable rotamer of the **65** precursor.

Although the isomerization of **65** → **65'** is disfavored, it could provide insight into the design of future *E*-selective catalysts. Catalyst **65'** was initially envisioned to determine the rate and selectivity via cycloreversion by facilitating product release. Indeed, for **65'**, the dissociation of *E*- and *Z*-2-butene is faster than the cycloreversion (Figure 9). While the dissociation of *Z*-2-butene is barrierless from the π complex **M87_Z** formed during cycloreversion, the preferred pathway for *E*-2-butene dissociation entails an initial rotation, with a barrier (21.3 kcal mol⁻¹) below that of cycloreversion. This rotation helps alleviate the mutual steric repulsion between the catalyst and butene in the initially formed π complex **M87_E**. From the resulting π complex **M89_E**, depicted with *E*-2-butene “upright” in-between the N-aryl groups, alleviating steric repulsion, dissociation of *E*-2-butene can occur barrierless with minimal geometric rearrangement from the catalyst. This is in stark contrast to the high (29–32 kcal mol⁻¹)¹⁹⁶ and rate-determining barriers for 2-butene dissociation calculated for **52a**, reinforcing the central hypothesis of this project: a smaller NHC facilitates product release for thioindolate-based complexes with the thiolate S atom positioned trans to the evolving MCB and the forming 2-butene.

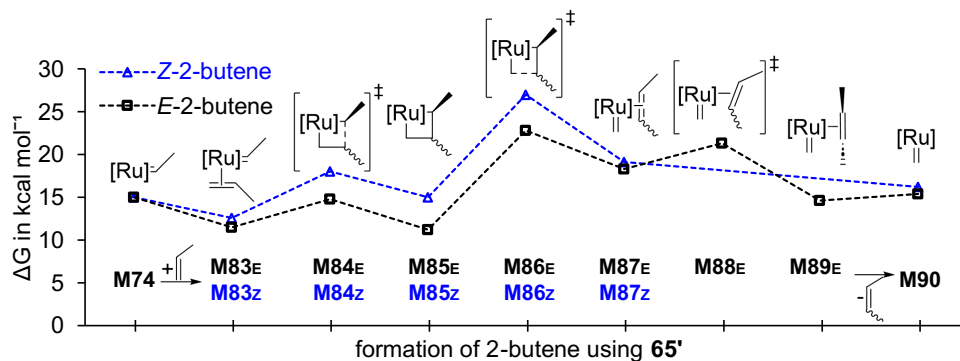


Figure 9. Gibbs free energies calculated for intermediates and transition states of propene self-metathesis for the originally intended catalyst isomer **65'**. The *Z*-2-butene pathway is indicated by blue triangles and that of *E*-2-butene by black squares. A standard state corresponding to an ideal 1 mol L⁻¹ solution (benzene) is assumed for all species, and free energies are given relative to the most stable rotamer of the **65** precursor.

In conclusion, if **65'** instead of **65** were thermodynamically favored, it would be limited by cycloreversion, showing a lower barrier (22.8 kcal mol⁻¹, via **M86E**) than **65**. Moreover, the calculated free energy difference between the *Z*- and *E*-pathways for cycloreversion in **65'** (4.1 kcal mol⁻¹) is greater than that in the bulkier **52a** (1.9 kcal mol⁻¹), confirming the other initial hypothesis: a larger open space between the *N*-aryl groups of carbene **C5** versus **C1** reduces steric repulsion between the NHC and the *E*-alkene product formed during the cycloreversion step.

The preceding implies that active and *E*-selective catalysts based on S^N bidentate ligands might be obtained by destabilizing the undesired isomer via a strong mutual carbene–thiolate trans influence and/or by stabilizing the desired isomer via a beneficial carbene–indolate trans influence. Similarly, a less π -accepting leaving donor than pyridine should destabilize the undesired precursor isomer.

7.3. Revision of S^NS and S^NN Ligands for *E*-Selectivity

In retrospect, I was overly optimistic in choosing the catecholthiolate system as the basis for my PhD project. Despite its excellent stereoretention for both *E*- and *Z*-olefins, there were warning signs present in the literature that should have cautioned me against using them as the starting point for my *E*-selective catalyst design.

For instance, catecholthiolate complex **37b** requires high catalyst loadings (averaging 5 mol%) and long reaction times to achieve high conversion of the starting material, indicating low stability or reactivity.⁵⁴ In contrast, the cyclometalated complex **33b** achieves full conversion with a catalyst loading as low as 0.01 mol%, and the monothiolate complex **27a** reaches equilibrium after only 5 min of reaction time.^{55,159}

The most significant warning sign should have been the incompatibility of the catecholthiolate system with terminal olefins, as it led to the formation of a methylenide specie, which can decompose at a rate comparable to metathesis.^{189,218} To overcome this issue, Hoveyda and co-workers designed the methylenide-capping strategy to convert terminal olefins into the desired internal olefins using *Z*-2-butene before further reactions.¹⁸⁹ While I was aware of this issue, I hoped to achieve some turnovers and *E*-selectivity with catalyst **52a**. Initially, I did not consider that enforcing the *anti*-configuration of the MCB would impose additional stress on the system, which would increase the barrier for product dissociation above the barrier for cycloreversion, lowering its activity and making decomposition more likely. The use of the more sterically accessible NHC **C5** released some of the strain but favored the formation of the latent complex **65**. The undesired orientation of the thioindolate was favored by the lower trans influence and steric size of NHC **C5** compared with **C1**. Increasing the trans influence of the carbene ligand, potentially using a cyclic alkyl amino carbene (CAAC),¹³⁸ is expected to enforce the desired *E*-selective orientation of the thioindolate ligand. However, a large trans influence of the carbene could destabilize the complex by the weakening Ru–N-indolate bond.

Ultimately, the flaws of the parent catecholthiolate catalysts with terminal olefins were inherited by the developed thioindolate and sulfonamide systems. Therefore, a new starting point must be found, where the parent system is robust and allows for olefin metathesis with terminal olefins. Additionally, the desired structure of an asymmetric system must be electronically favored to avoid the formation of inactive isomers due to steric changes over the reaction pathway.

7.4. A New Design Approach for Bidentate Ligands

To achieve a successful *E*-selective complex, it is important that the new bidentate ligand $X^{\cap}Y$ does not impose additional stress on the system. One approach to achieve this is to ensure that the bidentate ligand $X^{\cap}Y$ adopts the same preferred orientation as the combination of the two monodentate ligands *X* and *Y* (see Figure 10). This necessitates that the monodentate ligand *X* possesses a strong trans influence, favoring the formation of the side-bonded MCB **M91a** over the bottom-bonded MCB **M91c**, whereas ligand *Y* should possess a weak trans influence to increase the overall stability of the system. In addition, the formation of the side-bonded isomer **M91b** should be hindered by the repelling trans influence of *X* and the NHC. By employing this strategy, the bidentate ligand $X^{\cap}Y$ should favor the formation of **M92a** over **M92b** and **M92c**, primarily driven by electronic rather than steric factors. Additionally, the *Y* moiety should be small enough to allow metathesis to happen and large enough to favor the *E*-selective pathway. This approach minimizes the stress imposed on the system, promotes the desired orientation, and increases the stability of *E*-selective complexes.

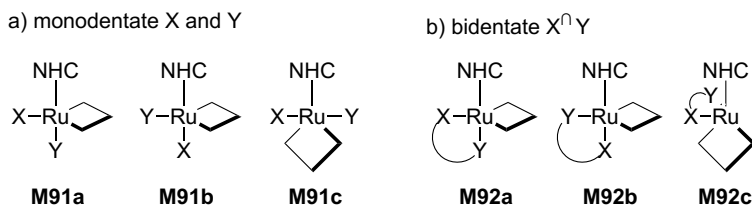


Figure 10. Possible isomers of the unsubstituted MCB using (a) two monodentate ligands *X* and *Y* or (b) one bidentate ligand $X^{\cap}Y$.

An example of such a system can be found in the cyclometalated catalysts **30-35**, where the side-bonded MCB is preferred even though the two anionic ligands are not directly linked together.¹⁷⁶ Furthermore, the stability and resistance to β -hydride elimination observed in **33b**, likely due to the strong trans influence of the adamantyl moiety, seemed promising.^{138,219} Exploring the possibility of carbon-based ligands with anionic character will be further investigated in the next chapter.

7.5. Anionic Carbon-Based Ligands for Olefin Metathesis

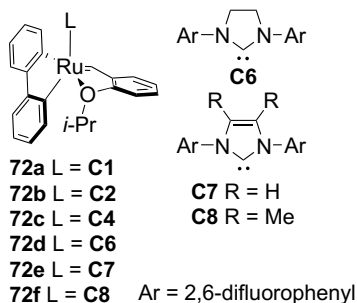
7.5.1 Background: Studies on Biphenyl Ru Complexes

A biphenyl ligand was subject of an initial investigation in our research group, which was conducted by Jonas Ekeli²²⁰ and Sven Nappen²²¹ as part of their master's theses under my supervision. Specifically, Jonas Ekeli employed DFT calculations to explore the performance of a biphenyl ligand in conjunction with various NHCs (**72a-f**) for the self-metathesis of propene (Table 3). Notably, a saturated backbone on the NHC was found to be advantageous for the electron-poor 14-electron ethylidene species (ΔG_{Et} , Table 3, entry 4 vs 5). Conversely, an unsaturated backbone was beneficial for the electron-rich cycloreversion transition state (ΔG_E^\ddagger , Table 3, entry 4 vs 5), preventing the overpopulation of electron density at the Ru center. Because the productivity of the reaction is governed by the overall barrier, the unsaturated NHC was determined to be the preferred choice for the biphenyl system.

Table 3. Predicted Free Energy to the Ethylidene Specie, Barriers to Propene Self-Metathesis, and Computed *E/Z* Selectivity for the Proposed Catalysts 72a-f.²²⁰

Entry	Cat.	ΔG_{Et}^a	ΔG_E^\ddagger ^a	ΔG_Z^\ddagger ^a	$\Delta\Delta G_{E/Z}^\ddagger$ ^b
1	72a	2.1	24.3	25.3	1.0
2	72b	8.4	23.8	26.0	2.3
3	72c	7.6	27.4	30.6	3.2
4	72d	5.4	26.9	29.0	2.1
5	72e	6.2	25.5	27.1	1.6
6	72f	6.0	25.7	27.5	2.8

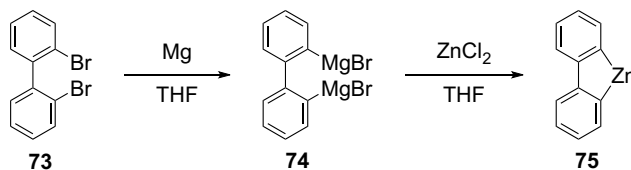
in kcal mol⁻¹. ^avs precatalyst. ^b $\Delta\Delta G_{E/Z}^\ddagger = \Delta G_E^\ddagger - \Delta G_Z^\ddagger$.



Based on his findings, complex **72b** was selected as the most promising candidate. Although the energy barrier with $\Delta G_{E,72b}^\ddagger = 23.8$ kcal mol⁻¹ for the cycloreversion is higher than that of the catecholthiolate complex **37b** ($\Delta G_{Z,37b}^\ddagger = 21.1$ kcal mol⁻¹) or cyclometalated complex **33a** ($\Delta G_{Z,33a}^\ddagger = 21.2$ kcal mol⁻¹), productive metathesis should still be feasible at room temperature. Additionally, the synthesis of aryl Ru olefin metathesis complexes holds the potential to introduce a new realm of anionic, easily modifiable ligands, enabling new possibilities for further exploration and development.

Sven Nappen undertook efforts to incorporate the biphenyl ligand into a Ru-based complex, targeting the synthesis of **72b**. The Grignard reaction of commercially available dibromodiphenyl **73** led to the formation of the organomagnesium compound **74**. Subsequent transmetalation with zinc chloride yielded the organozinc compound **75** (Scheme 20).

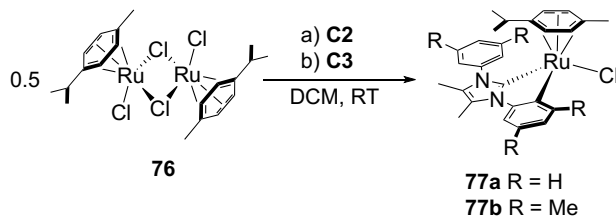
Scheme 20. Synthesis of the Biphenyl Organozinc Reagent 75.



The application of the organozinc compound **75** was more promising, as direct application of Grignard reagent **74** on various Ru alkylidene complexes resulted in a halogen exchange, forming the respective bromo ruthenium complexes instead of installing the biphenyl ligand, although attempts to combine zinc organyl **75** with the pyridine-stabilized complexes **51**, **62a**, or **62b** were unsuccessful. This could be due to steric congestion at the Ru center, which hinders transmetalation with **75**, likely due to the size of the biphenyl moiety.

As a result, Sven Nappen decided to construct the desired complex starting from the *p*-cymene dimer **76** (Scheme 21). However, during the installation of **C2** and **C3**, C–H activation of the aryl-NHC occurred, leading to the formation of the cyclometalated complex **77a** and **77b**, respectively (Figure 11). This C–H activation made the installation of the biphenyl ligand unfeasible.

Scheme 21. C–H Activation of the NHC during Installation of (a) C2 or (b) C3 on the *p*-Cymene Dimer 76.



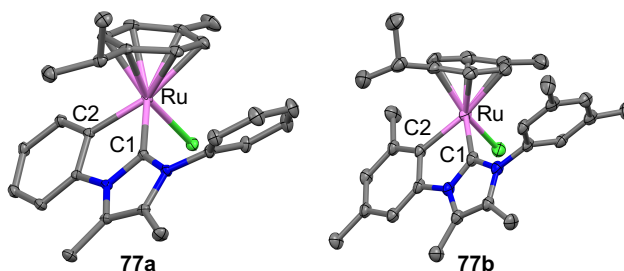
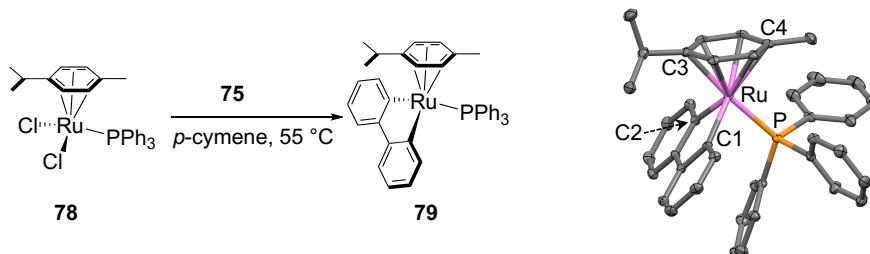


Figure 11. X-ray crystal structure of **77a** and **77b**, with displacement ellipsoids drawn at 50% probability. Ruthenium is shown in magenta, chloride in green, nitrogen in blue, and carbon in gray. Hydrogen atoms have been omitted for clarity. Selected geometrical parameters (bond distances in Å and angles in deg.) for **77a**: Ru–C1: 2.020(1), Ru–C7: 2.066(1), C1–Ru–C7 = 76.49(6); for **77b**: Ru–C1: 2.027(5), Ru–C7: 2.097(5), C1–Ru–C7 = 76.4(2).

To avoid C–H activation of the NHC, Sven Nappen decided to install the biphenyl ligand first and then add the NHC subsequently. He synthesized the biphenyl complex **79** via the monotriphenylphosphine complex **78**, as shown in Scheme 22.²²² However, attempts to exchange the PPh₃ ligand on **79** with **C2** or **C3** were unsuccessful.

Scheme 22. Synthesis of 79 by Transmetalation with Biphenylzinc Compound 75.



X-ray crystal structure of **79**, with displacement ellipsoids drawn at 50% probability. Ruthenium is shown in magenta, phosphorus in orange, and carbon in gray. Hydrogen atoms have been omitted for clarity. Selected geometrical parameters (bond distances in Å and angles in deg.): Ru–C1: 2.067(1), Ru–C2: 2.075(1), Ru–P: 2.3086(4), Ru–C3: 2.290(2), Ru–C4: 2.255(1); C1–Ru–C2: 78.23(5).

Subsequent testing of the biphenyl complex **79** in the ring-opening polymerization of 2-norbornene or the self-metathesis of allylbenzene showed no activity, even with activators such as (diazomethyl)trimethylsilane, in contrast to the precursor **78**, which had shown catalytic activity in these reactions.²²³

7.6. Aryl-Based Ru Olefin Metathesis Alkylidenes

Based on the analysis of the results from the master theses of Jonas Ekeli and Sven Nappen, it was determined that the biphenyl moiety might be too large for an effective olefin metathesis catalyst due to the limited space between the NHC aryls. Additionally, the presence of two aryl substituents may result in an unstable complex because of their significant trans influence. However, the exploration of a possible monophenyl-based Ru catalyst still offers great potential for tuning the electronic properties of the phenyl group, and ultimately the Ru catalyst.

Preliminary computational results showed promising findings, indicating that the unsubstituted side-bound MCB **M93a** of a monophenyl complex is only slightly energetically disfavored over the bottom-bound MCB **M93c** by 1.3 kcal mol⁻¹ (Figure 12a). Using a sterically more demanding 2,6-dimethylphenyl, which also possesses a stronger trans influence, the preference for the side-bound MCB **M94a** was increased to 7.4 kcal mol⁻¹ (Figure 12b).

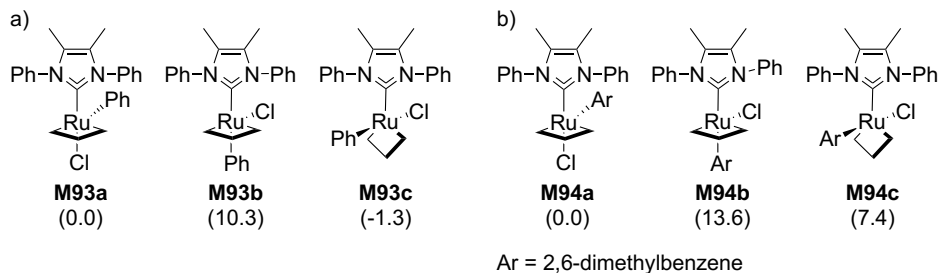
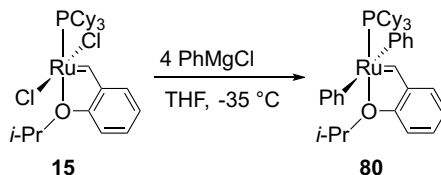


Figure 12. Relative stability of different isomers of the unsubstituted MCB of (a) a monophenyl- and (b) 2,6-dimethylphenyl-substituted Ru complex in kcal mol⁻¹.

Initial experiments using two equivalents of PhMgCl on complex **15** led to the formation of two new complexes indicated by their respective alkylidene proton ($\delta = 15.64$ and 13.43 ppm). After using four equivalents of PhMgCl, only the signal at $\delta = 13.43$ ppm remained. This indicates that the alkylidene signal at $\delta = 13.43$ ppm refers to a bisphenyl-substituted complex (Scheme 23), whereas the signal at $\delta = 15.64$ ppm relates to a monophenyl-substituted complex. High-resolution mass spectrometry

(HRMS) of the reaction mixture verified the successful substitution of both chlorides with phenyl groups.

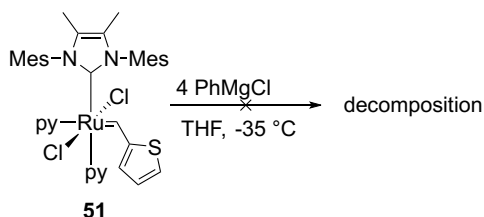
Scheme 23. Reaction of PhMgCl with Hoveyda First Generation



The observed preference for double phenyl substitution indicated that the first phenyl substitution weakens the secondary Ru–Cl bond because of the larger trans influence of the phenyl group, facilitating the second substitution. Additionally, DFT calculations suggest that the trans bisphenyl isomer **80** is favored by 2.6 kcal mol⁻¹ over the corresponding cis isomer. However, complex **80** exhibited high instability, undergoing decomposition at room temperature within minutes and necessitating handling at -35 °C. ¹³C NMR was not measured due to the instability of the complex. The low stability of complex **80** is attributed to the opposing position of the phenyl moieties, presumably leading to dissociation and decomposition of the catalyst at room temperature. Interestingly, the addition of the diphenyl complex **80** to allylbenzene resulted in isomerization and exclusive formation of *E*-propenylbenzene.

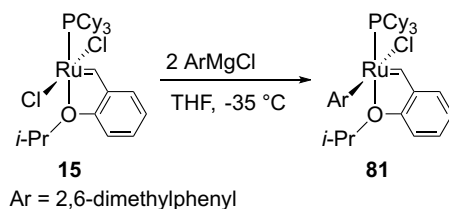
Attempts to combine commercially available NHC-based Ru complexes, such as Hoveyda second generation **16**, Stewart-Grubbs catalyst, or pyridine-stabilized complexes **18** and **51**, with PhMgCl resulted in an immediate loss of the alkylidene signal (Scheme 24).

Scheme 24. Reaction of PhMgCl with NHC-Based Catalyst 51.



In contrast, the application of 2,6-dimethylphenylmagnesium chloride on Hoveyda 1st generation **15** resulted only in the formation of one new alkyldiene signal ($\delta = 16.05$ ppm) despite the addition of three or more equivalences of the Grignard reagent. This indicates that only a monoaryl-substituted complex **81** is formed, which was confirmed via HRMS (Scheme 25). The sterically more demanding aryl, due to the two ortho positioned methyl groups, presumably prevents the second substitution due to sterics. Although it exhibits better stability than complex **80**, isolation and full characterization of complex **81** were not possible.

Scheme 25. Reaction of 2,6-Dimethylphenylmagnesium Chloride with Hoveyda First Generation.



Notably, these experiments represented the first successful application of a Grignard reagent on ruthenium alkyldiene complexes. Despite the challenges, the successful installation of an aryl group via transmetalation on a Ru alkyldiene complex encouraged further exploration of the potential and possible applications of these compounds in *E*-selective olefin metathesis.

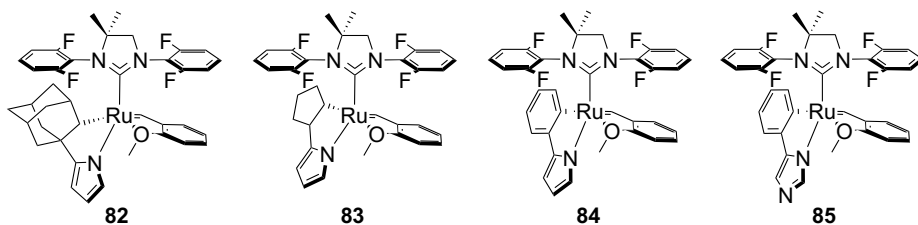
7.6.1 Application of C[∩]N-Based Ligands in Olefin Metathesis

Based on the experiments using arylmagnesium chlorides, it was determined that the bisphenyl complex **80** is unstable due to the opposing trans influences of the phenyl groups. To address this issue and design a ligand for *E*-selective olefin metathesis, it was previously hypothesized, that an ideal bidentate ligand, denoted as X[∩]Y, should possess an asymmetric nature with X having a strong trans influence and Y having a weak trans influence. This concept was discussed in detail in Chapter 7.4 of this thesis.

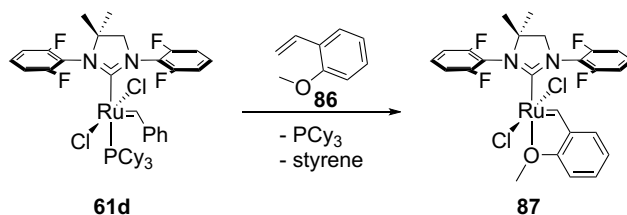
Considering the knowledge gained during this PhD work, a C[∩]N ligand would be well-suited for achieving *E*-selectivity, with pyrrole or imidazole as potential options for the

N moiety. Initially, a cyclometalated complex with a 2-adamantanylpyrrole ligand was considered. However, the geometrically optimized structure of complex **82** containing 2-adamantanylpyrrole exhibited significant distortion, suggesting that the size of the adamantyl group is incompatible with the sterically accessible ortho fluorinated NHC **C5** (Chart 7). As a result, smaller carbon-based ligands were explored. Three commercially available ligand precursors, namely 2-cyclopentylpyrrole, 2-phenylpyrrole, and 2-bromophenylimidazole, leading to complexes **83**, **84**, and **85**, respectively, were identified as potential candidates for further investigation (Chart 7). These ligands were selected on the basis of their suitability and availability for the desired asymmetric C[^]N ligand design. In addition, DFT calculations confirmed that the displayed and desired orientation of the C[^]N ligand in Chart 7, with the carbon atom binding cis, and the nitrogen atom trans, to the NHC, is preferred by 4-9 kcal mol⁻¹ for complex **83-85**.

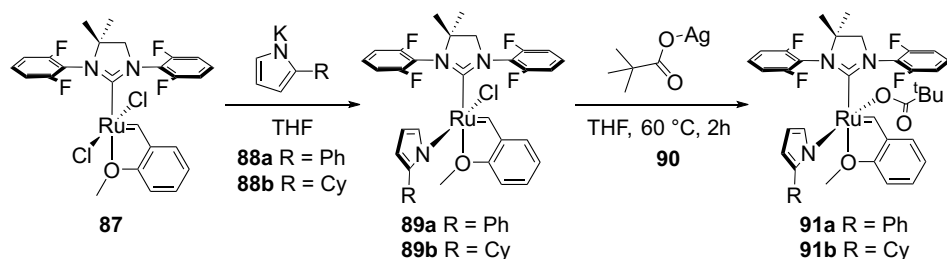
Chart 7. Computational Investigated C[^]N Complexes 82-85.



To synthesize the desired cyclometalated C[^]N complexes, the approach taken was based on the procedure established by Grubbs and co-workers.¹⁵⁸ The first step involved the synthesis of the methoxy-chelated complex **87** by reacting the known phosphine-based precursor **61d** with 2-vinylanisol (Scheme 26). The choice to use the methoxy derivative instead of the isopropoxy derivative was made to minimize steric hindrance around the Ru center.

Scheme 26. Synthesis of Complex 87.


The installation of the 2-phenylpyrrole ligand was performed using the potassium salt **88a**, which was formed by reacting the commercially available ligand with KH. The progress of the conversion was monitored by the alkyldiene signal in ^1H NMR, and the successful installation of the ligand was confirmed via HRMS. Subsequent treatment of complex **89a** with silver pivalate **90** did not result in the desired complex **84** via C–H activation. Instead, it stopped at the formation of the monopivalate complex **91a**, which was identified using HRMS as well (Scheme 27). While C–H activation from a monopivalate complex is energetically more demanding than that of a bispivalate complex for a cyclometalated system,²²⁴ increasing the temperature or reaction time did not result in the desired C–H activation, as indicated by the lack of changes in the alkyldiene signals of the ^1H NMR spectrum. Similar results were obtained when using 2-cyclopentylpyrrole, leading to the formation of complex **89b** and **91b** (Scheme 27), respectively.

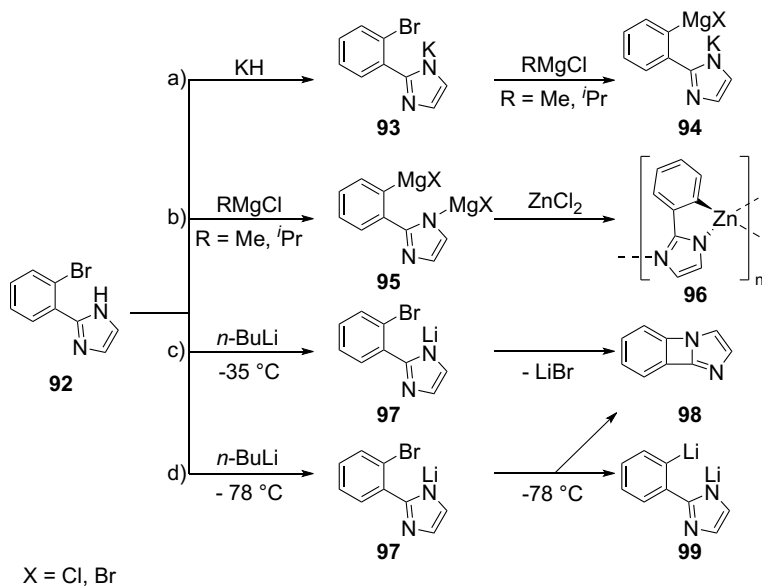
Scheme 27. Attempts of C–H Activation Using Pivalate via the N-bound Complexes 87a and 87b, Respectively.


After unsuccessful attempts to install the 2-phenylpyrrole ligand and 2-cyclopentylpyrrole via C–H activation, focus was shifted to the 2-bromophenylimidazole **92** ligand. Based on previous observations with PhMgCl , it

was hypothesized that the installation of the ligand via an organometallic reagent on Ru alkylidenes could be possible.

Initially, the synthesis of a Grignard reagent was attempted by deprotonation using KH, followed by the addition of *i*-PrMgCl or MeMgCl (**94**, Scheme 28a) or using *i*-PrMgCl or MeMgCl as the base and transmetalation reagent simultaneously (**95**, Scheme 28b). However, the reaction between the Grignard reagent **94** or **95** and the Ru complexes **15** and **51** resulted mainly in a bromide/chloride exchange (complex **100a**, **100b**, **102a**, and **102b**, Scheme 29), as confirmed by separately synthesizing the corresponding dibromo-complexes **100b** and **102b** using LiBr. The respective pyrrolate complexes, **101a**, **101b**, **103a**, and **103b**, were found as minor products.

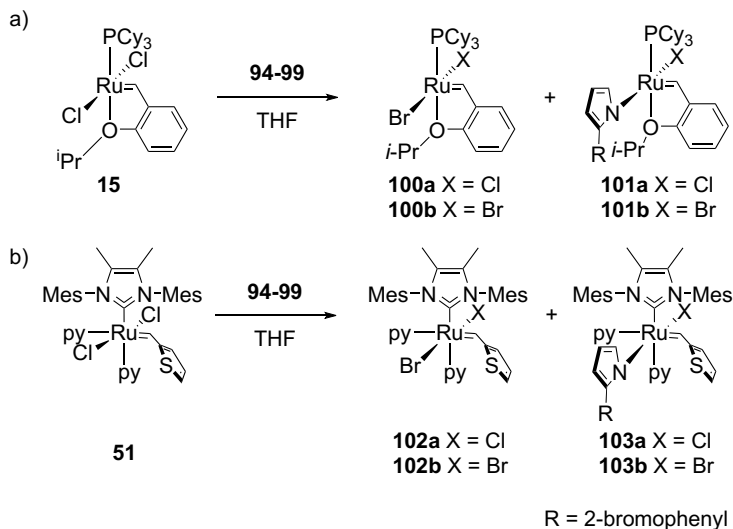
Scheme 28. Synthesis Routes for Transforming 2-Bromophenylimidazole into Various Organometallic Reagents.



An attempt was made to synthesize an organozinc compound via the addition of 1M ZnCl₂ solution in THF to the solution of **95**, although this resulted in the precipitation of a white solid that was insoluble in THF and pyridine. This indicated the formation of a coordination polymer possibly with a tetracoordinated Zn center, as indicated in compound **96** (Scheme 28b).

Another approach was investigated by reacting **92** with *n*-BuLi. The formation of Li organyl **99** and butyl bromide was expected to inhibit halogen exchange during the installation reaction. However, the bromo-complexes **100a**, **100b**, **102a**, and **102b** were still observed, suggesting that at -30 °C, the initially formed Li salt **97** may further react to form a benzoazetoimidazole **98** by eliminating LiBr (Scheme 28c). To prevent this intramolecular elimination reaction, the reaction was repeated at -78 °C, allowing for Li/Br exchange before the intramolecular elimination reaction. Using equimolar amounts of the reaction mixture on Hoveyda first generation **15** yielded the bromo-exchanged complexes **100a** and **100b**, but also new Ru alkylidene signals. However, further investigations involving excess amounts of the organolithium reagent indicated that the new complexes still contained either chloride or bromide and not the desired Ru–C bond. Consequently, the installation of 2-phenylimidazole was unsuccessful.

Scheme 29. Reaction of the Organometallic Compound 94-99 with (a) Phosphine-Based Complex 15 and (b) NHC-Based Complex 51.



These experiments demonstrate the challenges encountered in the installation of the desired C¹N ligands. To overcome these difficulties, an alternative pathway can be explored, starting from the Ru *p*-cymene dimer **76** and focusing on installing the ligand before addressing other transformations. By adopting this strategy, it may be possible to circumvent the issues related to intramolecular elimination and halogen exchange,

and potentially enhance the chances of obtaining the desired cyclometalated CⁿN complexes **83-85**.

8. Conclusions

In my pursuit of designing *E*-stereoselective metathesis catalysts, I started from a catecholthiolate-based, stereoretentive catalyst design that gives either *Z* or *E* internal olefins depending on the sacrificial co-substrate used. To create an *E*-selective catalyst, increasing the steric pressure on the β -substituent during the MCB intermediate is necessary. Using DFT calculations, I predicted that an S^N-chelated thioindolate could be suitable for designing an *E*-selective catalyst. The thioindolate is expected to bind to ruthenium in an orientation with S *cis*, and N *trans*, to the NHC. This would apply the desired steric pressure at the cycloreversion transition state, favoring the formation of *E*-isomeric products, specifically *E*-2-butene.

To validate this design strategy, I synthesized, isolated, and characterized the first metal complexes bearing bidentate thioindolate ligands (**52a-c**). Although these new complexes exhibited metathetic exchange with styrene and allylbenzene, releasing the 2-thienylmethylidene ligand, they did not generate any self-metathesis products. Even during the attempted self-metathesis of propene using complex **52a**, only small amounts of 2-butene (0.35 turnover; 73% *Z*-2-butene) were obtained. To gain insights into the observed low activity, detailed mechanistic DFT calculations on the propene self-metathesis reaction were conducted. The calculations revealed that the barriers to product release from the Ru-2-butene π -complex, where the release of *Z*-2-butene was favored, were much higher than those of the cycloreversion of the MCB. This hindered product dissociation was attributed to the combined steric pressure exerted by the NHC **C1** and the thioindolate ligand. The negative effect of steric bulk predicted by the calculations is consistent with the metathesis inactivity of the bulkier complexes **52b** and **52c**.

To enhance catalyst stability, mercaptophenyltrifluoromethanesulfonamide ligand **55** was introduced, which increased the N-acidity in catalyst **57**. Despite this, propene self-metathesis activity remained low (0.95 turnover), with more *Z*-2-butene (63%) than *E*-2-butene, indicating product dissociation as the rate- and selectivity-determining step.

To address product dissociation, more sterically accessible NHCs than **C1** were explored featuring hydrogen or fluorine in the ortho positions. In addition, the increased open space of NHCs is expected to increase the *E*-selectivity. Unfortunately, combining the S^ηN ligand **55** with Ru complexes containing smaller NHCs led to Ru nanoparticle formation. Furthermore, all attempts to synthesize thioindolate catalysts based on NHCs with N-phenyl or N-3,5-xylyl groups failed due to rapid decomposition via C–H activation. Incorporating the thioindolate ligand **49a** into catalyst **62d**, which contains the ortho fluorinated NHC **C2**, yielded catalyst **65**. However, the indolate unit binds cis to the NHC and trans to the leaving donor (pyridine) and the evolving MCB in **65**, thereby limiting its impact on selectivity. Catalyst **65** showed almost no activity in cross-metathesis and limited activity in ROMP using strained substrates. DFT calculations revealed that poor catalytic activity in **65** was indeed due to the orientation of the thioindolate ligand. The trans-disposed indolate's weak σ donation and considerable π donation hamper catalyst initiation by limiting the dissociation of the π -acceptor pyridine. Additionally, the weak σ donation contributes to slow cycloaddition, cycloreversion, and product dissociation. In contrast, calculations for the originally intended catalyst isomer **65'**, in which the indolate binds trans to the NHC, predict significantly increased catalytic activity and substantial *E*-selectivity. Regrettably, the barrier to S^ηN ligand rotation is too high for **65** \rightarrow **65'** isomerization to influence catalysis using **65**.

The exploration of anionic carbon-based ligands resulted in the first successful transmetalation between a Grignard reagent and a ruthenium alkylidene complex. Yet, the resulting aryl-substituted complexes **80** and **81** proved to be unstable at room temperature. Additional attempts to increase the stability and generate *E*-selective catalysts through the use of C^ηN-chelated ligands were unsuccessful, as the desired Ru–C bond, via transmetalation or cyclometalation, was not formed.

Even though my investigations faced challenges and yielded varying degrees of success, they provide valuable insights into the design and stability of future *E*-selective olefin metathesis catalysts: (i) The chelating ligand should consist of two anionic moieties with different electronic properties. One of these moieties must be a

strong σ electron donor with a pronounced trans influence and effect, while the second moiety, responsible for inducing selectivity, should have a weak trans influence.

(ii) The NHC must align with the chelating ligand to promote the desired configuration of the chelating ligand, and the steric bulk should facilitate effortless product dissociation.

The limitations and obstacles encountered in this doctoral work emphasize the need for further exploration and the development of new strategies to achieve highly active and stable catalysts for *E*-selective olefin metathesis reactions.

9. Future Directions

The design of new Ru-based catalysts faces obstacles due to the limitations of the complex framework **M95** and the restricted variety of available ligands (Figure 13). Anionic ligands, typically halides or pseudo-halides, dominate the

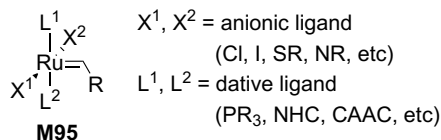


Figure 13. Ligand framework for Ru-based catalysts.

ligand scope, and the introduction of selective olefin metathesis has somewhat expanded the options but at the expense of stability. A significant advancement in recent years has been the substitution of NHCs with CAACs, which improved catalyst stability against β -hydride elimination. However, the overall catalyst design has remained largely unchanged, as the structural difference between NHC and CAAC ligands is marginal.

Predicting the future of *E*-selective olefin metathesis is challenging because exploring new ligand types often introduces new challenges. As discussed in Chapter 7.3, chelating $S^{\wedge}S$ and $S^{\wedge}N$ ligands have limitations in their performance with terminal olefins, suggesting that alternative approaches are needed. The $C^{\wedge}N$ -ligand framework is promising, particularly considering its similarity to the cyclometalated complexes, yet further investigations are necessary. A potential approach could involve a bottom-up strategy starting from the Ru *p*-cymene dimer **76**, similar to the development of the biphenyl complex **79**.

Additionally, it could be worthwhile to investigate the combination of even smaller NHCs, such as 1,3-methyl-imidazol-2-ylidene, with chelating ligands to further mitigate the steric bulk near the Ru center and restore catalytic activity.

10. References

- (1) Hughes, D.; Wheeler, P.; Ene, D. Olefin Metathesis in Drug Discovery and Development—Examples from Recent Patent Literature. *Org. Process Res. Dev.* **2017**, *21* (12), 1938–1962. <https://doi.org/10.1021/acs.oprd.7b00319>.
- (2) Schulz, M. D.; Wagener, K. B. Precision Polymers through ADMET Polymerization. *Macromol. Chem. Phys.* **2014**, *215* (20), 1936–1945. <https://doi.org/10.1002/macp.201400268>.
- (3) Walensky, L. D.; Bird, G. H. Hydrocarbon-Stapled Peptides: Principles, Practice, and Progress: Miniperspective. *J. Med. Chem.* **2014**, *57* (15), 6275–6288. <https://doi.org/10.1021/jm4011675>.
- (4) Vinogradova, E. V. Organometallic Chemical Biology: An Organometallic Approach to Bioconjugation. *Pure Appl. Chem.* **2017**, *89* (11), 1619–1640. <https://doi.org/10.1515/pac-2017-0207>.
- (5) Isenegger, P. G.; Davis, B. G. Concepts of Catalysis in Site-Selective Protein Modifications. *J. Am. Chem. Soc.* **2019**, *141* (20), 8005–8013. <https://doi.org/10.1021/jacs.8b13187>.
- (6) Messina, M. S.; Maynard, H. D. Modification of Proteins Using Olefin Metathesis. *Mater. Chem. Front.* **2020**, *4* (4), 1040–1051. <https://doi.org/10.1039/C9QM00494G>.
- (7) Higman, C. S.; Lummiss, J. A. M.; Fogg, D. E. Olefin Metathesis at the Dawn of Implementation in Pharmaceutical and Specialty-Chemicals Manufacturing. *Angew. Chem. Int. Ed.* **2016**, *55* (11), 3552–3565. <https://doi.org/10.1002/anie.201506846>.
- (8) Yu, M.; Lou, S.; Gonzalez-Bobes, F. Ring-Closing Metathesis in Pharmaceutical Development: Fundamentals, Applications, and Future Directions. *Org. Process Res. Dev.* **2018**, *22* (8), 918–946. <https://doi.org/10.1021/acs.oprd.8b00093>.
- (9) Cink, R. D.; Lukin, K. A.; Bishop, R. D.; Zhao, G.; Pelc, M. J.; Towne, T. B.; Gates, B. D.; Ravn, M. M.; Hill, D. R.; Ding, C.; Cullen, S. C.; Mei, J.; Leanna, M. R.; Henle, J.; Napolitano, J. G.; Nere, N. K.; Chen, S.; Sheikh, A.; Kallemeyn, J. M. Development of the Enabling Route for Glecaprevir via Ring-Closing Metathesis. *Org. Process Res. Dev.* **2020**, *24* (2), 183–200. <https://doi.org/10.1021/acs.oprd.9b00469>.
- (10) St-Pierre, G.; Cherney, A. H.; Chen, W.; Dong, X.; Dorman, P. K.; Griffin, D. J.; Houk, K. N.; Lin, J. B.; Osgood, S.; Silva Elipe, M. V.; Timmons, H. C.; Xie, Y.; Tedrow, J. S.; Thiel, O. R.; Smith, A. G. Accelerated Development of a Scalable Ring-Closing Metathesis to Manufacture AMG 176 Using a Combined High-Throughput Experimentation and Computational Modeling Approach. *Org. Process Res. Dev.* **2021**, *25* (3), 442–451. <https://doi.org/10.1021/acs.oprd.0c00416>.
- (11) Choi, T.-L.; Grubbs, R. H. Controlled Living Ring-Opening-Metathesis Polymerization by a Fast-Initiating Ruthenium Catalyst. *Angew Chem Int Ed Engl* **2003**, *42* (15), 1743–1746. <https://doi.org/10.1002/anie.200250632>.
- (12) Edwards, J. P.; Wolf, W. J.; Grubbs, R. H. The Synthesis of Cyclic Polymers by Olefin Metathesis: Achievements and Challenges. *J. Polym. Sci. Part Polym. Chem.* **2019**, *57* (3), 228–242. <https://doi.org/10.1002/pola.29253>.
- (13) Schrock, R. R. Synthesis of Stereoregular ROMP Polymers Using Molybdenum and Tungsten Imido Alkylidene Initiators. *Dalton Trans* **2011**, *40* (29), 7484–7495. <https://doi.org/10.1039/c1dt10215j>.
- (14) Debsharma, T.; Behrendt, F. N.; Laschewsky, A.; Schlaad, H. Ring-Opening Metathesis Polymerization of Biomass-Derived Levoglucosenol. *Angew. Chem. Int. Ed.* **2019**, *58* (20), 6718–6721. <https://doi.org/10.1002/anie.201814501>.
- (15) Jung, K.; Ahmed, T. S.; Lee, J.; Sung, J.-C.; Keum, H.; Grubbs, R. H.; Choi, T.-L. Living β -Selective Cyclopolymerization Using Ru Dithiolate Catalysts. *Chem. Sci.* **2019**, *10* (39), 8955–8963. <https://doi.org/10.1039/C9SC01326A>.
- (16) Feist, J. D.; Xia, Y. Enol Ethers Are Effective Monomers for Ring-Opening Metathesis Polymerization: Synthesis of Degradable and Depolymerizable Poly(2,3-Dihydrofuran). *J. Am. Chem. Soc.* **2020**, *142* (3), 1186–1189. <https://doi.org/10.1021/jacs.9b11834>.
- (17) Foster, J. C.; Grocott, M. C.; Arkinstall, L. A.; Varlas, S.; Redding, M. J.; Grayson, S. M.; O'Reilly, R. K. It Is Better with Salt: Aqueous Ring-Opening Metathesis Polymerization at

- Neutral pH. *J. Am. Chem. Soc.* **2020**, *142* (32), 13878–13885. <https://doi.org/10.1021/jacs.0c05499>.
- (18) Rizzo, A.; Peterson, G. I.; Bhaumik, A.; Kang, C.; Choi, T.-L. Sugar-Based Polymers from d-Xylose: Living Cascade Polymerization, Tunable Degradation, and Small Molecule Release. *Angew. Chem. Int. Ed.* **2021**, *60* (2), 849–855. <https://doi.org/10.1002/anie.202012544>.
- (19) Debsharma, T.; Schmidt, B.; Laschewsky, A.; Schlaad, H. Ring-Opening Metathesis Polymerization of Unsaturated Carbohydrate Derivatives: Levoglucosenyl Alkyl Ethers. *Macromolecules* **2021**, *54* (6), 2720–2728. <https://doi.org/10.1021/acs.macromol.0c02821>.
- (20) Dong, Y.; Matson, J. B.; Edgar, K. J. Olefin Cross-Metathesis in Polymer and Polysaccharide Chemistry: A Review. *Biomacromolecules* **2017**, *18* (6), 1661–1676. <https://doi.org/10.1021/acs.biomac.7b00364>.
- (21) Wittig, G.; Schöllkopf, U. Über Triphenyl-phosphin-methylene Als Olefinbildende Reagenzien (I. Mitteil. *Chem. Ber.* **1954**, *87* (9), 1318–1330. <https://doi.org/10.1002/cber.19540870919>.
- (22) Wadsworth, W. S.; Emmons, W. D. The Utility of Phosphonate Carbanions in Olefin Synthesis. *J. Am. Chem. Soc.* **1961**, *83* (7), 1733–1738. <https://doi.org/10.1021/ja01468a042>.
- (23) Julia, M.; Paris, J.-M. Synthèses a l'aide de Sulfones v(+)- Methode de Synthèse Generale de Doubles Liaisons. *Tetrahedron Lett.* **1973**, *14* (49), 4833–4836. [https://doi.org/10.1016/S0040-4039\(01\)87348-2](https://doi.org/10.1016/S0040-4039(01)87348-2).
- (24) Fürstner, A. Olefin Metathesis and Beyond. *Angew. Chem.* **2000**, *39* (17), 3012–3043. [https://doi.org/10.1002/1521-3773\(20000901\)39:17<3012::AID-ANIE3012>3.0.CO;2-G](https://doi.org/10.1002/1521-3773(20000901)39:17<3012::AID-ANIE3012>3.0.CO;2-G).
- (25) *Olefin Metathesis: Theory and Practice*; Grela, K., Ed.; John Wiley & Sons, Inc.: Hoboken, NJ, USA, 2014. <https://doi.org/10.1002/9781118711613>.
- (26) *Handbook of Metathesis*; Grubbs, R. H., Wenzel, A. G., O'Leary, D. J., Khosravi, E., Eds.; Wiley-VCH Verlag GmbH & Co. KGaA: Weinheim, Germany, 2015. <https://doi.org/10.1002/9783527674107>.
- (27) Fürstner, A. The Ascent of Alkyne Metathesis to Strategy-Level Status. *J. Am. Chem. Soc.* **2021**, *143* (38), 15538–15555. <https://doi.org/10.1021/jacs.1c08040>.
- (28) Ogba, O. M.; Warner, N. C.; O'Leary, D. J.; Grubbs, R. H. Recent Advances in Ruthenium-Based Olefin Metathesis. *Chem. Soc. Rev.* **2018**, *47* (12), 4510–4544. <https://doi.org/10.1039/C8CS00027A>.
- (29) Herndon, J. W. The Chemistry of the Carbon-Transition Metal Double and Triple Bond: Annual Survey Covering the Year 2017. *Coord. Chem. Rev.* **2018**, *377*, 86–190. <https://doi.org/10.1016/j.ccr.2018.08.007>.
- (30) Grubbs, R. H. Olefin-Metathesis Catalysts for the Preparation of Molecules and Materials (Nobel Lecture). *Angew. Chem.-Int. Ed.* **2006**, *45* (23), 3760–3765. <https://doi.org/10.1002/anie.200600680>.
- (31) Fischer, E. O.; Maasbol, A. D.-:Caplus. On the Existence of a Tungsten Carbonyl Carbene Complex. *Angew Chem Int Ed* **1964**, *3* (8), 580–581.
- (32) Toreki, R.; Schrock, R. R. A Well-Defined Rhenium(VII) Olefin Metathesis Catalyst. *J. Am. Chem. Soc.* **1990**, *112* (6), 2448–2449. <https://doi.org/10.1021/ja00162a071>.
- (33) Solans-Monfort, X.; Clot, E.; Coperet, C.; Eisenstein, O. D(0) Re-Based Olefin Metathesis Catalysts, Re(=CR)(=CHR)(X)(Y): The Key Role of X and Y Ligands for Efficient Active Sites. *J. Am. Chem. Soc.* **2005**, *127* (40), 14015–14025. <https://doi.org/10.1021/ja053528i>.
- (34) Farrell, W. S. Pushing the Bounds of Olefin Metathesis with Vanadium. *Z. Für Anorg. Allg. Chem.* **2021**, *647* (6), 584–592. <https://doi.org/10.1002/zaac.202000403>.
- (35) Jensen, V. R.; Occhipinti, G. Ruthenium and Osmium Heterocyclic Carbene Metathesis Catalysts. United States Patent US 9,303,100 B2, 2016.
- (36) Lapointe, A. M.; Schrock, R. R.; Davis, W. H. Alkyl, Alkylidene, and Alkylidyne Complexes of Osmium(VI). *J. Am. Chem. Soc.* **1995**, *117* (17), 4802–4813. <https://doi.org/10.1021/ja00122a010>.
- (37) Grau, B. W.; Neuhauser, A.; Aghazada, S.; Meyer, K.; Tsogoeva, S. B. Iron-Catalyzed Olefin Metathesis: Recent Theoretical and Experimental Advances. *Chem. – Eur. J.* **2022**, *28* (62), e202201414. <https://doi.org/10.1002/chem.202201414>.

- (38) Wised, K.; Nomura, K. Synthesis of (Imido)Niobium(V)–Alkylidene Complexes That Exhibit High Catalytic Activities for Metathesis Polymerization of Cyclic Olefins and Internal Alkynes. *Organometallics* **2016**, *35* (17), 2773–2777. <https://doi.org/10.1021/acs.organomet.6b00560>.
- (39) Takebayashi, S.; Iron, M. A.; Feller, M.; Rivada-Wheleaghan, O.; Leitus, G.; Diskin-Posner, Y.; Shimon, L. J. W.; Avram, L.; Carmieli, R.; Wolf, S. G.; Cohen-Ofri, I.; Sanguramath, R. A.; Shenhar, R.; Eisen, M.; Milstein, D. Iron-Catalysed Ring-Opening Metathesis Polymerization of Olefins and Mechanistic Studies. *Nat. Catal.* **2022**, *5* (6), 494–502. <https://doi.org/10.1038/s41929-022-00793-4>.
- (40) De Brito Sá, É.; Rodríguez-Santiago, L.; Sodupe, M.; Solans-Monfort, X. Toward Olefin Metathesis with Iron Carbene Complexes: Benefits of Tridentate σ -Donating Ligands. *Organometallics* **2016**, *35* (23), 3914–3923. <https://doi.org/10.1021/acs.organomet.6b00641>.
- (41) Dawood, K. M.; Nomura, K. Recent Developments in Z-Selective Olefin Metathesis Reactions by Molybdenum, Tungsten, Ruthenium, and Vanadium Catalysts. *Adv. Synth. Catal.* **2021**, *363* (8), 1970–1997. <https://doi.org/10.1002/adsc.202001117>.
- (42) Michaudel, Q.; Kempel, S. J.; de Gruyter, J. N. E vs Z Selectivity in Olefin Metathesis Through Catalyst Design. In *Comprehensive Organometallic Chemistry IV*; Elsevier: Amsterdam, 2023; Vol. 13, pp 265–388.
- (43) Trnka, T. M.; Grubbs, R. H. The Development of L_2X_2RuCHR Olefin Metathesis Catalysts: An Organometallic Success Story. *Acc. Chem. Res.* **2001**, *34* (1), 18–29. <https://doi.org/10.1021/ar000114f>.
- (44) Hoveyda, A. H.; Zhugralin, A. R. The Remarkable Metal-Catalysed Olefin Metathesis Reaction. *Nature* **2007**, *450* (7167), 243–251. <https://doi.org/10.1038/nature06351>.
- (45) Piola, L.; Nahra, F.; Nolan, S. P. Olefin Metathesis in Air. *Beilstein J. Org. Chem.* **2015**, *11*, 2038–2055. <https://doi.org/10.3762/bjoc.11.221>.
- (46) Kajetanowicz, A.; Chwalba, M.; Gawin, A.; Tracz, A.; Grela, K. Non-Glovebox Ethenolysis of Ethyl Oleate and FAME at Larger Scale Utilizing a Cyclic (Alkyl)(Amino)Carbene Ruthenium Catalyst. *Eur. J. Lipid Sci. Technol.* **2020**, *122* (1), 1900263. <https://doi.org/10.1002/ejlt.201900263>.
- (47) Solans-Monfort, X.; Copéret, C.; Eisenstein, O. Oxo vs Imido Alkylidene D0-Metal Species: How and Why Do They Differ in Structure, Activity, and Efficiency in Alkene Metathesis? *Organometallics* **2012**, *31* (19), 6812–6822. <https://doi.org/10.1021/om300576r>.
- (48) Jean-Louis Hérisson, P.; Chauvin, Y. Catalyse de Transformation Des Oléfines Par Les Complexes Du Tungstène. II. Télomérisation Des Oléfines Cycliques En Présence d'oléfines Acycliques. *Makromol. Chem.* **1971**, *141* (1), 161–176. <https://doi.org/10.1002/macp.1971.021410112>.
- (49) Chauvin, Y. Olefin Metathesis: The Early Days (Nobel Lecture). *Angew. Chem.-Int. Ed.* **2006**, *45* (23), 3740–3747. <https://doi.org/10.1002/anie.200601234>.
- (50) Fürstner, A. Teaching Metathesis “Simple” Stereochemistry. *Science* **2013**, *341* (6152), 1229713. <https://doi.org/10.1126/science.1229713>.
- (51) Keitz, B. K.; Fedorov, A.; Grubbs, R. H. Cis-Selective Ring-Opening Metathesis Polymerization with Ruthenium Catalysts. *J. Am. Chem. Soc.* **2012**, *134* (4), 2040–2043. <https://doi.org/10.1021/ja211676y>.
- (52) Meek, S. J.; O'Brien, R. V.; Llaveria, J.; Schrock, R. R.; Hoveyda, A. H. Catalytic Z-Selective Olefin Cross-Metathesis for Natural Product Synthesis. *Nature* **2011**, *471* (7339), 461–466. <https://doi.org/10.1038/nature09957>.
- (53) Herbert, M. B.; Grubbs, R. H. Z-Selective Cross Metathesis with Ruthenium Catalysts: Synthetic Applications and Mechanistic Implications. *Angew. Chem. Int. Ed.* **2015**, *54* (17), 5018–5024. <https://doi.org/10.1002/anie.201411588>.
- (54) Koh, M. J.; Khan, R. K. M.; Torker, S.; Yu, M.; Mikus, M. S.; Hoveyda, A. H. High-Value Alcohols and Higher-Oxidation-State Compounds by Catalytic Z-Selective Cross Metathesis. *Nature* **2015**, *517* (7533), 181–186. <https://doi.org/10.1038/nature14061>.
- (55) Occhipinti, G.; Törnroos, K. W.; Jensen, V. R. Pyridine-Stabilized Fast-Initiating Ruthenium Monothiolate Catalysts for Z-Selective Olefin Metathesis. *Organometallics* **2017**, *36* (17), 3284–3292. <https://doi.org/10.1021/acs.organomet.7b00441>.

-
- (56) Xu, C.; Liu, Z.; Torker, S.; Shen, X.; Xu, D.; Hoveyda, A. H. Synthesis of Z- or E-Trisubstituted Allylic Alcohols and Ethers by Kinetically Controlled Cross-Metathesis with a Ru Catechothiolate Complex. *J Am Chem Soc* **2017**, *139* (44), 15640–15643. <https://doi.org/10.1021/jacs.7b10010>.
- (57) Ahmed, T. S.; Montgomery, T. P.; Grubbs, R. H. Using Stereoretention for the Synthesis of E-Macrocycles with Ruthenium-Based Olefin Metathesis Catalysts. *Chem Sci* **2018**, *9* (14), 3580–3583. <https://doi.org/10.1039/c8sc00435h>.
- (58) Herbert, M. B.; Marx, V. M.; Pederson, R. L.; Grubbs, R. H. Concise Syntheses of Insect Pheromones Using Z-Selective Cross Metathesis. *Angew. Chem. Int. Ed.* **2013**, *52* (1), 310–314. <https://doi.org/10.1002/anie.201206079>.
- (59) Marx, V. M.; Herbert, M. B.; Keitz, B. K.; Grubbs, R. H. Stereoselective Access to Z and E Macrocycles by Ruthenium-Catalyzed Z-Selective Ring-Closing Metathesis and Ethenolysis. *J. Am. Chem. Soc.* **2013**, *135* (1), 94–97. <https://doi.org/10.1021/ja311241q>.
- (60) Montgomery, T. P.; Johns, A. M.; Grubbs, R. H. Recent Advancements in Stereoselective Olefin Metathesis Using Ruthenium Catalysts. *Catalysts* **2017**, *7* (3), 87. <https://doi.org/10.3390/catal7030087>.
- (61) Montgomery, T. P.; Ahmed, T. S.; Grubbs, R. H. Stereoretentive Olefin Metathesis: An Avenue to Kinetic Selectivity. *Angew. Chem. Int. Ed.* **2017**, *56* (37), 11024–11036. <https://doi.org/10.1002/anie.201704686>.
- (62) Müller, D. S.; Baslé, O.; Mauduit, M. A Tutorial Review of Stereoretentive Olefin Metathesis Based on Ruthenium Dithiolate Catalysts. *Beilstein J. Org. Chem.* **2018**, *14* (1), 2999–3010. <https://doi.org/10.3762/bjoc.14.279>.
- (63) Smit, W.; Foscatto, M.; Occhipinti, G.; Jensen, V. R. Ethylene-Triggered Formation of Ruthenium Alkylidene from Decomposed Catalyst. *ACS Catal.* **2020**, *10* (12), 6788–6797. <https://doi.org/10.1021/acscatal.0c02206>.
- (64) Bailey, G. A.; Foscatto, M.; Higman, C. S.; Day, C. S.; Jensen, V. R.; Fogg, D. E. Bimolecular Coupling as a Vector for Decomposition of Fast-Initiating Olefin Metathesis Catalysts. *J. Am. Chem. Soc.* **2018**, *140* (22), 6931–6944. <https://doi.org/10.1021/jacs.8b02709>.
- (65) Engel, J.; Smit, W.; Foscatto, M.; Occhipinti, G.; Törnroos, K. W.; Jensen, V. R. Loss and Reformation of Ruthenium Alkylidene: Connecting Olefin Metathesis, Catalyst Deactivation, Regeneration, and Isomerization. *J. Am. Chem. Soc.* **2017**, *139* (46), 16609–16619. <https://doi.org/10.1021/jacs.7b07694>.
- (66) Bailey, G. A.; Lummiss, J. A. M.; Foscatto, M.; Occhipinti, G.; McDonald, R.; Jensen, V. R.; Fogg, D. E. Decomposition of Olefin Metathesis Catalysts by Brønsted Base: Metallacyclobutane Deprotonation as a Primary Deactivating Event. *J. Am. Chem. Soc.* **2017**, *139* (46), 16446–16449. <https://doi.org/10.1021/jacs.7b08578>.
- (67) Higman, C. S.; Lanterna, A. E.; Marin, M. L.; Scaiano, J. C.; Fogg, D. E. Catalyst Decomposition during Olefin Metathesis Yields Isomerization-Active Ruthenium Nanoparticles. *ChemCatChem* **2016**, *8* (15), 2446–2449. <https://doi.org/10.1002/cctc.201600738>.
- (68) McClennan, W. L.; Rufh, S. A.; Lummiss, J. A.; Fogg, D. E. A General Decomposition Pathway for Phosphine-Stabilized Metathesis Catalysts: Lewis Donors Accelerate Methylidene Abstraction. *J Am Chem Soc* **2016**, *138* (44), 14668–14677. <https://doi.org/10.1021/jacs.6b08372>.
- (69) Ireland, B. J.; Dobigny, B. T.; Fogg, D. E. Decomposition of a Phosphine-Free Metathesis Catalyst by Amines and Other Brønsted Bases: Metallacyclobutane Deprotonation as a Major Deactivation Pathway. *ACS Catal.* **2015**, *5* (8), 4690–4698. <https://doi.org/10.1021/acscatal.5b00813>.
- (70) Nelson, D. J.; Manzini, S.; Urbina-Blanco, C. A.; Nolan, S. P. Key Processes in Ruthenium-Catalysed Olefin Metathesis. *Chem. Commun.* **2014**, *50* (72), 10355. <https://doi.org/10.1039/C4CC02515F>.
- (71) Higman, C. S.; Plais, L.; Fogg, D. E. Isomerization During Olefin Metathesis: An Assessment of Potential Catalyst Culprits. *ChemCatChem* **2013**, *5* (12), 3548–3551. <https://doi.org/10.1002/cctc.201300886>.

-
- (72) Hong, S. H.; Wenzel, A. G.; Salguero, T. T.; Day, M. W.; Grubbs, R. H. Decomposition of Ruthenium Olefin Metathesis Catalysts. *J. Am. Chem. Soc.* **2007**, *129* (25), 7961–7968. <https://doi.org/10.1021/ja0713577>.
- (73) Janse van Rensburg, W.; Steynberg, P. J.; Meyer, W. H.; Kirk, M. M.; Forman, G. S. DFT Prediction and Experimental Observation of Substrate-Induced Catalyst Decomposition in Ruthenium-Catalyzed Olefin Metathesis. *J. Am. Chem. Soc.* **2004**, *126* (44), 14332–14333. <https://doi.org/10.1021/ja0453174>.
- (74) Maechling, S.; Zaja, M.; Blechert, S. Unexpected Results of a Turnover Number (TON) Study Utilising Ruthenium-Based Olefin Metathesis Catalysts. *Adv. Synth. Catal.* **2005**, *347* (10), 1413–1422. <https://doi.org/10.1002/adsc.200505053>.
- (75) Conrad, J. C.; Fogg, D. E. Ruthenium-Catalyzed Ring-Closing Metathesis: Recent Advances, Limitations and Opportunities. *Curr. Org. Chem.* **2006**, *10* (2), 185–202. <https://doi.org/10.2174/138527206775192942>.
- (76) du Toit, J. I.; van der Gryp, P.; Loock, M. M.; Tole, T. T.; Marx, S.; Jordaan, J. H. L.; Vosloo, H. C. M. Industrial Viability of Homogeneous Olefin Metathesis: Beneficiation of Linear Alpha Olefins with the Diphenyl-Substituted Pyridinyl Alcoholato Ruthenium Carbene Precatalyst. *Catal. Today* **2016**, *275*, 191–200. <https://doi.org/10.1016/j.cattod.2015.12.004>.
- (77) Schrodi, Y.; Ung, T.; Vargas, A.; Mkrtumyan, G.; Lee, C. W.; Champagne, T. M.; Pederson, R. L.; Hong, S. H. Ruthenium Olefin Metathesis Catalysts for the Ethenolysis of Renewable Feedstocks. *CLEAN – Soil Air Water* **2008**, *36* (8), 669–673. <https://doi.org/10.1002/clen.200800088>.
- (78) Hagen, J. *Industrial Catalysis: A Practical Approach*, 2nd ed.; Wiley-VCH, 2006.
- (79) Occhipinti, G.; Hansen, F. R.; Törnroos, K. W.; Jensen, V. R. Simple and Highly Z-Selective Ruthenium-Based Olefin Metathesis Catalyst. *J. Am. Chem. Soc.* **2013**, *135* (9), 3331–3334. <https://doi.org/10.1021/ja311505v>.
- (80) Ziegler, K.; Holzkamp, E.; Breil, H.; Martin, H. Das Mülheimer Normaldruck-Polyäthylen-Verfahren. *Angew. Chem.* **1955**, *67*, 541–547. <https://doi.org/10.1002/ange.19550671902>.
- (81) Truett, W. L.; Johnson, D. R.; Robinson, I. M.; Montague, B. A. Polynorbornene by Coördination Polymerization¹. *J. Am. Chem. Soc.* **1960**, *82* (9), 2337–2340. <https://doi.org/10.1021/ja01494a057>.
- (82) Banks, R. L.; Bailey, G. C. Olefin Disproportionation. A New Catalytic Process. *IEC Prod. Res. Dev.* **1964**, *3* (3), 170–173. <https://doi.org/10.1021/i360011a002>.
- (83) Calderon, N.; Ofstead, E. A.; Ward, J. P.; Judy, W. A.; Scott, K. W. Olefin Metathesis. I. Acyclic Vinylenic Hydrocarbons. *J. Am. Chem. Soc.* **1968**, *90* (15), 4133–4140. <https://doi.org/10.1021/ja01017a039>.
- (84) Bradshaw, C. P. C.; Howman, E. J.; Turner, L. Olefin Dismutation: Reactions of Olefins on Cobalt Oxide-Molybdenum Oxide-Alumina. *J. Catal.* **1967**, *7* (3), 269–276. [https://doi.org/10.1016/0021-9517\(67\)90105-4](https://doi.org/10.1016/0021-9517(67)90105-4).
- (85) Woodward, R. B.; Hoffmann, R. The Conservation of Orbital Symmetry. *Angew. Chem. Int. Ed. Engl.* **1969**, *8* (11), 781–853. <https://doi.org/10.1002/anie.196907811>.
- (86) Mango, F. D.; Schachtschneider, J. H. Molecular Orbital Symmetry Conservation in Transition Metal Catalyzed Transformations. *J. Am. Chem. Soc.* **1967**, *89* (10), 2484–2486. <https://doi.org/10.1021/ja00986a044>.
- (87) Calderon, N. Olefin Metathesis Reaction. *Acc. Chem. Res.* **1972**, *5* (4), 127–132. <https://doi.org/10.1021/ar50052a002>.
- (88) Grubbs, R. H.; Burk, P. L.; Carr, D. D. Mechanism of the Olefin Metathesis Reaction. *J. Am. Chem. Soc.* **1975**, *97* (11), 3265–3267. <https://doi.org/10.1021/ja00844a082>.
- (89) Katz, T. J.; McGinnis, J. Mechanism of the Olefin Metathesis Reaction. *J. Am. Chem. Soc.* **1975**, *97* (6), 1592–1594. <https://doi.org/10.1021/ja00839a063>.
- (90) Katz, T. J.; Rothchild, R. Mechanism of the Olefin Metathesis of 2,2'-Divinylbiphenyl. *J. Am. Chem. Soc.* **1976**, *98* (9), 2519–2526. <https://doi.org/10.1021/ja00425a021>.
- (91) Grubbs, R. H.; Carr, D. D.; Hoppin, C.; Burk, P. L. Consideration of the Mechanism of the Metal Catalyzed Olefin Metathesis Reaction. *J. Am. Chem. Soc.* **1976**, *98* (12), 3478–3483. <https://doi.org/10.1021/ja00428a015>.

-
- (92) Sanford, M. S.; Ulman, M.; Grubbs, R. H. New Insights into the Mechanism of Ruthenium-Catalyzed Olefin Metathesis Reactions. *J. Am. Chem. Soc.* **2001**, *123* (4), 749–750. <https://doi.org/10.1021/ja003582t>.
- (93) Tebbe, F. N.; Parshall, G. W.; Reddy, G. S. Olefin Homologation with Titanium Methylene Compounds. *J. Am. Chem. Soc.* **1978**, *100* (11), 3611–3613. <https://doi.org/10.1021/ja00479a061>.
- (94) Gilliom, L. R.; Grubbs, R. H. Titanacyclobutanes Derived from Strained, Cyclic Olefins: The Living Polymerization of Norbornene. *J. Am. Chem. Soc.* **1986**, *108* (4), 733–742. <https://doi.org/10.1021/ja00264a027>.
- (95) Howard, T. R.; Lee, J. B.; Grubbs, R. H. Titanium Metallacarbene-Metallacyclobutane Reactions: Stepwise Metathesis. *J. Am. Chem. Soc.* **1980**, *102* (22), 6876–6878. <https://doi.org/10.1021/ja00542a050>.
- (96) Schrock, R. R. Alkylcarbene Complex of Tantalum by Intramolecular Alpha-Hydrogen Abstraction. *J. Am. Chem. Soc.* **1974**, *96* (21), 6796–6797. <https://doi.org/10.1021/ja00828a061>.
- (97) McLain, S. J.; Wood, C. D.; Schrock, R. R. Preparation and Characterization of Tantalum(III) Olefin Complexes and Tantalum(V) Metallacyclopentane Complexes Made from Acyclic .Alpha. Olefins. *J. Am. Chem. Soc.* **1979**, *101* (16), 4558–4570. <https://doi.org/10.1021/ja00510a022>.
- (98) Calderon, N.; Chen, H. Y.; Scott, K. W. Olefin Metathesis - A Novel Reaction for Skeletal Transformations of Unsaturated Hydrocarbons. *Tetrahedron Lett.* **1967**, *8* (34), 3327–3329. [https://doi.org/10.1016/S0040-4039\(01\)89881-6](https://doi.org/10.1016/S0040-4039(01)89881-6).
- (99) Novak, B. M.; Risse, W.; Grubbs, R. H. The Development of Well-Defined Catalysts for Ring-Opening Olefin Metathesis Polymerizations (Romp). *Adv. Polym. Sci.* **1992**, *102*, 47–72. https://doi.org/10.1007/3-540-55090-9_2.
- (100) Wengrovius, J. H.; Schrock, R. R.; Churchill, M. R.; Missert, J. R.; Youngs, W. J. Multiple Metal-Carbon Bonds. 16. Tungsten-Oxo Alkylidene Complexes as Olefins Metathesis Catalysts and the Crystal Structure of W(O)(CHCMe₃(PEt₃)Cl₂). *J. Am. Chem. Soc.* **1980**, *102* (13), 4515–4516. <https://doi.org/10.1021/ja00533a035>.
- (101) Schaverien, C. J.; Dewan, J. C.; Schrock, R. R. Multiple Metal-Carbon Bonds. 43. Well-Characterized, Highly Active, Lewis Acid Free Olefin Metathesis Catalysts. *J. Am. Chem. Soc.* **1986**, *108* (10), 2771–2773. <https://doi.org/10.1021/ja00270a056>.
- (102) Schrock, R. R.; Feldman, J.; Cannizzo, L. F.; Grubbs, R. H. Ring-Opening Polymerization of Norbornene by a Living Tungsten Alkylidene Complex. *Macromolecules* **1987**, *20* (5), 1169–1172. <https://doi.org/10.1021/ma00171a053>.
- (103) Schrock, R. R.; Murdzek, J. S.; Bazan, G. C.; Robbins, J.; DiMare, M.; O'Regan, M. Synthesis of Molybdenum Imido Alkylidene Complexes and Some Reactions Involving Acyclic Olefins. *J. Am. Chem. Soc.* **1990**, *112* (10), 3875–3886. <https://doi.org/10.1021/ja00166a023>.
- (104) Flook, M. M.; Jiang, A. J.; Schrock, R. R.; Müller, P.; Hoveyda, A. H. Z-Selective Olefin Metathesis Processes Catalyzed by a Molybdenum Hexaisopropylterphenoxide Monopyrrolide Complex. *J. Am. Chem. Soc.* **2009**, *131* (23), 7962–7963. <https://doi.org/10.1021/ja902738u>.
- (105) Jiang, A. J.; Zhao, Y.; Schrock, R. R.; Hoveyda, A. H. Highly Z-Selective Metathesis Homocoupling of Terminal Olefins. *J. Am. Chem. Soc.* **2009**, *131* (46), 16630–16631. <https://doi.org/10.1021/ja908098t>.
- (106) Peryshkov, D. V.; Schrock, R. R.; Takase, M. K.; Muller, P.; Hoveyda, A. H. Z-Selective Olefin Metathesis Reactions Promoted by Tungsten Oxo Alkylidene Complexes. *J Am Chem Soc* **2011**, *133* (51), 20754–20757. <https://doi.org/10.1021/ja210349m>.
- (107) Gulyás, H.; Hayano, S.; Madarász, Á.; Pápai, I.; Szabó, M.; Bucsa, Á.; Martin, E.; Benet-Buchholz, J. Air-Stable 18-Electron Adducts of Schrock Catalysts with Tuned Stability Constants for Spontaneous Release of the Active Species. *Commun. Chem.* **2021**, *4* (1), 1–11. <https://doi.org/10.1038/s42004-021-00503-4>.
- (108) Hauser, P. M.; Musso, J. V.; Frey, W.; Buchmeiser, M. R. Cationic Tungsten Oxo Alkylidene N-Heterocyclic Carbene Complexes via Hydrolysis of Cationic Alkylidyne Progenitors. *Organometallics* **2021**, *40* (7), 927–937. <https://doi.org/10.1021/acs.organomet.1c00035>.

- (109) Benedikter, M. J.; Musso, J. V.; Frey, W.; Schowner, R.; Buchmeiser, M. R. Cationic Group VI Metal Imido Alkylidene N-Heterocyclic Carbene Nitrile Complexes: Bench-Stable, Functional-Group-Tolerant Olefin Metathesis Catalysts. *Angew. Chem. Int. Ed.* **2021**, *60* (3), 1374–1382. <https://doi.org/10.1002/anie.202011666>.
- (110) Heppekausen, J.; Fürstner, A. Rendering Schrock-Type Molybdenum Alkylidene Complexes Air Stable: User-Friendly Precatalysts for Alkene Metathesis. *Angew. Chem. Int. Ed.* **2011**, *50* (34), 7829–7832. <https://doi.org/10.1002/anie.201102012>.
- (111) Buchmeiser, M. R.; Sen, S.; Unold, J.; Frey, W. N-Heterocyclic Carbene, High Oxidation State Molybdenum Alkylidene Complexes: Functional-Group-Tolerant Cationic Metathesis Catalysts. *Angew. Chem. Int. Ed.* **2014**, *53* (35), 9384–9388. <https://doi.org/10.1002/anie.201404655>.
- (112) Solans-Monfort, X.; Copéret, C.; Eisenstein, O. Metallacyclobutanes from Schrock-Type D0 Metal Alkylidene Catalysts: Structural Preferences and Consequences in Alkene Metathesis. *Organometallics* **2015**, *34* (9), 1668–1680. <https://doi.org/10.1021/acs.organomet.5b00147>.
- (113) Rhers, B.; Salameh, A.; Baudouin, A.; Quadrelli, E. A.; Taoufik, M.; Copéret, C.; Lefebvre, F.; Basset, J.-M.; Solans-Monfort, X.; Eisenstein, O.; Lukens, W. W.; Lopez, L. P. H.; Sinha, A.; Schrock, R. R. A Well-Defined, Silica-Supported Tungsten Imido Alkylidene Olefin Metathesis Catalyst. *Organometallics* **2006**, *25* (15), 3554–3557. <https://doi.org/10.1021/om060279d>.
- (114) Poater, A.; Solans-Monfort, X.; Clot, E.; Coperet, C.; Eisenstein, O. Understanding d(0)-Olefin Metathesis Catalysts: Which Metal, Which Ligands? *J. Am. Chem. Soc.* **2007**, *129* (26), 8207–8216. <https://doi.org/10.1021/ja070625y>.
- (115) Nguyen, T. T.; Koh, M. J.; Shen, X.; Romiti, F.; Schrock, R. R.; Hoveyda, A. H. Kinetically Controlled E-Selective Catalytic Olefin Metathesis. *Science* **2016**, *352* (6285), 569–575. <https://doi.org/10.1126/science.aaf4622>.
- (116) Nguyen, S. T.; Johnson, L. K.; Grubbs, R. H.; Ziller, J. W. Ring-Opening Metathesis Polymerization (ROMP) of Norbornene by a Group VIII Carbene Complex in Protic Media. *J. Am. Chem. Soc.* **1992**, *114* (10), 3974–3975. <https://doi.org/10.1021/ja00036a053>.
- (117) Schwab, P.; Grubbs, R. H.; Ziller, J. W. Synthesis and Applications of RuCl₂(CHR')(PR₃)₂: The Influence of the Alkylidene Moiety on Metathesis Activity. *J. Am. Chem. Soc.* **1996**, *118* (1), 100–110. <https://doi.org/10.1021/ja952676d>.
- (118) Nguyen, S. T.; Grubbs, R. H.; Ziller, J. W. Syntheses and Activities of New Single-Component, Ruthenium-Based Olefin Metathesis Catalysts. *J. Am. Chem. Soc.* **1993**, *115* (21), 9858–9859. <https://doi.org/10.1021/ja00074a086>.
- (119) Schwab, P.; France, M. B.; Ziller, J. W.; Grubbs, R. H. A Series of Well-Defined Metathesis Catalysts—Synthesis of [RuCl₂(=CHR')(PR₃)₂] and Its Reactions. *Angew. Chem. Int. Ed. Engl.* **1995**, *34* (18), 2039–2041. <https://doi.org/10.1002/anie.199520391>.
- (120) Grubbs, R. H.; Chang, S. Recent Advances in Olefin Metathesis and Its Application in Organic Synthesis. *Tetrahedron* **1998**, *54* (18), 4413–4450. [https://doi.org/10.1016/S0040-4020\(97\)10427-6](https://doi.org/10.1016/S0040-4020(97)10427-6).
- (121) Chang, S.; Jones, L.; Wang, C. M.; Henling, L. M.; Grubbs, R. H. Synthesis and Characterization of New Ruthenium-Based Olefin Metathesis Catalysts Coordinated with Bidentate Schiff-Base Ligands. *Organometallics* **1998**, *17* (16), 3460–3465. <https://doi.org/10.1021/om970910y>.
- (122) Dias, E. L.; Grubbs, R. H. Synthesis and Investigation of Homo- and Heterobimetallic Ruthenium Olefin Metathesis Catalysts Exhibiting Increased Activities. *Organometallics* **1998**, *17* (13), 2758–2767. <https://doi.org/10.1021/om9708788>.
- (123) Sanford, M. S.; Henling, L. M.; Grubbs, R. H. Synthesis and Reactivity of Neutral and Cationic Ruthenium(II) Tris(Pyrazolyl)Borate Alkylidenes. *Organometallics* **1998**, *17* (24), 5384–5389. <https://doi.org/10.1021/om980683f>.
- (124) Weskamp, T.; Schattenmann, W. C.; Spiegler, M.; Herrmann, W. A. A Novel Class of Ruthenium Catalysts for Olefin Metathesis. *Angew. Chem.-Int. Ed.* **1998**, *37* (18), 2490–2493. [https://doi.org/10.1002/\(SICI\)1521-3773\(19981002\)37:18<2490::AID-ANIE2490>3.0.CO;2-X](https://doi.org/10.1002/(SICI)1521-3773(19981002)37:18<2490::AID-ANIE2490>3.0.CO;2-X).
- (125) Weskamp, T.; Kohl, F. J.; Hieringer, W.; Gleich, D.; Herrmann, W. A. Highly Active Ruthenium Catalysts for Olefin Metathesis: The Synergy of N-Heterocyclic Carbenes and

- Coordinatively Labile Ligands. *Angew. Chem. Int. Ed.* **1999**, *38* (16), 2416–2419. [https://doi.org/10.1002/\(SICI\)1521-3773\(19990816\)38:16<2416::AID-ANIE2416>3.0.CO;2-#](https://doi.org/10.1002/(SICI)1521-3773(19990816)38:16<2416::AID-ANIE2416>3.0.CO;2-#).
- (126) Huang, J.; Stevens, E. D.; Nolan, S. P.; Petersen, J. L. Olefin Metathesis-Active Ruthenium Complexes Bearing a Nucleophilic Carbene Ligand. *J. Am. Chem. Soc.* **1999**, *121* (12), 2674–2678. <https://doi.org/10.1021/ja9831352>.
- (127) Scholl, M.; Trnka, T. M.; Morgan, J. P.; Grubbs, R. H. Increased Ring Closing Metathesis Activity of Ruthenium-Based Olefin Metathesis Catalysts Coordinated with Imidazolin-2-Ylidene Ligands. *Tetrahedron Lett.* **1999**, *40* (12), 2247–2250. [https://doi.org/10.1016/S0040-4039\(99\)00217-8](https://doi.org/10.1016/S0040-4039(99)00217-8).
- (128) Ackermann, L.; Furstner, A.; Weskamp, T.; Kohl, F. J.; Herrmann, W. A. Ruthenium Carbene Complexes with Imidazolin-2-Ylidene Ligands Allow the Formation of Tetrasubstituted Cycloalkenes by RCM. *Tetrahedron Lett.* **1999**, *40* (26), 4787–4790. [https://doi.org/10.1016/S0040-4039\(99\)00919-3](https://doi.org/10.1016/S0040-4039(99)00919-3).
- (129) Scholl, M.; Ding, S.; Lee, C. W.; Grubbs, R. H. Synthesis and Activity of a New Generation of Ruthenium-Based Olefin Metathesis Catalysts Coordinated with 1,3-Dimesityl-4,5-Dihydroimidazol-2-Ylidene Ligands. *Org. Lett.* **1999**, *1* (6), 953–956. <https://doi.org/10.1021/ol990909q>.
- (130) Kingsbury, J. S.; Harrity, J. P. A.; Bonitatebus, P. J.; Hoveyda, A. H. A Recyclable Ru-Based Metathesis Catalyst. *J. Am. Chem. Soc.* **1999**, *121* (4), 791–799. <https://doi.org/10.1021/ja983222u>.
- (131) Garber, S. B.; Kingsbury, J. S.; Gray, B. L.; Hoveyda, A. H. Efficient and Recyclable Monomeric and Dendritic Ru-Based Metathesis Catalysts. *J. Am. Chem. Soc.* **2000**, *122* (34), 8168–8179. <https://doi.org/10.1021/ja001179g>.
- (132) Gessler, S.; Randl, S.; Blechert, S. Synthesis and Metathesis Reactions of a Phosphine-Free Dihydroimidazole Carbene Ruthenium Complex. *Tetrahedron Lett.* **2000**, *41* (51), 9973–9976. [https://doi.org/10.1016/S0040-4039\(00\)01808-6](https://doi.org/10.1016/S0040-4039(00)01808-6).
- (133) Grela, K.; Harutyunyan, S.; Michrowska, A. A Highly Efficient Ruthenium Catalyst for Metathesis Reactions. *Angew. Chem. Int. Ed.* **2002**, *41* (21), 4038–4040. [https://doi.org/10.1002/1521-3773\(20021104\)41:21<4038::AID-ANIE4038>3.0.CO;2-0](https://doi.org/10.1002/1521-3773(20021104)41:21<4038::AID-ANIE4038>3.0.CO;2-0).
- (134) Kajetanowicz, A.; Grela, K. Nitro and Other Electron Withdrawing Group Activated Ruthenium Catalysts for Olefin Metathesis Reactions. *Angew. Chem. Int. Ed.* **2021**, *60* (25), 13738–13756. <https://doi.org/10.1002/anie.202008150>.
- (135) Sanford, M. S.; Love, J. A.; Grubbs, R. H. A Versatile Precursor for the Synthesis of New Ruthenium Olefin Metathesis Catalysts. *Organometallics* **2001**, *20* (25), 5314–5318. <https://doi.org/10.1021/om010599r>.
- (136) Love, J. A.; Morgan, J. P.; Trnka, T. M.; Grubbs, R. H. A Practical and Highly Active Ruthenium-Based Catalyst That Effects the Cross Metathesis of Acrylonitrile. *Angew. Chem.-Int. Ed.* **2002**, *41* (21), 4035–4037. [https://doi.org/10.1002/1521-3773\(20021104\)41:21<4035::AID-ANIE4035>3.0.CO;2-I](https://doi.org/10.1002/1521-3773(20021104)41:21<4035::AID-ANIE4035>3.0.CO;2-I).
- (137) Nascimento, D. L.; Fogg, D. E. Origin of the Breakthrough Productivity of Ruthenium–Cyclic Alkyl Amino Carbene Catalysts in Olefin Metathesis. *J. Am. Chem. Soc.* **2019**, *141* (49), 19236–19240. <https://doi.org/10.1021/jacs.9b10750>.
- (138) Occhipinti, G.; Nascimento, D. L.; Foscatto, M.; Fogg, D. E.; Jensen, V. R. The Janus Face of High Trans-Effect Carbenes in Olefin Metathesis: Gateway to Both Productivity and Decomposition. *Chem. Sci.* **2022**, *13* (18), 5107–5117. <https://doi.org/10.1039/D2SC00855F>.
- (139) Lehman, S. E.; Schwendeman, J. E.; O'Donnell, P. M.; Wagener, K. B. Olefin Isomerization Promoted by Olefin Metathesis Catalysts. *Inorganica Chim. Acta* **2003**, *345*, 190–198. [https://doi.org/10.1016/s0020-1693\(02\)01307-5](https://doi.org/10.1016/s0020-1693(02)01307-5).
- (140) Hong, S. H.; Sanders, D. P.; Lee, C. W.; Grubbs, R. H. Prevention of Undesirable Isomerization during Olefin Metathesis. *J. Am. Chem. Soc.* **2005**, *127* (49), 17160–17161. <https://doi.org/10.1021/ja052939w>.
- (141) Jawiczuk, M.; Marczyk, A.; Trzaskowski, B. Decomposition of Ruthenium Olefin Metathesis Catalyst. *Catalysts* **2020**, *10* (8), 887. <https://doi.org/10.3390/catal10080887>.

- (142) Lummiss, J. A. M.; McClennan, W. L.; McDonald, R.; Fogg, D. E. Donor-Induced Decomposition of the Grubbs Catalysts: An Intercepted Intermediate. *Organometallics* **2014**, *33* (23), 6738–6741. <https://doi.org/10.1021/om501011y>.
- (143) Lummiss, J. A. M.; Ireland, B. J.; Sommers, J. M.; Fogg, D. E. Amine-Mediated Degradation in Olefin Metathesis Reactions That Employ the Second-Generation Grubbs Catalyst. *Chemcatchem* **2014**, *6* (2), 459–463. <https://doi.org/10.1002/cctc.201300861>.
- (144) Nascimento, D. L.; Reim, I.; Foscatto, M.; Jensen, V. R.; Fogg, D. E. Challenging Metathesis Catalysts with Nucleophiles and Brønsted Base: Examining the Stability of State-of-the-Art Ruthenium Carbene Catalysts to Attack by Amines. *ACS Catal.* **2020**, *10* (19), 11623–11633. <https://doi.org/10.1021/acscatal.0c02760>.
- (145) Nascimento, D. L.; Foscatto, M.; Occhipinti, G.; Jensen, V. R.; Fogg, D. E. Bimolecular Coupling in Olefin Metathesis: Correlating Structure and Decomposition for Leading and Emerging Ruthenium-Carbene Catalysts. *J. Am. Chem. Soc.* **2021**, *143* (29), 11072–11079. <https://doi.org/10.1021/jacs.1c04424>.
- (146) Marx, V. M.; Sullivan, A. H.; Melaimi, M.; Virgil, S. C.; Keitz, B. K.; Weinberger, D. S.; Bertrand, G.; Grubbs, R. H. Cyclic Alkyl Amino Carbene (CAAC) Ruthenium Complexes as Remarkably Active Catalysts for Ethenolysis. *Angew. Chem. Int. Ed.* **2015**, *54* (6), 1919–1923. <https://doi.org/10.1002/anie.201410797>.
- (147) Patel, J.; Mujcinovic, S.; Jackson, W. R.; Robinson, A. J.; Serelis, A. K.; Such, C. High Conversion and Productive Catalyst Turnovers in Cross-Metathesis Reactions of Natural Oils with 2-Butene. *Green Chem.* **2006**, *8* (5). <https://doi.org/10.1039/b600956e>.
- (148) Ulman, M.; Grubbs, R. H. Relative Reaction Rates of Olefin Substrates with Ruthenium(II) Carbene Metathesis Initiators. *Organometallics* **1998**, *17* (12), 2484–2489. <https://doi.org/10.1021/om9710172>.
- (149) Occhipinti, G.; Koudriavtsev, V.; Törnroos, K. W.; Jensen, V. R. Theory-Assisted Development of a Robust and Z-Selective Olefin Metathesis Catalyst. *Dalton Trans.* **2014**, *43* (29), 11106–11117. <https://doi.org/10.1039/C4DT00409D>.
- (150) Nelson, J. W.; Grundy, L. M.; Dang, Y.; Wang, Z.-X.; Wang, X. Mechanism of Z-Selective Olefin Metathesis Catalyzed by a Ruthenium Monothiolate Carbene Complex: A DFT Study. *Organometallics* **2014**, *33* (16), 4290–4294. <https://doi.org/10.1021/om500612r>.
- (151) Smit, W.; Koudriavtsev, V.; Occhipinti, G.; Törnroos, K. W.; Jensen, V. R. Phosphine-Based Z-Selective Ruthenium Olefin Metathesis Catalysts. *Organometallics* **2016**, *35*, 1825–1837. <https://doi.org/10.1021/acs.organomet.6b00214>.
- (152) Smit, W.; Ekeli, J. B.; Occhipinti, G.; Woźniak, B.; Törnroos, K. W.; Jensen, V. R. Z-Selective Monothiolate Ruthenium Indenylidene Olefin Metathesis Catalysts. *Organometallics* **2020**, *39* (3), 397–407. <https://doi.org/10.1021/acs.organomet.9b00641>.
- (153) Renom-Carrasco, M.; Mania, P.; Sayah, R.; Veyre, L.; Occhipinti, G.; Jensen, V. R.; Thieuleux, C. Silica-Supported Z-Selective Ru Olefin Metathesis Catalysts. *Mol. Catal.* **2020**, *483*, 110743. <https://doi.org/10.1016/j.mcat.2019.110743>.
- (154) Dang, Y.; Wang, Z.-X.; Wang, X. A Thorough DFT Study of the Mechanism of Homodimerization of Terminal Olefins through Metathesis with a Chelated Ruthenium Catalyst: From Initiation to Z Selectivity to Regeneration. *Organometallics* **2012**, *31* (20), 7222–7234. <https://doi.org/10.1021/om300784k>.
- (155) Bronner, S. M.; Herbert, M. B.; Patel, P. R.; Marx, V. M.; Grubbs, R. H. Ru-Based Z-Selective Metathesis Catalysts with Modified Cyclometalated Carbene Ligands. *Chem Sci* **2014**, *5* (10), 4091–4098. <https://doi.org/10.1039/C4SC01541J>.
- (156) Herbert, M. B.; Suslick, B. A.; Liu, P.; Zou, L.; Dornan, P. K.; Houk, K. N.; Grubbs, R. H. Cyclometalated Z-Selective Ruthenium Metathesis Catalysts with Modified N-Chelating Groups. *Organometallics* **2015**, *34* (12), 2858–2869. <https://doi.org/10.1021/acs.organomet.5b00185>.
- (157) Dang, Y.; Wang, Z.-X.; Wang, X. Does the Ruthenium Nitrate Catalyst Work Differently in Z-Selective Olefin Metathesis? A DFT Study. *Organometallics* **2012**, *31* (24), 8654–8657. <https://doi.org/10.1021/om300972h>.
- (158) Endo, K.; Grubbs, R. H. Chelated Ruthenium Catalysts for Z-Selective Olefin Metathesis. *J. Am. Chem. Soc.* **2011**, *133* (22), 8525–8527. <https://doi.org/10.1021/ja202818v>.

- (159) Dumas, A.; Tarrieu, R.; Vives, T.; Roisnel, T.; Dorcet, V.; Baslé, O.; Mauduit, M. A Versatile and Highly Z-Selective Olefin Metathesis Ruthenium Catalyst Based on a Readily Accessible N-Heterocyclic Carbene. *ACS Catal.* **2018**, *8* (4), 3257–3262. <https://doi.org/10.1021/acscatal.8b00151>.
- (160) Xu, Y.; Wong, J. J.; Samkian, A. E.; Ko, J. H.; Chen, S.; Houk, K. N.; Grubbs, R. H. Efficient Z -Selective Olefin-Acrylamide Cross-Metathesis Enabled by Sterically Demanding Cyclometalated Ruthenium Catalysts. *J. Am. Chem. Soc.* **2020**, *142* (50), 20987–20993. <https://doi.org/10.1021/jacs.0c11334>.
- (161) Monfette, S.; Fogg, D. E. Ruthenium Metathesis Catalysts Containing Chelating Aryloxide Ligands. *Organometallics* **2006**, *25* (8), 1940–1944. <https://doi.org/10.1021/om050952j>.
- (162) Krause, J. O.; Nuyken, O.; Wurst, K.; Buchmeiser, M. R. Synthesis and Reactivity of Homogeneous and Heterogeneous Ruthenium-Based Metathesis Catalysts Containing Electron-Withdrawing Ligands. *Chem.- Eur. J.* **2004**, *10* (3), 777–784. <https://doi.org/10.1002/chem.200305031>.
- (163) Teo, P.; Grubbs, R. H. Facile Synthesis of Efficient and Selective Ruthenium Olefin Metathesis Catalysts with Sulfonate and Phosphate Ligands. *Organometallics* **2010**, *29* (22), 6045–6050. <https://doi.org/10.1021/om1007924>.
- (164) Jensen, V. R.; Occhipinti, G.; Hansen, F. R. Novel Olefin Metathesis Catalysts. WO2012032131, 2012.
- (165) Jensen, V. R.; Occhipinti, G. Improved Olefin Metathesis Catalysts. United States Patent US 10,265,691 B2, 2019.
- (166) Marx, V. M.; Rosebrugh, L. E.; Herbert, M. B.; Grubbs, R. H. Cyclometalated Ruthenium Alkylidene Complexes: A Powerful Family of Z-Selective Olefin Metathesis Catalysts. In *Ruthenium in Catalysis*; Dixneuf, P. H., Bruneau, C., Eds.; Topics in Organometallic Chemistry; Springer International Publishing: Cham, 2014; Vol. 48, pp 1–17. https://doi.org/10.1007/3418_2014_76.
- (167) Hong, S. H.; Chlenov, A.; Day, M. W.; Grubbs, R. H. Double C-H Activation of an N-Heterocyclic Carbene Ligand in a Ruthenium Olefin Metathesis Catalyst. *Angew. Chem. Int. Ed.* **2007**, *46* (27), 5148–5151. <https://doi.org/10.1002/anie.200701234>.
- (168) Jazzar, R. F. R.; Macgregor, S. A.; Mahon, M. F.; Richards, S. P.; Whittlesey, M. K. C-C and C-H Bond Activation Reactions in N-Heterocyclic Carbene Complexes of Ruthenium. *J. Am. Chem. Soc.* **2002**, *124* (18), 4944–4945. <https://doi.org/10.1021/ja012475b>.
- (169) Trnka, T. M.; Morgan, J. P.; Sanford, M. S.; Wilhelm, T. E.; Scholl, M.; Choi, T. L.; Ding, S.; Day, M. W.; Grubbs, R. H. Synthesis and Activity of Ruthenium Alkylidene Complexes Coordinated with Phosphine and N-Heterocyclic Carbene Ligands. *J. Am. Chem. Soc.* **2003**, *125* (9), 2546–2558. <https://doi.org/10.1021/ja021146w>.
- (170) Leitao, E. M.; Dubberley, S. R.; Piers, W. E.; Wu, Q.; McDonald, R. Thermal Decomposition Modes for Four-Coordinate Ruthenium Phosphonium Alkylidene Olefin Metathesis Catalysts. *Chem. - Eur. J.* **2008**, *14* (36), 11565–11572. <https://doi.org/10.1002/chem.200801584>.
- (171) Endo, K.; Herbert, M. B.; Grubbs, R. H. Investigations into Ruthenium Metathesis Catalysts with Six-Membered Chelating NHC Ligands: Relationship between Catalyst Structure and Stereoselectivity. *Organometallics* **2013**, *32* (18), 5128–5135. <https://doi.org/10.1021/om4006966>.
- (172) Keitz, B. K.; Endo, K.; Patel, P. R.; Herbert, M. B.; Grubbs, R. H. Improved Ruthenium Catalysts for Z-Selective Olefin Metathesis. *J. Am. Chem. Soc.* **2012**, *134* (1), 693–699. <https://doi.org/10.1021/ja210225e>.
- (173) Pribisko, M. A.; Ahmed, T. S.; Grubbs, R. H. Z -Selective Ruthenium Metathesis Catalysts: Comparison of Nitrate and Nitrite X-Type Ligands. *Polyhedron* **2014**, *84*, 144–149. <https://doi.org/10.1016/j.poly.2014.06.055>.
- (174) Rosebrugh, L. E.; Herbert, M. B.; Marx, V. M.; Keitz, B. K.; Grubbs, R. H. Highly Active Ruthenium Metathesis Catalysts Exhibiting Unprecedented Activity and Z-Selectivity. *J. Am. Chem. Soc.* **2013**, *135* (4), 1276–1279. <https://doi.org/10.1021/ja311916m>.
- (175) Xu, Y.; Gan, Q.; Samkian, A. E.; Ko, J. H.; Grubbs, R. H. Bulky Cyclometalated Ruthenium Nitrates for Challenging Z -Selective Metathesis: Efficient One-Step Access to α -Oxygenated

- Z* -Olefins from Acrylates and Allyl Alcohols. *Angew. Chem. Int. Ed.* **2022**, *61* (4). <https://doi.org/10.1002/anie.202113089>.
- (176) Liu, P.; Xu, X.; Dong, X.; Keitz, B. K.; Herbert, M. B.; Grubbs, R. H.; Houk, K. N. *Z*-Selectivity in Olefin Metathesis with Chelated Ru Catalysts: Computational Studies of Mechanism and Selectivity. *J. Am. Chem. Soc.* **2012**, *134* (3), 1464–1467. <https://doi.org/10.1021/ja2108728>.
- (177) Rosebrugh, L. E.; Marx, V. M.; Keitz, B. K.; Grubbs, R. H. Synthesis of Highly *Cis*, Syndiotactic Polymers via Ring-Opening Metathesis Polymerization Using Ruthenium Metathesis Catalysts. *J. Am. Chem. Soc.* **2013**, *135* (27), 10032–10035. <https://doi.org/10.1021/ja405559y>.
- (178) Morvan, J.; McBride, T.; Curbet, I.; Colombel-Rouen, S.; Roisnel, T.; Crévisy, C.; Browne, D. L.; Mauduit, M. Continuous Flow *Z*-Stereoselective Olefin Metathesis: Development and Applications in the Synthesis of Pheromones and Macrocyclic Odorant Molecules. *Angew. Chem. Int. Ed.* **2021**, *60* (36), 19685–19690. <https://doi.org/10.1002/anie.202106410>.
- (179) Khan, R. K.; Torker, S.; Hoveyda, A. H. Readily Accessible and Easily Modifiable Ru-Based Catalysts for Efficient and *Z*-Selective Ring-Opening Metathesis Polymerization and Ring-Opening/Cross-Metathesis. *J. Am. Chem. Soc.* **2013**, *135* (28), 10258–10261. <https://doi.org/10.1021/ja404208a>.
- (180) Torker, S.; Khan, R. K.; Hoveyda, A. H. The Influence of Anionic Ligands on Stereoisomerism of Ru Carbenes and Their Importance to Efficiency and Selectivity of Catalytic Olefin Metathesis Reactions. *J. Am. Chem. Soc.* **2014**, *136* (9), 3439–3455. <https://doi.org/10.1021/ja410606b>.
- (181) Johns, A. M.; Ahmed, T. S.; Jackson, B. W.; Grubbs, R. H.; Pederson, R. L. High *Trans* Kinetic Selectivity in Ruthenium-Based Olefin Cross-Metathesis through Stereoretention. *Org. Lett.* **2016**, *18* (4), 772–775. <https://doi.org/10.1021/acs.orglett.6b00031>.
- (182) Mikus, M. S.; Torker, S.; Xu, C.; Li, B.; Hoveyda, A. H. Pentacoordinate Ruthenium(II) Catecholthiolate and Mercaptophenolate Catalysts for Olefin Metathesis: Anionic Ligand Exchange and Ease of Initiation. *Organometallics* **2016**, *35* (22), 3878–3892. <https://doi.org/10.1021/acs.organomet.6b00773>.
- (183) Montgomery, T. P.; Grandner, J. M.; Houk, K. N.; Grubbs, R. H. Synthesis and Evaluation of Sterically Demanding Ruthenium Dithiolate Catalysts for Stereoretentive Olefin Metathesis. *Organometallics* **2017**, *36* (20), 3940–3953. <https://doi.org/10.1021/acs.organomet.7b00555>.
- (184) Liu, Z.; Xu, C.; Del Pozo, J.; Torker, S.; Hoveyda, A. H. Ru-Based Catecholthiolate Complexes Bearing an Unsaturated NHC Ligand: Effective Cross-Metathesis Catalysts for Synthesis of (*Z*)- α,β -Unsaturated Esters, Carboxylic Acids, and Primary, Secondary, and Weinreb Amides. *J. Am. Chem. Soc.* **2019**, *141* (17), 7137–7146. <https://doi.org/10.1021/jacs.9b02318>.
- (185) Morvan, J.; Vermersch, F.; Lorkowski, J.; Talcik, J.; Vives, T.; Roisnel, T.; Crévisy, C.; Vanthuynne, N.; Bertrand, G.; Jazzar, R.; Mauduit, M. Cyclic(Alkyl)(Amino)Carbene Ruthenium Complexes for *Z*-Stereoselective (Asymmetric) Olefin Metathesis. *Catal. Sci. Technol.* **2023**, *13* (2), 381–388. <https://doi.org/10.1039/D2CY01795D>.
- (186) Grzesiński, L.; Milewski, M.; Nadirova, M.; Kajetanowicz, A.; Grela, K. Unexpected Latency of *Z*-Stereoretentive Ruthenium Olefin Metathesis Catalysts Bearing Unsymmetrical *N*-Heterocyclic Carbene or Cyclic(Alkyl)(Amino)Carbene Ligands. *Organometallics* **2022**, *acs.organomet.2c00428*. <https://doi.org/10.1021/acs.organomet.2c00428>.
- (187) Khan, R. K.; Torker, S.; Hoveyda, A. H. Reactivity and Selectivity Differences between Catecholate and Catecholthiolate Ru Complexes. Implications Regarding Design of Stereoselective Olefin Metathesis Catalysts. *J. Am. Chem. Soc.* **2014**, *136* (41), 14337–14340. <https://doi.org/10.1021/ja505961z>.
- (188) Ahmed, T. S.; Grubbs, R. H. Fast-Initiating, Ruthenium-Based Catalysts for Improved Activity in Highly *E*-Selective Cross Metathesis. *J. Am. Chem. Soc.* **2017**, *139* (4), 1532–1537. <https://doi.org/10.1021/jacs.6b11330>.
- (189) Xu, C.; Shen, X.; Hoveyda, A. H. In Situ Methylene Capping: A General Strategy for Efficient Stereoretentive Catalytic Olefin Metathesis. The Concept, Methodological Implications, and Applications to Synthesis of Biologically Active Compounds. *J. Am. Chem. Soc.* **2017**, *139* (31), 10919–10928. <https://doi.org/10.1021/jacs.7b06552>.

- (190) Grandner, J. M.; Shao, H. L.; Grubbs, R. H.; Liu, P.; Houk, K. N. Origins of the Stereoretentive Mechanism of Olefin Metathesis with Ru-Dithiolate Catalysts. *J. Org. Chem.* **2017**, *82* (19), 10595–10600. <https://doi.org/10.1021/acs.joc.7b02129>.
- (191) Wang, T.; Xie, Q.; Guo, W.; Wu, S.; Zhang, H.; Wang, J.; Wu, B. A 3,4-Dimercapto-3-Cyclobutene-1,2-Dione-Chelated Ruthenium Carbene Catalyst for *Z*-Stereoretentive/Stereoselective Olefin Metathesis. *Dalton Trans.* **2019**, *48* (19), 6473–6483. <https://doi.org/10.1039/C9DT01016E>.
- (192) Boisvert, E.-J. Y.; Max, H. C.; Fogg, D. E. Rapid Aerial Oxidation of Ruthenium-Dithiocatecholate Catalysts: A Challenge to Stereoretentive Olefin Metathesis. *ACS Catal.* **2023**, *13* (5), 2885–2891. <https://doi.org/10.1021/acscatal.2c06168>.
- (193) Lee, C. W.; Grubbs, R. H. Catalysts for (E)-Selective Olefin Metathesis. US 20170022231, January 26, 2017. https://content2.cas.org/v1/AUTH_9a355bb5cefd4c378bde0d541c6a11ce/patentpak-cdr-full-text-28/patent/77681252_1537160410.pdf?temp_url_sig=5ff6f725e712c5d75fa37be83415ce15aba6de9&temp_url_expires=1654598658&inline.
- (194) Fulmer, G. R.; Miller, A. J. M.; Sherden, N. H.; Gottlieb, H. E.; Nudelman, A.; Stoltz, B. M.; Bercaw, J. E.; Goldberg, K. I. NMR Chemical Shifts of Trace Impurities: Common Laboratory Solvents, Organics, and Gases in Deuterated Solvents Relevant to the Organometallic Chemist. *Organometallics* **2010**, *29* (9), 2176–2179. <https://doi.org/10.1021/om100106e>.
- (195) Frisch, M. J.; Trucks, G. W.; Schlegel, H. B.; Scuseria, G. E.; Robb, M. A.; Cheeseman, J. R.; Scalmani, G.; Barone, V.; Petersson, G. A.; Nakatsuji, H.; Li, X.; Caricato, M.; Marenich, A. V.; Bloino, J.; Janesko, B. G.; Gomperts, R.; Mennucci, B.; Hratchian, H. P.; Ortiz, J. V.; Izmaylov, A. F.; Sonnenberg, J. L.; Williams-Young, D.; Ding, F.; Lipparini, F.; Egidi, F.; Goings, J.; Peng, B.; Petrone, A.; Henderson, T.; Ranasinghe, D.; Zakrzewski, V. G.; Gao, J.; Rega, N.; Zheng, G.; Liang, W.; Hada, M.; Ehara, M.; Toyota, K.; Fukuda, R.; Hasegawa, J.; Ishida, M.; Nakajima, T.; Honda, Y.; Kitao, O.; Nakai, H.; Vreven, T.; Throssell, K.; Montgomery, J. A. Jr.; Peralta, J. E.; Ogliaro, F.; Bearpark, M. J.; Heyd, J. J.; Brothers, E. N.; Kudin, K. N.; Staroverov, V. N.; Keith, T. A.; Kobayashi, R.; Normand, J.; Raghavachari, K.; Rendell, A. P.; Burant, J. C.; Iyengar, S. S.; Tomasi, J.; Cossi, M.; Millam, J. M.; Klene, M.; Adamo, C.; Cammi, R.; Ochterski, J. W.; Martin, R. L.; Morokuma, K.; Farkas, O.; Foresman, J. B.; Fox, D. J. Gaussian 16 Revision C.01, 2016.
- (196) Reim, I.; Occhipinti, G.; Törnroos, K. W.; Fogg, D. E.; Jensen, V. R. Toward E-Selective Olefin Metathesis: Computational Design and Experimental Realization of Ruthenium Thio-Indolate Catalysts. *Top. Catal.* **2022**, *65* (1–4), 448–461. <https://doi.org/10.1007/s11244-021-01468-3>.
- (197) Peterson, K. A.; Figgen, D.; Dolg, M.; Stoll, H. Energy-Consistent Relativistic Pseudopotentials and Correlation Consistent Basis Sets for the 4d Elements Y–Pd. *J. Chem. Phys.* **2007**, *126* (12), 124101. <https://doi.org/10.1063/1.2647019>.
- (198) *Energy-consistent Pseudopotentials of the Stuttgart/Cologne Group.* <http://www.tc.uni-koeln.de/PP/clickpse.en.html>.
- (199) Dunning, T. H. Gaussian Basis Sets for Use in Correlated Molecular Calculations. I. The Atoms Boron through Neon and Hydrogen. *J. Chem. Phys.* **1989**, *90* (2), 1007–1023. <https://doi.org/10.1063/1.456153>.
- (200) Schuchardt, K. L.; Didier, B. T.; Elsethagen, T.; Sun, L. S.; Gurumoorthi, V.; Chase, J.; Li, J.; Windus, T. L. Basis Set Exchange: A Community Database for Computational Sciences. *J. Chem. Inf. Model.* **2007**, *47* (3), 1045–1052. <https://doi.org/10.1021/ci600510j>.
- (201) Ribeiro, R. F.; Marenich, A. V.; Cramer, C. J.; Truhlar, D. G. Use of Solution-Phase Vibrational Frequencies in Continuum Models for the Free Energy of Solvation. *J. Phys. Chem. B* **2011**, *115* (49), 14556–14562. <https://doi.org/10.1021/jp205508z>.
- (202) Zhao, Y.; Truhlar, D. G. Computational Characterization and Modeling of Buckyball Tweezers: Density Functional Study of Concave–Convex $\Pi\cdots\pi$ Interactions. *Phys Chem Chem Phys* **2008**, *10*, 2813–2818. <https://doi.org/10.1039/B717744E>.
- (203) Grimme, S. Supramolecular Binding Thermodynamics by Dispersion-Corrected Density Functional Theory. *Chem.-Eur. J.* **2012**, *18* (32), 9955–9964. <https://doi.org/10.1002/chem.201200497>.

- (204) Smith, D. G. A.; Burns, L. A.; Patkowski, K.; Sherrill, C. D. Revised Damping Parameters for the D3 Dispersion Correction to Density Functional Theory. *J. Phys. Chem. Lett.* **2016**, *7* (12), 2197–2203. <https://doi.org/10.1021/acs.jpcclett.6b00780>.
- (205) Minenkov, Y.; Occhipinti, G.; Jensen, V. R. Complete Reaction Pathway of Ruthenium-Catalyzed Olefin Metathesis of Ethyl Vinyl Ether: Kinetics and Mechanistic Insight from DFT. *Organometallics* **2013**, *32* (7), 2099–2111. <https://doi.org/10.1021/om301192a>.
- (206) Fukata, Y.; Asano, K.; Matsubara, S. Facile Net Cycloaddition Approach to Optically Active 1,5-Benzothiazepines. *J. Am. Chem. Soc.* **2015**, *137* (16), 5320–5323. <https://doi.org/10.1021/jacs.5b02537>.
- (207) Thiam, A.; Iojoiu, C.; Leprêtre, J. C.; Sanchez, J. Y. Lithium Salts Based on a Series of New Anilinylnyl-Perfluorosulfonamide Salts and Their Polymer Electrolytes. *J. Power Sources* **2017**, *364*, 138–147. <https://doi.org/10.1016/j.jpowsour.2017.07.104>.
- (208) Chung, C. K.; Grubbs, R. H. Olefin Metathesis Catalyst: Stabilization Effect of Backbone Substitutions of N-Heterocyclic Carbene. *Org. Lett.* **2008**, *10* (13), 2693–2696. <https://doi.org/10.1021/ol800824h>.
- (209) Kuhn, K. M.; Bourg, J.-B.; Chung, C. K.; Virgil, S. C.; Grubbs, R. H. Effects of NHC-Backbone Substitution on Efficiency in Ruthenium-Based Olefin Metathesis. *J. Am. Chem. Soc.* **2009**, *131* (14), 5313–5320. <https://doi.org/10.1021/ja900067c>.
- (210) Hirano, K.; Urban, S.; Wang, C.; Glorius, F. A Modular Synthesis of Highly Substituted Imidazolium Salts. *Org. Lett.* **2009**, *11* (4), 1019–1022. <https://doi.org/10.1021/ol8029609>.
- (211) Aidouni, A.; Demonceau, A.; Delaude, L. Microwave-Assisted Synthesis of N-Heterocyclic Carbene Precursors. *Synlett* **2006**, *2006* (03), 0493–0495. <https://doi.org/10.1055/s-2006-932455>.
- (212) Rayner, P. J.; Norcott, P.; Appleby, K. M.; Iali, W.; John, R. O.; Hart, S. J.; Whitwood, A. C.; Duckett, S. B. Fine-Tuning the Efficiency of Para-Hydrogen-Induced Hyperpolarization by Rational N-Heterocyclic Carbene Design. *Nat. Commun.* **2018**, *9* (1), 4251. <https://doi.org/10.1038/s41467-018-06766-1>.
- (213) Poater, A.; Cavallo, L. Mechanistic Insights into the Double C–H (de)Activation Route of a Ru-Based Olefin Metathesis Catalyst. *J. Mol. Catal. Chem.* **2010**, *324* (1–2), 75–79. <https://doi.org/10.1016/j.molcata.2010.02.023>.
- (214) Grisi, F.; Mariconda, A.; Costabile, C.; Bertolasi, V.; Longo, P. Influence of Syn and Anti Configurations of NHC Backbone on Ru-Catalyzed Olefin Metathesis. *Organometallics* **2009**, *28* (17), 4988–4995. <https://doi.org/10.1021/om900497q>.
- (215) Ritter, T.; Day, M. W.; Grubbs, R. H. Rate Acceleration in Olefin Metathesis through a Fluorine-Ruthenium Interaction. *J. Am. Chem. Soc.* **2006**, *128* (36), 11768–11769. <https://doi.org/10.1021/ja064091x>.
- (216) Mikus, M. S.; Torker, S.; Hoveyda, A. H. Controllable ROMP Tacticity by Harnessing the Fluxionality of Stereogenic-at-Ruthenium Complexes. *Angew. Chem. Int. Ed.* **2016**, *55* (16), 4997–5002. <https://doi.org/10.1002/anie.201601004>.
- (217) Occhipinti, G.; Bjørsvik, H.-R.; Jensen, V. R. Quantitative Structure–Activity Relationships of Ruthenium Catalysts for Olefin Metathesis. *J. Am. Chem. Soc.* **2006**, *128* (21), 6952–6964. <https://doi.org/10.1021/ja060832i>.
- (218) Kirkland, T. A.; Lynn, D. M.; Grubbs, R. H. Ring-Closing Metathesis in Methanol and Water. *J. Org. Chem.* **1998**, *63* (26), 9904–9909. <https://doi.org/10.1021/jo981678o>.
- (219) Chval, Z.; Sip, M.; Burda, J. V. The Trans Effect in Square-Planar Platinum(II) Complexes—A Density Functional Study. *J. Comput. Chem.* **2008**, *29* (14), 2370–2381. <https://doi.org/10.1002/jcc.20980>.
- (220) Ekeli, J. B. Computational Studies and Design of Stereoselective Ruthenium-Based Catalysts for Olefin Metathesis. Masterthesis, University of Bergen, Bergen, Norway, 2020.
- (221) Nappen, S. T. The Introduction and Effect of Bidentate L-L and X-X Ligands in Ruthenium-Based Olefin Metathesis Catalysts. Masterthesis, University of Bergen, Bergen, Norway, 2020.
- (222) Zelonka, R. A.; Baird, M. C. Benzene Complexes of Ruthenium(II). *Can. J. Chem.* **1972**, *50* (18), 3063–3072. <https://doi.org/10.1139/v72-486>.

-
- (223) Demonceau, A.; Stumpf, A. W.; Saive, E.; Noels, A. F. Novel Ruthenium-Based Catalyst Systems for the Ring-Opening Metathesis Polymerization of Low-Strain Cyclic Olefins. *Macromolecules* **1997**, *30* (11), 3127–3136. <https://doi.org/10.1021/ma961040j>.
- (224) Cannon, J. S.; Zou, L.; Liu, P.; Lan, Y.; O'Leary, D. J.; Houk, K. N.; Grubbs, R. H. Carboxylate-Assisted C(Sp³)–H Activation in Olefin Metathesis-Relevant Ruthenium Complexes. *J. Am. Chem. Soc.* **2014**, *136* (18), 6733–6743. <https://doi.org/10.1021/ja5021958>.



Toward E-selective Olefin Metathesis: Computational Design and Experimental Realization of Ruthenium Thio-Indolate Catalysts

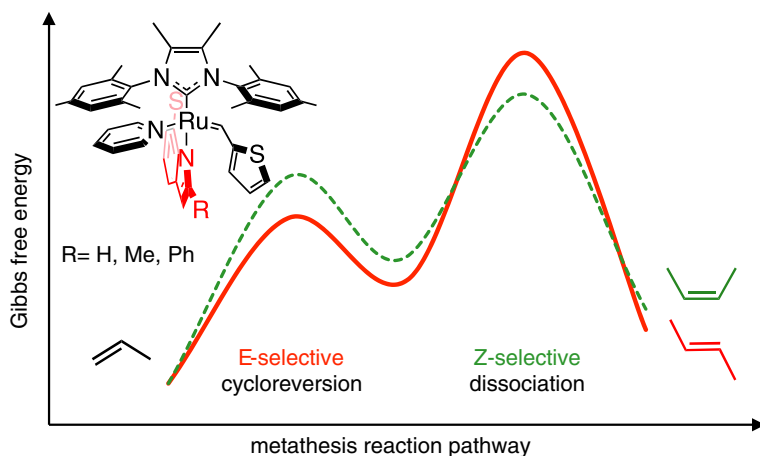
Immanuel Reim¹ · Giovanni Occhipinti¹ · Karl W. Törnroos¹ · Deryn E. Fogg^{1,2} · Vidar R. Jensen¹

Accepted: 29 June 2021 / Published online: 5 August 2021
© The Author(s) 2021

Abstract

The selective transformation of 1-alkenes into E-olefins is a long-standing challenge in olefin metathesis. Density functional theory (DFT) calculations predict high E-selectivity for catalysts incorporating a bidentate, dianionic thio-indolate ligand within a RuXX'(NHC)(py)(=CHR) platform (NHC = N-heterocyclic carbene; py = pyridine). Such complexes are predicted to yield E-olefins by favoring anti-disposed substituents in the transition state expected to be rate-determining: specifically, that for cycloreversion of the metallacyclobutane intermediate. Three pyridine-stabilized catalysts **Ru21a-c** were synthesized, in which the thio-indolate ligand bears a H, Me, or Ph substituent at the C2 position, and the NHC ligand is the unsaturated imidazoline-2-ylidene Me₂IMes (which bears N-mesityl groups and methyl groups on the C4,5 backbone). Single-crystal X-ray diffraction analysis of **Ru21c** confirms the ligand orientation required for E-selective metathesis, with the thio-indolate sulfur atom binding cis to the NHC, and the indolate nitrogen atom trans to the NHC. However, whereas the new complexes mediated metathetic exchange of their 2-thienylmethylidene ligand in the presence of the common metathesis substrates styrene and allylbenzene, no corresponding self-metathesis products were obtained. Only small amounts of 2-butene (73% (Z)-2-butene) were obtained in self-metathesis of propene using **Ru21a**. Detailed DFT analysis of this process revealed that product release is surprisingly slow, limiting the reaction rate and explaining the low metathesis activity. With the barrier to dissociation of (Z)-2-butene being lower than that of (E)-2-butene, the calculations also account for the observed Z-selectivity of **Ru21a**. These findings provide guidelines for catalyst redesign in pursuit of the ambitious goal of E-selective 1-alkene metathesis.

Graphic abstract



Extended author information available on the last page of the article

Keywords Olefin metathesis · Ruthenium · Alkylidene · Stereoselectivity · Density functional theory · Reaction mechanism

1 Introduction

E-olefins, with substituents trans-disposed across the double bond, are important structural features in molecular entities ranging from antibiotics [1] and anticancer therapeutics [2, 3] to precision polymers [4]. Traditionally, such compounds have been generated from aldehydes via stoichiometric approaches such as the Wittig [5], Horner-Wadsworth-Emmons [6] and Julia [7] olefination reactions. Interest in catalytic methodologies is spurred by the low atom-efficiency of these classic methods (most notoriously, the Wittig reaction, with its stoichiometric formation of triphenylphosphine oxide as coproduct). Olefin metathesis offers an atom-efficient catalytic alternative, in which olefinic fragments are rearranged by scission and regeneration of carbon–carbon double bonds [8–10]. Thanks to the ease of handling and functional-group tolerance of ruthenium catalysts [11–13], olefin metathesis has been widely adopted for the synthesis of complex organic molecules [14–17], including pharmaceuticals [18–21], and soft materials [22–31].

A plethora of ruthenium olefin metathesis catalysts has been developed since the 1990s [32–34]. Whereas many of these catalysts have been optimized for specific reactions and purposes, they typically generate E-Z (cis–trans) product mixtures. Separating the target product from its undesired isomer is costly, wasteful, and sometimes impossible. The most direct, atom-economic, and elegant solution is offered by catalysts that enable selective synthesis of the single-isomer target [33, 35–37]. However, design of such catalysts is challenging. Kinetically Z-selective catalysts for 1-alkene metathesis have been achieved only in the last decade, and only two such classes of catalyst exist: cyclometalated (Chart 1a, **Ru1–8**) [38–44], and monothiolate catalysts (Chart 1a, **Ru9–12**) [45–51].

Even more elusive are catalysts for E-selective olefin metathesis. Despite more than 20 years of effort, no catalyst for E-selective metathesis of 1-alkenes has yet been achieved. To date, metathetical access to E-olefin products can be achieved only via “stereoretentive” catalysts (Chart 1b), which can transform stereochemically defined E-olefin substrates into E-configured products (Scheme 1) [36, 52–55]. The utility of stereoretentive metathesis is limited by the cost and accessibility of the isomerically pure starting materials required. Production of E-olefinic products from 1-alkenes represents an intellectually and economically attractive alternative.

Here we describe work toward the design of catalysts for E-selective 1-alkene metathesis. Building on insights obtained in earlier modifications of stereoretentive catalysts

[56], we explore a new family of thio-indolate catalysts for which E-selectivity is predicted on the basis of density functional theory (DFT) calculations.

2 Results and Discussion

2.1 Initial Considerations

Stereoselective metathesis is achieved by controlling the catalyst stereochemistry in of the rate-determining step of the Chauvin mechanism [57], typically cycloreversion to release

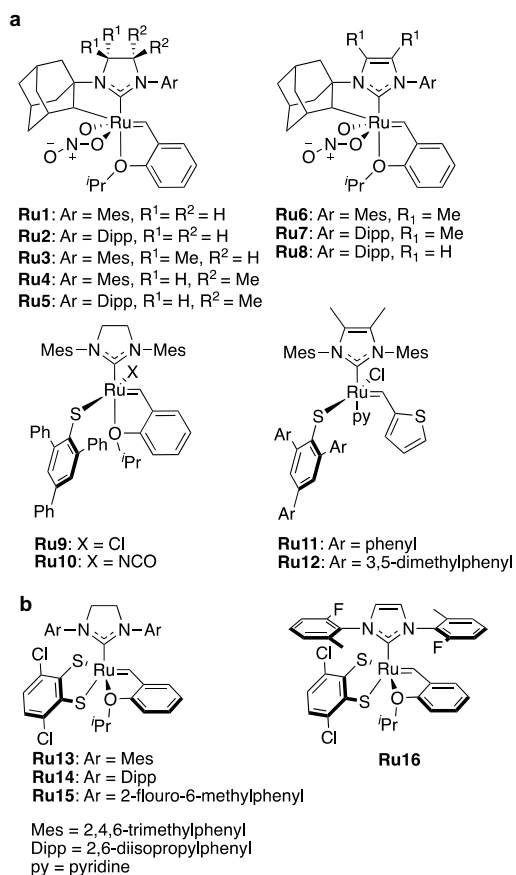
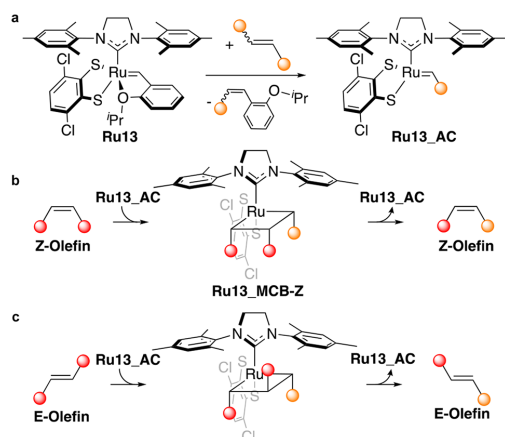


Chart 1 Examples of (a) Z-Selective Ru Catalysts and (b) Stereoretentive Ru Catalysts



Scheme 1 Mechanism for Stereoretentive Metathesis, Illustrated with Thio-catecholate Catalyst **Ru13**. **a** Precatalyst Initiation, Stereoretentive Metathesis for **b** Z-olefin and **c** E-olefin

the product olefin from the metallacyclobutane (MCB) intermediate [53, 58–60]. A syn relationship between the substituents in the MCB results in a Z-configured product; anti-disposed MCB substituents yield an E-configured product.

Seminal computational mechanistic work showed that the MCB intermediates and the associated transition states of the preferred dissociative reaction pathways adopt trigonal bipyramidal (TBP) geometries, in which the η^2 -C $_{\alpha}$ -C $_{\beta}$ -C $_{\alpha}$ ring occupies the equatorial plane [61]. Such a geometry is likewise observed for stereoretentive catalysts **Ru13-16** (Scheme 1b) [36, 53–55, 62–64]. In the MCB intermediate, the NHC ligand occupies one of the two axial sites; that is, it is cis to the MCB ring. This positions the NHC N-aryl substituents in close proximity to the MCB α -carbon atoms. Steric pressure from the N-Ar groups hence forces orientation of the C $_{\alpha}$ -substituents away from the NHC.

If stereochemically-defined internal olefins are used as substrates, this also sets the orientation of the β -substituent. The substrate stereochemistry thus controls the stereochemistry of the metathesis product. That is, use of an E-olefin dictates formation of an E-configured product; a Z-olefin substrate yields a Z-configured product (Scheme 1) [60]. These stereoretentive catalysts offer the only current metathetical route to E-olefins. They are therefore an attractive starting point for the next logical step: developing catalysts that selectively convert 1-alkenes to E-configured alkene products, and circumventing the need for isomerically pure starting materials.

Discussed above is the means by which steric pressure on the α -substituent of the MCB enables formation of Z- (Scheme 1b) or E-configured products (Scheme 1c)

via retention of the substrate stereochemistry. E-selective metathesis of 1-alkenes, in contrast, requires steric pressure on the β -substituent. Grubbs and co-workers pursued this objective by introducing a phenanthrene-dithiolate ligand (Fig. 1) [56]. In the key MCB intermediate, however, the favored isomer is the undesired **Ru17_22**, in which the phenanthrene ring system is oriented away from the MCB β -position. Moreover, even for the target isomer **Ru17_22'**, DFT calculations on a model, unsubstituted MCB predicted a 5 Å separation between H $_{\beta}$ and the phenanthrene ring. Larger substituents would reduce this distance, but the catecholthiolate ligand appears too distant to influence the orientation of the β -substituent to any great extent. This prompted us to pursue design of alternative dianionic ligands with greater influence on the β -site of the MCB, using DFT calculations as a guide.

2.2 Computational Ligand Design

To reduce the distance between the selectivity-inducing group and the MCB β -position, we envisaged replacing one S-donor with a trivalent, anionic donor, thereby retaining a neutral Ru complex. Specifically, we considered introduction of a nitrogen center bearing a substituent that would reduce the distance to the MCB ring. We further stipulated a planar, rigid, and bicyclic κ^2 -S,N ligand, to maximize steric pressure on the MCB β -position.

These requirements led us to the thio-indolate scaffold shown in the model unsubstituted MCB (**Ru19a_22**) in Chart 2. The DFT-optimized geometry of **Ru19a_22** revealed a much shorter distance between H $_{\beta}$ and the indole ring than between H $_{\beta}$ and the thio-catecholate ring in **Ru13_22** (2.35 Å vs 5.95 Å, respectively; Chart 2). Substitution at position 2 of the indole ring should reduce the distance further, increasing the steric pressure. Using propene as a computationally efficient model 1-alkene, we investigated the impact of different substituents at the indole 2-position using DFT calculations.

Thio-indolate catalyst **Ru19a**, with only a hydrogen atom at position 2 of the indole ring, is predicted to be E-selective, as judged from the difference in free energy between the transition states leading to (Z)- or (E)-2-butene ($\Delta\Delta G^{\ddagger}_{(E/Z)} = \Delta G^{\ddagger}_{Z} - \Delta G^{\ddagger}_{E} = 3.4 \text{ kcal mol}^{-1}$; see Table 1). In contrast, the state-of-the-art catecholthiolate catalyst **Ru13** [53] (Chart 1) is predicted to be Z-selective ($\Delta\Delta G^{\ddagger}_{(E/Z)} = -1.2 \text{ kcal mol}^{-1}$), in agreement with experiment: using **Ru13**, 83% Z-selectivity is obtained in self-metathesis of propene.¹ Also of note, lower barriers to metathesis are predicted for thio-indolate

¹ NMR experiment: A J. Young NMR tube was loaded with 5 mg (10 mmol) **Ru13** and 0.5 mg (3.3 mmol) hexamethylbenzene as internal standard in 0.65 mL C $_6$ D $_6$. The solution was degassed via 3 freeze–pump–thaw cycles, thawed under propene and mixed, at which point the timer was started. The selectivity was determined

Fig. 1 Phenanthrene-dithiolate complex **Ru17** and its TBP-like MCB intermediates [56]. The steric bulk of the extended dithiolate ligand is located far from the critical β -position in the favored isomer **Ru17_22**

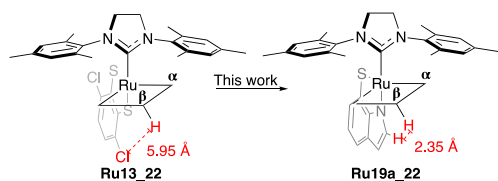
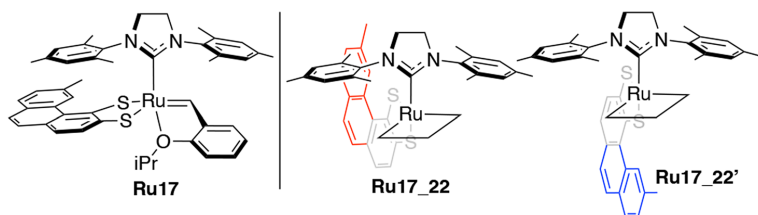


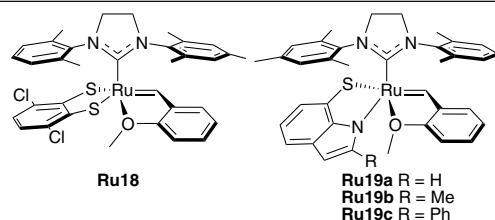
Chart 2 Thio-catecholate vs Thio-indolate Ligands: Amplifying Steric Pressure at the MCB β -Position. DFT-calculated interatomic distances

catalysts **Ru19a** and **Ru19b** (the latter bearing a 2-Me substituent) vs **Ru13** ($\Delta G_{Z}^{\ddagger} = 21.0$ kcal mol⁻¹) as well vs a corresponding (hypothetical) catalyst precursor **Ru18** bearing the same methoxybenzylidene as **Ru19a-c**. These data reinforce the potential of the thio-indolate ruthenium alkylidenes as olefin metathesis catalysts.

2-Substitution destabilizes the Z-transition state more than the corresponding E-isomer, leading to increasing E-selectivity with increasing substituent size (Table 1). With a methyl substituent, for example (**Ru19b**), $\Delta\Delta G_{(E/Z)}^{\ddagger}$ is 0.6 kcal mol⁻¹ higher than that of **Ru19a**. A phenyl substituent (**Ru19c**) is predicted to increase the selectivity substantially ($\Delta\Delta G_{(E/Z)}^{\ddagger} = 11.5$ kcal mol⁻¹), but the significantly higher barrier to metathesis is expected to limit the catalytic activity of **Ru19c** relative to **Ru19a** and **Ru19b**.

The increased selectivity predicted for **Ru19a** is a result of the steric pressure on the MCB β -substituent, as discussed above. This pressure is reflected in the increased Ru-C β -CH₃ angle (119° in **Ru13_TS4,5_Z**, vs 126° in **Ru19a_TS4,5_Z**; Fig. 2), and the decreased C_{NHC}-Ru-C β angle (which declines from 105° to 92°).

Table 1 Predicted barriers to propene self-metathesis, and computed E-Z selectivity for catalysts **Ru18** and **Ru19a-c**^d



Cat	R	ΔG_{E}^{\ddagger}	ΔG_{Z}^{\ddagger}	$\Delta\Delta G_{E/Z}^{\ddagger}$ ^b
Ru19a	H	17.9	21.3	3.4
Ru19b	Me	19.0	23.2	4.0
Ru19c	Ph	24.1	35.5	11.5
Ru18	–	22.7	21.5	– 1.2
Ru13 ^c	–	22.2	21.0	– 1.2

^aEnergies (kcal mol⁻¹) calculated relative to the Gibbs free energy of the [Ru]=CHAR precursor. ^bFree energy difference $\Delta\Delta G_{E/Z}^{\ddagger} = \Delta G_{Z}^{\ddagger} - \Delta G_{E}^{\ddagger}$. ^cSee Chart 1 for the structure of **Ru13**

2.3 Experimental Realization

In light of the promising effect of the thio-indolate ligands on metathesis stereoselectivity, we proceeded to synthesize the first versions of ruthenium alkylidenes bearing such ligands. The required 7-bromoindoles **L1a-c** (Scheme 2) are commercially available.

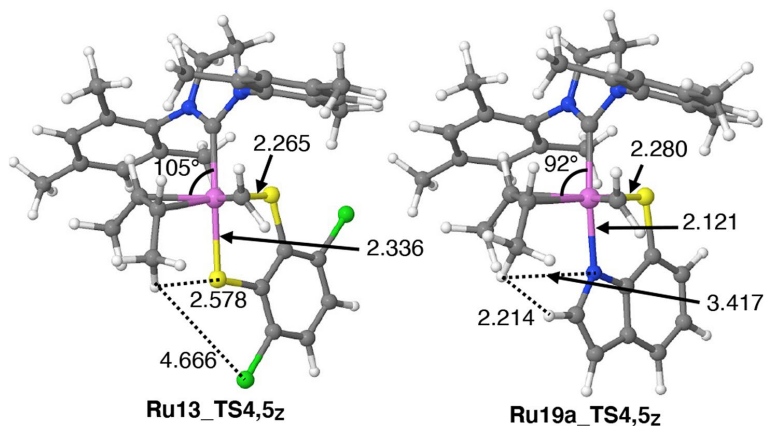
A thiol group was installed in place of the bromine atom by Pd-catalyzed exchange with a silylthiolester [65], following which the thiol was deprotected with HCl (R = Me, Ph) or NⁿBu₄F (R = H). This two-step protocol delivered the corresponding thio-indoles **L3a-c** in yields of 68–72%. Ensuating treatment with KH in THF afforded the dianions as potassium salts (**L4a-c**), which were extracted with hexane to remove PPh₃ residues introduced in the prior steps.

Salt metathesis of **L4a-c** with the second-generation Hoveyda catalyst **HII** to give **Ru19a-c** failed, despite the success of the corresponding reactions with unsubstituted [53,

Footnote 1 (continued)

from the ratio of (Z)- and (E)-2-butene (86:14) in the first ¹H NMR spectrum ($t = 5$ min), to reduce the effect of isomerization (see Table S1).

Fig. 2 Optimized geometries of the Z-isomeric transition states for cycloreversion in propene self-metathesis by complexes **Ru13** and **Ru19a**. Ruthenium is shown in violet, sulfur in blue, nitrogen in green, chlorine in yellow, and carbon in gray. Distances in [Å], angles in [°]



62] or sterically demanding [56] catecholthiolates. Reaction of **L4c** with the third-generation Grubbs catalyst **GIII** proceeded, but the formed complex was unstable and could not be purified. Greater success was achieved in salt metathesis with the Evonik catalyst **Ru20**, perhaps because of the reduced steric demand of the 2-thienylmethylidene and the unsaturated NHC ligand. It may be noted that **Ru20** has been successfully used as a precursor to other Z-selective catalysts bearing sterically demanding thiolates [49]. The target thio-indolate alkylidene complexes **Ru21a–c** (a: R = H; b: R = 2-Me; c: R = 2-Ph; Scheme 2) were obtained in 60–65% yield. These are, to our knowledge, the first transition-metal complexes bearing thio-indolate chelate ligands. The new complexes were characterized by NMR and MS analysis, and, in the case of **Ru21a** and **Ru21c**, single-crystal X-ray diffraction (Fig. 3). The X-ray crystal structure of **Ru21a** confirms that the atom connectivity is analogous to that of **Ru21c**, but the diffraction quality is too low for detailed structural analysis.

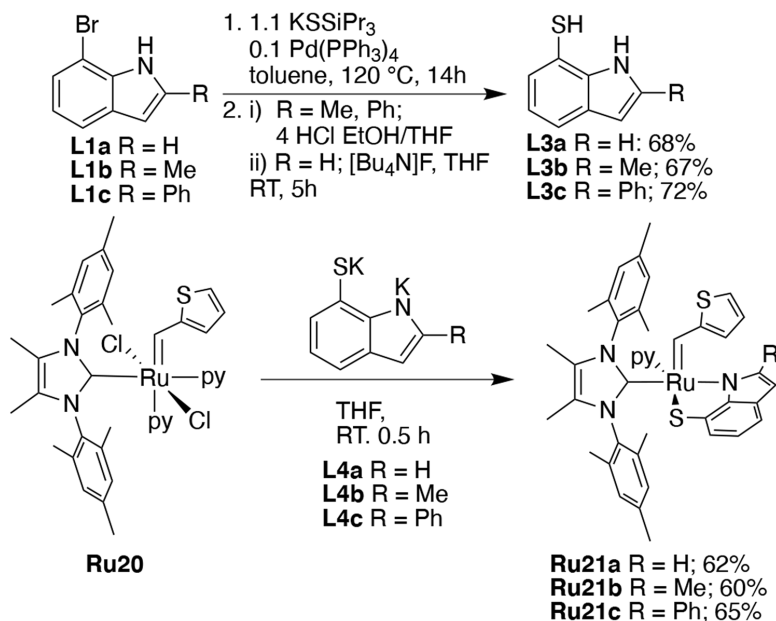
The X-ray structure confirms binding of the thio-indolate fragment as a S,N-chelate. Crucially, and as predicted by the DFT calculations, the dianionic ligand adopts the orientation required for E-selective metathesis, with the thiolate sulfur cis, and the indolate nitrogen trans, to the NHC (Table S6). However, DFT calculations predict that the unintended isomer (**Ru21a'**), with the thiolate sulfur trans and the indolate nitrogen cis to the NHC, is only 1.9 kcal mol⁻¹ less stable and may thus also be present (see Table S7). Indeed, ¹H NMR spectra of catalyst **Ru21a** consistently exhibit a minor alkylidene singlet (5%) at $\delta = 15.4$ ppm, with the main alkylidene signal located at $\delta = 16.2$. A NOESY experiment confirms the existence of an exchange equilibrium between these two alkylidene singlets, with the minor alkylidene species being 1.8 kcal mol⁻¹ less stable than the dominating species. From the agreement between the NMR experiments

and the DFT calculations, the minor species is presumed to be **Ru21a'**. Such minor alkylidene species are not observed for the larger complexes **Ru21b–c**, and calculations also indicate that the isomers **Ru21b'** and **Ru21c'** with rotated S,N ligands are high in energy (Table S6).

Despite **Ru21c** having a slightly more acute N1–Ru–S chelate bite angle than the corresponding S–Ru–S angle in **Ru13** ((85.11(4)° vs 88.23(3)°, respectively) [53], its N–Ru–C_{NHC} is considerably greater (162.78(6)°, vs 148.03(11)° in **Ru13**). This presumably reflects the weaker trans influence of nitrogen relative to sulfur. The mutual trans disposition of the NHC and indolate nitrogen in **Ru21c** weakens the Ru–N1 indolate bond (2.1301(5) Å), which is longer than known Ru–pyrrole bonds (2.065–2.115 Å) [66–68].

The metathesis activity of **Ru21a–b** was initially assessed by reaction with styrene at room temperature (Scheme 3). Unexpectedly, ¹H NMR analysis showed no evidence of the stilbene self-metathesis product. However, a new alkylidene singlet was observed, along with vinylthiophene, in the experiments involving **Ru21a** and **Ru21b** (δ 17.2 and 16.9 ppm, respectively, in C₆D₆; Fig. S2, S3). The new alkylidene species, identified as the benzylidene analogues of **Ru21a** and **Ru21b** (labeled **Ru21a_29** and **Ru21b_29**, respectively) result from unproductive metathesis of styrene, via **Ru21a_28** (see Scheme 3, Fig. S2–S4, and Scheme S1).² Complex **Ru21a** reaches equilibrium within 15 min, vs nearly an hour for catalyst **Ru21b**. The slower reaction of **Ru21b** is consistent with the higher barrier to metathesis

² The NMR experiment showed that the consumption of styrene and starting complex **Ru21a** or **Ru21b** corresponds to the formation of the new alkylidenes, respectively, as well as of 2-vinylthiophene. Therefore, the new alkylidenes were assigned to benzylidene complexes **Ru21a_29** and **Ru21b_29** (see S1).

Scheme 2 Ligand synthesis and installation

calculated for the bulkier thio-indolate ligands of the H₂IMes analogues **Ru19** (Table 1). Increasing the reaction temperature or time resulted in loss of the alkylidene signals as well as a black precipitate indicating catalyst decomposition and formation of Ru nanoparticles [69].

In light of the low reactivity documented above, especially for **Ru21b**, we speculated that unfavorable steric interactions may hamper productive metathesis. Formation of stilbene would necessitate an MCB structure in which the β -phenyl substituent approaches the two N-mesityl groups (for the (E)-stilbene), or the thio-indolate ligand (for the (Z)-stilbene). The impact on the barriers to metathesis is explored computationally below.

To test whether reduced steric bulk at C $_{\beta}$ would enable productive metathesis, we examined the reaction with allylbenzene (Fig. S5). Again, however, no metathesis products were detected. In the case of **Ru21b**, 35% vinylthiophene was detected by ¹H NMR analysis (Fig. S5, S6), but 17% **Ru21b** remained even after 12 h, confirming slow initiation and a relatively stable precatalyst. Isomerization of allylbenzene was also observed, presumably catalyzed by decomposed Ru species [69, 70]. In sum, attempts at self-metathesis of allylbenzene led to catalyst decomposition and substrate isomerization, rather than productive metathesis.

Next, to reduce the steric pressure as much as possible, with the goal of facilitating productive metathesis, we attempted self-metathesis of propene in NMR experiments

with **Ru21a-c**.³ **Ru21a** gave the expected butene product in low yield (11 mol% vs catalyst loading), and the proportion of the Z-isomer was slightly lower than that obtained with catalyst **Ru13** (73% vs 83%). The more sterically demanding catalysts **Ru21b-c** afforded no butene product. For catalyst **Ru21b**, this is clearly due in part to low metathesis activity, as unreacted **Ru21b** remained even after 96 h at 50 °C. In contrast, the alkylidene signal of catalyst **Ru21c** disappeared within 12 h of reaction time.

The small amount of butene obtained using **Ru21a** in propene self-metathesis may be due to either low catalytic activity, perhaps caused by the steric hindrance of the thio-indolate ligand, or to catalyst decomposition. To probe its susceptibility to β -hydride elimination from the unsubstituted MCB (a key decomposition pathway in 1-alkene metathesis for a range of Ru-NHC catalysts [71]), **Ru21a**

³ ¹H-NMR-Experiment A J. Young NMR tube was loaded with 10 mmol catalyst **Ru21a-c** and 0.5 mg (3.3 mmol) hexamethylbenzene as internal standard in 0.65 mL C₆D₆. The solution was degassed via three freeze-pump-thaw cycles and then charged with propene gas, mixed and the timer was started. For **Ru21b** and **Ru21c** no 2-butene formation was observed even after 24 h and heating the reaction mixture to 50 °C. For **Ru21a**, the selectivity was determined as the ratio of the formed (Z)- and (E)-2-butene (73:27) of a quantitative ¹H NMR spectrum (t=60 min) to reduce the effect of isomerisation and higher accuracy (see Table S1).

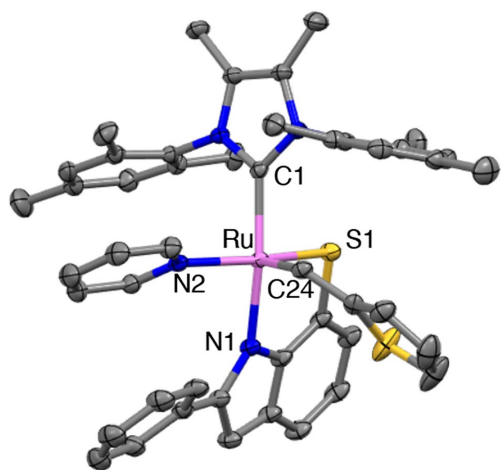


Fig. 3 X-ray crystal structure of **Ru21c**, with displacement ellipsoids drawn at 50% probability. Ruthenium is shown in violet, sulfur in yellow, nitrogen in blue, and carbon in gray. Hydrogen atoms have been omitted for clarity. Key bond metrics: Ru–C1: 2.0704(17) Å, Ru–N1: 2.1295(15) Å, Ru–S1: 2.3031(5) Å, Ru–N2: 2.1316(16) Å, Ru–C24: 1.8490(18) Å; N1–Ru–S1: 85.11(4)°, S1–Ru–C1: 87.27(5)°, N1–Ru–C1: 162.78(6)°

was reacted with ethylene. Both vinylthiophene and propene⁴ were detected, evidence for alkylidene exchange (catalyst initiation), and β -hydride elimination (Fig. S7, S8). The proportion of propene is consistent with decomposition of ca. 40% of the catalyst via β -hydride elimination. (Bimolecular decomposition of the 4-coordinate methylidene species may also occur [72], but the ethylene product is indistinguishable from ethylene formed via metathesis). The competition between metathesis and decomposition is further explored in the mechanistic computational analysis below.

2.4 Mechanistic Calculations

The calculated barrier to cycloreversion – the presumed rate-determining step – for **Ru19a** (the H_2IMes analogue of **Ru21a**) is similar to that of the known metathesis catalyst **Ru13** [53, 58–60]. Nevertheless, **Ru21a** is inactive in metathesis of styrene or allylbenzene, and produced only small proportions of 2-butene in self-metathesis of propene. Moreover, the major stereoisomer produced was (Z)-2-butene, despite the predicted E-selectivity of **Ru19a** (Table 1).

To uncover the factors underlying the discrepancy between the catalytic properties predicted for **Ru19a** and those observed for **Ru21a**, the latter was subjected to detailed computational analysis.

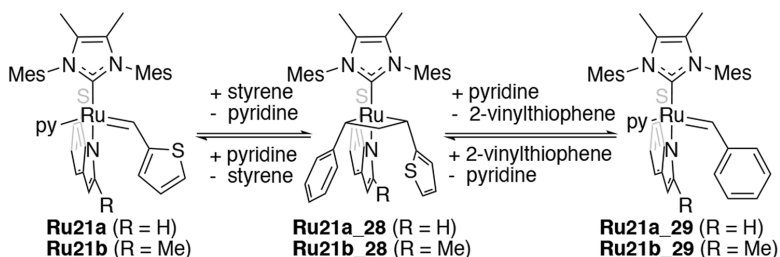
The calculated barrier to cycloreversion in self-metathesis of styrene and allylbenzene to E-configured products by **Ru21a** is 36.9 and 37.5 kcal mol^{−1} (Scheme S12, Table S7), respectively, consistent with the absence of product⁵ observed experimentally. In contrast, for propene, the cycloreversion barrier (via **Ru21a_TS4.5_E**, 23.8 kcal mol^{−1} vs the precursor **Ru21a**) leading to formation of (E)-2-butene, is only 2.8 kcal mol^{−1} higher than that of the state-of-the-art catecholthiolate catalyst **Ru13** (Table 1), indicating that the critical bond rupture and formation of propene metathesis should be within reach for **Ru21a**. The catalytic potential of **Ru21a** seems even clearer when eliminating the effect of the precursor (the pyridine-coordinated **Ru21a** vs the isopropoxybenzylidene-coordinated **Ru13**), by calculating free energies relative to the two active ethylidene complexes derived from **Ru21a** (**Ru21a_2**) and **Ru13** (**Ru13_2**), respectively (Scheme 4). In fact, with initiation completed, **Ru21a_2** should mediate both cycloaddition and cycloreversion faster than **Ru13_2**. However, **Ru21a** is observed to be less active in metathesis than **Ru13**. Because **Ru21a** is unlikely to be limited by slow initiation (initiation was observed even for styrene and allylbenzene; see above), the most likely explanation for its slow metathesis lies in a reaction step other than cycloreversion.

In searching for an alternative rate-limiting step, we did not initially consider 2-butene dissociation. However, Cavallo and co-workers, in an early computational study of the stereoselectivity of propene self-metathesis using a $RuCl_2(H_2IMes)$ -ethylidene catalyst [73], found the methylidene complex and 2-butene to be of higher energy than any other minimum or transition state in the catalytic cycle. Even if this is not the case for **Ru21a**, the relatively high energies of complexes toward the end of the pathway indicate that product release could be slow. For example, the 2-butene π -complexes **Ru21a_5** are significantly less stable than the propene counterparts **Ru21a_3**. We therefore considered whether product release from **Ru21a_5** might be rate determining. Indeed, product release is surprisingly costly (10–13 kcal mol^{−1} vs **Ru21a_5**, see Scheme 4, or 29–32 kcal mol^{−1} vs **Ru21a**), and is the undisputed bottleneck for the thio-indolate catalyst. This step, which is difficult to follow computationally,⁶ was not investigated for the corresponding thio-catecholate catalyst **Ru13**. However,

⁴ Indolate-induced deprotonation of the MCB [71] was ruled out as a source of propene, since calculations with stepwise reduced N–H_{CP} distance invariably led, instead, to β -hydride elimination. Also, upon completion of the reaction, no NH signals were observed in the ¹H-¹⁵N-HSQC-NMR spectrum.

⁵ Transition-state theory suggests that reactions with free-energy barriers approaching 30 kcal mol^{−1} will be impractically slow. See the SI for details.

⁶ The flat potential energy surfaces in the transition regions at long Ru–butene distances make these transition states hard to find.

Scheme 3 Metathesis of Styrene


product release is not expected to be a bottleneck for the latter, which is less bulky than **Ru21a**. Previous computational studies of this catalyst do not suggest rate-limiting product dissociation [53, 55, 60]. Instead, cycloreversion has been suggested to be rate limiting for this and other stereoretentive catalysts [60].

In summary, with cycloreversion assumed to be rate determining for **Ru13** and product release being identified as the bottleneck for **Ru21a**, the calculations are consistent with the much lower catalytic activity of **Ru21a** relative to the closely related thio-catecholate catalyst **Ru13**. The calculations are also consistent with the observed Z-selectivity of both **Ru21a** and **Ru13**, given the lower barrier to dissociation of (Z)-2-butene than (E)-2-butene from **Ru21a_5**,

and the lower barrier to cycloreversion via **Ru13_TS4,5_Z** than **Ru13_TS4,5_E**.

The calculations indicate that product release is a two-step process. Surprisingly high barriers for the thio-indolate catalyst are located in the first step, involving rearrangement from η^2 - to η^1 -coordinated 2-butene (Fig. 4). This rearrangement requires considerable activation, as the Ru–butene π -bond is lost at the same time as the steric repulsion between the ligands (the NHC and the thio-indolate) and the leaving, but still largely η^2 -coordinated, 2-butene, is large. The steric repulsion is lower for (Z)-2-butene than for (E)-2-butene, resulting in lower barriers to rearrangement to the agostic complex. The reduced steric hindrance results, at least in part, from (Z)-2-butene being more compact than its

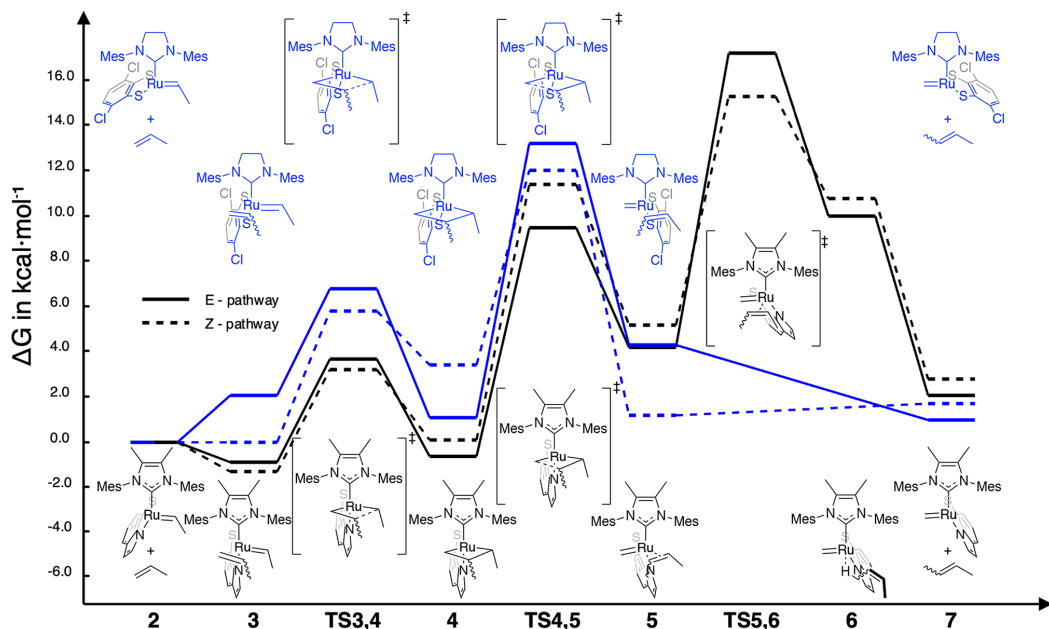
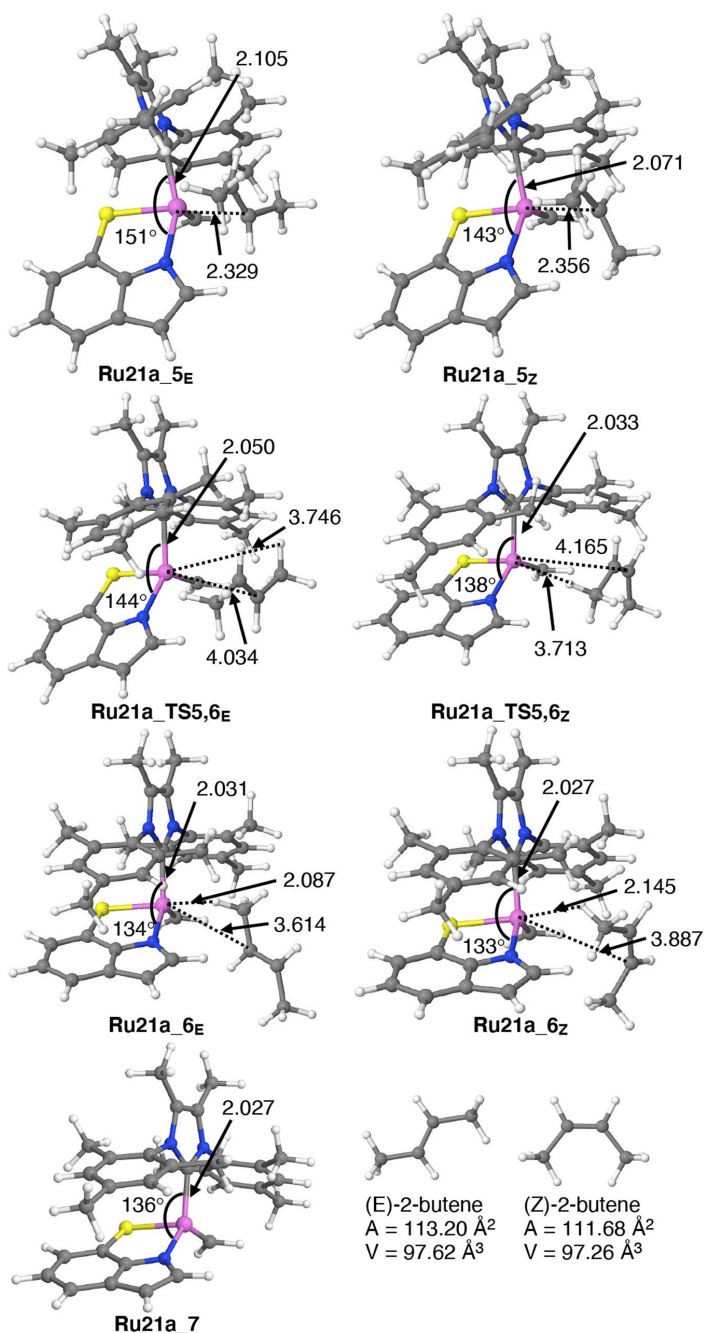

Scheme 4 Calculated Free Energies of Propene Metathesis vs **Ru21a_2** (black) and **Ru13_2** (blue)

Fig. 4 The optimized transition states for rearrangement of η^2 -bound to η^1 -bound 2-butene in π -complexes **Ru21a_5E** and **Ru21a_5Z** to give the corresponding agostic complexes **Ru21a_6E** and **Ru21a_6Z**, respectively. This rearrangement is the rate-determining step of **Ru21a**-mediated propene metathesis and initiates product release. The subsequent (E- or (Z)-2-butene dissociation to give methylene complex **Ru21a_7** requires less geometric adaption and less activation. Distances in [Å], angles in [°]. Molecular volumes (V) and surface areas (A) are those of the solute cavity in the continuum solvent-model calculations (see SI)



E-counterpart, with a smaller molecular volume and surface area, (Fig. 4). Faster release of the Z-configured product is likely to be a challenge extending far beyond the current thio-indolate catalyst design: regardless which of the existing catalyst frameworks is chosen as a starting point for design of E-selective catalysts, substitution is likely to be essential to disfavor formation of Z-configured products. This substitution will increase the overall steric pressure and tend to make product release the kinetic bottleneck.

The slowest step of the product release, the η^2 -to- η^1 -bound 2-butene rearrangement, leads to sterically less encumbered complexes **Ru21a_6**, in which 2-butene is bound to Ru via an agostic methyl C–H bond. From **Ru21a_6**, the continued 2-butene dissociation to methylidene **Ru21a_7** and free 2-butene requires much less geometric adaption (see Fig. 4) and is thus expected to require little activation. Constrained geometry optimizations at increasing R–H_{agostic} distances and failed attempts at locating the corresponding transition states,⁶ confirm that this, the final part of the product release, requires only negligible enthalpic activation from **Ru21a_6**.

To shed further light on the factors underlying the low observed metathesis activity, we also investigated a range of decomposition modes for **Ru21a** and its isomer **Ru21a'**. Specifically, we considered β -H elimination [74] and nucleophilic attack of the thio-indolate ligand on the alkylidene [53] during productive (Scheme S5), non-productive (Scheme S6) and regenerative propene metathesis (i.e., regeneration of the ethylidene **Ru21a_2**; Scheme S7). In addition, nucleophilic attack and β -hydride elimination, occurring during reaction of the Ru-methylidene with ethylene, were examined (Scheme S8).

Consistent with the observed formation of propene on reaction of **Ru21a** with ethylene (see above), the calculations indicate a relatively low barrier to β -H elimination of the unsubstituted MCB ($\Delta G^\ddagger = 21.7$ kcal mol⁻¹ vs **Ru21a**). However, the barrier to β -hydride elimination is consistently higher (by 4.5–6.2 kcal mol⁻¹) than that of cycloreversion during metathesis itself (Scheme S5–S8). Thus, thio-indolate catalyst **Ru21a** does not appear to be particularly vulnerable to β -H elimination.

The calculations suggest that nucleophilic attack is more likely (Scheme S5–S8). Indeed, consistent with the previously reported nucleophilic attacks of both catechthiolates [53] and amines [75, 76] on alkylidenes, indolate attack on the ethylidene during regenerative metathesis emerges as the dominant decomposition pathway ($\Delta G^\ddagger = 19.7$ kcal mol⁻¹ vs **Ru21a**, Scheme S7). This reaction releases ethylene, which, in turn, may react with a second ruthenium ethylidene or methylidene complex, thereby accelerating decomposition. However, the calculations do not suggest that this vulnerability to nucleophilic attack is inherent to the design of **Ru21a**, with the indolate nitrogen atom trans to the NHC.

In fact, the thiolate moiety of the unintended isomer **Ru21a'** more readily attacks the ethylidene ($\Delta G^\ddagger = 17.8$ kcal mol⁻¹ vs **Ru21a**, Scheme S7) than does the indolate of **Ru21a**. In fact, the corresponding barrier to thiolate attack for the well-known dithiolate catalyst **Ru13** is even lower ($\Delta G^\ddagger = 12.6$ kcal mol⁻¹ vs **Ru13**, Scheme S3).

In short, the calculations reveal no decomposition modes intrinsic to the thio-indolate catalyst design that should make these catalysts more vulnerable than, e.g., the related dithiolate catalyst **Ru13**. Instead, the low catalytic activity and the decomposition observed for these catalysts appear to be the result of unusually high barriers to releasing the internal-olefin product at the end of the metathesis reaction. The exceptional height of these barriers originates from the added steric pressure of the thio-indolate ligand required to achieve E-selectivity.

3 Conclusion

Based on considerations of the geometries of stereoretentive metathesis catalysts [77] and on catechthiolate modifications aimed at increasing the share of E-isomeric product [56], a thio-indolate ligand scaffold was designed to exert steric pressure on the β -substituent of the MCB, and the MCB-like transition states for cycloaddition and cycloreversion. DFT calculations predicted that the S,N-thio-indolate chelate should bind to ruthenium with an orientation suitable to exert the desired steric pressure. Furthermore, DFT-calculated energy differences ($\Delta\Delta G^\ddagger_{(E/Z)}$) between the cycloreversion transition states for propene self-metathesis leading to (Z)-2-butene and (E)-2-butene suggested that ruthenium-alkylidene thio-indolate complexes would favor E-isomer products.

To follow up the computational predictions, the first metal complexes bearing bidentate thio-indolate ligands were synthesized, isolated, and characterized (**Ru21a-c**). The thio-indolate chelates are compatible with the 2-thienylmethylidene and Me₂IMes ligands present in known, active metathesis catalysts, and the general robustness of complexes **Ru21a-c** is comparable to that of other ruthenium catalysts for olefin metathesis.

However, whereas the new complexes participated in metathetic exchange with styrene and allylbenzene, liberating the 2-thienylmethylidene ligand, no self-metathesis products were obtained. Even self-metathesis of propene using **Ru21a** yielded only small proportions of 2-butene (73% (Z)).

Detailed mechanistic DFT calculations of propene self-metathesis by **Ru21a** and its isomer **Ru21a'** revealed barriers to product release from the Ru–2-butene π -complex much higher than those of cycloreversion of the MCB, the step repeatedly identified as rate limiting in computational studies

of ruthenium-catalyzed olefin metathesis [53, 58–60]. The barriers to product release are also much higher than those of common decomposition reactions, and are caused by the additional steric bulk of the thio-indolate. This steric bulk leaves little room for the escaping, bulky disubstituted olefin, which experiences steric repulsion from the thio-indolate ligand, in particular, and the mesityl methyl groups of the Me₂IMes ligand. This repulsion adds to the cost of losing the Ru–olefin π -bond, resulting in unusually high barriers to product release. The negative effect of steric bulk predicted by the calculations is consistent with the metathesis inactivity of the bulkier complexes **Ru21b** and **Ru21c**.

E-selective 1-alkene metathesis catalysts have been sought in vain for more than two decades. The present study reveals the dual challenge of this molecular-design goal: (1) Steric pressure must be exerted in opposite directions to closely-spaced substituents of the nascent disubstituted olefin. (2) The net steric congestion must be sufficiently low to permit productive metathesis and, in particular, for the product olefin to dissociate from the metal. The thio-indolate complexes described herein are, to our knowledge, the first catalysts for which calculations suggest that Challenge 1 can be met. However, these findings also underline the difficulty in achieving E-selectivity without incurring excessive steric congestion.

Supplementary Information The online version contains supplementary material available at <https://doi.org/10.1007/s11244-021-01468-3>.

Acknowledgements The authors gratefully acknowledge financial support from the Research Council of Norway (RCN) via the FRIPRO program (grant number 262370) and via the Norwegian NMR Platform, NNP (226244). The RCN is also thanked for CPU (NN2506K) and storage resources (NS2506K). Bjarte Holmelid is thanked for assistance with the HRMS ESI⁺ analyses and Inger Johanne Fjellanger for assistance with the elemental analysis.

Funding Open access funding provided by University of Bergen (incl Haukeland University Hospital). The authors gratefully acknowledge financial support from the Research Council of Norway (RCN) via the FRIPRO program (grant number 262370) and via the Norwegian NMR Platform, NNP (226244). The RCN is also thanked for CPU (NN2506K) and storage resources (NS2506K).

Availability of data and material The crystal structure of compound **Ru21c** is available in the Cambridge Structural Database (CSD, as compound number CCDC- 2,086,885). The following is available in an additional supporting file (PDF): A description of the experimental procedures and of additional experimental results, NMR, MS, and X-ray data for new compounds, a description of the computational details and of additional computational results, and calculated electronic and free energies of all computationally investigated minima and transition states. The corresponding DFT-optimized molecular Cartesian coordinates are available in an additional supporting file, in a format convenient for visualization (XYZ).

Declaration

Conflict of interest The authors declare no competing financial interest.

Open Access This article is licensed under a Creative Commons Attribution 4.0 International License, which permits use, sharing, adaptation, distribution and reproduction in any medium or format, as long as you give appropriate credit to the original author(s) and the source, provide a link to the Creative Commons licence, and indicate if changes were made. The images or other third party material in this article are included in the article's Creative Commons licence, unless indicated otherwise in a credit line to the material. If material is not included in the article's Creative Commons licence and your intended use is not permitted by statutory regulation or exceeds the permitted use, you will need to obtain permission directly from the copyright holder. To view a copy of this licence, visit <http://creativecommons.org/licenses/by/4.0/>.

References

- Kukla DL, Canchola J, Mills JJ (2020) Synthesis of the cyanobacterial antibiotics anaephenes A and B. *J Nat Prod* 83:2036–2040. <https://doi.org/10.1021/acs.jnatprod.0c00279>
- Martin-Galvez F, Garcia-Ruiz C, Sanchez-Ruiz A, Valeriote FA, Sarabia F (2013) An array of bengamide E analogues modified at the terminal olefinic position: synthesis and antitumor properties. *ChemMedChem* 8:819–831. <https://doi.org/10.1002/cmdc.201300033>
- Teranishi T, Kuwahara S (2014) Stereoselective approach to the DEF ring system of terpendole E. *Tetrahedron Lett* 55:1486–1487. <https://doi.org/10.1016/j.tetlet.2014.01.050>
- Schulz MD, Wagener KB (2014) Precision polymers through ADMET polymerization. *Macromol Chem Phys* 215:1936–1945. <https://doi.org/10.1002/macp.201400268>
- Wittig G, Schöllkopf U (1954) Über Triphenyl-phosphin-methylene als olefinbildende Reagenzien (I. Mitteil. *Chemische Berichte* 87:1318–1330. <https://doi.org/10.1002/cber.19540870919>
- Wadsworth WS, Emmons WD (1961) The utility of phosphonate carbanions in olefin synthesis. *J Am Chem Soc* 83:1733–1738. <https://doi.org/10.1021/ja01468a042>
- Julia M, Paris J-M (1973) Syntheses a l'aide de sulfones v(+)-methode de synthese generale de doubles liaisons. *Tetrahedron Lett* 14:4833–4836. [https://doi.org/10.1016/s0040-4039\(01\)87348-2](https://doi.org/10.1016/s0040-4039(01)87348-2)
- Hoveyda AH, Zhugralin AR (2007) The remarkable metal-catalysed olefin metathesis reaction. *Nature* 450:243–251. <https://doi.org/10.1038/nature06351>
- Grela K (2014) Olefin metathesis: Theory and practice. John Wiley & Sons Inc: Hoboken. <https://doi.org/10.1002/9781118711613>
- Grubbs RH, Wenzel AG, O'Leary DJ, Khosravi E (2015) Handbook of Metathesis. Wiley-VCH, Weinheim. <https://doi.org/10.1002/9783527674107>
- Trnka TM, Grubbs RH (2001) The development of L2X2Ru=CHR olefin metathesis catalysts: an organometallic success story. *Acc Chem Res* 34:18–29. <https://doi.org/10.1021/ar000114f>
- Piola L, Nahra F, Nolan SP (2015) Olefin metathesis in air. *Beilstein J Org Chem* 11:2038–2056. <https://doi.org/10.3762/bjoc.11.221>





13. Kajetanowicz A, Chwalba M, Gawin A, Tracz A, Grell K (2019) Non-glovebox ethenolysis of ethyl oleate and FAME at larger scale utilizing a cyclic (Alkyl)(Amino)Carbene Ruthenium catalyst. *Eur J Lipid Sci Technol*. <https://doi.org/10.1002/ejlt.20190263>
14. Walensky LD, Bird GH (2014) Hydrocarbon-stapled peptides: principles, practice, and progress. *J Med Chem* 57:6275–6288. <https://doi.org/10.1021/jm4011675>
15. Vinogradova EV (2017) Organometallic chemical biology: an organometallic approach to bioconjugation. *Pure Appl Chem* 89:1619–1640. <https://doi.org/10.1515/pac-2017-0207>
16. Isenegger PG, Davis BG (2019) Concepts of catalysis in site-selective protein modifications. *J Am Chem Soc* 141:8005–8013. <https://doi.org/10.1021/jacs.8b13187>
17. Messina MS, Maynard HD (2020) Modification of proteins using olefin metathesis. *Materials Chemistry Frontiers* 4:1040–1051. <https://doi.org/10.1039/c9qm00494g>
18. Higan CS, Lummiss JA, Fogg DE (2016) Olefin metathesis at the dawn of implementation in pharmaceutical and specialty-chemicals manufacturing. *Angew Chem Int Ed Engl* 55:3552–3565. <https://doi.org/10.1002/anie.201506846>
19. Yu M, Lou S, Gonzalez-Bobes F (2018) Ring-closing metathesis in pharmaceutical development: fundamentals, applications, and future directions. *Org Process Res Dev* 22:918–946. <https://doi.org/10.1021/acs.oprd.8b00093>
20. Cink RD, Lukin KA, Bishop RD, Zhao G, Pelc MJ, Towne TB, Gates BD, Ravn MM, Hill DR, Ding C, Cullen SC, Mei J, Leanna MR, Henle J, Napolitano JG, Nere NK, Chen S, Sheikh A, Kallemejn JM (2019) Development of the enabling route for glecaprevir via ring-closing metathesis. *Org Process Res Dev* 24:183–200. <https://doi.org/10.1021/acs.oprd.9b00469>
21. St-Pierre G, Cherney AH, Chen W, Dong X, Dornan PK, Griffin DJ, Houk KN, Lin JB, Osgood S, Silva Elipse MV, Timmons HC, Xie Y, Tedrow JS, Thiel OR, Smith AG (2020) Accelerated development of a scalable ring-closing metathesis to manufacture AMG 176 using a combined high-throughput experimentation and computational modeling approach. *Org Process Res Dev* 25:442–451. <https://doi.org/10.1021/acs.oprd.0c00416>
22. Choi TL, Grubbs RH (2003) Controlled living ring-opening-metathesis polymerization by a fast-initiating ruthenium catalyst. *Angew Chem Int Ed Engl* 42:1743–1746. <https://doi.org/10.1002/anie.200250632>
23. Schrock RR (2011) Synthesis of stereoregular ROMP polymers using molybdenum and tungsten imido alkylidene initiators. *Dalton Trans* 40:7484–7495. <https://doi.org/10.1039/c1dt10215j>
24. Dong Y, Matson JB, Edgar KJ (2017) Olefin cross-metathesis in polymer and polysaccharide chemistry: a review. *Biomacromol* 18:1661–1676. <https://doi.org/10.1021/acs.biomac.7b00364>
25. Edwards JP, Wolf WJ, Grubbs RH (2018) The synthesis of cyclic polymers by olefin metathesis: Achievements and challenges. *J Polym Sci, Part A: Polym Chem* 57:228–242. <https://doi.org/10.1002/pola.29253>
26. Debsharma T, Behrendt FN, Laschewsky A, Schlaad H (2019) Ring-opening metathesis polymerization of biomass-derived levoglucosenol. *Angew Chem Int Ed Engl* 58:6718–6721. <https://doi.org/10.1002/anie.201814501>
27. Jung K, Ahmed TS, Lee J, Sung JC, Keum H, Grubbs RH, Choi TL (2019) Living beta-selective cyclopolymerization using Ru dithiolate catalysts. *Chem Sci* 10:8955–8963. <https://doi.org/10.1039/c9sc01326a>
28. Feist JD, Xia Y (2020) Enol ethers are effective monomers for ring-opening metathesis polymerization: synthesis of degradable and depolymerizable Poly(2,3-dihydrofuran). *J Am Chem Soc* 142:1186–1189. <https://doi.org/10.1021/jacs.9b11834>
29. Foster JC, Grocott MC, Arkinstall LA, Varlas S, Redding MJ, Grayson SM, O'Reilly RK (2020) It is better with salt: aqueous ring-opening metathesis polymerization at neutral pH. *J Am Chem Soc* 142:13878–13885. <https://doi.org/10.1021/jacs.0c05499>
30. Rizzo A, Peterson GI, Bhaumik A, Kang C, Choi TL (2021) Sugar-based polymers from d-Xylose: Living cascade polymerization, tunable degradation, and small molecule release. *Angew Chem Int Ed Engl* 60:849–855. <https://doi.org/10.1002/anie.202012544>
31. Debsharma T, Schmidt B, Laschewsky A, Schlaad H (2021) Ring-opening metathesis polymerization of unsaturated carbohydrate derivatives: levoglucosenyl alkyl ethers. *Macromolecules* 54:2720–2728. <https://doi.org/10.1021/acs.macromol.0c02821>
32. Vougioukalakis GC, Grubbs RH (2010) Ruthenium-based heterocyclic carbene-coordinated olefin metathesis catalysts. *Chem Rev* 110:1746–1787. <https://doi.org/10.1021/cr9002424>
33. Montgomery TP, Johns AM, Grubbs RH (2017) Recent advancements in stereoselective olefin metathesis using ruthenium catalysts. *Catalysts*. <https://doi.org/10.3390/catal7030087>
34. Ogba OM, Warner NC, O'Leary DJ, Grubbs RH (2018) Recent advances in ruthenium-based olefin metathesis. *Chem Soc Rev* 47:4510–4544. <https://doi.org/10.1039/c8cs00027a>
35. Fürstner A (2013) Teaching metathesis “simple” stereochemistry. *Science* 341:1229713. <https://doi.org/10.1126/science.1229713>
36. Muller DS, Basle O, Mauduit M (2018) A tutorial review of stereoregulative olefin metathesis based on ruthenium dithiolate catalysts. *Beilstein J Org Chem* 14:2999–3010. <https://doi.org/10.3762/bjoc.14.279>
37. Dawood KM, Nomura K (2021) Recent developments in Z-selective olefin metathesis reactions by molybdenum, tungsten, ruthenium, and vanadium Catalysts. *Adv Synth Catal* 363:1970–1997. <https://doi.org/10.1002/adsc.202001117>
38. Endo K, Grubbs RH (2011) Chelated ruthenium catalysts for Z-selective olefin metathesis. *J Am Chem Soc* 133:8525–8527. <https://doi.org/10.1021/ja202818v>
39. Dang Y, Wang Z-X, Wang X (2012) Does the ruthenium nitrate catalyst work differently in Z-selective olefin metathesis? A DFT study. *Organometallics* 31:8654–8657. <https://doi.org/10.1021/om300972h>
40. Dang Y, Wang Z-X, Wang X (2012) A thorough DFT study of the mechanism of homodimerization of terminal olefins through metathesis with a chelated ruthenium catalyst: from initiation to Z selectivity to regeneration. *Organometallics* 31:7222–7234. <https://doi.org/10.1021/om300784k>
41. Bronner SM, Herbert MB, Patel PR, Marx VM, Grubbs RH (2014) Ru-based Z-selective metathesis catalysts with modified cyclometalated carbene ligands. *Chem Sci* 5:4091–4098. <https://doi.org/10.1039/C4SC01541J>
42. Herbert MB, Suckling BA, Liu P, Zou L, Dornan PK, Houk KN, Grubbs RH (2015) Cyclometalated Z-selective ruthenium metathesis catalysts with modified N-chelating groups. *Organometallics* 34:2858–2869. <https://doi.org/10.1021/acs.organomet.5b00185>
43. Dumas A, Tarrieu R, Vives T, Roisnel T, Dorcet V, Baslé O, Mauduit M (2018) A versatile and highly Z-selective olefin metathesis ruthenium catalyst based on a readily accessible N-Heterocyclic Carbene. *ACS Catal* 8:3257–3262. <https://doi.org/10.1021/acscatal.8b00151>
44. Xu Y, Wong JJ, Samkian AE, Ko JH, Chen S, Houk KN, Grubbs RH (2020) Efficient Z-selective Olefin-Acrylamide cross-metathesis enabled by sterically demanding cyclometalated ruthenium catalysts. *J Am Chem Soc* 142:20987–20993. <https://doi.org/10.1021/jacs.0c11334>
45. Occhipinti G, Hansen FR, Törnroos KW, Jensen VR (2013) Simple and highly Z-selective ruthenium-based olefin metathesis catalyst. *J Am Chem Soc* 135:3331–3334. <https://doi.org/10.1021/ja311505v>

46. Occhipinti G, Koudriavtsev V, Törnroos KW, Jensen VR (2014) Theory-assisted development of a robust and Z-selective olefin metathesis catalyst. *Dalton Trans* 43:11106–11117. <https://doi.org/10.1039/c4dt00409d>
47. Nelson JW, Grundy LM, Dang Y, Wang Z-X, Wang X (2014) Mechanism of Z-selective olefin metathesis catalyzed by a ruthenium monothiolate carbene complex: A DFT study. *Organometallics* 33:4290–4294. <https://doi.org/10.1021/om500612r>
48. Smit W, Koudriavtsev V, Occhipinti G, Törnroos KW, Jensen VR (2016) Phosphine-Based Z-Selective Ruthenium Olefin Metathesis Catalysts. *Organometallics* 35:1825–1837. <https://doi.org/10.1021/acs.organomet.6b00214>
49. Occhipinti G, Törnroos KW, Jensen VR (2017) Pyridine-stabilized fast-initiating ruthenium monothiolate catalysts for Z-selective olefin metathesis. *Organometallics* 36:3284–3292. <https://doi.org/10.1021/acs.organomet.7b00441>
50. Smit W, Ekeli JB, Occhipinti G, Woźniak B, Törnroos KW, Jensen VR (2020) Z-selective monothiolate ruthenium indenylidene olefin metathesis catalysts. *Organometallics* 39:397–407. <https://doi.org/10.1021/acs.organomet.9b00641>
51. Renom-Carrasco M, Mania P, Sayah R, Veyre L, Occhipinti G, Jensen VR, Thieuleux C (2020) Silica-supported Z-selective Ru olefin metathesis catalysts. *Molecular Catalysis*. <https://doi.org/10.1016/j.mcat.2019.110743>
52. Khan RK, Torker S, Hoveyda AH (2014) Reactivity and selectivity differences between catecholate and catechthiolate Ru complexes. Implications regarding design of stereoselective olefin metathesis catalysts. *J Am Chem Soc* 136:14337–14340. <https://doi.org/10.1021/ja505961z>
53. Koh MJ, Khan RK, Torker S, Yu M, Mikus MS, Hoveyda AH (2015) High-value alcohols and higher-oxidation-state compounds by catalytic Z-selective cross-metathesis. *Nature* 517:181–186. <https://doi.org/10.1038/nature14061>
54. Xu C, Shen X, Hoveyda AH (2017) In situ methylene capping: a general strategy for efficient stereoretentive catalytic olefin metathesis. The concept, methodological implications, and applications to synthesis of biologically active compounds. *J Am Chem Soc* 139:10919–10928. <https://doi.org/10.1021/jacs.7b06552>
55. Liu Z, Xu C, Del Pozo J, Torker S, Hoveyda AH (2019) Ru-based catechthiolate complexes bearing an unsaturated nhc ligand: effective cross-metathesis catalysts for synthesis of (Z)-alpha, beta-unsaturated esters, carboxylic acids, and primary, secondary, and Weinreb amides. *J Am Chem Soc* 141:7137–7146. <https://doi.org/10.1021/jacs.9b02318>
56. Montgomery TP, Grandner JM, Houk KN, Grubbs RH (2017) Synthesis and evaluation of sterically demanding ruthenium dithiolate catalysts for stereoretentive olefin metathesis. *Organometallics* 36:3940–3953. <https://doi.org/10.1021/acs.organomet.7b00555>
57. Jean-Louis Hérisson P, Chauvin Y (1971) Catalyse de transformation des oléfines par les complexes du tungstène. *Die Makromolekulare Chemie* 141:161–176. <https://doi.org/10.1002/macp.1971.021410112>
58. Miyazaki H, Herbert MB, Liu P, Dong X, Xu X, Keitz BK, Ung T, Mkrtyumyan G, Houk KN, Grubbs RH (2013) Z-Selective ethenolysis with a ruthenium metathesis catalyst: experiment and theory. *J Am Chem Soc* 135:5848–5858. <https://doi.org/10.1021/ja4010267>
59. Minenkov Y, Occhipinti G, Jensen VR (2013) Complete reaction pathway of ruthenium-catalyzed olefin metathesis of ethyl vinyl ether: kinetics and mechanistic insight from DFT. *Organometallics* 32:2099–2111. <https://doi.org/10.1021/om301192a>
60. Grandner JM, Shao H, Grubbs RH, Liu P, Houk KN (2017) Origins of the stereoretentive mechanism of olefin metathesis with Ru-dithiolate catalysts. *J Org Chem* 82:10595–10600. <https://doi.org/10.1021/acs.joc.7b02129>
61. Vyboishchikov SF, Bühl M, Thiel W (2002) Mechanism of olefin metathesis with catalysis by ruthenium carbene complexes: density functional studies on model systems. *Chem Eur J* 8:3962–3975
62. Khan RK, Torker S, Hoveyda AH (2013) Readily accessible and easily modifiable Ru-based catalysts for efficient and Z-selective ring-opening metathesis polymerization and ring-opening/cross-metathesis. *J Am Chem Soc* 135:10258–10261. <https://doi.org/10.1021/ja404208a>
63. Johns AM, Ahmed TS, Jackson BW, Grubbs RH, Pederson RL (2016) High trans kinetic selectivity in ruthenium-based olefin cross-metathesis through stereorention. *Org Lett* 18:772–775. <https://doi.org/10.1021/acs.orglett.6b00031>
64. Mikus MS, Torker S, Xu C, Li B, Hoveyda AH (2016) Pentacoordinate ruthenium(II) catecholthiolate and mercaptophenolate catalysts for olefin metathesis: anionic ligand exchange and ease of initiation. *Organometallics* 35:3878–3892. <https://doi.org/10.1021/acs.organomet.6b00773>
65. Testaferri L, Tingoli M, Tiecco M (1980) A convenient synthesis of aromatic thiols from unactivated aryl halides. *Tetrahedron Lett* 21:3099–3100. [https://doi.org/10.1016/s0040-4039\(00\)77418-1](https://doi.org/10.1016/s0040-4039(00)77418-1)
66. Drouin SD, Foucault HM, Yap GPA, Fogg DE (2005) New pseudohalide ligands in Ru-catalyzed olefin metathesis - A robust, air-activated iminopyrrolato catalyst. *Can J Chem* 83:748–754. <https://doi.org/10.1139/v05-039>
67. Neumann B, Krininger C, Lorenz I-P (2007) Synthesis, Structures and Comparison of Neutral Complexes Formed by 2-(2'-Pyridyl)indole and d6 Transition Metals. *Eur J Inorg Chem* 2007:472–480. <https://doi.org/10.1002/ejic.200600730>
68. Ueno A, Kayaki Y, Ikariya T (2014) Heterolysis of NH-Indoles by bifunctional amido complexes and applications to carboxylation with carbon dioxide. *Organometallics* 33:4479–4485. <https://doi.org/10.1021/om500695a>
69. Higman CS, Lanterna AE, Marin ML, Scaiano JC, Fogg DE (2016) Catalyst decomposition during olefin metathesis yields isomerization-active ruthenium Nanoparticles. *ChemCatChem* 8:2446–2449. <https://doi.org/10.1002/cctc.201600738>
70. Higman CS, Plais L, Fogg DE (2013) Isomerization during olefin metathesis: an assessment of potential catalyst culprits. *ChemCatChem* 5:3548–3551. <https://doi.org/10.1002/cctc.201300886>
71. Bailey GA, Lummiss JAM, Foscatto M, Occhipinti G, McDonald R, Jensen VR, Fogg DE (2017) Decomposition of olefin metathesis catalysts by bronsted base: metallacyclobutane deprotonation as a primary deactivating event. *J Am Chem Soc* 139:16446–16449. <https://doi.org/10.1021/jacs.7b08578>
72. Bailey GA, Foscatto M, Higman CS, Day CS, Jensen VR, Fogg DE (2018) Bimolecular coupling as a vector for decomposition of fast-initiating olefin metathesis catalysts. *J Am Chem Soc* 140:6931–6944. <https://doi.org/10.1021/jacs.8b02709>
73. Bahri-Laleh N, Credendino R, Cavallo L (2011) The intriguing modeling of cis-trans selectivity in ruthenium-catalyzed olefin metathesis. *Beilstein J Org Chem* 7:40–45. <https://doi.org/10.3762/bjoc.7.7>
74. Janse van Rensburg W, Steynberg PJ, Meyer WH, Kirk MM, Forman GS (2004) DFT prediction and experimental observation of substrate-induced catalyst decomposition in ruthenium-catalyzed olefin metathesis. *J Am Chem Soc* 126:14332–14333. <https://doi.org/10.1021/ja0453174>
75. Lummiss JAM, Botti AGG, Fogg DE (2014) Isotopic probes for ruthenium-catalyzed olefin metathesis. *Catal Sci Technol* 4:4210–4218. <https://doi.org/10.1039/c4cy01118j>
76. Ireland BJ, Dobbigny BT, Fogg DE (2015) Decomposition of a phosphine-free metathesis catalyst by amines and other bronsted bases: metallacyclobutane deprotonation as a major deactivation pathway. *ACS Catal* 5:4690–4698. <https://doi.org/10.1021/acscatal.5b00813>

77. Montgomery TP, Ahmed TS, Grubbs RH (2017) Stereoretentive Olefin Metathesis: An Avenue to Kinetic Selectivity. *Angew Chem Int Ed Engl* 56:11024–11036. <https://doi.org/10.1002/anie.201704686>

Publisher's Note Springer Nature remains neutral with regard to jurisdictional claims in published maps and institutional affiliations.

Authors and Affiliations

Immanuel Reim¹  · Giovanni Occhipinti¹  · Karl W. Törnroos¹  · Deryn E. Fogg^{1,2}  · Vidar R. Jensen¹ 

✉ Vidar R. Jensen
Vidar.Jensen@uib.no

² Center for Catalysis Research & Innovation, and Department of Chemistry and Biomolecular Sciences, University of Ottawa, Ottawa, ON K1N 6N5, Canada

¹ Department of Chemistry, University of Bergen, Allégaten 41, N-5007 Bergen, Norway

Supplementary Information for:

Toward E-Selective Olefin Metathesis:
Computational Design and Experimental Realization
of Ruthenium Thio-Indolate Catalysts

Immanuel Reim¹, Giovanni Occhipinti¹, Karl W. Törnroos¹, Deryn E. Fogg^{1,2}, Vidar R. Jensen^{1,}*

¹Department of Chemistry, University of Bergen, Allégaten 41, N-5007 Bergen, Norway

²Centre for Catalysis Research & Innovation, Chemistry Department, University of Ottawa,
Ottawa, Ontario, Canada K1N 6N5

Table of Contents

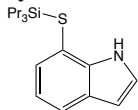
S1. Experimental Procedures and Additional Experimental Results.....	S3
General Procedures.....	S3
Synthesis of 7-((triisopropylsilyl)thio)-1H-indole (L2a).....	S4
Synthesis of 2-methyl-7-((triisopropylsilyl)thio)-1H-indole (L2b).....	S4
Synthesis of 2-H-7-Thio-1H-indole (L3a).....	S4
Synthesis of 2-Methyl-7-Thio-1H-indole (L3b).....	S5
Synthesis of potassium 7-sulfidoindol-1-ide (L4a).....	S5
Synthesis of potassium 2-methyl-7-sulfidoindol-1-ide (L4b).....	S5
Synthesis of potassium 2-phenyl-7-sulfidoindol-1-ide (L4c).....	S5
Synthesis of Complex Ru20	S6
Synthesis of Complex Ru21a/Ru21a'	S6
Synthesis of Complex Ru21b	S7
Synthesis of Complex Ru21c	S7
Isomer Ru21a and Ru21a'	S8
Metathesis Reaction of catalysts Ru21a-b	S9
Self-Metathesis of Styrene.....	S9
Self-Metathesis of Allylbenzene.....	S12
Self-Metathesis of Ethylene.....	S14
Self-Metathesis of Propene.....	S16
S3. Computational Methods.....	S18
Geometry Optimization.....	S18
Single-Point Energy Calculations.....	S18
Free Energies Calculations Including Standard State Correction.....	S19
S4. Validation and Selection of the Computational Approach.....	S20
Choice of Functional for Geometry Optimization.....	S20
Choice of Functional for Single-Point Calculations.....	S21
S5. Computational Results.....	S22
Computational Results for Complexes Ru13 , Ru18 and Ru19a-c	S23
Computational Results for Complexes Ru21	S27
S4. NMR Spectra.....	S36
S5. X-ray Crystal Structures.....	S49
X-ray Crystal Structure of Ru21a	S49
X-ray Crystal Structure of Ru21c	S51
S6. References.....	S53

S1. Experimental Procedures and Additional Experimental Results

General Procedures.

Reactions were carried out in an argon-filled glovebox at room temperature (25 ± 2 °C), unless otherwise indicated. Solvents were dried and degassed using a Glass Contour solvent purification system, then stored under argon in the glovebox over 4 Å molecular sieves for at least 16 h prior to use, unless otherwise indicated. Liquid reagents were degassed by five consecutive freeze/pump/thaw cycles, and then stored under argon in the glovebox freezer (-35 °C)., Triisopropylsilanethiol, tetrakis(triphenylphosphine)-palladium(0), allylbenzene, styrene, pyridine, potassium hydride, tetrabutylammonium fluoride and propene were obtained from Sigma Aldrich. Tricyclohexylphosphine[4,5-dimethyl-1,3-bis(2,4,6-trimethylphenyl)imidazol-2-ylidene][2-thienylmethylene] ruthenium(II) dichloride (catMETium® RF3) was kindly supplied by Evonik Industries. 7-Bromo-1H-indole and 2-Methyl-7-Bromo-1H-indole were obtained from Enamine. 2-Phenyl-7-Thiol-1H-indole was purchased from Santai Lab. NMR spectra were recorded on Bruker Biospin AV500 and 850 Ascend spectrometers at 298 K, and referenced against the residual proton signals of the deuterated solvents (^1H) [1]. HRMS ESI mass spectra were recorded by means of an orthogonal electron spray ionization ion source (ESI) interfaced to a JMS-T100LC AccuTOF mass spectrometer from JEOL USA, Inc. (Peabody, MA). The ions were transported into the orthogonal accelerating time-of-flight (TOF) single-stage reflectron mass analyzer by a high-frequency and high-voltage quadrupole ion guide. Detection was achieved with a dual microchannel plate detector. Elemental analyses were performed using an Elementar Vario EL III analyzer. GC quantification was performed on an Agilent 7890A series GC equipped with a flame ionization detector (FID), an Agilent 7683B series autosampler, and an Agilent HP-5 polysiloxane column (30 m length, 320 μm diameter). Calibration curves (peak areas vs. concentration for solutions with ca. 1:1 w/w decane/analyte) in the relevant concentration regimes were constructed using commercial samples (styrene, *trans*-stilbene, allylbenzene) [2]. Yields in catalytic runs were determined from the integrated peak areas (referenced against decane), compared to the substrate/decane ratio at time zero (t_0). GC samples were quenched using ca. 10 equiv of potassium tris(pyrazolyl)borohydride [3] in THF prior to analysis. Suitable crystals for diffraction experiments were immersed in Paratone-N (Hampton Research) in a nylon loop. Data collection was done on a Bruker AXS TXS rotating anode system with an APEXII Pt¹³⁵ CCD detector using graphite-monochromated Mo K α radiation ($\lambda = 0.71073$ Å).

Synthesis of 7-((triisopropylsilyl)thio)-1H-indole (L2a)



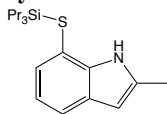
In a glovebox, a Schlenk finger was charged with 88 mg (2.2 mmol, 1.1 eq) KH in 10 mL of toluene. 457 μ L (2.4 mmol, 1.2 eq) triisopropylsilylanethiol was added to the suspension at once and the reaction was stirred for 30 minutes to form a colorless solution. 392 mg (2 mmol, 1 eq.) 7-Bromoindole in 10 mL of toluene and 231 mg (0.2 mmol, 0.1 eq) tetrakis(triphenylphosphine)-palladium(0) was added to the flask. The solution was then taken out of the glovebox and heated for 14 h at 120 °C. After cooling the reaction to room temperature, the reaction mixture was filtered through a plug of SiO₂ with DCM as eluent. After removal of the solvent, the reaction was filtered through SiO₂ with hexane as eluent. After the removal of the solvent, the residual was taken up in THF and 50 mg Merrifield-Resin was added to the flask to remove residual triphenylphosphine. After 15 h the suspension was filtered over silica gel, the filtrate concentrated and purified via flash chromatography (SiO₂, 1:5 DCM:Hexane) to deliver the product as a colorless oil.

Yield: 420 mg (69 %)

¹H NMR (400 MHz, CDCl₃) δ 8.57 (s, 1H), 7.51 (dt, J = 7.9, 0.9 Hz, 1H), 7.29 – 7.20 (m, 2H), 6.98 (dd, J = 7.9, 7.4 Hz, 1H), 6.53 (dd, J = 3.2, 2.2 Hz, 1H), 1.33 – 1.14 (m, 3H), 1.02 (d, J = 7.4 Hz, 18H).

¹³C-NMR (CDCl₃, 300 MHz): 139.0, 128.7, 127.5, 124.0, 120.2, 119.7, 112.4, 103.2, 18.4, 13.3.

Synthesis of 2-methyl-7-((triisopropylsilyl)thio)-1H-indole (L2b)

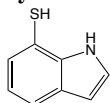


In a glovebox, a Schlenk finger was charged with 66 mg (1.65 mmol, 1.1 eq) KH in 7.5 mL of toluene. 386 μ L (1.8 mmol, 1.2 eq) triisopropylsilylanethiol was added to the suspension at once and the reaction was stirred for 30 minutes to form a colorless solution. 214 μ L (1.5 mmol, 1 eq.) 2-Methyl-7-Bromo-1H-indole in 7.5 mL of toluene and 173.3 mg (0.15 mmol, 0.1 eq) tetrakis(triphenylphosphine)-palladium(0) was added to the flask. The solution was then taken out of the glovebox and heated for 14 h at 120 °C. After cooling the reaction to room temperature, the reaction mixture was filtered through a plug of SiO₂ with DCM as eluent. After removal of the solvent, the reaction was filtered through SiO₂ with hexane as eluent. After the removal of the solvent, the residual was taken up in THF and 20 mg Merrifield-Resin was added to the flask to remove residual triphenylphosphine. After 15 h the suspension was filtered over silica gel, the solvent removed, and the resulting colorless solid used without further purification.

Yield: 291 mg (61%)

¹H NMR (300 MHz, CDCl₃) δ 8.27 (s, 1H), 7.38 (dt, J = 7.8, 0.9 Hz, 1H), 7.18 (dd, J = 7.5, 1.0 Hz, 1H), 6.93 (dd, J = 7.8, 7.4 Hz, 1H), 6.20 (dd, J = 2.4, 1.1 Hz, 1H), 2.47 (d, J = 0.6 Hz, 3H), 1.38 – 1.12 (m, 3H), 1.12 – 0.80 (m, 18H).

Synthesis of 2-H-7-Thio-1H-indole (L3a)



A Schlenk finger was charged with 427 mg (1.4 mmol, 1 eq) of **L2a** and 14.5 mL of THF and cooled to 0 °C. To this solution 2.8 mL (2.8 mmol, 2 eq) of 1 M tert-butylammonium fluoride solution was added and the solution was stirred for 1 h at 0 °C and then warmed up to rt and stirred for additional 30 min. The solution was cooled to 0 °C and 15 mL of 3 M HCl solution was added. The organic phase was separated, and the aqueous phase was extracted 3x with DCM. The combined organic phase was dried over MgSO₄ and concentrated under removed reduced pressure. The residual oil was purified via flash chromatography (SiO₂, 2:3 DCM:hexane), yielding the desired product as yellow solid.

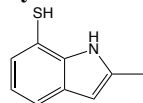
Yield: 92 mg (44 %)

^1H NMR (400 MHz, CDCl_3) δ 8.44 (s, 1H), 7.59 (dq, $J = 7.9, 0.9$ Hz, 1H), 7.34 – 7.25 (m, 2H), 7.10 – 7.01 (m, 1H), 6.60 (dd, $J = 3.2, 2.1$ Hz, 1H), 3.28 (s, 1H).

^{13}C NMR (101 MHz, CDCl_3) δ 137.42, 127.88, 127.54, 124.46, 120.71, 120.37, 108.99, 103.62.

HRMS(ESI) m/z : $[\text{M}-\text{H}]^-$ Calcd for $\text{C}_8\text{H}_6\text{NS}$ 148.0221; Found 148.0218.

Synthesis of 2-Methyl-7-Thio-1H-indole (L3b)



A Schlenk finger was charged with 287 mg (0.85 mmol, 1 eq) of **1b**, 2.8 mL of THF and 2.8 mL of Ethanol. To this solution 0.28 mL concentrated HCl (3.4 mmol, 4 eq) was added and the solution was stirred for 5 h. Afterwards, the solvents were removed under reduced pressure, re-dissolved in 2 mL of DCM. To the DCM solution 10 mL of hexane was added and the suspension was filtered through a plug of SiO_2 to remove the formed red solid. The solvent of the filtrate was removed under reduced pressure to yield the desired product as a colorless oil.

Yield: 90 mg (61 %)

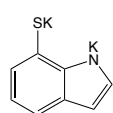
^1H NMR (400 MHz, CDCl_3) δ 8.13 (s, 1H), 7.46 (dt, $J = 7.9, 0.9$ Hz, 1H), 7.22 (dt, $J = 7.4, 1.0$ Hz, 1H), 7.05 – 6.96 (m, 1H), 6.26 (dq, $J = 2.1, 1.0$ Hz, 1H), 3.25 (d, $J = 1.0$ Hz, 1H), 2.48 (d, $J = 1.0$ Hz, 3H).

^{13}C NMR (101 MHz, CDCl_3) δ 137.64, 135.54, 129.05, 126.48, 120.20, 119.59, 107.85, 101.37, 13.75.

HRMS(ESI) m/z : $[\text{M}-\text{H}]^-$ Calcd for $\text{C}_9\text{H}_8\text{NS}$ 162.03774; Found 162.03750.

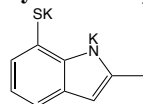
Elemental Analysis, calculated for $\text{C}_9\text{H}_9\text{NS}$: C, 66.22, H, 5.56, N, 8.58; found: C, 65.80, H, 5.33, N, 8.34.

Synthesis of potassium 7-sulfidoindol-1-ide (L4a)



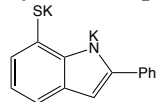
To 31.3 mg (0.21 mmol, 1 eq) **L3a** in 4 mL THF was 17.6 mg (0.44 mmol, 2.1 eq) KH added. Upon addition of KH, hydrogen was formed and the solution turned into a pink suspension. The reaction mixture was stirred for 14 h. The resulting pink suspension was filtered and the solid was washed with hexane (2x 5 mL) and dried. The dried compound indicates a quantitative conversion, measured by weight, and was used without further purification.

Synthesis of potassium 2-methyl-7-sulfidoindol-1-ide (L4b)



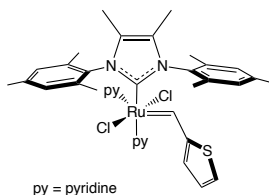
To 101 mg (0.6 mmol, 1 eq) **2b** in 4 mL THF was 52.1 mg (1.3 mmol, 2.1 eq) KH added. Upon addition of KH, hydrogen was formed and the solution turned into a pink suspension. The reaction mixture was stirred for 14 h. The resulting pink suspension was filtered and the solid was washed with hexane (2x 5 mL) and dried. The dried compound indicates a quantitative conversion, measured by weight, and was used without further purification.

Synthesis of potassium 2-phenyl-7-sulfidoindol-1-ide (L4c)



To 45 mg (0.2 mmol, 1 eq) of 2-Phenyl-7-Thio-1H-indole in 4 mL THF was 16.8 mg (0.42 mmol, 2.1 eq) KH added and the reaction mixture was stirred for 14 h to form a yellow solution. The solvent was removed under reduced pressure. The dried compound indicates a quantitative conversion, measured by weight, and was used without further purification.

Synthesis of Complex Ru20



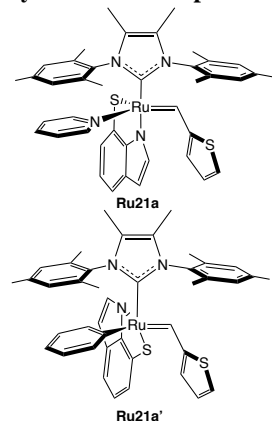
py = pyridine

The synthesis was performed after a literature known procedure [4]. In a glovebox, a 25 mL vial, equipped with a magnetic stirring bar and a screw cap, was charged with complex tricyclohexylphosphine[4,5-dimethyl-1,3-bis(2,4,6-trimethylphenyl)imidazole-2-ylidene][2-thienylmethylene] ruthenium(II) dichloride (1087 mg, 1.234 mmol) and pyridine (4 mL). The vial was closed and the mixture stirred at room temperature for 1 hour. Then pentane (5 mL) was added to the reaction mixture causing the precipitation of a green solid. The solid was allowed to sediment (settle out) and then was isolated by vacuum filtration through a frit, washed three times with 5 mL of pentane and dried in the glovebox to give a green microcrystalline solid. Yield: 786 mg (84 % of yield).

The ^1H NMR is consistent with literature [4].

^1H NMR (500 MHz, C_6D_6) δ 18.94 (s, 1H), 8.79 (s, 2H), 8.62 – 8.57 (m, 2H), 7.74 (s, 1H), 7.40 (dt, $J = 4.9, 1.1$ Hz, 1H), 7.13 (s, 1H), 6.91 (t, $J = 7.7$ Hz, 1H), 6.74 (s, 5H), 6.59 (t, $J = 6.3$ Hz, 2H), 6.50 (dd, $J = 5.0, 3.8$ Hz, 1H), 6.42 (t, $J = 7.7$ Hz, 1H), 6.15 (t, $J = 6.8$ Hz, 2H), 2.64 (s, 6H), 2.33 (s, 6H), 2.14 (s, 6H), 1.54 (s, 6H)

Synthesis of Complex Ru21a/Ru21a'



In a glovebox, a 20 mL vial was charged with 49.8 mg (0.68 mmol, 1 eq) of **Ru20** in 10 mL THF and 16.8 mg (0.075 mmol, 1.1) of **L4a** was added to the solution. A color change from green to red was observed immediately. After 30 min the reaction was completed, and the solvent removed under reduced pressure. The crude reaction mixture was redissolved in toluene, filtered through a pad of Celite and concentrated to about 2 mL. To this solution 10 mL hexane was added and cooled to $-20\text{ }^\circ\text{C}$ for 15 h. The resulting microcrystalline solid was collected and washed with cold pentane (2 x 4 mL) to yield the desired product as brown/red solid. The ^1H NMR analysis shows the presence of two isomeric complexes **Ru21a** and **Ru21a'** in the ratio 95:5.

Yield: 31.1 mg (62 %)

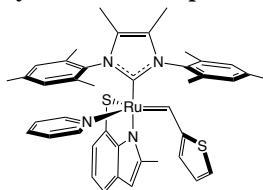
Ru21a: ^1H NMR (850 MHz, C_6D_6) δ 16.21 (s, 1H), 8.12 (dd, $J = 7.3, 0.9$ Hz, 1H), 7.80 (dd, $J = 7.6, 0.9$ Hz, 1H), 7.53 (t, $J = 7.4$ Hz, 1H), 6.94 (dt, $J = 4.9, 1.0$ Hz, 1H), 6.76 – 6.72 (m, 2H), 6.53 (s, 2H), 6.44 (dd, $J = 3.9, 1.2$ Hz, 1H), 6.29 (d, $J = 2.1$ Hz, 2H), 6.26 – 6.19 (m, 4H), 5.94 (d, $J = 2.6$ Hz, 1H), 2.42 (s, 6H), 1.98 (s, 6H), 1.69 (s, 6H), 1.36 (s, 6H).

^{13}C -NMR (C_6D_6 , 850 MHz): 263.2, 181.5, 152.5, 149.2, 148.2, 140.4, 138.3, 133.8, 129.0, 126.5, 126.2, 123.6, 123.0, 122.5, 119.8, 117.7, 114.2, 105.0, 31.6, 20.7, 19.5, 8.7

Ru21a': ^1H NMR (850 MHz, C_6D_6) δ 15.38 (s, 1H), 8.71 (dt, $J = 5.0, 1.5$ Hz, 2H), 7.96 (dd, $J = 7.7, 0.9$ Hz, 1H), 7.86 (d, $J = 7.0$ Hz, 1H), 7.46 (t, $J = 7.3$ Hz, 1H), 7.25 (t, $J = 1.2$ Hz, 2H), 7.10 – 7.00 (m, 4H), 6.91 – 6.87 (m, 2H), 6.66 (tt, $J = 7.4, 1.5$ Hz, 1H), 6.28 – 6.27 (m, 2H), 5.84 (dd, $J = 17.9, 12.1$ Hz, 1H), 2.42 (s, 6H), 1.98 (s, 6H), 1.69 (s, 6H), 1.36 (s, 6H).

HRMS(ESI $^+$) m/z : $[\text{M}-\text{NC}_3\text{H}_5]^+$ Calcd for $\text{C}_{36}\text{H}_{36}\text{N}_3\text{RuS}_2$ 676.1394; Found 676.9120.

Synthesis of Complex Ru21b



In a glovebox, a 20 mL vial was charged with 36.6 mg (0.05 mmol, 1 eq) of Ru20 in 10 mL THF and 13.2 mg (0.055 mmol, 1.1) of L4b was added to the solution. A color change from green to red was observed immediately. After 30 min the reaction was completed, and the solvent was removed under reduced pressure. The crude reaction mixture was redissolved in toluene, filtered through Celite and concentrated to about 2 mL. To this solution 10 mL hexane was added and cooled to -20 °C for 15 h. The resulting solid was collected and washed with cold hexane (2 x 4 mL) to yield the desired product as red microcrystalline solid.

Yield: 16.0 mg (42 %).

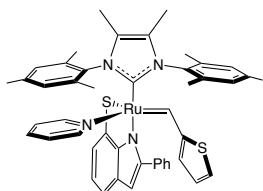
¹H NMR (500 MHz, C₆D₆) δ 15.89 (s, 1H), 9.07 (d, *J* = 5.6 Hz, 1H), 8.06 (dd, *J* = 7.2, 0.9 Hz, 1H), 7.79 (dd, *J* = 7.6, 1.0 Hz, 1H), 7.55 – 7.49 (m, 1H), 7.12 (s, 1H), 7.10 – 7.05 (m, 1H), 6.95 (dt, *J* = 4.9, 1.0 Hz, 1H), 6.64 (tt, *J* = 7.5, 1.5 Hz, 2H), 6.57 (d, *J* = 0.9 Hz, 1H), 6.36 (dd, *J* = 3.8, 1.2 Hz, 1H), 6.30 (tt, *J* = 5.6, 1.5 Hz, 1H), 6.23 (t, *J* = 4.4 Hz, 1H), 6.21 (s, 2H), 5.88 (ddd, *J* = 6.9, 5.2, 1.4 Hz, 1H), 2.51 (s, 6H), 1.98 (s, 6H), 1.65 (br, 6H) 1.36 (s, 6H), 0.94 (d, *J* = 0.9 Hz, 3H).

¹³C-NMR (C₆D₆, 850 MHz): 261.0, 181.8, 165.3, 152.5, 151.6, 149.2, 144.3, 138.1, 134.6, 133.9, 132.3, 129.2, 129.0, 126.1, 123.3, 122.9, 119.2, 116.9, 113.6, 101.7, 20.7, 18.5, 14.4, 8.8.

HRMS(ESI⁺) *m/z*: [M-NC₅H₅]⁺ Calcd for C₃₇H₃₉N₃RuS₂ 690.1550; Found 690.9360.

Elemental Analysis: Anal. Calcd for C₄₂H₄₄N₄RuS₂ · 0.1 CH₂Cl₂: C, 64.95; H, 5.72; N, 7.20. Found: C, 64.60; H, 5.53; N, 6.74. The 0.1 eq DCM were determined from a ¹H NMR spectrum of the sample in C₆D₆. Due to the lability of the bound pyridine, prolonged time under reduced pressure, led to partial decomposition of the catalyst.

Synthesis of Complex Ru21c



In a glovebox, a 20 mL vial was charged with 60.0 mg (0.08 mmol, 1 eq) of Ru20 in 10 mL THF and 27.3 mg (0.09 mmol, 1.1 eq) of L4c was added to the solution. A color change from green to red was observed immediately. After 30 min the reaction was completed, and the solvent was removed under reduced pressure. The crude reaction mixture was redissolved in toluene, filtered through a pad of Celite and concentrated to about 2 mL. To this solution 10 mL hexane was

added and cooled to -20 °C for 15 h. The resulting solid was collected and was washed with cold pentane (2 x 4 mL) to yield the desired product as red crystals.

Yield: 31.1 mg (46 %).

¹H NMR (850 MHz, C₆D₆) δ 15.87 (s, 1H), 8.86 (d, *J* = 5.4 Hz, 1H), 8.07 (dt, *J* = 7.3, 0.8 Hz, 1H), 7.74 (dt, *J* = 7.7, 0.7 Hz, 1H), 7.54 – 7.50 (m, 1H), 7.05 – 6.97 (m, 2H), 6.85 – 6.77 (m, 4H), 6.62 (td, *J* = 7.3, 1.0 Hz, 2H), 6.60 – 6.55 (m, 2H), 6.47 (tt, *J* = 7.4, 1.5 Hz, 1H), 6.18 (s, 6H), 5.78 (s, 2H), 2.56 – 1.84 (m, 18H), 1.32 (s, 6H).

¹³C-NMR (C₆D₆, 850 MHz): 261.6, 181.2, 152.4, 152.3, 149.1, 148.1, 141.2, 140.4, 138.2, 133.8, 129.0, 126.5, 126.2, 123.6, 122.9, 122.4, 119.7, 117.6, 114.1, 104.9, 20.5, 18.4, 13.9, 8.7.

HRMS(ESI⁺) *m/z*: [M-NC₅H₅]⁺ Calcd for C₄₂H₄₁N₃RuS₂ 753.1785; Found 753.9206.

Elemental Analysis: Anal. Calcd for C₄₇H₄₆N₄RuS₂ · 0.1 C₅H₁₂: C, 69.07; H, 6.47; N, 6.20. Found: C, 68.85; H, 4.63; N, 5.92. The 0.1 eq pentane were determined from a ¹H NMR spectrum of the sample in C₆D₆. Due to the lability of the bound pyridine, prolonged time under reduced pressure, led to partial decomposition of the catalyst.

Isomer **Ru21a** and **Ru21a'**

The ^1H NMR of the complex **Ru21a** shows a minor component **Ru21a'** (5%) with an alkylidene resonance at $\delta = 15.38$ ppm. Several crystallization attempts, in toluene/pentane or DCM/pentane, did not change the **Ru21a**/**Ru21a'** ratio (19:1). This ratio is also temperature-independent in the range 10 – 50 $^\circ\text{C}$, persistent in solution even with visible precipitation (decomposition) in a monitored J-Young tube (7 days), and constant during reaction with propene. Furthermore, a NOESY experiment of a solution containing **Ru21a** and **Ru21a'** (Fig. S1) shows a positive cross-signal between the alkylidene resonances of **Ru21a** and **Ru21a'**, confirming that the two isomers are in a dynamic equilibrium with each other. The free energy difference between the two isomers can thus be estimated as $\Delta G_{(\text{Ru21a}'-\text{Ru21a})} = 1.8 \text{ kcal mol}^{-1}$ (Eq. 1). Hoveyda and co-workers has previously shown that a bidentate dithiolate ligand can rotate to interchange the position of the two S atoms [5]. This suggests that the observed complex **Ru21a'** could be the less stable S,N rotamer of **Ru21a**. Indeed, the isomer with the S-atom located trans to the NHC ligand has a DFT-calculated free energy (relative to that of **Ru21a**) only 0.1 kcal/mol higher than that of the NOESY-derived energy difference ($\Delta G_{\text{Ru21a}}^{\text{DFT}} = 1.9 \text{ kcal mol}^{-1}$, see the Computational Results section below), and we thus assume the observed minor component **Ru21a'** is due to this isomer.

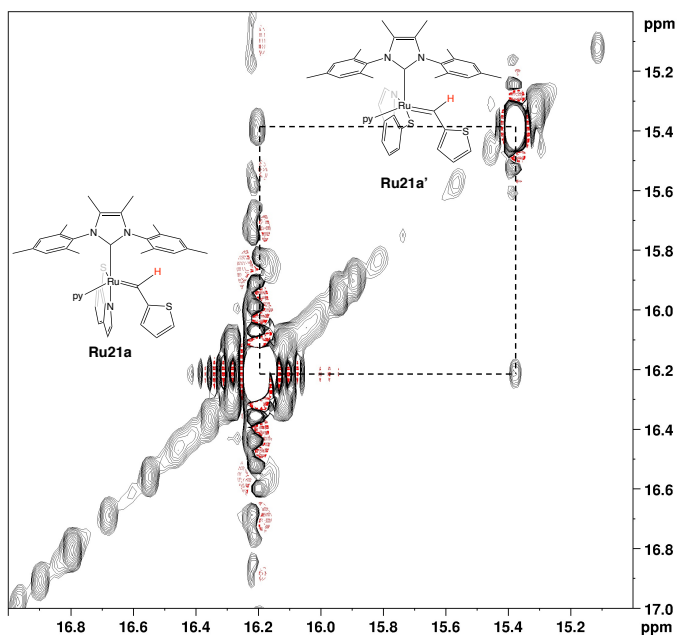


Fig. S1 NOESY-Experiment of complex **Ru21a** and **Ru21a'** showing the exchange between **Ru21a** and **Ru21a'** (C_6D_6 , 850 MHz) (py = pyridine)

$$\Delta G_{(\text{Ru21a}'-\text{Ru21a})} = -RT \ln K_{eq} = -RT \ln \frac{5}{95} = 1.8 \text{ kcal mol}^{-1} \quad (\text{Eq. 1})$$

Metathesis Reaction of catalysts Ru21a-b

Self-Metathesis of Styrene

In a 4 mL vial, a stock solution of catalyst Ru21a (19.6 mg, 0.026 mmol) and anthracene (I.S., 4.6 mg, 0.026 mmol, 1 eq) in 2.6 mL C₆D₆ (10 mM in Ru) was made. The resulting solution was filtered through a pipette filter stuffed with a Kimwipe to remove any undissolved solids. 600 μ L of this solution was transferred to a J-Young NMR tube. An initial ¹H NMR spectrum was recorded to establish a starting ratio between starting alkylidene vs anthracene. The J-Young NMR was reimported into the Glovebox and styrene (3.7 μ L, 0.0325 mol, 5 eq) was added and the timer started. The solution was mixed in the NMR tube at 298 K, and ¹H NMR spectra were recorded periodically to track the disappearance of starting material and appearance of products over time. The experiment was repeated using a stock solution of Ru21b (15.4 mg, 0.026 mmol) with anthracene (I.S., 4.6 mg, 0.026 mmol, 1 eq) in 2.6 mL C₆D₆ (10 mM in Ru).

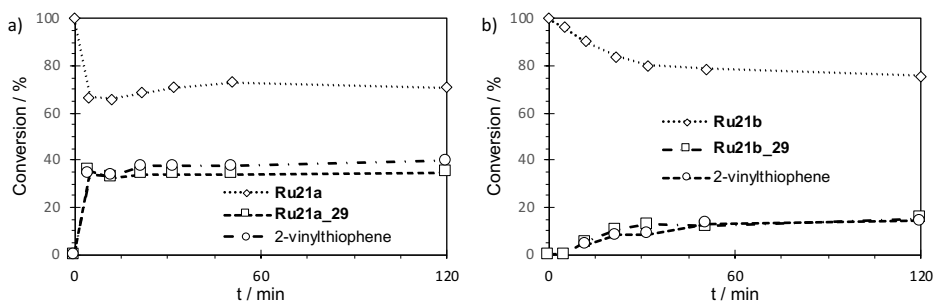


Fig. S2 Self-metathesis of styrene with catalyst **Ru21a** (a) and **Ru21b** (b) in C₆D₆ over 2 hours. No stilbene formation was observed, but new alkylidene signals emerged. The reaction was monitored by ¹H-NMR analysis relative to internal standard (See Fig. S3 and S4)

The reaction with styrene of both catalysts, **Ru21a** and **Ru21b**, showed no formation of stilbene (See Fig. S2 and S3). However, during the reaction a new alkylidene signal appeared at 17.2 ppm and 16.9 ppm, respectively, which correlates with the disappearance of the starting material ($\delta = 16.2$ and 15.9 ppm,) and the formation of 2-vinylthiophene (C₅H₃S-CH₂: $\delta = 5.48, 4.89$ ppm) [6]. The appearance of 2-vinylthiophene requires the exchange of the alkylidene with styrene via a non-productive metathesis (see Scheme S1). Therefore, the alkylidene signal was assigned to complex **Ru21a_29** and **Ru21b_29**. Interestingly, the equilibrium between **Ru21a** and **Ru21a_29** is reached immediately, while the equilibrium with the more sterically hindered complex **Ru21b** is reached after 30 min. The slower exchange indicates a higher energy barrier for olefin metathesis which agrees with the computational results (see Table S5).

Scheme S1 Alkylidene Exchange of Catalyst Ru21a and Ru21b with Styrene via Non-Productive Metathesis

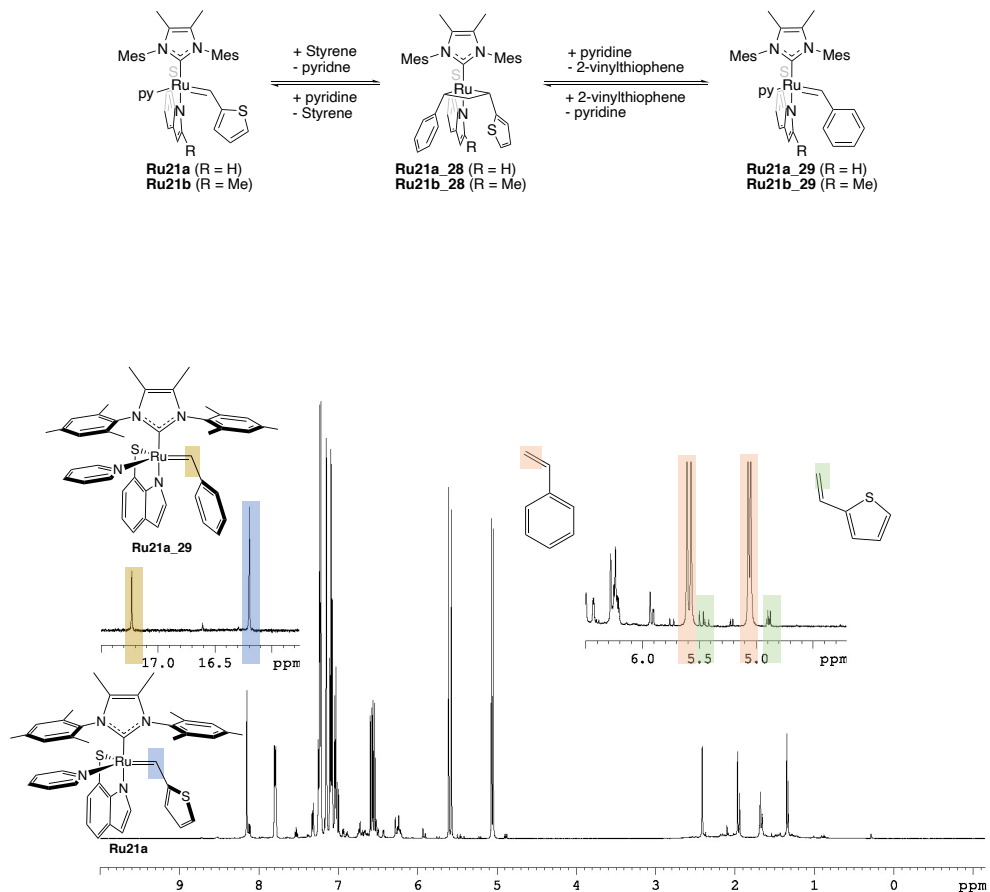


Fig. S3 ^1H NMR spectrum of reaction of catalyst **Ru21a** with 5 eq. styrene after 2 h. Inset shows the key organic products. The signals of 2-vinylthiophene are in agreement with literature [6]. (C_6D_6 , 300.1 MHz)

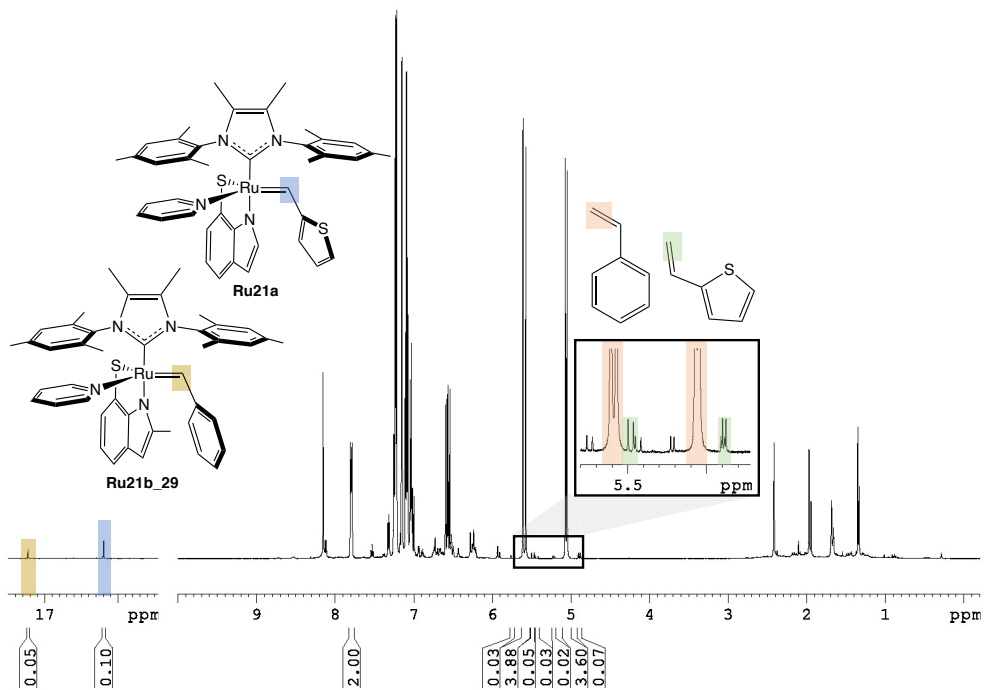


Fig. S4 ^1H NMR spectrum of reaction of catalyst **Ru21b** with 5 eq styrene after 2h. Inset shows the key organic products. The 2-vinylthiophene signals are in agreement with literature [6]. (C_6D_6 , 300.1 MHz)

Self-Metathesis of Allylbenzene

(a) The stock solutions of the catalyst from the styrene experiment were used. Similarly, 600 μL of the solution containing **Ru21b** and anthracene was transferred to a J-Young NMR tube. An initial ^1H NMR spectrum was recorded to establish a starting ratio between starting alkylidene vs anthracene. The J-Young NMR was reimported into the Glovebox and allylbenzene (4.3 μL , 0.325 mmol, 5 eq) was added and the timer started. The solution was mixed in the NMR tube at 298 K and ^1H NMR spectra were recorded periodically to track the disappearing of starting material and appearing of products over time.

(b) In a 4 mL vial, a solution containing dodecane (I.S., 24.0 μL , 0.1 mmol) and allylbenzene (14.0 μL , 0.1 mmol) and 2 mL THF was made. An aliquot was taken to record the initial concentration. 1 mL of the THF solution was then added to a 4 mL vial containing catalyst **Ru21a** (2 mg, 0.0026 mmol, 5mol%) and the timer started. The reaction was conducted at room temperature. Aliquots were taken periodically and the reaction in each aliquot was quenched with ca. 10 equiv of potassium tris(pyrazolyl)borohydride. The samples were analyzed by GC/FID.

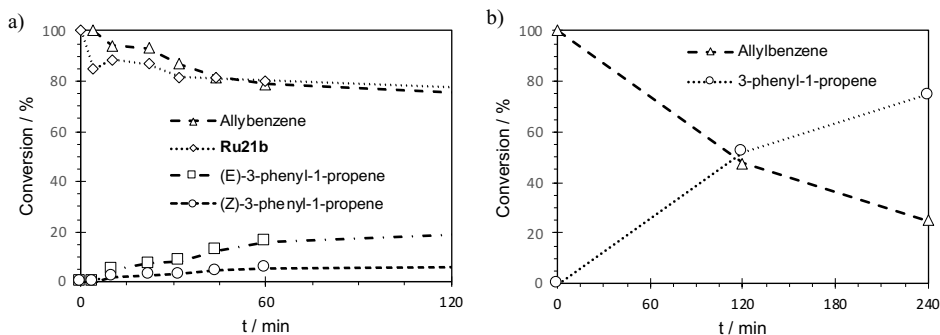


Fig. S5 Self-metathesis of allylbenzene with catalyst (a) **Ru21b** in C_6D_6 and (b) **Ru21a** in THF. Only isomerization allylbenzene to 3-phenyl-1-propene was observed. Reaction was monitored (a) by ^1H -NMR analysis relative to internal standard and (b) via GC analysis of aliquots

The reaction of catalyst **Ru21b** with allylbenzene showed no formation of 1,4-diphenylbut-2-ene. The isomerization of allylbenzene to 3-phenyl-1-propene (*E*:*Z*, 75:25) correlates with the disappearance of allylbenzene (Fig. S3). Since no metathesis occurred after 60 min, the J-Young NMR tube was heated to 50 $^\circ\text{C}$ for 12 h. After 12 h, still 17 % of catalyst **Ru21b** was visible, probably due to reduced initiation because of steric hindrance compared of catalyst **Ru21a**. Furthermore, after 12 h 2-vinylthiophene ($\text{C}_5\text{H}_3\text{S}-\text{CH}_2$: $\delta = 5.48, 4.89$ ppm) [6] and styrene ($\text{C}_7\text{H}_6-\text{CH}_2$: $\delta = 5.60, 5.07$ ppm) was observed. 2-Vinylthiophene is evidence for the occurrence of non-productive metathesis with allylbenzene. The formation of styrene is a product of metathesis with prop-1-en-1-ylbenzene forming a benzylidene complex. Styrene is then released by non-productive metathesis with allylbenzene.

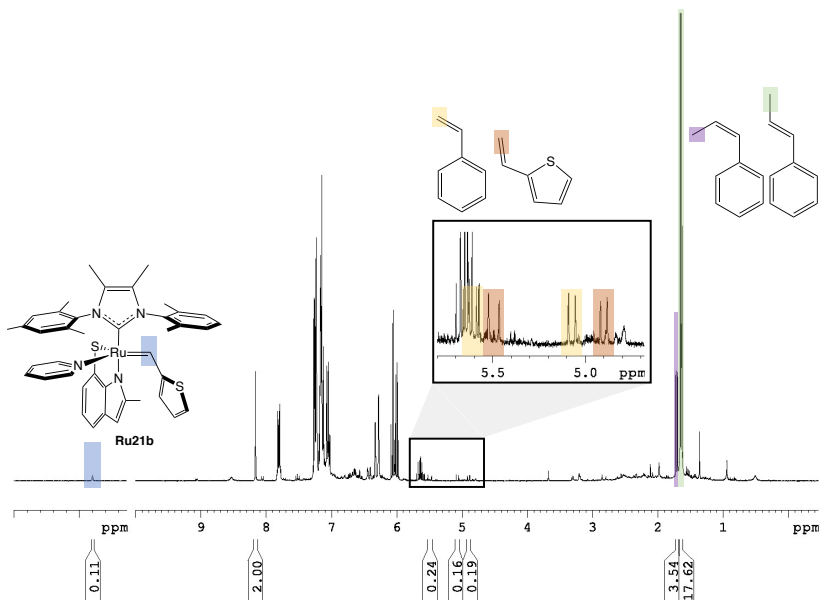


Fig. S6 ^1H NMR spectrum of reaction after 12 h at 50 °C of catalyst **Ru21b** with allylbenzene. Inset shows the key organic products. The signals of 3-phenylprop-2-ene, 2-vinylthiophene and styrene are in agreement with literature. (C_6D_6 , 300.1 MHz)

Similarly, no 1,4-diphenylbut-2-ene was detected when a reaction of the smaller **Ru21a** with allylbenzene was followed via GC. Computational models indicate a higher barrier of the key intermediate, the rupture of the metallacyclobutane for catalyst **Ru21a**, for the formation of stilbene ($\Delta G_{\text{TS}29}^\ddagger = 36.9 \text{ kcal mol}^{-1}$, see Scheme S12) and 1,4-diphenylbut-2-ene ($\Delta G_{\text{TS}31}^\ddagger = 37.5 \text{ kcal mol}^{-1}$, see Scheme S12) reaching the kinetic limit for metathesis. The high barrier for the productive metathesis is caused by the steric congestion of metallacyclobutane (MCB) intermediate and of the corresponding cycloreversion transition state, which can be relieved via distortion of the metallacyclobutane geometry which also enables the decomposition of the catalyst via β -H elimination [7].

Self-Metathesis of Ethylene

In a 4 mL vial, catalyst **Ru21a** (14.3 mg, 0.02 mmol) and anthracene (I.S., 3.6 mg, 0.02 mmol, 1 eq) were dissolved in 1 mL C₆D₆ (20 mM Ru). The resulting solution was filtered through a pipette filter stuffed with a Kimwipe to remove any undissolved solids. 600 μ L of this solution was transferred to a J-Young NMR tube. An initial ¹H NMR spectrum was recorded to establish a starting ratio between starting alkylidene vs anthracene. The NMR tube was attached to a Schlenk line and degassed (4 freeze-pump-thaw cycles), then allowed to thaw under ethylene atmosphere. After 3 min, the tube was sealed, shaken, and the timer started. A ¹H NMR spectrum was immediately recorded to confirm the presence of ethylene ($\delta = 5.25$ ppm). Additional spectra were recorded periodically to track the disappearing of starting material and appearing of products over time at room temperature, see Fig. S8. For conversion plot, see Fig. S7. The ¹H NMR spectrum after 60 min showing [Ru]=CHR and organic products, see Fig. S8.

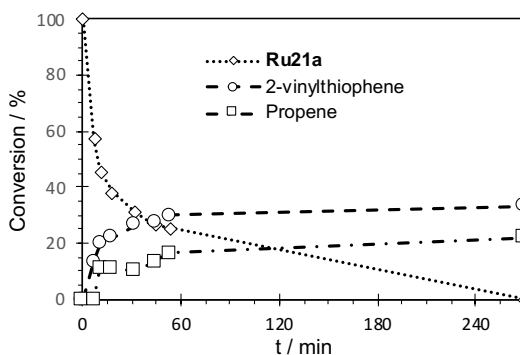


Fig. S7 Loss of precatalyst **Ru21a** with the formation of vinylthiophene and propene during the reaction with ethylene in C₆D₆ (see Fig. S8 and S9). Reaction was monitored by ¹H-NMR analysis relative to internal standard

During the reaction with ethylene, the liberation of vinylthiophene (C₅H₃S-CH₂: $\delta = 5.48, 4.89$ ppm) [6] indicates the initiation of the catalyst via non-productive metathesis. The propene (H₃CCHCH₂: $\delta = 5.71, 5.03, 4.97$ ppm) is a decomposition product of the unsubstituted MCB (see Fig. S8). The reduced amount of propene compared to vinylthiophene is due to the gas phase-solvation equilibrium within the J-Young NMR tube. The catalyst **Ru21a** is completely decomposed after 270 min. The relative fast decomposition of catalyst **Ru21a** in ethylene compared to the reaction with allylbenzene is another indicator that the reaction with allylbenzene is hindered by steric reasons. Computational analysis of the reaction indicates that decomposition via β -hydride elimination (formation of propene) and nucleophilic attack are energetically similar ($\Delta\Delta G^\ddagger = 0.2$ kcal mol⁻¹, **Ru21a_TS22,24** vs **Ru21a_TS21,23**), see Scheme S8. and Table S7. Decomposition via nucleophilic attack would not release propene, thus explaining the low yield of it.

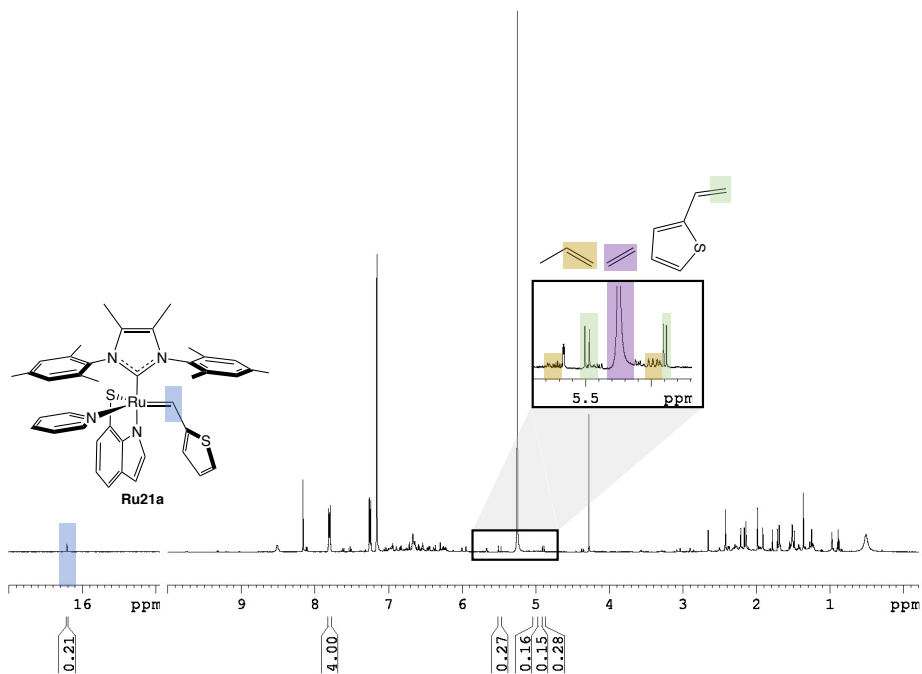


Fig. S8 ^1H NMR spectrum of reaction of catalyst Ru21a with ethylene, after 60 min. Inset shows the key organic products. The signals of 2-vinylthiophene and propene are in agreement with literature [6]. (C_6D_6 , 300.1 MHz)

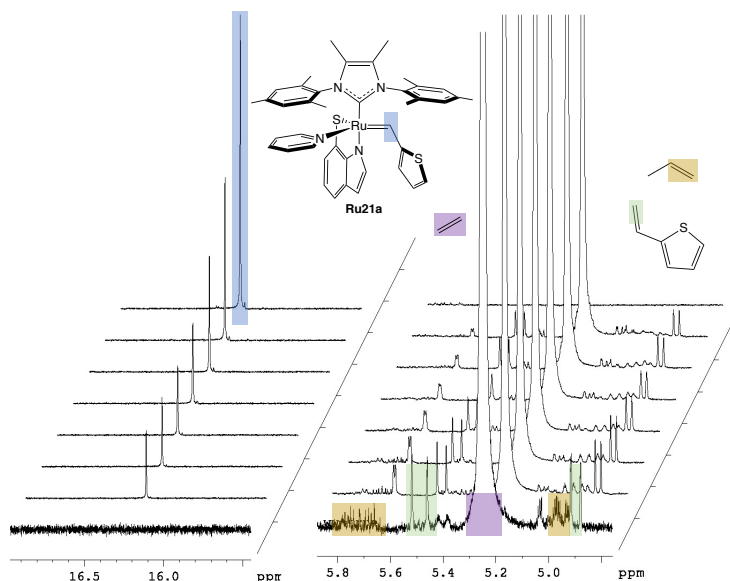


Fig. S9 Stacked ^1H NMR spectrum of reaction of catalyst **Ru21a** with ethylene. The signals of 2-vinylthiophene and propene are in agreement with literature [6]. (C_6D_6 , 300.1 MHz)

Self-Metathesis of Propene

In a 4 mL vial, catalyst **Ru21a** (7.5 mg, 0.01 mmol) and hexamethylbenzene (I.S., 1.6 mg, 0.01 mmol, 1 eq) were dissolved in 1 mL C_6D_6 (20 mM Ru). The resulting solution was filtered through a pipette filter stuffed with a Kimwipe to remove any undissolved solids. 600 μL of this solution was transferred to a J-Young NMR tube. An initial ^1H NMR spectrum was recorded to establish a starting ratio between starting alkylidene vs hexamethylbenzene. The NMR tube was attached to a Schlenk line and degassed (4 freeze-pump-thaw cycles), then pressured with propene. The tube was sealed, shaken, and the timer started. A ^1H NMR spectrum was immediately recorded to confirm the presence of propene ($\delta = 5.72, 4.97$ and 1.54 ppm). Additional spectra were recorded periodically to track the disappearing of starting material and appearing of products (ethylene ($\delta = 5.25$ ppm), E-butene ($\delta = 5.38$ ppm) and Z-butene ($\delta = 5.48$ ppm)) over time. The selectivity was determined by the formation of E- and Z-butene in a quantitative ^1H -NMR experiment [8]. The experiment was repeated using **Ru21b** (7.6 mg, 0.01 mmol) and **Ru21c** (8.2 mg, 0.01 mmol), see Table S1.

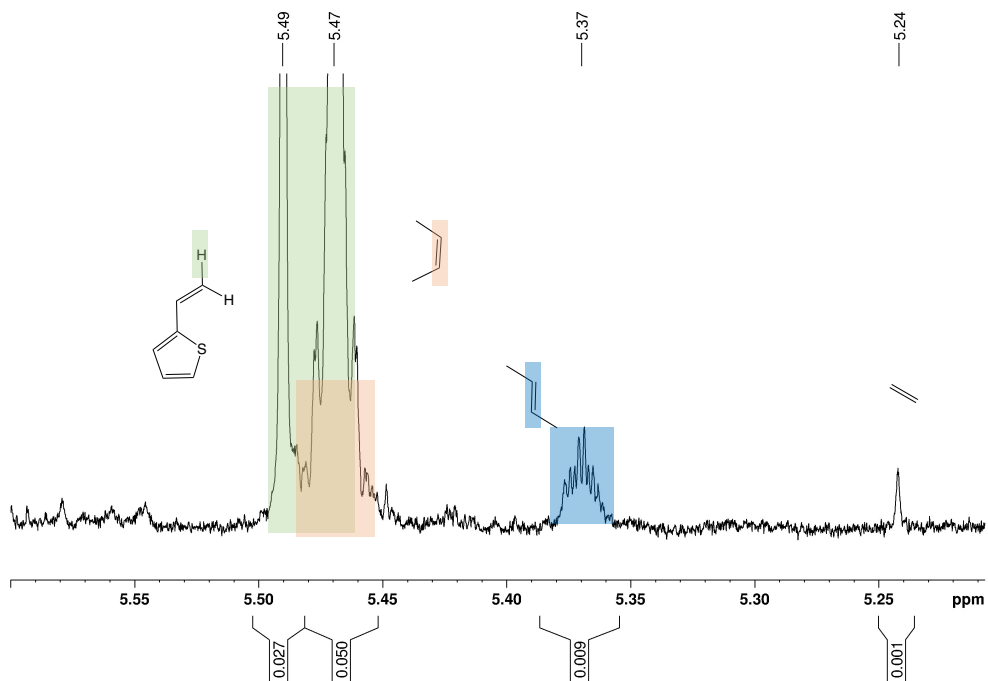


Fig. S10 ¹H NMR spectrum of reaction of catalyst **Ru21a** with propene. The signals of vinylthiophene, Z-Butene, E-Butene and ethylene are in agreement with literature [6,9]. Due to overlapping of 2-vinylpropene and Z-butene, Z-Butene (orange) was determined by the different between the two signals of the doublet of 2-vinylpropene (green) (C₆D₆, 850 MHz)

Table S1 The Stereoselectivity of Propene Metathesis Using Ru13 and Ru21a. No Butene Was Obtained using Ru21b and Ru21c

Entry	Catalyst	Selectivity ^a	$\Delta\Delta G_{(E/Z)}^\ddagger$ ^b	TON ^c
		E:Z	[kcal mol ⁻¹]	
1	Ru13	17:83	-0.9	-
2	Ru21a	23:77	-0.7	-
3	Ru21b	-	-	-
4	Ru21c	-	-	-

^a Selectivity was determined by the ratio of E-butene and Z-butene in solution, see Fig. S10. ^b Derived from the observed stereoselectivity via the Eyring equation. ^c Due to the low conversion, turnover numbers were not determined.

S3. Computational Methods

DFT calculations were performed with Gaussian 16 with revisions C.01 [10] using the built-in ultrafine grid for numerical integrations.

Geometry Optimization

Three different density functionals were considered for geometry optimization; see the below subsection on validation of the various computational approaches. The functionals considered for geometry optimization were: PBE [11] (Approach A), ω B97XD [12] (Approach B) and M06-L [13-15] (Approach C). All PBE calculations included Grimme's empirical D3 dispersion corrections [16], with revised Becke–Johnson damping parameters (labelled D3(MBJ) for brevity) [17]. The Stuttgart/Cologne 28-electron relativistic effective core potentials (ECP28MDF) [18] were used for Ru atoms, in conjunction with the corresponding correlation-consistent valence double- ζ plus polarization basis set augmented by diffuse functions (aug-cc-pVDZ-PP) [18], as obtained from the Stuttgart/Cologne basis set repository¹. Correlation-consistent, valence double- ζ plus polarization basis sets (cc-pVDZ [19] from the EMSL basis set exchange website) [20] were used for H, C, H and O atoms, whereas a corresponding quadruple- ζ plus polarization basis set (cc-pVQZ) [19] was used for S atoms.

Geometries were optimized using tight convergence criteria (max. force $1.5 \cdot 10^{-5}$ a.u., RMS force $1.0 \cdot 10^{-5}$ a.u., max. displacement $6.0 \cdot 10^{-5}$ a.u., RMS displacement $4.0 \cdot 10^{-5}$ a.u.), without symmetry constraints, using tighter convergence criteria for the self-consistent field (SCF) optimization procedure (RMS change in density matrix $< 1.0 \cdot 10^{-9}$, max. change in density matrix $= 1.0 \cdot 10^{-7}$), and with a spin multiplicity of 1. All stationary points were confirmed to be either minima (all-positive Hessian eigenvalues) or transition states (a single negative Hessian eigenvalue) by analytical calculation of the second derivatives, i.e., the Hessian matrix. Textbook procedures were used to calculate the translational, rotational, and vibrational components of the thermal corrections to enthalpies and Gibbs free energies within the ideal-gas, rigid-rotor, and harmonic oscillator approximations, with one exception: All frequencies below 100 cm^{-1} were shifted to 100 cm^{-1} when calculating the vibrational component of the entropy, which is often referred to as the quasi-harmonic oscillator approximation [15,21]. This approach is aimed at preventing breakdown (i.e., the asymptote corresponding to infinite entropy) of the harmonic approximation for low-frequency modes [22].

Single-Point Energy Calculations

The geometries obtained as described above were adopted in single-point energy calculations using the PBE [11] and M06-L [13-15] functionals in conjunction with the PCM [23] polarizable continuum solvent model, with default parameters for benzene as solvent. All PBE calculations included Grimme's empirical D3 dispersion corrections [16], with revised Becke–Johnson damping parameters (labelled D3(MBJ) for brevity) [17]. In all single-point calculations, the above basis set were extended to the valence quadruple- ζ level. Specifically, Ru was described by combining the 28-electron relativistic effective core potential (ECP28MDF) [18] with the corresponding correlation-consistent valence quadruple- ζ plus polarization basis set augmented by

¹ Energy-consistent Pseudopotentials of the Stuttgart/Cologne Group (<http://www.tc.uni-koeln.de/PP/clickpse.en.html>)

diffuse functions (aug-cc-pVQZ-PP) [18] from the Stuttgart/Cologne basis set repository [20]. The other atoms were described by correlation-consistent, valence quadruple- ζ plus polarization basis sets (cc-pVQZ [19] from the EMSL repository) [20]. The convergence criteria for the SCF procedure were relaxed in single-point calculations (RMS change in density matrix $< 1.0 \cdot 10^{-5}$, max. change in density matrix $< 1.0 \cdot 10^{-3}$).

Free Energies Calculations Including Standard State Correction

Free energies in solution were calculated from the following:

$$G_X = E_X + \Delta G_{Y,qh}^{T=298.15 K} + \Delta G_{1atm \rightarrow 1M}^{T=298.15 K},$$

where E_X is the SP energy calculated with the computational model X, where X = PBE-D3(MBJ)-PCM(Benzene), or M06L-PCM(Benzene), $\Delta G_{Y,qh}^{T=298.15 K}$, where Y = PBE- D3(MBJ), ω B97XD or M06L, is the thermal correction to the Gibbs free energy calculated at the geometry-optimization level with the quasi-harmonic oscillator approximation as described above, and $\Delta G_{1atm \rightarrow 1M}^{T=298.15 K}$ is the standard state correction from the ideal gas at 1 atm to a 1 M solution (but exhibiting infinite-dilution, ideal-gas-like behavior), which is equal to 1.89 kcal/mol at RT [24].

S4. Validation and Selection of the Computational Approach

Choice of Functional for Geometry Optimization

The design of an E-selective catalyst is delicate as the difference between the two rate-determining transition states between the E- and Z-pathway may be tiny. Therefore, three computational approaches, A, B, and C, were validated against the experimentally observed stereoselectivity of propene metathesis using the known catalyst **Ru13** (Table S2). The latter catalyst may be regarded as the parent of the thio-indolate catalysts designed in this work.

Approach A: Geometries were optimized using PBE-D3(MBJ)/cc-pVDZ. Single-point energy calculations were performed using PBE-D3(MBJ)/cc-pVQZ and M06-L/cc-pVQZ in conjunction with the PCM polarizable continuum solvent model to account for solvation effects using default parameters for benzene as solvent.

Approach B: Geometries were optimized using wB97XD/cc-pVDZ. Single-point energy calculations were performed using PBE-D3(MBJ)/cc-pVQZ and M06-L/cc-pVQZ in conjunction with the PCM polarizable continuum solvent model to account for solvation effects using default parameters for benzene as solvent.

Approach C: Geometries were optimized using M06L/cc-pVDZ. Single-point energy calculations were performed using PBE-D3(MBJ)/cc-pVQZ and M06-L/cc-pVQZ in conjunction with the PCM polarizable continuum solvent model to account for solvation effects using default parameters for benzene as solvent.

Table S2: The Stereoselectivity of Propene Metathesis Using Catalyst Ru13 as Predicted by Computational Approaches A-C.

Approach	Model ID	E [a.u.]	$\Delta G_{qh}^{T=298.15 K}$ [a.u.]	$E_{\text{PBE-D3(MBJ)-PCM(benzene)}}$ [a.u.]	$E_{\text{M06L-PCM(benzene)}}$ [a.u.]	$\Delta G_{\text{PBE-D3(MBJ)-PCM(benzene)}}$ [kcal/mol]	$\Delta G_{\text{M06L-PCM(benzene)}}$ [kcal/mol]
A	Ru13_TS4,5E	-3161.106433	0.535016	-3161.083020	-3163.200665	0.0	0.0
	Ru13_TS4,5Z	-3161.108143	0.535273	-3161.083373	-3163.202574	-0.2	-1.2
B	Ru13_TS4,5E	-3162.956002	0.560327	-3161.060050	-3163.187954	0.0	0.0
	Ru13_TS4,5Z	-3162.956957	0.559158	-3161.062104	-3163.189691	-1.3	-1.1
C	Ru13_TS4,5E	-3163.265390	0.553430	-3161.066822	-3163.194177	0.0	0.0
	Ru13_TS4,5Z	-3163.267741	0.553282	-3161.067650	-3163.196344	-0.5	-1.4

The suffix **TS4,5E** indicates the rupture for the MCB forming E-Butene and **TS4,5Z** for the formation of Z-Butene (see Scheme S2)

Expressed (via the Eyring equation) as a difference in free energy between the rate-determining transition states leading to (Z)- or (E)-2-butene, i.e., $\Delta\Delta G_{(E/Z)}^\ddagger = \Delta G_{Z}^\ddagger - \Delta G_{E}^\ddagger$, the experimentally determined stereoselectivity of propene metathesis using catalyst **Ru13** is $\Delta\Delta G_{(E/Z)}^\ddagger = -0.9$ kcal mol⁻¹(see

Table S1). Using Approach B, PBE and M06L predict E-selectivities that are slightly too high but quite consistent. Therefore, ω B97XD was chosen as the standard functional for geometry optimization in this work.

Choice of Functional for Single-Point Calculations

Based on the experimentally observed stereoselectivity of catalyst **Ru13**, Approach B, i.e. the ω B97XD functional, was chosen for geometry optimization. Among the two functionals tested for single-point energy calculations, PBE and M06L, only PBE predicts the correct orientation of the bidentate S,N-ligand in the catalyst precursor, i.e., M06L predicts Ru21a' to have lower energy than Ru21a (see Table S6). Moreover M06L also predicts, in contrast to experimental observation,[5] Ru18 to initiate faster than Ru13 (see Table S4). Therefore, PBE, in conjunction with empirical dispersion corrections to give the overall functional here labeled PBE-D3(MBJ), was chosen as the standard functional for single-point energy calculations in the present work.

S5. Computational Results

Calculated Barrier Heights and Kinetic Feasibility: Initial Considerations

Relying on transition-state theory, the relation between the rate constant k of a reaction and the corresponding activation free energy, ΔG^\ddagger is given by the Eyring equation as $k = \frac{k_B T}{h} e^{-\frac{\Delta G^\ddagger}{RT}}$ or, equivalently, as $\Delta G^\ddagger = -RT \ln\left(\frac{kh}{k_B T}\right)$. We may thus use the activation free energy as an indicator of the feasibility of a chemical reaction, i.e., whether it can be expected to occur within the time available. For example, for a unimolecular reaction ($A \rightarrow B$), the relation between the half-life $t_{1/2}$ and reaction rate k is $k = \frac{t_{1/2}}{\ln 2}$. The activation free energy corresponding to different half-lives is thus given by Equation 2.

$$\Delta G^\ddagger = -RT \ln\left(\frac{\ln(2) h}{k_B T t_{1/2}}\right) \quad (\text{Eq. 2})$$

Examples of pairs of half-lives and activation free energies that obey Equation 2 are given in Table S3.

Table S3 Examples of Pairs of Half-Lives $t_{1/2}$ and Activation Free Energies ΔG^\ddagger obeying Equation 2

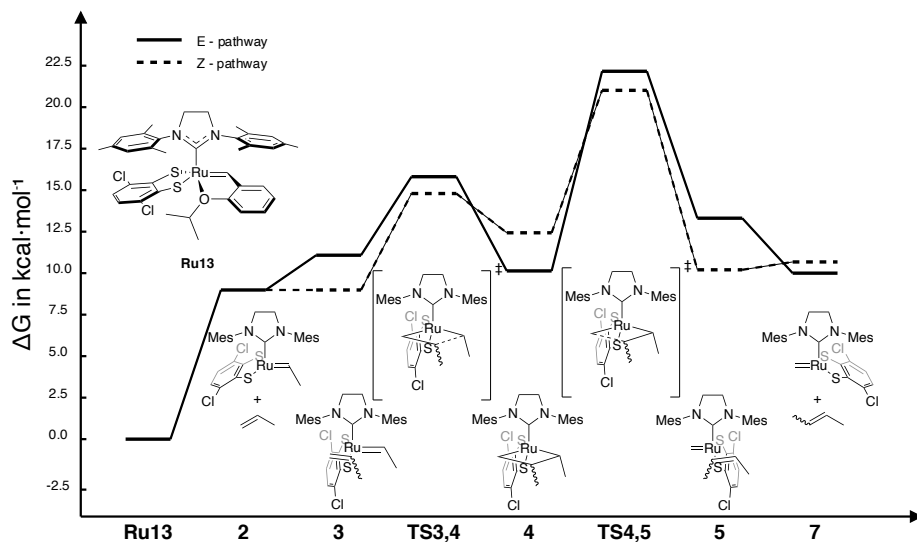
Half life $t_{1/2}$	ΔG^\ddagger [kcal mol ⁻¹]
2 h	22.9
1 d	24.4
7 d	25.5
31 d	26.4
365 d	27.9

with $T = 298 \text{ K}$, $R = 1.985 \cdot 10^{-3} \text{ kcal K}^{-1} \text{ mol}^{-1}$, $h = 6.626 \cdot 10^{-34} \text{ J s}$, $k_B = 1.380 \cdot 10^{-23} \text{ J K}^{-1}$

The estimates in Table S3 suggest that reactions start to become impractical at room temperature when the activation free energy rises above 25 kcal/mol. Allowing for some inaccuracies in DFT-calculated relative free energies, we may therefore expect reactions with DFT-estimated activation free energies above 30 kcal/mol to be unrealistic at room temperature [25].

Computational Results for Complexes Ru13, Ru18 and Ru19a-c.

Scheme S2 Energy Profile for the Productive Metathesis of Ru13 with Propene leading to (E)-2-Butene (full) and (Z)-2-Butene (dashed)



Scheme S3 During the Regeneration of the Active Species Ru13_2, the Catalyst is prone to decompose via nucleophilic attack Ru13_TS18,19

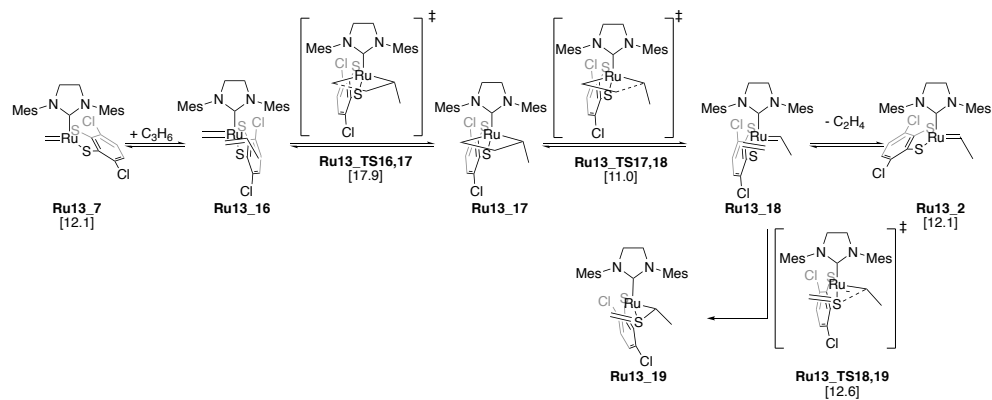


Chart S1 Additional Structure for Precursor Ru18 (a) and Ru13 (b-d), Showing the Unsubstituted MCB and Decomposition via c) β -Hydride Elimination and d) Nucleophilic Attack during Productive Metathesis

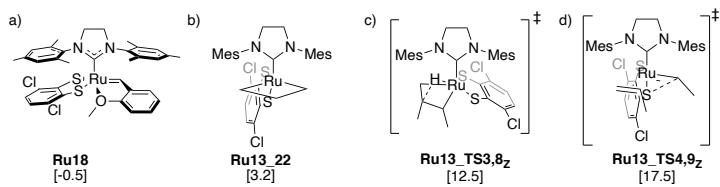
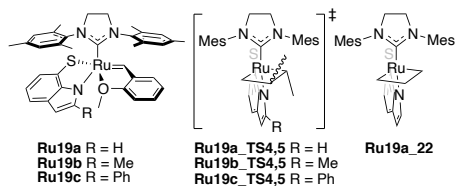


Table S4 Gibbs Free Energies Calculated for Propene Metathesis Using Catalyst Ru13 Displayed in Scheme S2, Scheme S3 and Chart S1^a

Model ID	$E_{\omega B97XD}$ [a.u.]	$\Delta G_{\omega B97XD,qh}^{T=298.15 K}$ [a.u.]	$E_{PPBE-D3M(BI)-PCM(benzene)}$ [a.u.]	$E_{M06L-PCM(benzene)}$ [a.u.]	$\Delta G_{PPBE-D3M(BI)-PCM(benzene)}$ [kcal/mol] ^a	$\Delta G_{M06L-PCM(benzene)}$ [kcal/mol] ^a
Ru13	-3429.915882	0.618805	-3428.443990	-3430.839043	0.0	0.0
Ru18	-3351.301249	0.562961	-3349.889345	-3352.190338	-0.5	4.4
Ru13_2	-3045.082345	0.477603	-3043.816001	-	9.0	-
Ru13_3E	-3162.976186	0.564371	-3161.632534	-	11.1	-
Ru13_3Z	-3162.974397	0.560697	-3161.632110	-	9.0	-
Ru13_TS3,4E	-3162.967268	0.560938	-3161.621480	-	15.8	-
Ru13_TS3,4Z	-3162.968273	0.560583	-3161.622805	-	14.8	-
Ru13_4E	-3162.980512	0.560326	-3161.630040	-	10.1	-
Ru13_4Z	-3162.979753	0.564127	-3161.630109	-	12.4	-
Ru13_TS4,5E	-3162.956002	0.560327	-3161.610703	-	22.2	-
Ru13_TS4,5Z	-3162.956957	0.559158	-3161.611420	-	21.0	-
Ru13_5E	-3162.968283	0.561501	-3161.626063	-	13.3	-
Ru13_5Z	-3162.973114	0.560132	-3161.629651	-	10.2	-
Ru13_7E	-3005.766850	0.451525	-3004.528870	-	11.9	-
Ru13_7Z	-3005.766850	0.451525	-3004.528870	-	12.6	-
Ru13_TS3,8Z	-3162.963995	0.561112	-3161.619072	-	17.5	-
Ru13_TS4,9Z	-3162.964283	0.561428	-3161.627230	-	12.5	-
Ru13_TS16,17	-3123.651078	0.533234	-3122.334439	-	17.9	-
Ru13_TS17,18	-3123.661517	0.532916	-3122.345132	-	11.0	-
Ru13_TS18,19	-3123.658421	0.532949	-3122.342640	-	12.6	-
Ru13_22	-3084.369671	0.509590	-3083.078212	-	3.2	-
Isopropoxystyrene	-502.669414	0.186608	-502.395132	-502.947572	-	-
Methoxystyrene	-424.051895	0.133273	-423.842229	-424.308368	-	-
Propene	-117.870108	0.054855	-117.790929	-117.939778	-	-
Ethylene	-78.560878	0.028971	-78.508999	-78.612024	-	-

a See Scheme S2, Scheme S3 and Chart S1 for molecular structures.

Table S5 Gibbs Free Energies calculated for the Rate-Determining Transition State (Rupture of the Metallacyclobutane) of the *E*- and *Z*-pathway of Propene Metathesis of complex Ru19a-c



Model ID	Substituent R	$E_{\omega\text{B97XD}}$ [a.u.]	$\Delta G_{\omega\text{B97XD},q/h}^{T=298.15\text{ K}}$ [a.u.]	$E_{\text{PBE-D3M(BJ)-PCM(benzene)}}$ [a.u.]	$E_{\text{M06L-PCM(benzene)}}$ [a.u.]	$\Delta G_{\text{PBE-D3M(BJ)-PCM(benzene)}}$ [kcal/mol]	$\Delta G_{\text{M06L-PCM(benzene)}}$ [kcal/mol]
Ru19a	H	-2165.396001	0.613910	-2164.387625	-2166.315982	0.0	0.0
Ru19a_22	H	-1898.470826	0.558601	-1897.584819	-1899.257749	-0.9	-3.8
Ru19a_TS4,5_E	H	-1977.055101	0.610232	-1976.115625	-1977.881986	17.9	13.8
Ru19a_TS4,5_Z	H	-1977.049754	0.609467	-1976.109430	-1977.875135	21.3	17.7
Ru19b	Me	-2204.703290	0.640500	-2203.665344	-2205.641347	0.0	0.0
Ru19b_TS4,5_E	Me	-2016.359743	0.636485	-2015.391014	-2017.206420	19.1	14.2
Ru19b_TS4,5_Z	Me	-2016.354106	0.636110	-2015.384219	-2017.199423	23.2	18.4
Ru19c	Ph	-2396.402809	0.692316	-2395.262202	-2397.437938	0.0	0.0
Ru19c_TS4,5_E	Ph	-2208.052638	0.687222	-2206.978894	-2208.991215	24.1	20.9
Ru19c_TS4,5_Z	Ph	-2208.032632	0.686810	-2206.960226	-2208.973542	35.5	31.8

Computational Results for Complexes Ru21

The Catalyst Precursors Ru21a-c. A minor, constant alkylidene resonance $\delta = 15.38$ ppm always occurred alongside the resonance of **Ru21a**, in a 5:95 ratio. The minor component could not be isolated, and its identification via experimental methods (NMR, MS, X-ray) was thus not possible. The structure of this component was, instead, inferred with the help of DFT calculations and NOESY experiment (Fig. S1). The NOESY experiment shows that the two alkylidene species are in equilibrium with each other in solution.

The most obvious candidate for this component (labeled **Ru21a'**) is that of an isomer with the S,N ligand rotated compared to **Ru21a**, i.e, an isomer with the thiolate sulfur atom trans, and the indolate nitrogen atom cis, to the NHC. Indeed, DFT predicts a $\Delta G_{\text{Ru21a'}/\text{Ru21a}}$ (1.9 kcal mol⁻¹, Table S6) almost identical to that of the NOESY experiments ($\Delta G_{7a'/7a}^{\text{Exp}} = 1.8$ kcal mol⁻¹).

No corresponding minor component was observed in the ¹H NMR spectra of **Ru21b** and **Ru21c**, which is in agreement with the much lower DFT-predicted stability for the rotated S,N-ligands in these complexes ($\Delta G_{\text{Ru21b'}/\text{Ru21b}} = 4.0$ kcal mol⁻¹ and $\Delta G_{\text{Ru21c'}/\text{Ru21c}} = 11.3$ kcal mol⁻¹). In both **Ru21b'** and **Ru21c'**, the larger substituent at position 2 of the indole ring experiences substantial steric repulsion against NHC mesityl-groups.

Table S6 Gibbs Free Energies of Catalysts Ru21a-c and their Isomers

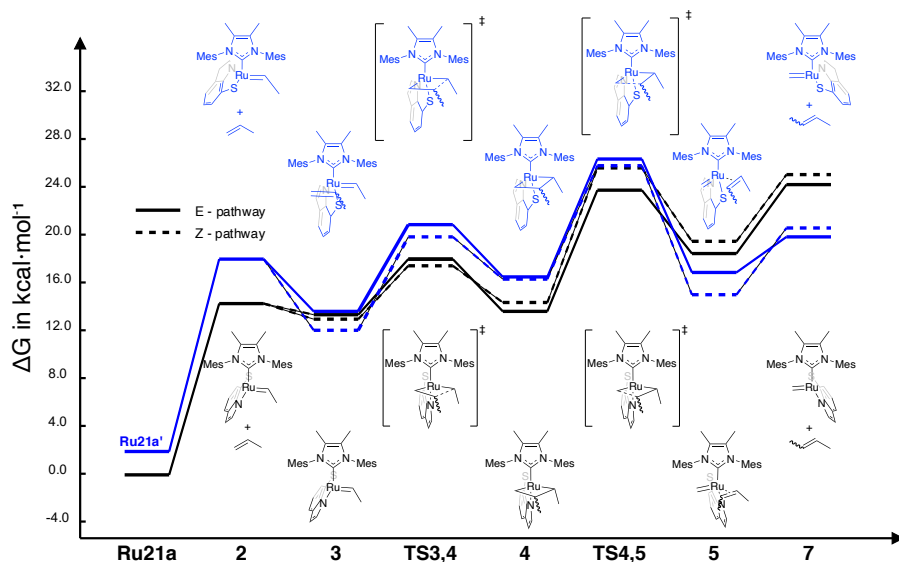
Model ID	$E_{\omega\text{B97XD}}$ [a.u.]	$\Delta G_{\omega\text{B97XD},q/h}^{T=298.15\text{K}}$ [a.u.]	$E_{\text{PBE-D3M(BJ)-PCM}(\text{benzene})}$ [a.u.]	$E_{\text{M06L-PCM}(\text{benzene})}$ [a.u.]	$\Delta G_{\text{PBE-D3M(BJ)-PCM}(\text{benzene})}$ [kcal/mol] ^a	$\Delta G_{\text{M06L-PCM}(\text{benzene})}$ [kcal/mol] ^a
Ru21a	-2697.355932	0.664475	-2696.109762	-2698.343345	0.0	0.0
Ru21a'	-2697.360618	0.666795	-2696.109034	-2698.346686	1.9	-0.6
Ru21b	-2736.665839	0.691396	-2735.390335	-2737.672841	0.0	0.0
Ru21b'	-2736.667085	0.692509	-2735.385095	-2737.674362	4.0	-0.3
Ru21c	-2928.362067	0.741391	-2926.983308	-2929.463517	0.0	0.0
Ru21c'	-2928.353369	0.744667	-2926.968584	-2929.453291	11.3	8.5

Catalytic Cycle and Decomposition Reactions. Low catalytic activity and low turnover numbers were obtained in metathesis experiments using one of the **Ru21** compounds (the mixture of isomers **Ru21a/Ru21a'**). Surprisingly, in contrast to the E-selectivity initially predicted for the thio-indolate-coordinated catalysts **Ru19a** and **Ru21a**, the **Ru21a/Ru21a'** mixture gave ca. 73% (Z)-2-butene in propene metathesis, which corresponds, via the Eyring equation, to a $\Delta\Delta G_{E/Z}^\ddagger = -0.7$ kcal mol⁻¹. To uncover possible explanations for the difference between the predicted and observed stereoselectivity, we have conducted additional DFT calculations.

One possibility is that the minor component **Ru21a'** of the **Ru21a/Ru21a'** mixture is responsible for the observed Z-selectivity. Propene metathesis using both these isomers was therefore studied in DFT calculations (Scheme S4), at the outset with the stereoselectivity estimated as the free energy difference between the transition states of cycloreversion, the elementary step typically found to be rate determining [26], to give (E)- and (Z)-2-butene, respectively.

This approach predicts **Ru21a** to be E-selective ($\Delta\Delta G_{TS4,5Z-TS4,5E}^\ddagger = 1.9$ kcal mol⁻¹) and **Ru21a'** to be weakly Z-selective ($\Delta\Delta G_{TS4,5'Z-TS4,5'E}^\ddagger = -0.5$ kcal mol⁻¹). The selectivity predicted for **Ru21a'** is close to that experimentally observed for the **Ru21a/Ru21a'** mixture, suggesting that the metathesis performed by the mixture might be due to **Ru21a'** rather than to the intended isomer **Ru21a**.

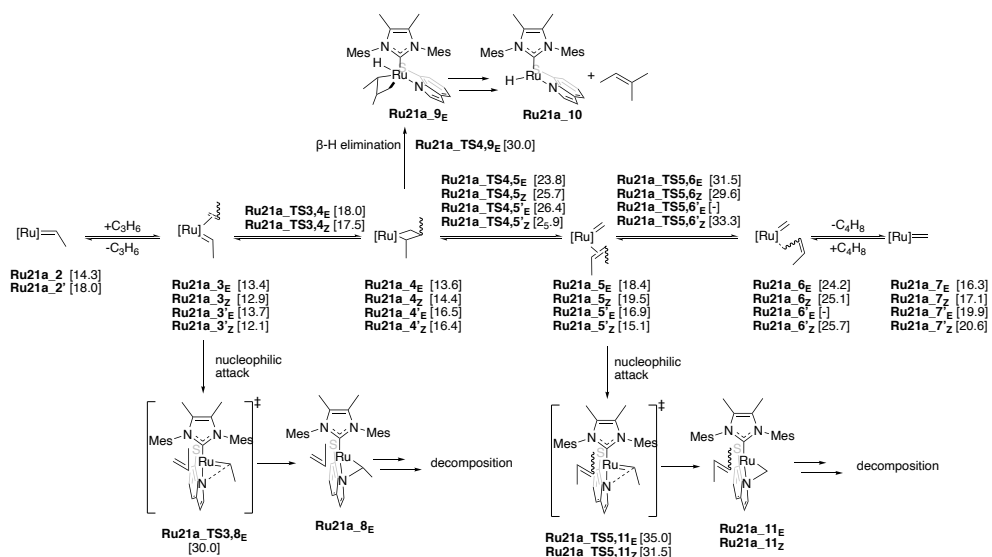
Scheme S4 Energy Profile for the Productive Metathesis of Ru21a (black) and Ru21a' (blue) with Propene Leading to (E)-2-butene (full) and (Z)-2-butene (dashed)



However, for the unintended isomer **Ru21a'** to be the dominating metathesis-active catalyst one of the following two requirements must be fulfilled: (i) **Ru21a** decomposes fast compared to **Ru21a'**, or (ii) the rate-determining barrier to propene metathesis using **Ru21a'** must be lower than that of **Ru21a**, so that **Ru21a'** is the dominating catalyst even in the presence of intact **Ru21a**. The extent to which either of the two requirements is fulfilled is discussed in the following:

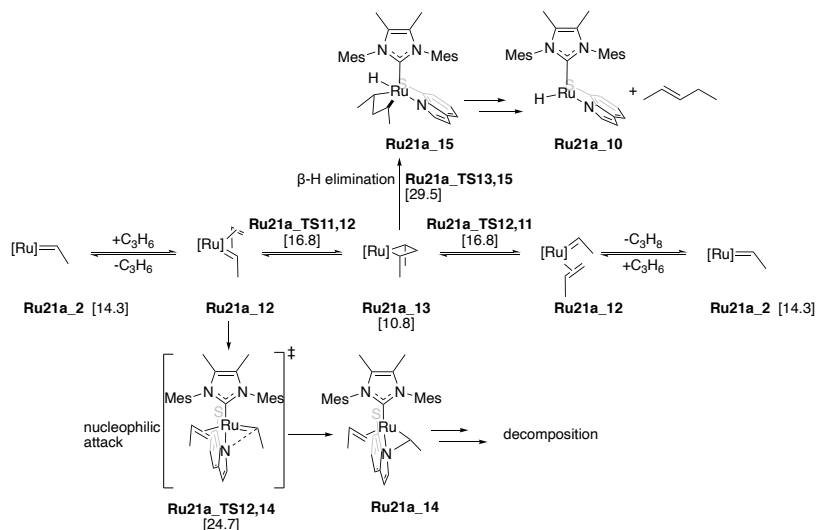
A range of decomposition modes were investigated for **Ru21a** and **Ru21a'**, covering β -H elimination [27,28] and nucleophilic attack of the thio-indolate ligand on the alkylidene [7] during productive (Scheme S5) and non-productive metathesis (Scheme S6), regeneration of the ethylidene from the methylidene species (Scheme S7) as well as during and after the formation of the unsubstituted MCB (Scheme S8). These calculations show, in agreement with experiments, that the decomposition via β -H elimination is favorable for the unsubstituted MCB (**Ru21a_TS22,24** vs **Ru21a_TS21,23**, Scheme S8), but it becomes more difficult with an increasing number of substituents around the MCB, hampering the distortion of the MCB necessary for hydride elimination.

Scheme S5 Free Energies of Productive Propene Metathesis Calculated Relative to Ru21a and Ru21a', respectively

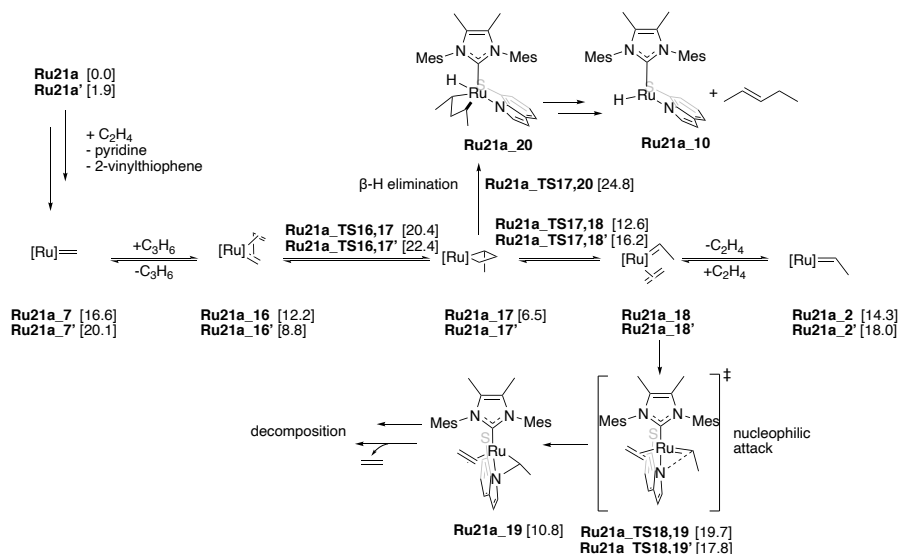


Isomers with the unintended orientation of the bidentate S,N-thio-indolate ligand (i.e., with S positioned trans to the NHC ligand) are indicated with an apostrophe ('). Isomers of the E- and Z-pathways are labeled using an E- and Z superscript suffix, respectively.

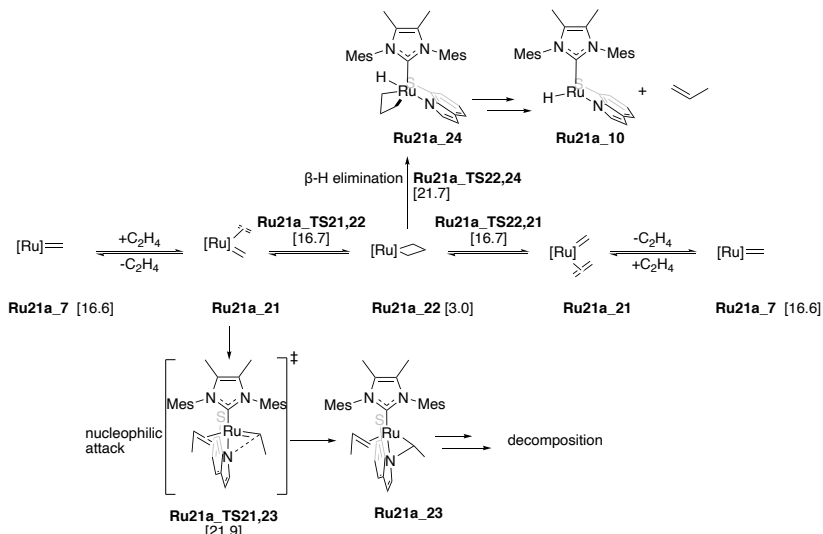
Scheme S6 Non-Productive Propene Metathesis (Ethylidene Exchange) and Associated Decomposition Reactions for Ru21a_2



Scheme S7 Regeneration of Ru21a_2 and Ru21a_2' from Methylidene Species, and Associated Decomposition Reactions



Scheme S8 Formation and Decomposition of the Unsubstituted MCB by Reacting Methylidene Ru21a_7 with Ethylene



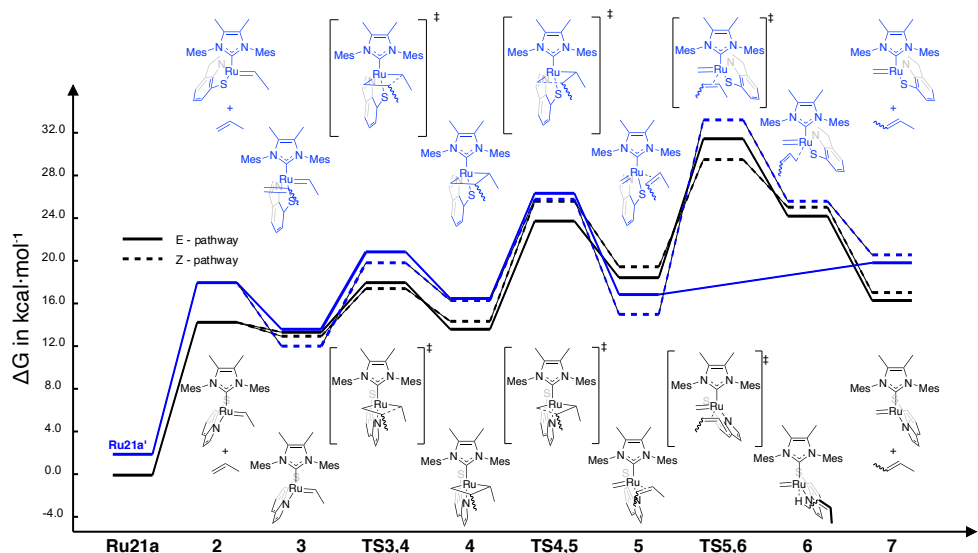
The slightly lower barrier for β-H elimination (via **Ru21a_TS21,23**) compared to that of the nucleophilic attack (via **Ru21a_TS20,22**) is consistent with propene being observed when **Ru21a** is reacted with ethylene.

For the productive and non-productive metathesis as well as for the ethylidene regeneration step, the calculations predict nucleophilic attack (via **Ru21a_TS3,8_E**, **Ru21a_TS5,11_E**, **Ru21a_TS5,11_Z**, **Ru21a_TS12,14** and **Ru21a_TS18,19**, Scheme S5-S8) to be the more important than β-H elimination (via **Ru21a_TS4,9_E** and **Ru21a_TS,24**, Scheme S5 and S8). Furthermore, nucleophilic attack via **Ru21a_TS18,19** is presumable the major decomposition pathway, since formation of **Ru21a_19** releases ethylene (Scheme S8). The free ethylene may react with a second **Ru21a_2** to form **Ru21a_18**, leading to autocatalytic decomposition of the catalyst. While this might explain the fast catalyst decomposition, it does not explain the observed *Z*-selectivity. With the unintended ligand orientation, the barrier to decomposition (via **Ru21a_TS18,19'**) is 1.9 kcal/mol lower than via **Ru21a_TS18,19**, and, more generally, no decomposition reaction has been found to be faster for the intended ligand orientation.

Calculations on closely related dithiolate-coordinated catalysts show that the barrier to rotation of the *S,S*-ligands are low (ca. 8 kcal/mol vs the 14-electron complex) [29] in four-coordinate 14-electron complexes and high in five-coordinate 16-electron complexes [5]. The observed **Ru21a/Ru21a'** equilibrium thus probably involves pyridine dissociation, facile ligand rotation in the four-coordinate, 14-electron complex, followed by re-binding of pyridine. Judged from the barriers to cycloreversion, the olefin metathesis pathway offered by the intended isomer **Ru21a** (with a barrier to cycloreversion $\Delta G_{TS4,5E}^\ddagger = 23.8$ kcal/mol vs **Ru21a**) is preferred, by 2.1 kcal/mol, relative to that of the unintended isomer **Ru21a'** (with a barrier to cycloreversion $\Delta G_{TS4,5'Z}^\ddagger = 25.9$ kcal/mol). Thus, if **Ru21a'** is the dominating metathesis catalyst in the mixture and responsible

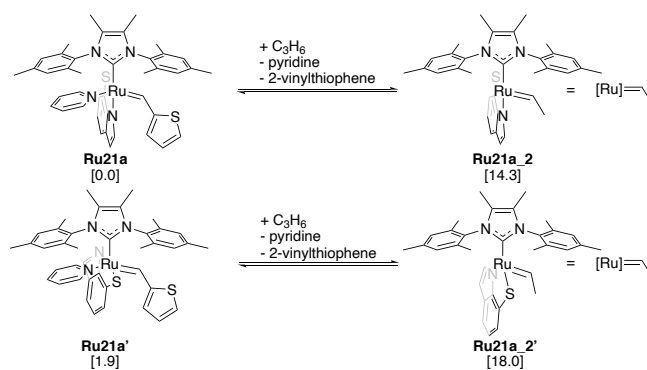
for the observed Z-selectivity, another elementary step than that of cycloreversion must be rate limiting, at least for **Ru21a**. A candidate step is the dissociation of the product olefin from the π -complexes **Ru21a_5** and **Ru21a_5'** (Scheme S9). These product π -complexes are already high in energy, with a clear preference (>3 kcal/mol) for the Z-configured **Ru21a_5'z** over the E-configured **Ru21a_5e**. Indeed, the dissociation of 2-butene from **Ru21_5** is rate-limiting for both **Ru21a** and **Ru21a'** (see Scheme S9).

Scheme S9 Complete Energy Profile for the Productive Metathesis of Ru21a (black) and Ru21a' (blue) with Propene Leading to (E)-2-butene (full) and (Z)-2-butene (dashed) Including the Transition State for 2-butene Dissociation



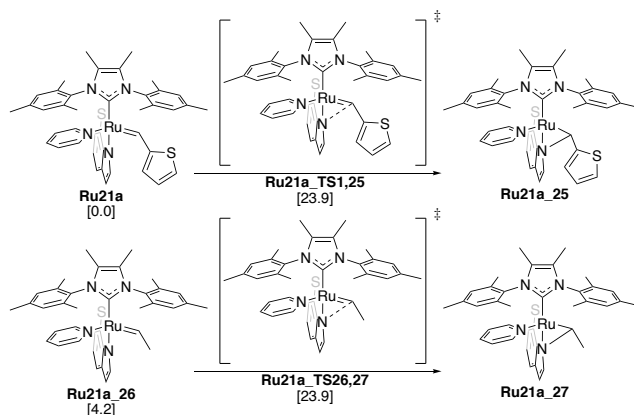
However, the DFT calculations show that the dissociation of (Z)-2-butene is favored from the intended **Ru21a** (with a barrier for dissociation of $\Delta G_{TS5,6z}^\ddagger = 29.6$ kcal/mol vs **Ru21a**) by nearly 4 kcal/mol relative to the unintended isomer **Ru21a'** (with a barrier for dissociation of $\Delta G_{TS5,6'e}^\ddagger = 33.3$ kcal/mol; the corresponding transition state **TS5,6'e** could not be located) excluding the minor-component, unintended **Ru21a'** as an explanation for the experimentally observed Z-selectivity. Instead, the detailed DFT calculations predict **Ru21a** itself to be Z-selective. This unexpected selectivity is determined during product release, which is associated with a high barrier. This barrier thus explains both the low catalytic activity and the Z-selectivity recorded for **Ru21a**. Additionally, due to the high metathesis barrier, nucleophilic attack via **Ru21a_TS3,8** and **Ru21a_TS5,11** becomes competitive (Scheme S5), and this catalyst decomposition mode should further contribute to the low yields observed in the catalytic experiments.

Scheme S10 Initiation of Catalyst Ru21a and Ru21a' with Propene



Both **Ru21a** and **Ru21a₂** are lower in energy compared to the rotamer counterpart, **Ru21a'** and **Ru21a₂'**, respectively. Therefore, we assumed that the desired orientation of the thiolate-indolate ligand should be dominant during catalysis.

Scheme S11 Decomposition of the Catalyst Precursor Ru21a and the Corresponding Pyridine-stabilized Ethylidene Species Ru21a₂₅ via Nucleophilic Attack of the Thio-indolate ligand on the Alkylidene



Scheme S12 Initiation and Metathesis of Ru21a with Styrene and Allylbenzene

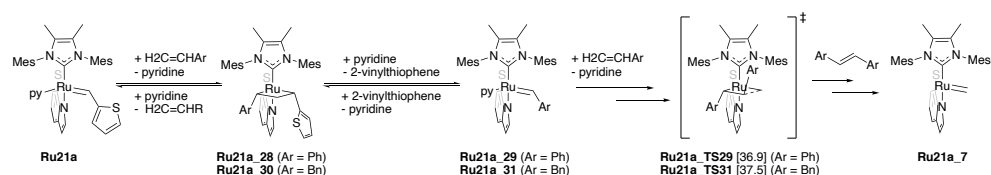


Table S7 Gibbs Free Energies of Catalyst Ru21a and Ru21a' in Olefin Metathesis (Scheme S4-12)

Model ID	E_{totB97XD} [a.u.]	$\Delta G_{\text{totB97XD},qh}^{T=298.15\text{ K}}$ [a.u.]	$E_{\text{PBE-D3M(BJ)-PCM(benzene)}}$ [a.u.]	$\Delta G_{\text{PBE-D3M(BJ)-PCM(benzene)}}$ [kcal/mol] ^a
Ru21a	-2697.355932	0.664475	-2696.109762	0.0
Ru21a'	-2697.360618	0.666795	-2696.109034	1.9
Ru21a_2	-1936.599244	0.557204	-1935.685517	14.3
Ru21a_2'	-1936.596176	0.557561	-1935.679892	18.0
Ru21a_3E	-2054.490362	0.639216	-2053.501974	13.4
Ru21a_3Z	-2054.491931	0.639149	-2053.502621	12.9
Ru21a_3'E	-2054.496890	0.641585	-2053.503787	13.7
Ru21a_3'Z	-2054.498186	0.641000	-2053.505748	12.1
Ru21a_TS3,4E	-2054.488530	0.640266	-2053.495739	18.0
Ru21a_TS3,4Z	-2054.487601	0.639020	-2053.495251	17.5
Ru21a_TS3,4'E	-2054.487845	0.641485	-2053.492400	20.8
Ru21a_TS3,4'Z	-2054.487962	0.640969	-2053.493519	19.8
Ru21a_4E	-2054.504418	0.643615	-2053.505965	13.6
Ru21a_4Z	-2054.501219	0.642821	-2053.504033	14.4
Ru21a_4'E	-2054.503723	0.644210	-2053.501999	16.5
Ru21a_4'Z	-2054.502650	0.644755	-2053.502665	16.4
Ru21a_TS4,5E	-2054.477152	0.639007	-2053.485211	23.8
Ru21a_TS4,5Z	-2054.472273	0.637626	-2053.480792	25.7
Ru21a_TS4,5'E	-2054.478071	0.641170	-2053.483118	26.4
Ru21a_TS4,5'Z	-2054.478310	0.640906	-2053.483663	25.9
Ru21a_5E	-2054.483160	0.640503	-2053.495232	18.4
Ru21a_5Z	-2054.482927	0.640123	-2053.493143	19.5
Ru21a_5'E	-2054.489193	0.641082	-2053.498174	16.9
Ru21a_5'Z	-2054.492602	0.640976	-2053.500928	15.1
Ru21a_TS5,6E	-2054.468797	0.636473	-2053.470428	31.5
Ru21a_TS5,6Z	-2054.472557	0.634588	-2053.471556	29.6
Ru21a_TS5,6'E	-	-	-	-
Ru21a_TS5,6'Z	-2054.468627	0.634813	-2053.465778	33.3
Ru21a_6E	-2054.477492	0.635618	-2053.481121	24.2
Ru21a_6Z	-2054.478311	0.636813	-2053.480974	25.1

Ru21a_6'E	-	-	-	-
Ru21a_6'z	-2054.477038	0.636062	-2053.47924	25.7
Ru21a_7	-1897.284227	0.530006	-1896.398580	16.6
Ru21a_7'	-1897.280929	0.530301	-1896.393209	20.1
Ru21a_7E	-1897.284227	0.530006	-1896.398580	16.3
Ru21a_7z	-1897.284227	0.530006	-1896.398580	17.1
Ru21a_7'E	-1897.280929	0.530301	-1896.393209	19.9
Ru21a_7'z	-1897.280929	0.530301	-1896.393209	20.6
Ru21a_TS4,9E	-2054.473604	0.641711	-2053.478065	30.0
Ru21a_TS3,8E	-2054.466387	0.640816	-2053.477110	30.0
Ru21a_TS5,11E	-2054.456933	0.639644	-2053.467883	35.0
Ru21a_TS5,11z	-2054.461372	0.638397	-2053.472248	31.5
Ru21a_TS12,13	-2054.490549	0.640213	-2053.497524	16.8
Ru21a_13	-2054.507086	0.642073	-2053.509008	10.8
Ru21a_TS12,14	-2054.473914	0.639050	-2053.483851	24.7
Ru21a_TS13,15	-2054.471277	0.641354	-2053.478453	29.5
Ru21a_16	-2015.180436	0.613642	-2014.222266	12.2
Ru21a_16'	-2015.190804	0.614203	-2014.228295	8.8
Ru21a_TS16,17	-2015.171824	0.613631	-2014.209193	20.4
Ru21a_TS16,17'	-2015.172348	0.614061	-2014.206856	22.1
Ru21a_17	-2015.200702	0.615084	-2014.232697	6.5
Ru21a_TS17,18	-2015.183260	0.612693	-2014.220658	12.6
Ru21a_TS17,18'	-2015.181467	0.613576	-2014.215818	16.2
Ru21a_TS18,19	-2015.170107	0.612650	-2014.209362	19.7
Ru21a_TS18,19'	-2015.177554	0.614086	-2014.213688	17.8
Ru21a_19	-2015.202320	0.616426	-2014.227241	10.8
Ru21a_TS17,20	-2015.167037	0.612748	-2014.201205	24.8
Ru21a_TS21,22	-1975.862161	0.585097	-1974.930482	16.7
Ru21a_22	-1975.893731	0.588854	-1974.956018	3.0
Ru21a_TS21,23	-1975.851195	0.584605	-1974.921696	21.9
Ru21a_TS22,24	-1975.855492	0.584776	-1974.922133	21.7
Ru21a_TS1,25	-2697.322853	0.664852	-2696.072076	23.9
Ru21_26	-2184.852578	0.646098	-2183.814011	4.2
Ru21a_TS26,27	-2184.821662	0.645454	-2183.782032	23.9
Ru21a_TS29	-2437.859282	0.742683	-2436.665841	36.9
Ru21a_TS31	-2516.469924	0.798578	-2515.215479	37.5
Vinylthiophene	-630.360711	0.069869	-630.076561	-
Pyridine	-248.211971	0.062066	-248.088721	-
Styrene	-309.557280	0.103658	-309.388691	-
Allylbenzene	-348.530228	0.124270	-348.654961	-

a Relative to Ru21a

S4. NMR Spectra.

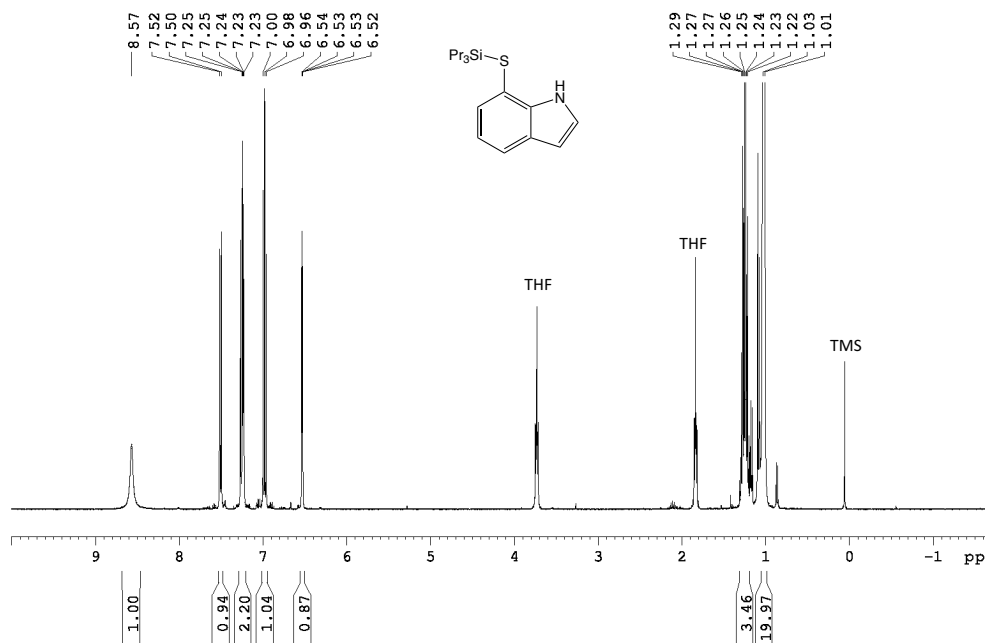


Fig. S11 ¹H NMR spectrum of L2a. Solvent impurities are indicated in the spectrum (CDCl₃, 300.1 MHz)

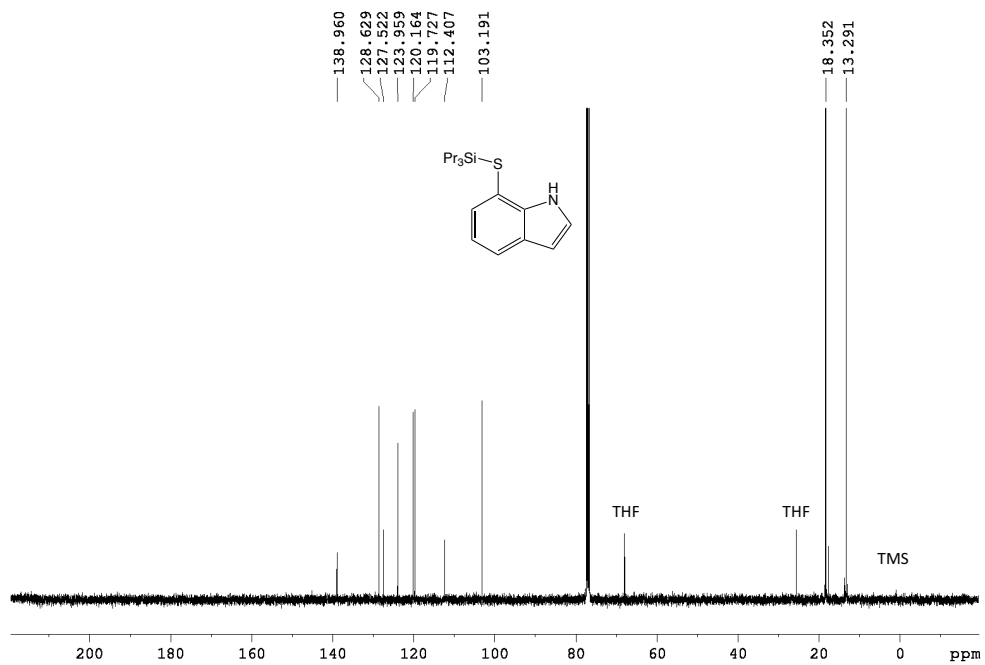


Fig. S12 ¹³C NMR spectrum of L2a (CDCl₃, 300.1 MHz)

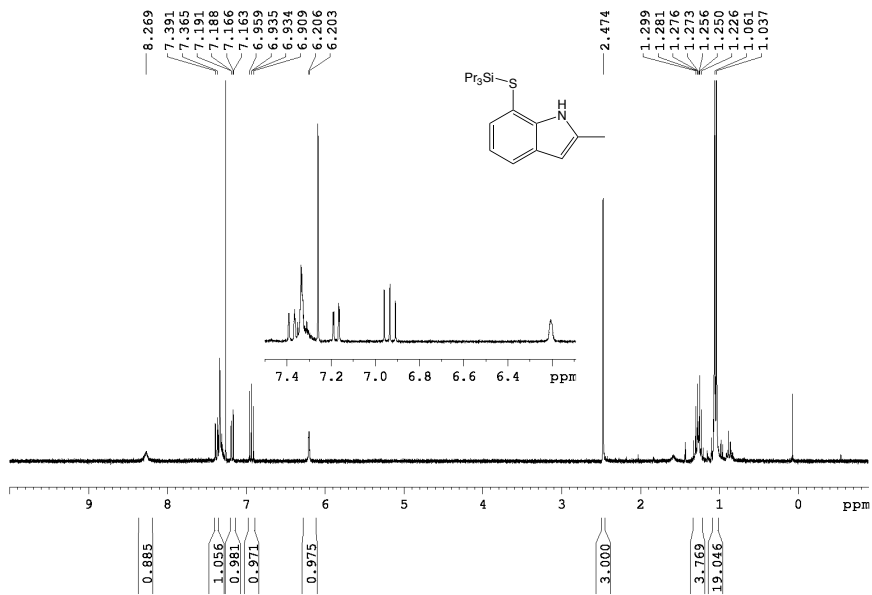


Fig. S13 ^1H NMR spectrum of **L2b** (CDCl_3 , 300.1 MHz)

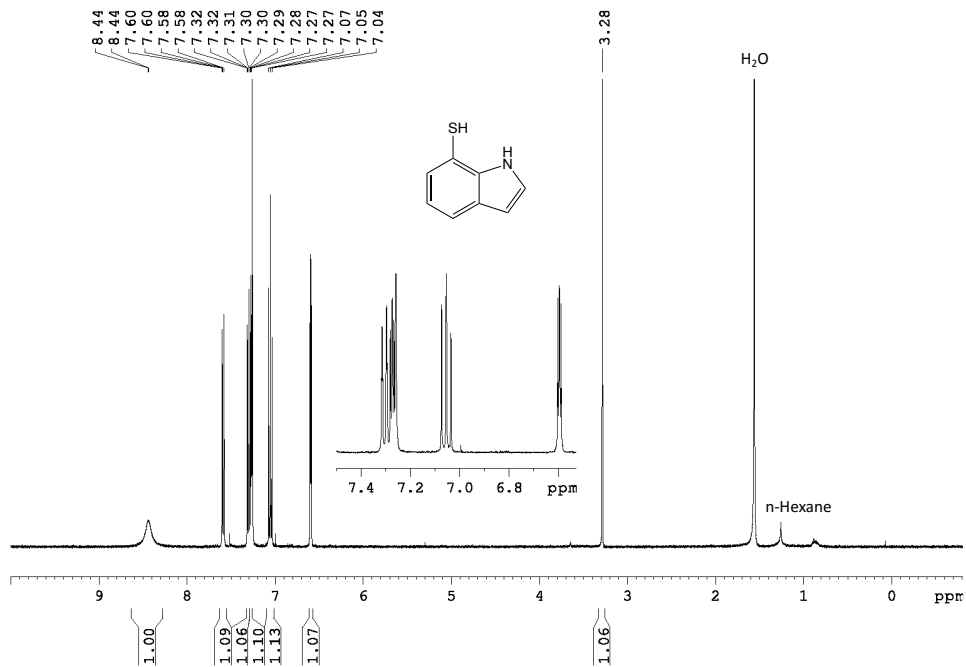


Fig. S14 ^1H NMR spectrum of **L3a** (CDCl_3 , 300.1 MHz)

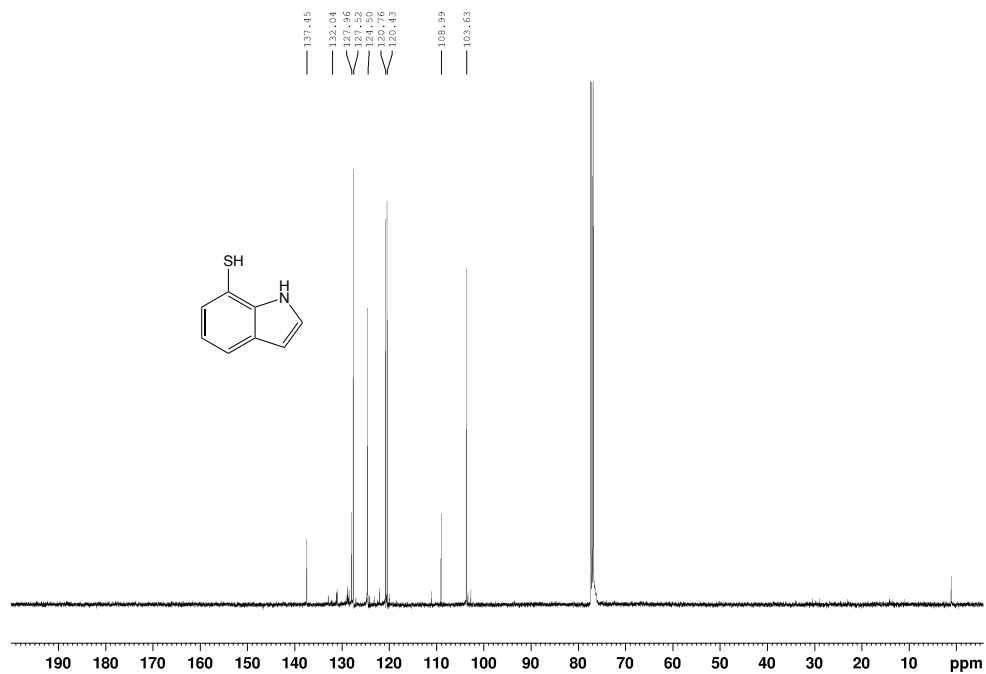


Fig. S15 ^{13}C NMR spectrum of **L3a** (CDCl_3 , 300.1 MHz)

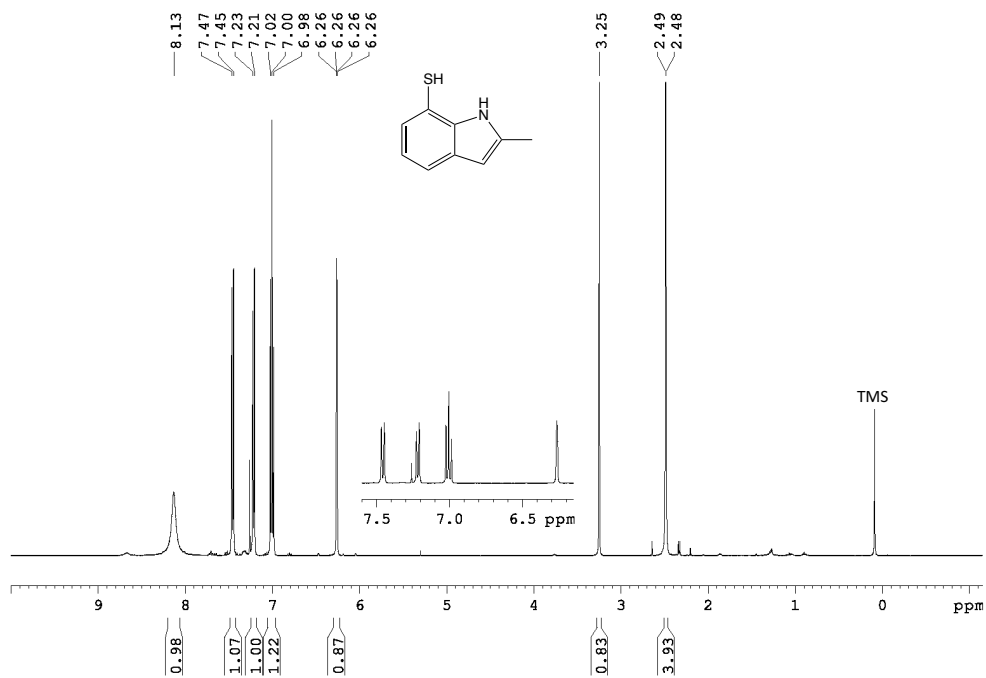


Fig. S16 ^1H NMR spectrum of **L3b** (CDCl_3 , 300.1 MHz)

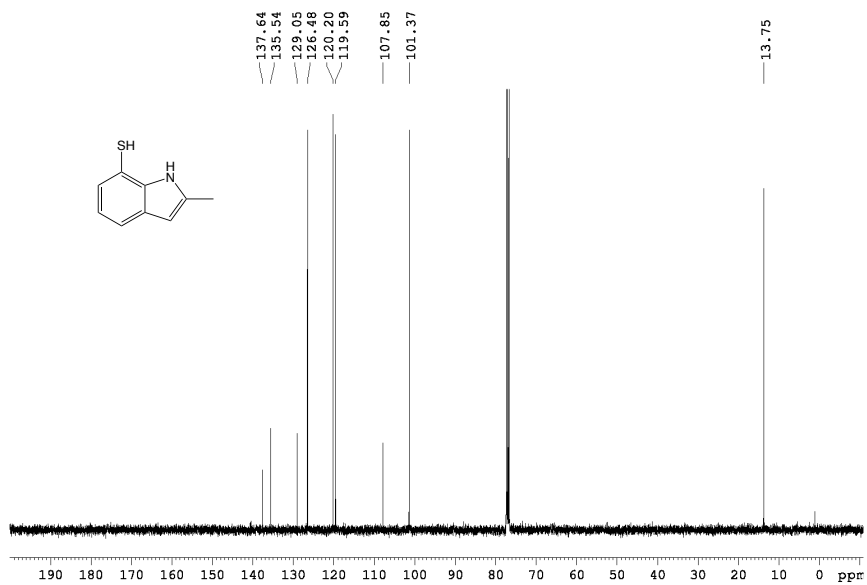


Fig. S17 ¹³C NMR spectrum of L3b (CDCl₃, 300.1 MHz)

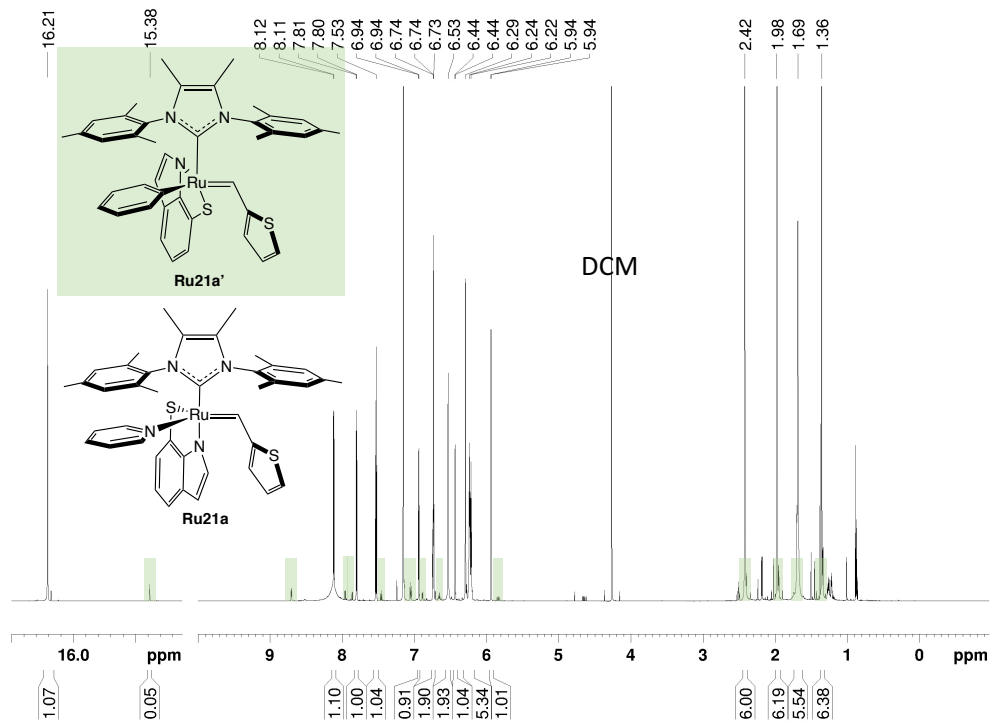


Fig. S18 ¹H NMR spectrum of **Ru21a** and **Ru21a'** (C₆D₆, 850 MHz)

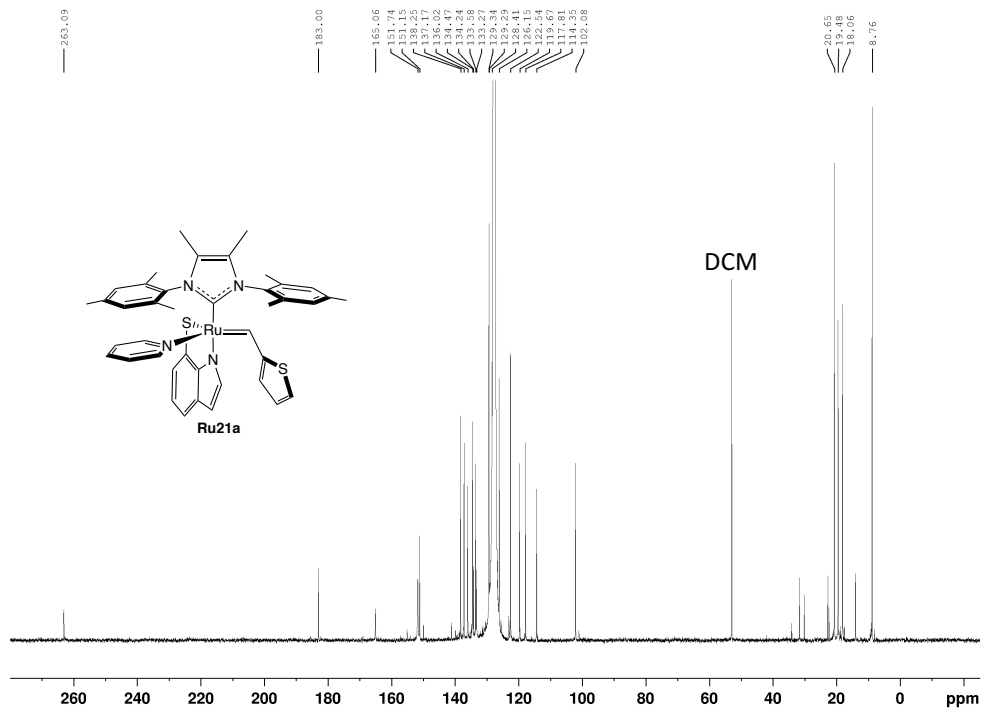


Fig. S19 ^{13}C NMR spectrum of Ru21a (C_6D_6 , 850 MHz)

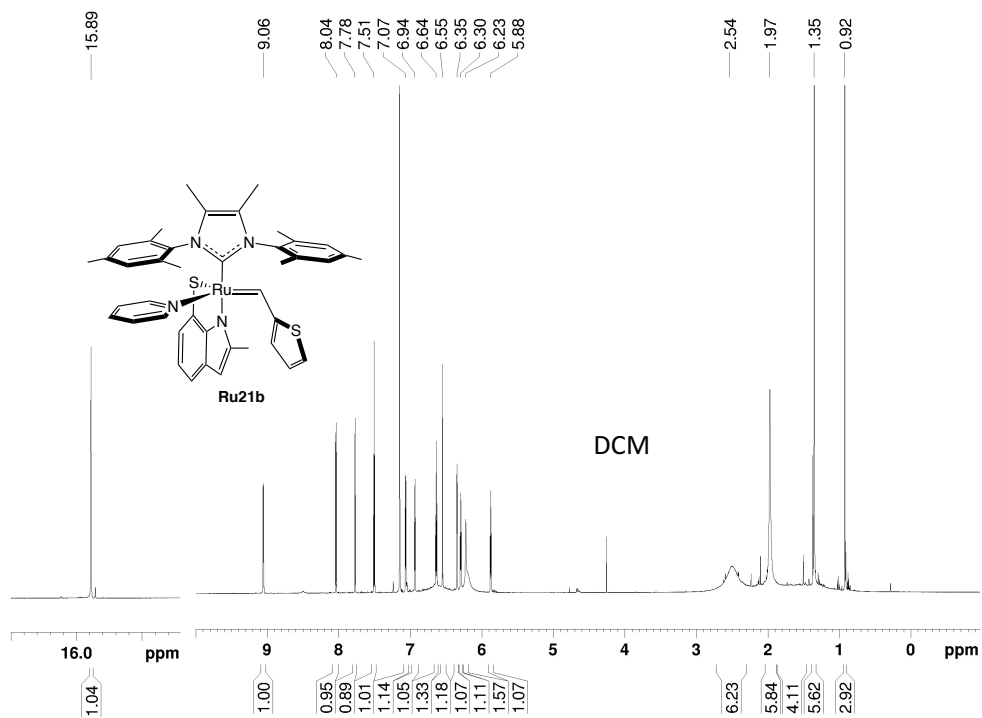


Fig. S20 ^1H NMR spectrum of Ru21b (C_6D_6 , 500 MHz)

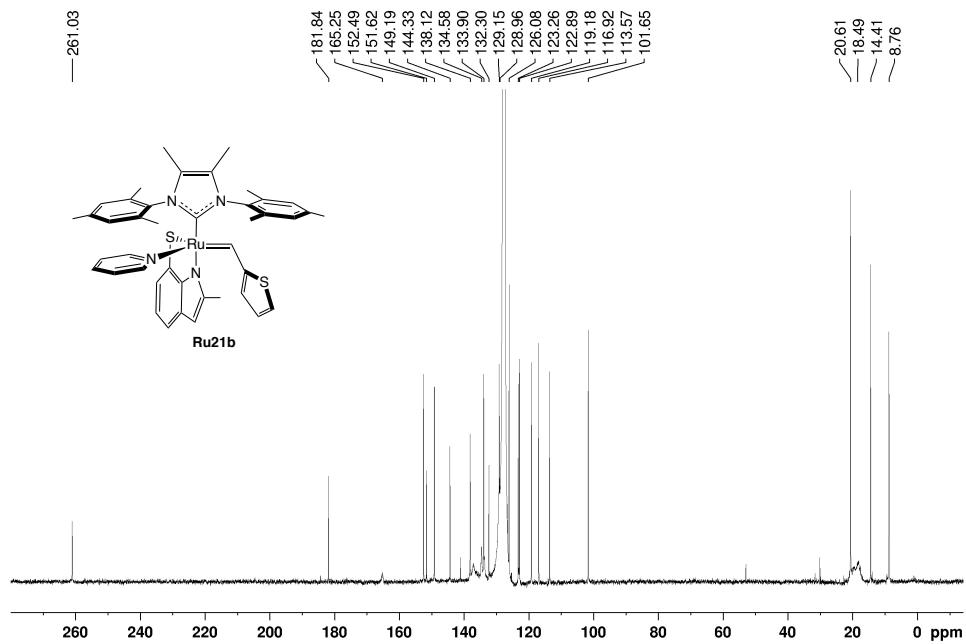


Fig. S21 ^{13}C NMR spectrum of **Ru21b** (C₆D₆, 850 MHz)

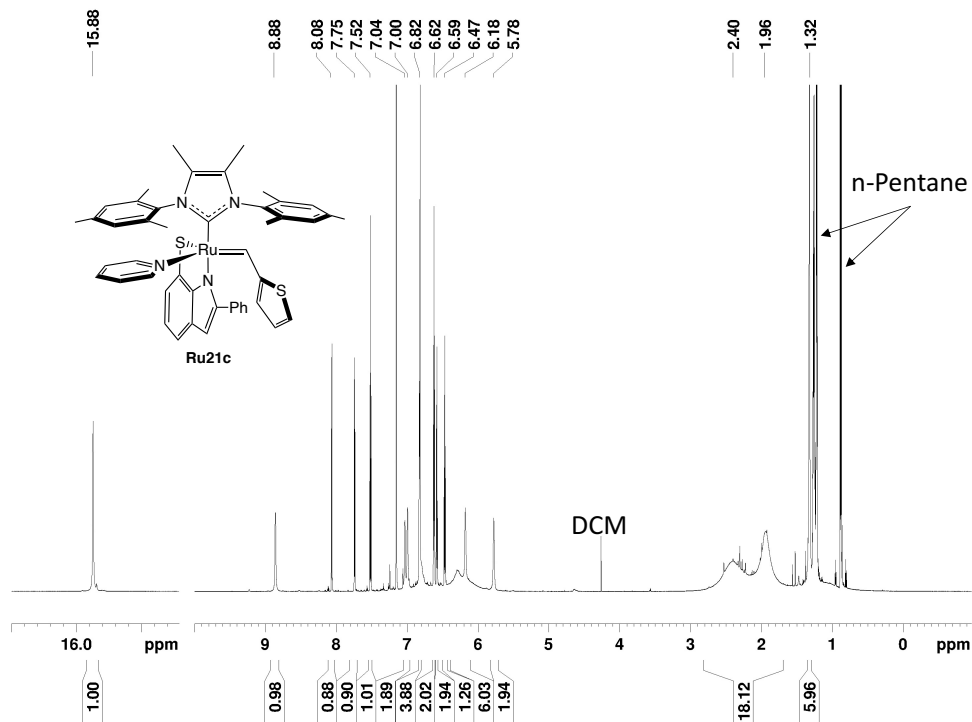


Fig. S22 ^1H NMR spectrum of **Ru21c** (C_6D_6 , 850 MHz)

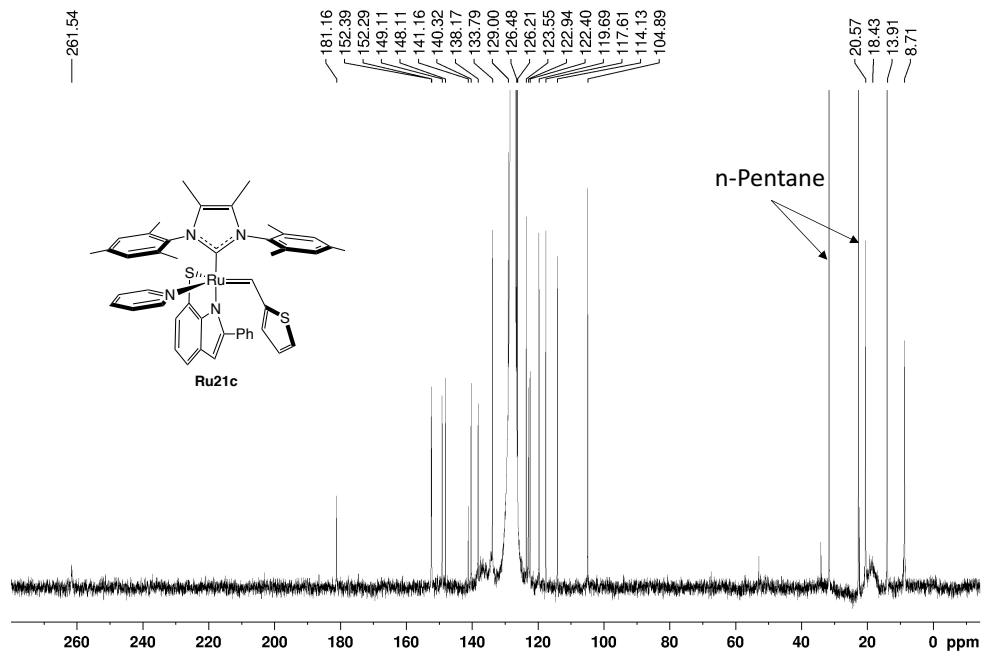


Fig. S23 ^{13}C NMR spectrum of Ru21c (C_6D_6 , 850 MHz)

S5. X-ray Crystal Structures

Data collection on compound **Ru21a** was done on beamline BM01 at the Swiss-Norwegian Beamlines at the ESRF synchrotron in Grenoble, France, using Si double-mirror monochromated radiation ($\lambda = 0.62379$ Å) applying a 360-degree phi-scan and a Pilatus2M detector. The technical assistance of the Dr. Dmitry Chernyshov, and the SNBL at the ESRF is gratefully acknowledged.

X-ray Crystal Structure of Ru21a

X-Ray suitable crystal were obtained by layering a concentrated DCM solution of **Ru21a** with pentane at -30 °C. The quality of the obtained crystals was good for proof of connectivity, but not for qualitative comparison. The thiophene group is rotationally disordered.

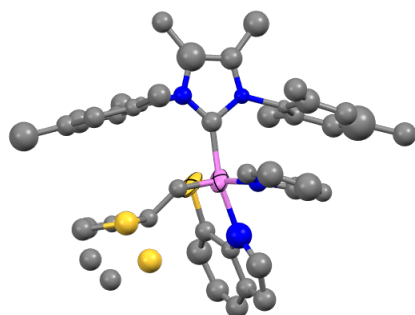


Fig. S24 X-ray crystal structure of **Ru21a**, with displacement ellipsoids drawn at 50% probability. The Ruthenium is shown in violet, sulfur in yellow, nitrogen in blue, and carbon in gray. Hydrogen atoms have been omitted for clarity.

Table S8: Crystal Data and Structure Refinement for Ru21a

Identification code	Ru21a	
Empirical formula	C41 H42 N4 Ru S2 + Solvents	
Formula weight	755.97	
Temperature	200(2) K	
Wavelength	0.62379 Å	
Crystal system	Orthorhombic	
Space group	Pbca	
Unit cell dimensions	a = 19.596(3) Å	$\alpha = 90^\circ$.
	b = 19.404(4) Å	$\beta = 90^\circ$.
	c = 22.551(7) Å	$\gamma = 90^\circ$.
Volume	8575(3) Å ³	
Z	8	

Density (calculated)	1.171 Mg/m ³
Absorption coefficient	0.344 mm ⁻¹
F(000)	3136
Crystal size	0.11 x 0.04 x 0.01 mm ³
Theta range for data collection	1.585 to 16.469°.
Index ranges	-15<=h<=15, -17<=k<=17, -20<=l<=20
Reflections collected	20069
Independent reflections	3222 [R(int) = 0.3880]
Completeness to theta = 16.469°	95.8 %
Absorption correction	Semi-empirical from equivalents
Max. and min. transmission	1.00000 and 0.73091
Refinement method	Full-matrix least-squares on F ²
Data / restraints / parameters	3222 / 11 / 224
Goodness-of-fit on F ²	1.167
Final R indices [I>2sigma(I)]	R1 = 0.1788, wR2 = 0.3671
R indices (all data)	R1 = 0.2459, wR2 = 0.4044
Extinction coefficient	n/a
Largest diff. peak and hole	0.764 and -0.630 e.Å ⁻³

X-ray Crystal Structure of Ru21c

X-Ray suitable crystals were obtained by layering a concentrated toluene solution of **Ru21c** with pentane at -30 °C. The thiophene group is rotationally disordered.

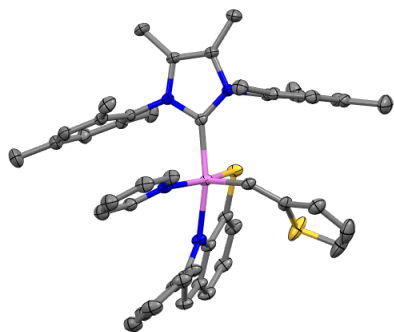


Fig. S25 X-ray crystal structure of **Ru21c**, with displacement ellipsoids drawn at 50% probability. Ruthenium is shown in violet, sulfur in yellow, nitrogen in blue, and carbon in gray. Hydrogen atoms have been omitted for clarity

Table S9: Crystal Data and Structure Refinement for Ru21c

Identification code	Ru21c (CCDC: 2086885)	
Empirical formula	C _{55.50} H ₆₂ N ₄ Ru S ₂	
Formula weight	950.28	
Temperature	123(2) K	
Wavelength	0.71073 Å	
Crystal system	Triclinic	
Space group	P-1	
Unit cell dimensions	a = 10.9904(8) Å	α = 94.1084(11)°.
	b = 14.3209(11) Å	β = 100.7967(11)°.
	c = 16.6513(12) Å	γ = 111.5795(10)°.
Volume	2365.4(3) Å ³	
Z	2	
Density (calculated)	1.334 Mg/m ³	
Absorption coefficient	0.462 mm ⁻¹	
F(000)	998	
Crystal size	0.682 x 0.379 x 0.052 mm ³	
Theta range for data collection	1.548 to 32.023°.	
Index ranges	-16 ≤ h ≤ 16, -21 ≤ k ≤ 21, -24 ≤ l ≤ 24	

Reflections collected	45464
Independent reflections	16392 [R(int) = 0.0863]
Completeness to theta = 25.242°	100.0 %
Absorption correction	Semi-empirical from equivalents
Max. and min. transmission	0.95801 and 0.72930
Refinement method	Full-matrix least-squares on F ²
Data / restraints / parameters	16392 / 591 / 615
Goodness-of-fit on F ²	1.041
Final R indices [I > 2sigma(I)]	R1 = 0.0451, wR2 = 0.1234
R indices (all data)	R1 = 0.0509, wR2 = 0.1273
Extinction coefficient	n/a
Largest diff. peak and hole	1.860 and -0.902 e.Å ⁻³

S6. References

1. Fulmer GR, Miller AJM, Sherden NH, Gottlieb HE, Nudelman A, Stoltz BM, Bercaw JE, Goldberg KI (2010) NMR Chemical Shifts of Trace Impurities: Common Laboratory Solvents, Organics, and Gases in Deuterated Solvents Relevant to the Organometallic Chemist. *Organometallics* 29:2176-2179. <https://doi.org/10.1021/om100106e>
2. Lummiss JAM, Oliveira KC, Pranckevicius A, Santos A, dos Santos EN, Fogg DE (2012) Chemical Plants: High-Value Molecules from Essential Oils. *J Am Chem Soc* 134:18889–18891
3. Blacquiere JM, Jurca T, Weiss J, Fogg DE (2008) Time as a Dimension in High-Throughput Homogeneous Catalysis. *Adv Synth Catal* 350:2849-2855. <https://doi.org/10.1002/adsc.200800596>
4. Occhipinti G, Törnroos KW, Jensen VR (2017) Pyridine-Stabilized Fast-Initiating Ruthenium Monothiolate Catalysts for Z-Selective Olefin Metathesis. *Organometallics* 36:3284-3292. <https://doi.org/10.1021/acs.organomet.7b00441>
5. Mikus MS, Torker S, Xu C, Li B, Hoveyda AH (2016) Pentacoordinate Ruthenium(II) Catecholthiolate and Mercaptophenolate Catalysts for Olefin Metathesis: Anionic Ligand Exchange and Ease of Initiation. *Organometallics* 35:3878-3892. <https://doi.org/10.1021/acs.organomet.6b00773>
6. Waser J, Gaspar B, Nambu H, Carreira EM (2006) Hydrazines and azides via the metal-catalyzed hydrohydrazination and hydroazidation of olefins. *J Am Chem Soc* 128:11693-11712. <https://doi.org/10.1021/ja062355+>
7. Koh MJ, Khan RK, Torker S, Yu M, Mikus MS, Hoveyda AH (2015) High-value alcohols and higher-oxidation-state compounds by catalytic Z-selective cross-metathesis. *Nature* 517:181-186. <https://doi.org/10.1038/nature14061>
8. Watanabe R, Sugai C, Yamazaki T, Matsushima R, Uchida H, Matsumiya M, Takatsu A, Suzuki T (2016) Quantitative Nuclear Magnetic Resonance Spectroscopy Based on PULCON Methodology: Application to Quantification of Invaluable Marine Toxin, Okadaic Acid. *Toxins (Basel)* 8. <https://doi.org/10.3390/toxins8100294>
9. Smit W, Ekelel JB, Occhipinti G, Woźniak B, Törnroos KW, Jensen VR (2020) Z-Selective Monothiolate Ruthenium Indenylidene Olefin Metathesis Catalysts. *Organometallics* 39:397-407. <https://doi.org/10.1021/acs.organomet.9b00641>
10. Frisch MJ, Trucks GW, Schlegel HB, Scuseria GE, Robb MA, Cheeseman JR, Scalmani G, Barone V, Petersson GA, Nakatsuji H, Li X, Caricato M, Marenich AV, Bloino J, Janesko BG, Gomperts R, Mennucci B, Hratchian HP, Ortiz JV, Izmaylov AF, Sonnenberg JL, Williams, Ding F, Lipparini F, Egidi F, Goings J, Peng B, Petrone A, Henderson T, Ranasinghe D, Zakrzewski VG, Gao J, Rega N, Zheng G, Liang W, Hada M, Ehara M, Toyota K, Fukuda R, Hasegawa J, Ishida M, Nakajima T, Honda Y, Kitao O, Nakai H, Vreven T, Throssell K, Montgomery Jr. JA, Peralta JE, Ogliaro F, Bearpark MJ, Heyd JJ, Brothers EN, Kudin KN, Staroverov VN, Keith TA, Kobayashi R, Normand J, Raghavachari K, Rendell AP, Burant JC, Iyengar SS, Tomasi J, Cossi M, Millam JM, Klene M, Adamo C, Cammi R, Ochterski JW, Martin RL, Morokuma K, Farkas O, Foresman JB, Fox DJ. *Gaussian 16 Rev. C.01*: Wallingford, CT, 2016
11. Perdew JP, Burke K, Ernzerhof M (1996) Generalized Gradient Approximation Made Simple. *Phys Rev Lett* 77:3865-3868. <https://doi.org/10.1103/PhysRevLett.77.3865>
12. Chai JD, Head-Gordon M (2008) Long-range corrected hybrid density functionals with damped atom-atom dispersion corrections. *Phys Chem Chem Phys* 10:6615-6620. <https://doi.org/10.1039/b810189b>

13. Zhao Y, Truhlar DG (2006) A new local density functional for main-group thermochemistry, transition metal bonding, thermochemical kinetics, and noncovalent interactions. *J Chem Phys* 125:194101. <https://doi.org/10.1063/1.2370993>
14. Zhao Y, Truhlar DG (2008) Density functionals with broad applicability in chemistry. *Acc Chem Res* 41:157-167. <https://doi.org/10.1021/ar700111a>
15. Ribeiro RF, Marenich AV, Cramer CJ, Truhlar DG (2011) Use of solution-phase vibrational frequencies in continuum models for the free energy of solvation. *J Phys Chem B* 115:14556-14562. <https://doi.org/10.1021/jp205508z>
16. Grimme S, Ehrlich S, Goerigk L (2011) Effect of the damping function in dispersion corrected density functional theory. *J Comput Chem* 32:1456-1465. <https://doi.org/10.1002/jcc.21759>
17. Smith DG, Burns LA, Patkowski K, Sherrill CD (2016) Revised Damping Parameters for the D3 Dispersion Correction to Density Functional Theory. *J Phys Chem Lett* 7:2197-2203. <https://doi.org/10.1021/acs.jpcllett.6b00780>
18. Peterson KA, Figgen D, Dolg M, Stoll H (2007) Energy-consistent relativistic pseudopotentials and correlation consistent basis sets for the 4d elements Y-Pd. *J Chem Phys* 126:124101. <https://doi.org/10.1063/1.2647019>
19. Dunning TH (1989) Gaussian basis sets for use in correlated molecular calculations. I. The atoms boron through neon and hydrogen. *J Chem Phys* 90:1007-1023. <https://doi.org/10.1063/1.456153>
20. Schuchardt KL, Didier BT, Elsethagen T, Sun L, Gurumoorthi V, Chase J, Li J, Windus TL (2007) Basis set exchange: a community database for computational sciences. *J Chem Inf Model* 47:1045-1052. <https://doi.org/10.1021/ci600510j>
21. Zhao Y, Truhlar DG (2008) Computational characterization and modeling of buckyball tweezers: density functional study of concave-convex $\pi \cdots \pi$ interactions. *Phys Chem Chem Phys* 10:2813-2818. <https://doi.org/10.1039/b717744e>
22. Grimme S (2012) Supramolecular binding thermodynamics by dispersion-corrected density functional theory. *Chemistry* 18:9955-9964. <https://doi.org/10.1002/chem.201200497>
23. Mennucci B, Tomasi J, Cammi R, Cheeseman JR, Frisch MJ, Devlin FJ, Gabriel S, Stephens PJ (2002) Polarizable Continuum Model (PCM) Calculations of Solvent Effects on Optical Rotations of Chiral Molecules. *J Phys Chem A* 106:6102-6113. <https://doi.org/10.1021/jp020124t>
24. Minenkov Y, Occhipinti G, Jensen VR (2013) Complete Reaction Pathway of Ruthenium-Catalyzed Olefin Metathesis of Ethyl Vinyl Ether: Kinetics and Mechanistic Insight from DFT. *Organometallics* 32:2099-2111. <https://doi.org/10.1021/om301192a>
25. Sperger T, Sanhueza IA, Kalvet I, Schoenebeck F (2015) Computational Studies of Synthetically Relevant Homogeneous Organometallic Catalysis Involving Ni, Pd, Ir, and Rh: An Overview of Commonly Employed DFT Methods and Mechanistic Insights. *Chem Rev* 115:9532-9586. <https://doi.org/10.1021/acs.chemrev.5b00163>
26. Grandner JM, Shao H, Grubbs RH, Liu P, Houk KN (2017) Origins of the Stereoretentive Mechanism of Olefin Metathesis with Ru-Dithiolate Catalysts. *J Org Chem* 82:10595-10600. <https://doi.org/10.1021/acs.joc.7b02129>
27. Janse van Rensburg W, Steynberg PJ, Meyer WH, Kirk MM, Forman GS (2004) DFT prediction and experimental observation of substrate-induced catalyst decomposition in ruthenium-catalyzed olefin metathesis. *J Am Chem Soc* 126:14332-14333. <https://doi.org/10.1021/ja0453174>

28. Romero PE, Piers WE (2007) Mechanistic studies on 14-electron ruthenacyclobutanes: degenerate exchange with free ethylene. *J Am Chem Soc* 129:1698-1704. <https://doi.org/10.1021/ja0675245>
29. Mikus MS, Torker S, Hoveyda AH (2016) Controllable ROMP Tacticity by Harnessing the Fluxionality of Stereogenic-at-Ruthenium Complexes. *Angew Chem Int Ed Engl* 55:4997-5002. <https://doi.org/10.1002/anie.201601004>

Pursuing *E*-Selective Olefin Metathesis: Tuning Steric and Electronic Properties of *S,N*-Chelated Ruthenium Alkylidenes

Immanuel Reim, Giovanni Occhipinti, Karl W. Törnroos, and Vidar R. Jensen*



Cite This: *Organometallics* 2024, 43, 726–736



Read Online

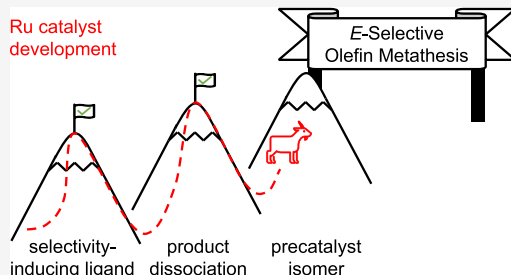
ACCESS |

Metrics & More

Article Recommendations

Supporting Information

ABSTRACT: Selective formation of *E*-olefins directly from 1-alkenes is still an unsolved problem more than 10 years after the first *Z*-selective metathesis catalysts were reported. Illustrating the challenge, the sulfidoindolide-based complex **Ru5** (Ru(L1)-(Me₂IMes)(py)(=CHR); Me₂IMes = 1,3-dimesityl-4,5-dimethylimidazol-2-ylidene; py = pyridine; R = 2-thienyl; L1 = 7-sulfidoindol-1-ide) was initially predicted, via density functional theory (DFT) calculations, to be *E*-selective. However, **Ru5** turned out to have low catalytic activity and to be moderately *Z*-selective due to an unusually hindered product dissociation [Reim et al. *Top. Catal.* 2022, 65, 448]. To lower the dissociation barrier, we here investigated *N*-heterocyclic carbene (NHC) ligands that are less bulky than Me₂IMes. We also hypothesized that a *S,N* ligand with a less nucleophilic nitrogen atom than that of indole might improve catalyst stability. However, catalyst **Ru7**, bearing 2-sulfidophenyltrifluoromethylsulfonamide **L2** instead of **L1**, was not significantly more productive or *E*-selective than **Ru5**. Whereas Ru nanoparticles formed on the addition of *S,N* ligand **L2** to Ru complexes containing less bulky NHCs, **L1** was found to be compatible with such NHCs. However, due to activation of *o*-C–H bonds of *N*-bound NHC phenyls, only the fluorinated 1,3-bis(2,6-difluorophenyl)-4,4-dimethyl-5,5-dihydroimidazol-2-ylidene (Me₂SIF₂Ph) led to a stable sulfidoindolide-coordinated catalyst **Ru12**. Surprisingly, in **Ru12**, **L1** bonds with the indolide positioned *trans* to pyridine, leading to low catalytic activity and *E*-selectivity in 1-alkene self-metathesis. DFT calculations show that the low activity originates in the weak *trans* influence and considerable π donation of the indolide. In contrast, the originally intended isomer **Ru12'**, with the thiolate positioned *trans* to pyridine, is predicted to be much more active and *E*-selective. Factors that might help achieve this isomer in future work are discussed.



INTRODUCTION

Present in antibiotics,¹ anticancer therapeutics,^{2,3} and precision polymers,⁴ *E*-olefins, with substituents *trans*-positioned across the double bond, are an important structural moiety. Traditionally, such substances were synthesized from aldehydes via stoichiometric approaches such as the Wittig,⁵ Horner–Wadsworth–Emmons,⁶ and Julia⁷ olefination reactions. However, the low atom efficiency of these classic methods (most notoriously, the Wittig reaction, with its stoichiometric formation of triphenylphosphine oxide as coproduct) encouraged interest in catalytic methodologies. Olefin metathesis offers an atom-efficient catalytic alternative. Here, the rearrangement of the carbon–carbon double bonds in olefins allows for the generation of new olefins.^{8,9} Specifically, the facile handling and functional-group tolerance of ruthenium catalysts,^{10–12} encouraged the application of olefin metathesis in synthesis of complex organic molecules,^{13–16} including pharmaceuticals,^{17–20} and soft materials.^{21–30}

Since the 1990s, numerous ruthenium olefin metathesis catalysts have been developed.^{31–34} Many of these catalysts

have been optimized for specific reactions and purposes. They typically produce *E*–*Z* (*cis*–*trans*) product mixtures in which the isolation of the target product from its undesired isomer is costly, wasteful, and sometimes impossible. Catalysts that enable selective synthesis of the single-isomer target offer the most atom-economic, direct, and elegant solution.^{31,34–36} However, the design of such catalysts is challenging. Kinetically *Z*-selective catalysts (Chart 1a) for 1-alkene metathesis have been achieved only in the past decade and a half, and only two such classes of catalyst exist: cyclometalated (**Ru1**),^{37–43} and monothiolate catalysts (**Ru2**).^{44–50}

Catalysts for *E*-selective olefin metathesis are even more elusive. Even after more than 20 years of effort, no catalyst for

Received: December 19, 2023

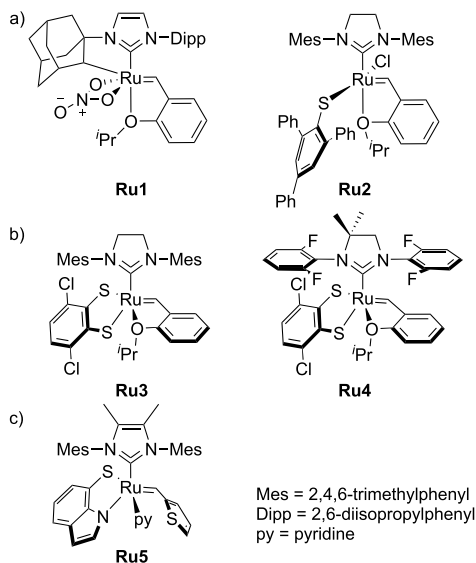
Revised: February 13, 2024

Accepted: March 4, 2024

Published: March 20, 2024



Chart 1. Examples of (a) Z-Selective Ru Catalysts, (b) Stereoretentive Catalysts, and (c) Previously Investigated Catalytic System for E-Selectivity



the *E*-selective metathesis of 1-alkenes has yet been achieved. To date, “stereoretentive” catalysts (**Chart 1b**, **Ru3** and **Ru4**), which transform stereochemically pure *E*-alkene substrates into *E*-configured alkene products, are the only reliable access point for metathetical *E*-olefins.^{35,51–54} The utility of stereoretentive metathesis is limited by the cost and accessibility of the isomerically pure starting materials required. Production of *E*-olefinic products from 1-alkenes represents an intellectually and economically attractive alternative. With the aim to develop an *E*-selective catalyst, we have previously reported compound **Ru5** (**Chart 1c**), which was originally predicted, via density functional theory (DFT) calculations, to be *E*-selective.⁵⁵

The predictive calculations showed that, in **Ru5**, position 2 of the indolide ring exerts steric pressure on the β -substituent of the metallacyclobutane-like (MCB-like) transition state for cycloreversion (**Figure 1a**), the step expected to be rate limiting.^{52,54,56} Although this indolide-induced steric pressure should favor the *E*-selective pathway, **Ru5** turned out to be weakly *Z*-selective in propene self-metathesis. Further investigation revealed a much higher barrier to product dissociation

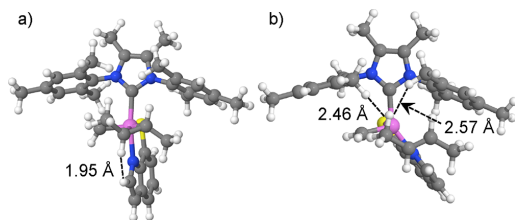


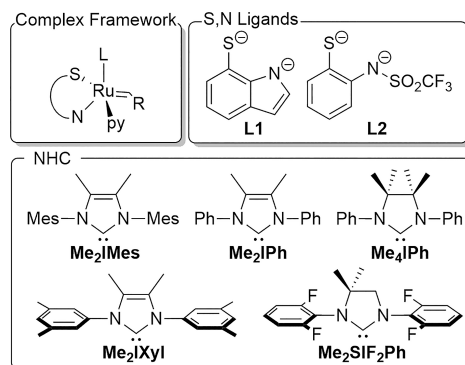
Figure 1. (a) MCB-like transition state and (b) product dissociation for the self-metathesis of propene to *E*-2-butene using **Ru5**.

(via the transition state shown in **Figure 1b**) than that of cycloreversion. The unexpectedly slow and *Z*-selective product dissociation resulted from the elevated steric demand of the catalyst.⁵⁵

We hypothesized that a less bulky NHC ligand would lower the barrier to product release so that the latter would not anymore be rate determining. This should bring *E*-selective catalysts within reach by letting the cycloreversion step control the rate and the stereoselectivity as shown in **Figure 1a**.

Here, we aim to test this hypothesis. To this end, we have replaced the **Me₂IMes** ligand in **Ru5** by the smaller **Me₂IPh** and **Me₂IXyl** (see overview of ligands in **Chart 2**), which were

Chart 2. S₂N and NHC Ligands Investigated in This Work



explicitly designed to not have *o*-methyl substituents at the *N*-bound aryl groups. Additionally, we investigated the known NHC **Me₂IPh** and **Me₂SIF₂Ph** ligands (**Chart 2**), which contain small *N*-bound phenyl and 2,6-difluorophenyl groups, respectively. **Me₂IPh** was selected because Grubbs and co-workers reported that a tetramethyl-substituted backbone should restrict rotation of the *N*-phenyl group, thereby preventing decomposition of the catalyst via C–H activation.^{57,58} **Me₂SIF₂Ph**, albeit bulkier than **Me₂IPh**, is immune to C–H activation decomposition, and it has been employed to make **Ru4**, which is a more efficient *E*-stereoretentive catalyst than **Ru3**. In addition to hopefully increasing the catalytic activity and establishing the cycloreversion step as rate limiting, the smaller NHCs, featuring a larger open space between the *N*-aryl substituents, are also expected to further favor the *E*-pathway by making room for the β -substituent in the MCB-like transition state.

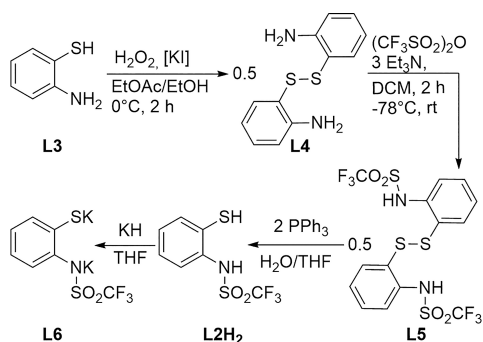
In addition to the above selectivity-related considerations, we intended to limit a catalyst decomposition mode, nucleophilic attack on the electrophilic alkylidene by the electron-rich, nucleophilic bidentate ligand, to which the closely related catechodithiolate-bearing stereoretentive catalysts are known to be prone.⁵² To suppress this decomposition mode, the dithiolate ligands are usually substituted by electronegative groups, a strategy that here should also help limit another potential decomposition mode, that of indolide/amide dissociation, via proton uptake. To avoid both these decomposition modes, we have tested a less nucleophilic ruthenium-binding nitrogen atom, that of 2-sulfidophenyltrifluoromethylsulfonamide **L2** (**Chart 2**), which has the amide

N atom flanked by a strongly electron-withdrawing trifluoromethylsulfonyl group.

RESULTS AND DISCUSSION

Synthesis and Installation of Ligand L2. Mercaptophenyltrifluoromethanesulfonamide (**L2H₂**) was prepared according to the protocol depicted in **Scheme 1**. 2-Aminothiophenol

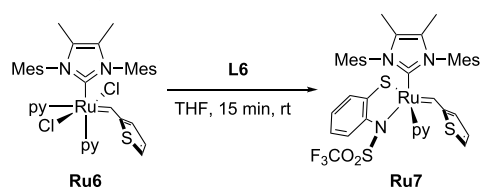
Scheme 1. Synthesis of S,N Ligand Precursor **L2H₂** and its Dipotassium Salt **L6**



(**L3**) was first reacted with hydrogen peroxide and catalytic amounts of KI to form bis(2-aminophenyl) disulfide **L4**. **L4** was then treated with an excess of trifluoromethanesulfonic anhydride at low temperature ($-78\text{ }^{\circ}\text{C}$) to give the corresponding sulfonamide derivative **L5**. The disulfide bond of **L5** was, finally, cleaved with triphenylphosphine and water to deliver two equivalents of **L2**.^{59,60}

To evaluate the properties of **L2** as a ligand, its dipotassium salt **L6** was reacted with **Ru6** at room temperature to give **Ru7** (**Scheme 2**). This allowed for comparison with complex **Ru5** (**Chart 1c**), which was obtained, in the same manner, using ligand **L1**.⁵⁵

Scheme 2. Synthesis of **Ru7**



Like **Ru5**, **Ru7** revealed a bidentate S,N ligand with S binding cis and N trans to the NHC (see X-ray structure in **Figure 2**) and also displayed low productivity in self-metathesis of propene (0.95 catalytic turnovers, vs 0.35 for **Ru5**) and moderate Z-selectivity (63%, vs 73% for **Ru5**). These results suggest that the reduced electron donation and basicity of the ruthenium-binding nitrogen atom do not improve the stability of S,N-based catalysts significantly.

Preparation of S,N-Coordinated Catalysts Bearing Small NHCs. Imidazolium salts **L9a** and **L9b**, precursors of NHCs **Me₂IPh** and **Me₂IXyl**, respectively, were prepared using the protocol developed by Glorius and co-workers for the synthesis of substituted imidazolium salts as a starting point.⁶¹

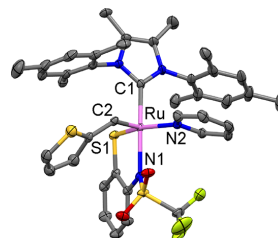
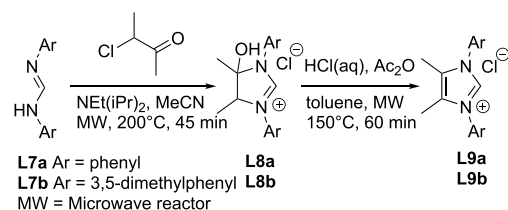


Figure 2. X-ray crystal structure of **Ru7**, with displacement ellipsoids drawn at 50% probability. Ru: pink; S: yellow; N: blue; O: red; F: green; C: gray. Hydrogen atoms were omitted for clarity. Selected geometrical parameters (bond distances in Å and angles in deg.): Ru–C1 = 2.056(2), Ru–N1 = 2.207(19), Ru–S1 = 2.264(7), Ru–N2 = 2.134(19), Ru–C2 = 1.850(2), N1–Ru–S1 = 83.03(5), S1–Ru–C1 = 86.49(6), N1–Ru–C1 = 167.30(8).

To reduce the reaction time from several days (standard heating, as in the original protocol) to less than 1 h, the protocol was modified by conducting the reactions in a microwave reactor (**Scheme 3**).⁶² Amidines **L7a**⁶³ and **L7b**

Scheme 3. Microwave-Assisted Synthesis of **L9a** and **L9b**

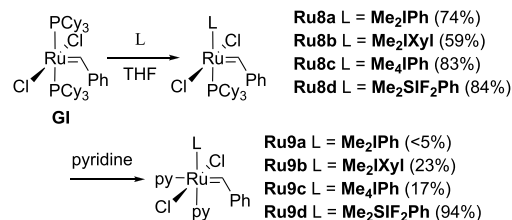


were first reacted with 3-chloro-2-butanone to give imidazolium salts **L8a** and **L8b**, respectively, which were then dehydrated with acetic anhydride and hydrochloric acid to the unsaturated imidazolium salts **L9a** and **L9b**.

Imidazolium salts **L9c** and **L9d**, precursors of NHCs **Me₄IPh** and **Me₂SIF₂Ph**, respectively, were prepared according to literature procedures.^{57,64}

In general, the carbene ligands were generated in situ by treating the imidazolium salts **L9a–L9d** with KHMDS. The carbenes were reacted with Grubbs first-generation catalyst **GI** to give phosphine-stabilized NHC complexes **Ru8a–Ru8d** (**Scheme 4**). The latter compounds were then treated with excess pyridine to yield the pyridine-stabilized complexes **Ru9a–Ru9d**.

Scheme 4. Synthesis of **Ru9a–d**



Whereas all carbenes could readily be installed on **G1**, the subsequent phosphine/pyridine exchange worked well only for **Ru8d**, delivering **Ru9d** in near-quantitative yield (94%). Preparation of pyridine derivatives **Ru9a–Ru9c** was challenging because of their poor stability, presumably resulting from C–H activation of the NHC ligand.^{65–67} For **Ru9a**, the stability problems resulted in yields that were insufficient for product isolation. **Ru9b**, which contains a more substituted NHC, was isolated in 23% yield, with single-crystal X-ray diffraction analysis revealing a cis-configuration for the two chloride ligands (Figure 3). During attempts to grow crystals of

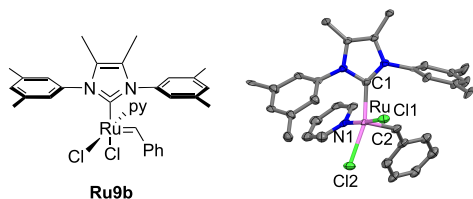


Figure 3. X-ray crystal structure of **Ru9b** with displacement ellipsoids drawn at a 50% probability. Ru: pink; Cl: green; N: blue; C: gray. Hydrogen atoms have been omitted for clarity. Selected geometrical parameters (bond distances in Å and angles in deg.): Ru–C1 = 2.03(2), Ru–N1 = 2.071(17), Ru–Cl1 = 2.402(5), Ru–Cl2 = 2.416(6), Ru–C2 = 1.84(2), Cl1–Ru–Cl2 = 88.09(19), Cl1–Ru–C1 = 89.6(5), Cl2–Ru–C1 = 160.9(6), Cl1–Ru–N1 = 173.2(6), C2–Ru–C1 = 96.1(9).

Ru9b in the glovebox freezer (−35 °C) a partial color change of the microcrystalline solid from green to blue was observed over time. No signal corresponding to the alkylidene proton could be observed in the ¹H NMR spectrum of the blue microcrystalline material, suggesting that a double C–H activation of the carbene N-aryl groups had occurred.^{65,66}

Our hope that the tetramethyl-substituted backbone of **Me₄IPh** would restrict the rotation of the N-phenyl moieties to prevent C–H activation and increase the stability of **Ru9c** was not realized.^{57,58} Whereas we were able to improve the yield of the PCy₃-stabilized complex **Ru8c** to 83% vs the previously reported 55%,⁵⁷ all attempts to optimize the phosphine/pyridine exchange reaction gave disappointing results, and only 17% of **Ru9c** was isolated.

Ru9c decomposes readily in solution, even in the glovebox freezer (−35 °C), accompanied by a color change from green to red. Attempts to grow crystals suitable for X-ray diffraction analysis instead resulted in complex **Ru10** (Figure 4). A similar ruthenium complex, stabilized by two PCy₃ ligands in addition to a chloride ligand, resulting from double NHC C–H activation, has been reported by Grubbs and co-workers.⁶⁸ The removal of free PCy₃ by washing **Ru9c** with hexane resulted in decomposition of the product, with the washing solution on a glass frit remaining reddish, while the green filter cake disappeared. In summary, our results suggest that steric bulk at the backbone could not prevent N-phenyl rotation and activation of the *o*-C–H bonds.

In contrast, **Ru9d**, which is based on fluorinated NHC **Me₂SIF₂Ph**, was isolated in 94% yield (Scheme 4). Presumably, **Me₂SIF₂Ph** cannot decompose via C–F activation.^{64,68} Thus, substitution of the N-aryl ortho positions with fluorine seems to be the only viable strategy with which to

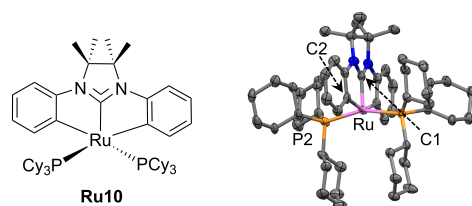
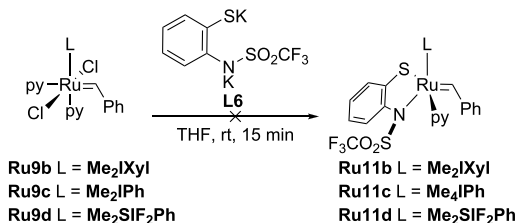


Figure 4. X-ray crystal structure of **Ru10**, with displacement ellipsoids drawn at 50% probability. Ru: pink; P: orange; N: blue; C: gray. Hydrogen atoms have been omitted for clarity. Selected geometrical parameters (bond distances in Å and angles in deg.): Ru–C1 = 1.915(4), Ru–C2 = 2.150(4), Ru–P2 = 2.372(15), C1–Ru–C2 = 76.07(16), C1–Ru–P2 = 101.79(16), C2–Ru–P2 = 92.32(14).

reduce steric bulk near the ruthenium center without compromising the catalyst stability.

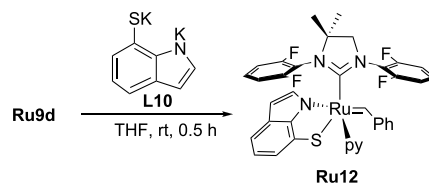
Installation of S,N Ligands on Pyridine-Stabilized Complexes Ru9b–Ru9d. On reaction of pyridine complexes **Ru9b–Ru9d** with the dipotassium salt **L6**, the alkylidene signal disappeared (Scheme 5). In addition, a black precipitate was observed in the reaction with **Ru9d**, suggesting the formation of ruthenium nanoparticles.

Scheme 5. Installation of Ligand L2 on Ru9b–d



Next, we investigated the installation of sulfidoindolide ligand **L1**. Reaction of **Ru9b** and **Ru9c** with its dipotassium salt **L10** led to unstable Ru–alkylidene complexes, which decomposed during purification procedures. In contrast, the corresponding reaction with **Ru9d** led to a stable complex **Ru12** (Scheme 6).

Scheme 6. Installation of Ligand L1 on Ru9d



X-ray diffraction analysis of **Ru12** (Figure 5) showed a sulfidoindolide ligand orientation opposite that of **Ru5** (Chart 1c). Whereas, in **Ru5**, the indolide nitrogen atom is bound trans to the NHC, it is bound cis to the NHC in **Ru12**. The preference for the cis configuration in **Ru12** is presumably the result of the weaker trans influence and steric pressure from the carbene ligand **Me₂SIF₂Ph** vs **Me₂IMes**: the mutual NHC–thiolate trans influence is low enough to stabilize the

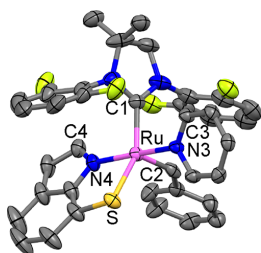


Figure 5. X-ray crystal structure of **Ru12**, with displacement ellipsoids drawn at 30% probability. Ru: pink; S: yellow; N: blue; F: green; C: gray. Hydrogen atoms have been omitted for clarity. Selected geometrical parameters (bond distances in Å and angles in deg.): Ru–C1 = 2.034(5), Ru–N4 = 2.056(4), Ru–S = 2.3627(13), Ru–N3 = 2.144(4), Ru–C2 = 1.810(6), N3–Ru–S = 88.59(10), S–Ru–C1 = 149.93(17), N3–Ru–C1 = 93.97(17), C4–N4–N3–C3 = 43.05.

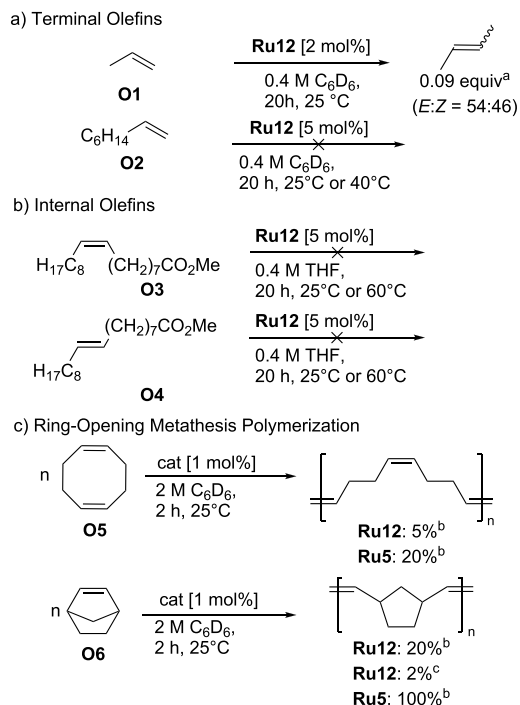
isomer (**Ru12**) in which the bulkier indolide part of the S,N ligand is placed near the smaller, fluorine-substituted NHC.

Ru12 displays low catalytic activity in the self-metathesis of propene (**O1**). After complete loss of starting complex **Ru12** in the propene self-metathesis experiment, only 23% free styrene was observed in the ^1H NMR spectrum. This suggests that 77% of the catalyst decomposes before completing the initiation. The initiated complex produces tiny amounts of 2-butene (9%, or 0.09 turnovers), slightly favoring the *E*-isomer (54%, vs 46% *Z*-isomer). The application of larger terminal olefins like 1-octene (**O2**), or internal olefins such as methyl oleate (**O3**) and methyl elaidate (**O4**) (Scheme 7a,b) showed no productive metathesis. In contrast, low catalytic activity was recorded in the ring-opening metathesis polymerization (ROMP) of cyclooctadiene (**O5**) and 2-norbornene (**O6**) (Scheme 7c). Whereas **Ru5** is *Z*-selective in ROMP of 2-norbornene (*E:Z* = 10:90), **Ru12** slightly favors the *E*-isomer, with a selectivity (*E:Z* = 53:47) similar to that of the above propene self-metathesis experiment (see Figure S2 in the Supporting Information).

To conclude, the catalytic activity of **Ru12** is lower than that of **Ru5**, which is more active in both ROMP and self-metathesis of propene.⁵⁵ The catalytic results of **Ru12** were disappointing as the reduced steric bulk of NHC **Me₂SIF₂Ph** vs **Me₂IMes** was expected to ease the product dissociation, which is the rate-limiting step of the catalytic cycle for **Ru5**.⁵⁵

Mechanistic Calculations. To determine why **Ru12** is less active than expected, we have investigated, using DFT calculations, the propene self-metathesis reaction catalyzed by **Ru12** as well as by **Ru12'**, the originally intended isomer, which has the indolide N atom positioned trans to the NHC. The DFT calculations predict that **Ru12** is 6.0 kcal mol⁻¹ more stable than **Ru12'**. This stability difference suggests that none of the two alkylidene-relevant singlet signals in the ^1H NMR spectrum (at 14.6 and 15.0 ppm, Figure S23) belongs to **Ru12'**. Instead, these signals more likely originate in the two NHC–Ru rotamers (due to the asymmetric **Me₂SIF₂Ph**)^{55,64} of the more stable **Ru12**. Additionally, whereas a NOESY experiment indicated dynamic exchange between the corresponding two isomers (the indolide *cis* and *trans* to the NHC, respectively) of **Ru5**,⁵⁵ no signs of a corresponding exchange between the 14.6 and 15.0 ppm signals were observed for **Ru12**.

Scheme 7. Olefin Metathesis Reactions of Catalyst **Ru12**



^aEquivalents vs **Ru12** determined by ^1H NMR analysis. ^bYield determined by ^1H NMR analysis. ^cIsolated yield using 0.1 mol % catalyst loading.

First, we investigated the initiation of **Ru12** (the molecular model of which is **M1**, Figure 6). Due to the weak trans influence of the indolide and the through-complex N(indolide)–Ru–N(pyridine) π interaction (the sulfidoindolide–pyridine dihedral angle is ca. 43° in **Ru12**; see Figure 5), pyridine dissociation from **Ru12** is costly, with a barrier of 26.6 kcal mol⁻¹ via transition state **TS1–2** to reach complex **M2** in which pyridine is located in the second coordination sphere of ruthenium and hydrogen bonded to a NHC fluorine. From **M2**, calculations at successively longer Ru–py distances resulted in monotonically and weakly increasing potential energies, and the complete loss of pyridine does not seem to involve a transition state on the potential energy surface (PES). Complete dissociation from the second coordination sphere, from **M2** or any other such weakly bound complex, involves significant stabilization due to solvation and entropy gain and can be assumed to be fast (close to the diffusion limit). The estimated barrier (26.6 kcal mol⁻¹) to pyridine loss from **M1** (**Ru12**) is thus that of **TS1–2**.

Initially, we assumed that the four-coordinate, 14-electron benzylidene species **M3** (derived from **Ru12**) may easily isomerize to the more stable **M19** (derived from **Ru12'**) by rotating the S,N ligand around an axis nearly parallel to the Ru alkylidene bond,⁶⁹ so that the indolide nitrogen atom ends up being *trans* to the NHC ligand (Figure 6). This assumption was made based on the observed, in NOESY experiments,⁵⁶ fast isomerization of **Ru5** and the low barrier calculated for the

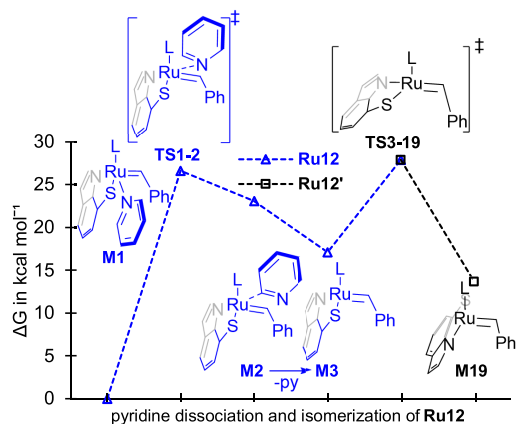


Figure 6. Gibbs free energies calculated for the initiation of **Ru12** (the model of which is **M1**) via pyridine dissociation and isomerization to the **Ru12'**-derived **M19**. Complexes with the thiolate sulfur atom trans to the L-ligand (as in the **Ru12** precursor) are indicated by blue triangles, and those with a corresponding cis-configuration are indicated by black squares. A standard state corresponding to an ideal 1 mol L⁻¹ solution (benzene) is assumed for all species, and free energies are given relative to the most stable rotamer of the **Ru12** precursor.

corresponding S,S ligand rotation in the 14-electron complex of the stereoretentive catalyst **Ru3**.^{69,70} Surprisingly, the barrier to S,N ligand rotation calculated here for **M3** is even higher than that of the above pyridine dissociation: 27.9 kcal mol⁻¹ (via **TS3-19**) vs the **Ru12** precursor **M1**. The faster isomerization observed for **Ru5** presumably results from its

bulkier **Me₂IMes** ligand, as calculations have found steric bulk to favor rotation of the bidentate catecholthiolate ligand in stereoretentive catalysts.⁷⁰

As shown in **Figure 7**, continued initiation of the catalyst involves coordination of substrate (here: propene) to either **M3** or **M19** to give π -complexes **M4** or **M20**, cycloaddition and cycloreversion to form the corresponding styrene π -complexes **M6** or **M22**, and styrene dissociation to form the 14-electron ethylidene species **M8** or **M24**. The free energies calculated for these intermediates and transition states reveal that the key metathetic bond rupture and formation steps are disfavored by the indolide moiety of the S,N ligand being situated trans to the evolving MCB. Cycloaddition and cycloreversion steps are known to benefit from ligand-to-metal σ donation from the trans-disposed ligand.⁷¹ The indolide is a poor σ donor, compared with both the thiolate of **Ru5** and **Ru12'** and with the NHCs and cyclic alkyl amino carbenes (CAACs) of leading metathesis catalysts. It is thus unsurprising that the cycloreversion barrier of **Ru12** (via **TSS-6**) is 4.7 kcal mol⁻¹ higher than that of **Ru12'** (via **TS21-22**). Due to the through-complex N(indolide)-Ru-styrene π donation (the styrene alkene bond being nearly orthogonal to the indolide plane) and the low trans influence of the indolide, the styrene π -complex **M6** of **Ru12** is more stable (by 2.0 kcal mol⁻¹) than the **Ru12'**-derived counterpart **M22**. However, although this stability adds to the barrier to styrene dissociation from **M6**, the dissociation barrier vs **M1** (24.6 kcal mol⁻¹) to reach complex **M7**, in which styrene is in the second coordination sphere, is only 0.3 kcal mol⁻¹ higher than that of **Ru12'** to reach the corresponding **M23**. As for the pyridine dissociation above, complete styrene dissociation from the weakly bound complexes **M7** and **M23** is associated with significant stabilization, does not involve transition states on the PES, and can be assumed to be fast.

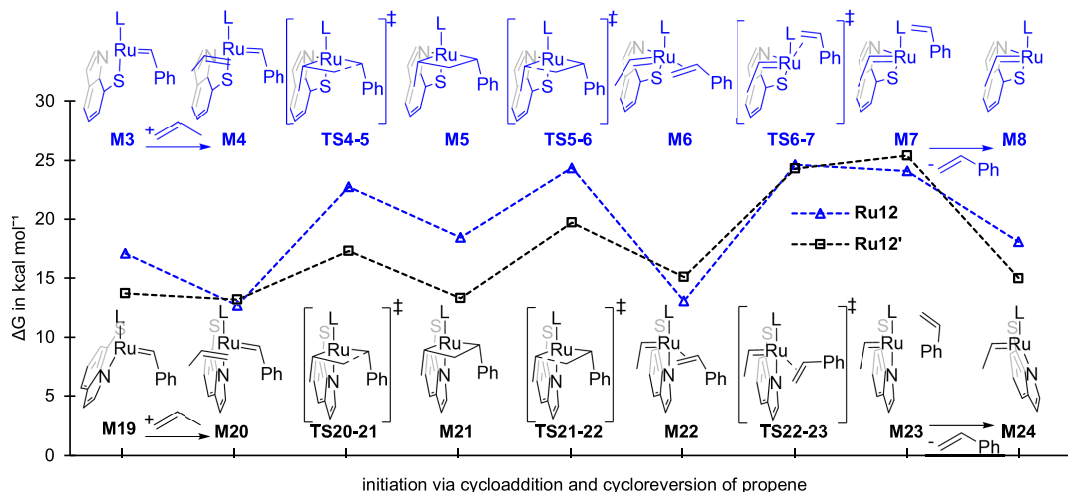


Figure 7. Gibbs free energies calculated for propene coordination, cycloaddition, cycloreversion, and styrene dissociation for the 14-electron, pyridine-free complexes **M3** and **M19** of catalyst isomers **Ru12** and **Ru12'**, respectively. See **Figure 6** for pyridine dissociation from catalyst precursor **Ru12** and isomerization to **Ru12'**. Intermediates and transition states with the thiolate sulfur atom trans to the L-ligand (as in the **Ru12** precursor) are indicated by blue triangles, and those with a corresponding cis-configuration are indicated by black squares. A standard state corresponding to an ideal 1 mol L⁻¹ solution (benzene) is assumed for all species, and free energies are given relative to the most stable rotamer of the **Ru12** precursor.

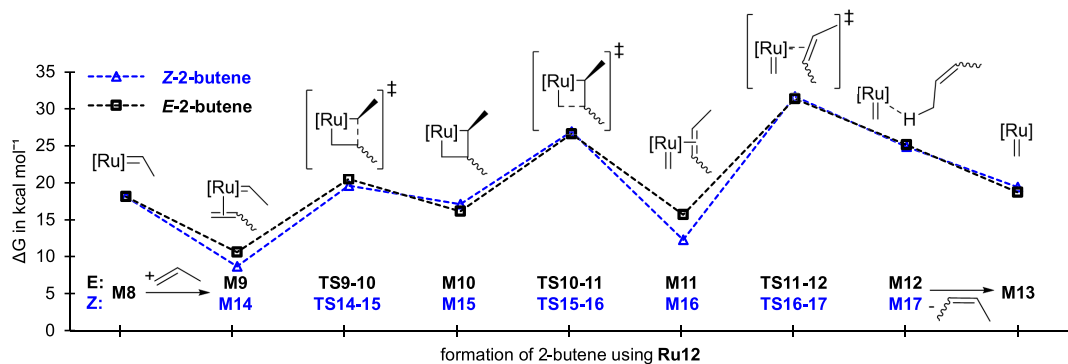


Figure 8. Gibbs free energies calculated for intermediates and transition states of propene self-metathesis for catalyst **Ru12**. The Z-2-butene pathway is indicated by blue triangles and that of E-2-butene by black squares. A standard state corresponding to an ideal 1 mol L⁻¹ solution (benzene) is assumed for all species, and free energies are given relative to the most stable rotamer of the **Ru12** precursor.

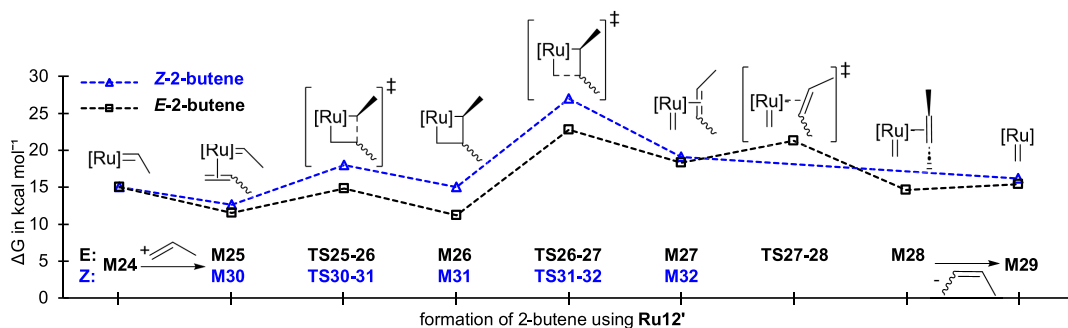


Figure 9. Gibbs free energies calculated for intermediates and transition states of propene self-metathesis for the originally intended catalyst isomer **Ru12'**. The Z-2-butene pathway is indicated by blue triangles and that of E-2-butene by black squares. A standard state corresponding to an ideal 1 mol L⁻¹ solution (benzene) is assumed for all species, and free energies are given relative to the most stable rotamer of the **Ru12** precursor.

Concluding, initiation of **Ru12** is likely to be limited by the initial pyridine dissociation, with a barrier of 26.6 kcal mol⁻¹, and is, due to the high barrier to S,N ligand rotation (27.9 kcal mol⁻¹), also likely to predominantly generate **Ru12**-derived ethylidene complex **M8**. Subsequent isomerization of the **M8** ethylidene to **M24** requires even more activation (31.6 kcal mol⁻¹, via **TS8–24**) and is unlikely. The high barrier to pyridine dissociation is consistent with initiation of **Ru12** being slow (perhaps taking days to complete at room temperature) and susceptible to competition from catalyst decomposition reactions, such as nucleophilic attack of the thiolate on the alkylidene, a prominent decomposition mode for the closely related **Ru3**.^{52,55} These results are thus consistent with the small amount (23%) of free styrene and the significant catalyst loss observed in the propene self-metathesis experiment (see above).

Similarly, the relative free energies calculated for **Ru12**-catalyzed propene self-metathesis (Figure 8) are, with high overall barriers and a marginal predicted E-selectivity (by 0.3 kcal mol⁻¹, via **TS11–12**), qualitatively consistent with the observed sluggish formation of self-metathesis products and the slight overweight of E-2-butene (E:Z = 54:46). Low metathesis activity is, as discussed above for the initiation, expected from a catalyst isomer with the indolide located trans

to the evolving MCB and 2-butene. In fact, the activity (0.09 equiv vs **Ru12** in 20 h) seems high given rate-determining barriers of >30 kcal mol⁻¹ (for product dissociation, vs **M1**). Assuming reversibility, these barriers also suggest that the observed 2-butene could be the result of catalyst isomerization via **TS3–19** (27.9 kcal mol⁻¹) followed by **Ru12'**-catalyzed propene self-metathesis as described below (Figure 9). However, the free energies of Figures 6–9 assume a standard state corresponding to an ideal 1 mol L⁻¹ solution (benzene) for all species, whereas the experimental catalyst concentration (0.01 M) was, in fact, 2 orders of magnitude lower than the propene concentration (0.95 M). Assuming, as observed, that 23% of the experimentally used catalyst precursor initiates (with the rest, 7.7 mM, remaining as **Ru12**), and using the corresponding concentration (2.3 mM) for all pyridine-free Ru species, the resulting **Ru12** product dissociation barriers (23.4 kcal mol⁻¹ for E-2-butene and 23.7 kcal mol⁻¹ for Z-2-butene) do indeed fall below that of catalyst isomerization (23.8 kcal mol⁻¹). During catalysis, **Ru12**-catalyzed 2-butene formation will be favored even more over catalyst isomerization by the smaller fractions (than 23%) with which individual intermediates and transition states will be present. Concluding, although a small contribution from **Ru12'** via **TS3–19** isomerization cannot be excluded, most of the observed 2-

butene likely resulted from **Ru12**-catalyzed self-metathesis of propene.

Although **Ru12** \rightarrow **Ru12'** isomerization is disfavored, analyzing the catalytic properties of the originally intended catalyst **Ru12'** may inform future design of *E*-selective catalysts (Figure 9). First, **Ru12'** was designed to let rate and selectivity be determined by cycloreversion by easing the product release. Indeed, for **Ru12'**, dissociation of both *E*- and *Z*-2-butene appears to be faster than cycloreversion. Whereas dissociation of *Z*-2-butene is barrierless from the π -complex **M32** formed on cycloreversion, the preferred pathway for *E*-2-butene dissociation involves first rotating the latter, with a barrier (21.3 kcal mol⁻¹) below that of cycloreversion, to reduce the mutual catalyst–butene steric repulsion in the initially formed π -complex **M27**. In the more stable complex **M28** formed on rotation, *E*-2-butene is oriented “upright” in-between the *N*-aryl groups, thereby minimizing steric repulsion. From **M28**, *E*-2-butene may dissociate in a barrierless fashion, requiring only minimal geometric rearrangement of the catalyst. This result starkly contrasts with the high (29–32 kcal mol⁻¹)⁵⁵ and rate-determining barriers to 2-butene dissociation calculated for **Ru5** and confirms the key hypothesis behind the current work: A smaller NHC ligand was expected to facilitate product release for sulfidoindolide-based complexes with the thiolate *S* atom positioned trans to the evolving MCB and the forming 2-butene.

In contrast to **Ru12**, the desired isomer **Ru12'** would, if it were thermodynamically preferred, be limited by cycloreversion, with a barrier (22.8 kcal mol⁻¹, via **TS26–27**) much lower than that for **Ru12**. Furthermore, the calculated free-energy difference between the barrier to cycloreversion for the *Z*- and *E*-pathways for **Ru12'** (4.1 kcal mol⁻¹) is greater than for the bulkier **Ru5** (1.9 kcal mol⁻¹).⁵⁵ This confirms another of our initial hypotheses: A larger open space between the *N*-aryl groups of carbene **Me₂SIF₂Ph** vs **Me₂IMes** was expected to reduce the steric repulsion between the NHC and the *E*-alkene product being formed during the cycloreversion step. The current computational investigation of **Ru12'** highlights that the main, and perhaps only, remaining obstacle to *E*-selective ruthenium-catalyzed olefin metathesis is to identify a combination of NHC and *S,N* ligands that retains the overall limited steric bulk of **Me₂SIF₂Ph** and **L1** at the same time as favoring the NHC–*N* trans-configuration of **Ru12'**.

CONCLUSIONS

In this follow-up of our previous attempt to achieve *E*-selective catalysts for 1-alkene metathesis,⁵⁵ we aimed to improve the catalyst stability and to reduce the overall steric congestion to speed up product dissociation, the step that limited the reaction rate of catalyst **Ru5** (**Ru(L1)(Me₂IMes)(py)** (=CHR); **Me₂IMes** = 1,3-dimesityl-4,5-dimethylimidazol-2-ylidene; py = pyridine; R = thiophene; **L1** = 7-sulfidoindol-1-ide) in the previous study.

First, to improve catalyst stability and productivity, we intended to reduce the basicity and nucleophilicity of the ruthenium-binding nitrogen atom of the *S,N* ligand, to avoid proton uptake and dissociation of the indole as well as nucleophilic attack on the alkylidene.⁵² We thus replaced the 7-sulfidoindol-1-ide ligand **L1** of **Ru5** with 2-sulfidophenyltrifluoromethylsulfonamide **L2** to obtain catalyst **Ru7**. This strategy only improved the turnover number slightly (from 0.35 with **Ru5**, to 0.95 with **Ru7**) in self-metathesis of propene

and, just as **Ru5**, **Ru7** produced more *Z*-2-butene (67%) than *E*-2-butene, indicating that product dissociation remained the rate- and selectivity-determining step.

To speed up product dissociation, we explored the use of sterically more accessible NHCs than **Me₂IMes**, with *N*-aryl groups featuring hydrogen or fluorine in the ortho positions. In addition, the increased open space between the *N*-aryl groups was expected to improve the *E*-selectivity. Unfortunately, addition of *S,N* ligand **L2** to Ru complexes containing such small NHCs immediately led to the formation of Ru nanoparticles. Furthermore, all attempts to prepare sulfidoindolide catalysts based on NHCs with *N*-phenyl or *N*-3,5-xyllyl groups failed due to rapid decomposition via C–H activation. However, using the original 7-sulfidoindol-1-ide ligand **L1** in combination with a fluorinated NHC, 1,3-bis(2,6-difluorophenyl)-4,4-dimethyl-5,5-dihydro-imidazol-2-ylidene (**Me₂SIF₂Ph**), we obtained complex **Ru12**.

Surprisingly, the indolide unit in **Ru12** turned out to bind cis to the NHC and trans to the leaving donor (pyridine) and the evolving MCB. In other words, the indolide, which is the structural unit designed to induce *E*-selectivity, was too far from the evolving MCB to affect the selectivity. In addition, **Ru12** proved to be almost inactive in cross metathesis and only barely active with strained substrates in ROMP. DFT calculations showed that the poor catalytic activity is indeed due to the orientation of the sulfidoindolide ligand in the complex. The pyridine, a π acceptor, dissociates slowly and limits catalyst initiation due to the weak σ donation and non-negligible π donation of the trans-disposed indolide. The weak σ donation of the latter also leads to slow cycloaddition, cycloreversion, and product dissociation.

In contrast, calculations predict much higher catalytic activity, as well as considerable *E*-selectivity, for the originally intended catalyst isomer **Ru12'**, in which the indolide binds trans to the NHC. Unfortunately, the barrier to *S,N* ligand rotation is too high for **Ru12** \rightarrow **Ru12'** isomerization to play a significant role in catalysis using **Ru12**.

The foregoing suggests that active and *E*-selective catalysts based on *S,N* bidentate ligands might be obtained by destabilizing the undesired isomer via strong mutual carbene–thiolate trans influence. Increasing the trans influence of the donor L ligand, perhaps by using a cyclic alkyl amino carbene (CAAC),⁷² and/or of the thiolate unit of the bidentate ligand should favor the desired catalyst isomer. Similarly, a less π -accepting leaving donor than pyridine should destabilize the undesired precursor isomer.

ASSOCIATED CONTENT

Supporting Information

The Supporting Information is available free of charge at <https://pubs.acs.org/doi/10.1021/acs.organomet.3c00522>.

Experimental methods and procedures, additional experimental results, NMR and MS spectra, X-ray crystallographic structures and data, computational methods, additional computational results, and calculated electronic and free energies (PDF)

DFT-optimized molecular models in a format convenient for visualization (XYZ)

Accession Codes

CCDC 2314686–2314691 contain the supplementary crystallographic data for this paper. These data can be obtained free of charge via www.ccdc.cam.ac.uk/data_request/cif, or by

emailing data_request@ccdc.cam.ac.uk, or by contacting The Cambridge Crystallographic Data Centre, 12 Union Road, Cambridge CB2 1EZ, UK; fax: +44 1223 336033.

AUTHOR INFORMATION

Corresponding Author

Vidar R. Jensen – Department of Chemistry, University of Bergen, Bergen N-5007, Norway; orcid.org/0000-0003-2444-3220; Email: Vidar.Jensen@uib.no

Authors

Immanuel Reim – Department of Chemistry, University of Bergen, Bergen N-5007, Norway; orcid.org/0000-0001-7448-9572

Giovanni Occhipinti – Department of Chemistry, University of Bergen, Bergen N-5007, Norway; orcid.org/0000-0002-7279-6322

Karl W. Törnroos – Department of Chemistry, University of Bergen, Bergen N-5007, Norway; orcid.org/0000-0001-6140-5915

Complete contact information is available at:
<https://pubs.acs.org/10.1021/acs.organomet.3c00522>

Author Contributions

V.R.J. and G.O. designed and supervised the project. I.R. performed the DFT calculations and the experiments and wrote the initial manuscript draft. G.O. revised the draft, and V.R.J. finalized the manuscript. K.W.T. performed the X-ray diffraction structural analyses. All authors have approved the final version of the manuscript.

Funding

The authors gratefully acknowledge financial support from the Research Council of Norway (RCN) via grant numbers 262370, 288135, and 331967, and via the Norwegian NMR Platform, NNP (226244). The RCN is also thanked for CPU (NN2506K) and storage resources (NS2506K).

Notes

The authors declare no competing financial interest.

ACKNOWLEDGMENTS

Bjarte Holmelid is thanked for assistance with the HRMS ESI⁺ analyses and Sven T. Nappen for the synthesis of the silver carbene complexes. Dr. Dmitry Chernyshov is thanked for his technical support at the SNBL at the ESRF.

REFERENCES

- (1) Kukla, D. L.; Canchola, J.; Mills, J. J. Synthesis of the Cyanobacterial Antibiotics Anaephenes A and B. *J. Nat. Prod.* **2020**, *83* (6), 2036–2040.
- (2) Martín-Gálvez, F.; García-Ruiz, C.; Sánchez-Ruiz, A.; Valeriote, F. A.; Sarabia, F. An Array of Bengamide E Analogues Modified at the Terminal Olefinic Position: Synthesis and Antitumor Properties. *ChemMedChem.* **2013**, *8* (5), 819–831.
- (3) Teranishi, T.; Kuwahara, S. Stereoselective Approach to the DEF Ring System of Terpendole E. *Tetrahedron Lett.* **2014**, *55* (8), 1486–1487.
- (4) Schulz, M. D.; Wagener, K. B. Precision Polymers through ADMET Polymerization. *Macromol. Chem. Phys.* **2014**, *215* (20), 1936–1945.
- (5) Wittig, G.; Schöllkopf, U. Über Triphenyl-phosphin-methylene Als Olefinbildende Reagenzien (I. Mitteil. *Chem. Ber.* **1954**, *87* (9), 1318–1330.
- (6) Wadsworth, W. S.; Emmons, W. D. The Utility of Phosphonate Carbanions in Olefin Synthesis. *J. Am. Chem. Soc.* **1961**, *83* (7), 1733–1738.
- (7) Julia, M.; Paris, J.-M. Syntheses a l'aide de Sulfones v(+)-Methode de Synthese Generale de Doubles Liaisons. *Tetrahedron Lett.* **1973**, *14* (49), 4833–4836.
- (8) *Olefin Metathesis: Theory and Practice*; Grell, K., Ed.; John Wiley & Sons, Inc.: Hoboken, NJ, USA, 2014. DOI: [10.1002/9781118711613](https://doi.org/10.1002/9781118711613).
- (9) *Handbook of Metathesis*; Grubbs, R. H., Wenzel, A. G., O'Leary, D. J., Khosravi, E., Eds.; Wiley-VCH Verlag GmbH & Co. KGaA: Weinheim, Germany, 2015. DOI: [10.1002/9783527674107](https://doi.org/10.1002/9783527674107).
- (10) Trnka, T. M.; Grubbs, R. H. The Development of L₂X₂RuCHR Olefin Metathesis Catalysts: An Organometallic Success Story. *Acc. Chem. Res.* **2001**, *34* (1), 18–29.
- (11) Piola, L.; Nahra, F.; Nolan, S. P. Olefin Metathesis in Air. *Beilstein J. Org. Chem.* **2015**, *11*, 2038–2055.
- (12) Kajetanowicz, A.; Chwalba, M.; Gawin, A.; Tracz, A.; Grell, K. Non-Glovebox Ethenolysis of Ethyl Oleate and FAME at Larger Scale Utilizing a Cyclic (Alkyl)(Amino)Carbene Ruthenium Catalyst. *Eur. J. Lipid Sci. Technol.* **2020**, *122* (1), 1900263.
- (13) Walensky, L. D.; Bird, G. H. Hydrocarbon-Stapled Peptides: Principles, Practice, and Progress: Miniperspective. *J. Med. Chem.* **2014**, *57* (15), 6275–6288.
- (14) Vinogradova, E. V. Organometallic Chemical Biology: An Organometallic Approach to Bioconjugation. *Pure Appl. Chem.* **2017**, *89* (11), 1619–1640.
- (15) Isenegger, P. G.; Davis, B. G. Concepts of Catalysis in Site-Selective Protein Modifications. *J. Am. Chem. Soc.* **2019**, *141* (20), 8005–8013.
- (16) Messina, M. S.; Maynard, H. D. Modification of Proteins Using Olefin Metathesis. *Mater. Chem. Front.* **2020**, *4* (4), 1040–1051.
- (17) Higman, C. S.; Lummiss, J. A. M.; Fogg, D. E. Olefin Metathesis at the Dawn of Implementation in Pharmaceutical and Specialty-Chemicals Manufacturing. *Angew. Chem., Int. Ed.* **2016**, *55* (11), 3552–3565.
- (18) Yu, M.; Lou, S.; Gonzalez-Bobes, F. Ring-Closing Metathesis in Pharmaceutical Development: Fundamentals, Applications, and Future Directions. *Org. Process Res. Dev.* **2018**, *22* (8), 918–946.
- (19) Cink, R. D.; Lukin, K. A.; Bishop, R. D.; Zhao, G.; Pelc, M. J.; Towne, T. B.; Gates, B. D.; Ravn, M. M.; Hill, D. R.; Ding, C.; Cullen, S. C.; Mei, J.; Leanna, M. R.; Henle, J.; Napolitano, J. G.; Nere, N. K.; Chen, S.; Sheikh, A.; Kallemeyn, J. M. Development of the Enabling Route for Glecaprevir via Ring-Closing Metathesis. *Org. Process Res. Dev.* **2020**, *24* (2), 183–200.
- (20) St-Pierre, G.; Cherney, A. H.; Chen, W.; Dong, X.; Dorman, P. K.; Griffin, D. J.; Houk, K. N.; Lin, J. B.; Osgood, S.; Silva Elipse, M. V.; Timmons, H. C.; Xie, Y.; Tedrow, J. S.; Thiel, O. R.; Smith, A. G. Accelerated Development of a Scalable Ring-Closing Metathesis to Manufacture AMG 176 Using a Combined High-Throughput Experimentation and Computational Modeling Approach. *Org. Process Res. Dev.* **2021**, *25* (3), 442–451.
- (21) Choi, T.-L.; Grubbs, R. H. Controlled Living Ring-Opening-Metathesis Polymerization by a Fast-Initiating Ruthenium Catalyst. *Angew. Chem., Int. Ed. Engl.* **2003**, *42* (15), 1743–1746.
- (22) Edwards, J. P.; Wolf, W. J.; Grubbs, R. H. The Synthesis of Cyclic Polymers by Olefin Metathesis: Achievements and Challenges. *J. Polym. Sci. Part Polym. Chem.* **2019**, *57* (3), 228–242.
- (23) Schrock, R. R. Synthesis of Stereoregular ROMP Polymers Using Molybdenum and Tungsten Imido Alkylidene Initiators. *Dalton Trans.* **2011**, *40* (29), 7484–7495.
- (24) Debsharma, T.; Behrendt, F. N.; Laschewsky, A.; Schlaad, H. Ring-Opening Metathesis Polymerization of Biomass-Derived Levoglucosenol. *Angew. Chem., Int. Ed.* **2019**, *58* (20), 6718–6721.
- (25) Jung, K.; Ahmed, T. S.; Lee, J.; Sung, J.-C.; Keum, H.; Grubbs, R. H.; Choi, T.-L. Living β -Selective Cyclopolymerization Using Ru Dithiolate Catalysts. *Chem. Sci.* **2019**, *10* (39), 8955–8963.
- (26) Feist, J. D.; Xia, Y. Enol Ethers Are Effective Monomers for Ring-Opening Metathesis Polymerization: Synthesis of Degradable

- and Depolymerizable Poly(2,3-Dihydrofuran). *J. Am. Chem. Soc.* **2020**, *142* (3), 1186–1189.
- (27) Foster, J. C.; Grocott, M. C.; Arkininstall, L. A.; Varlas, S.; Redding, M. J.; Grayson, S. M.; O'Reilly, R. K. It Is Better with Salt: Aqueous Ring-Opening Metathesis Polymerization at Neutral pH. *J. Am. Chem. Soc.* **2020**, *142* (32), 13878–13885.
- (28) Rizzo, A.; Peterson, G. I.; Bhaumik, A.; Kang, C.; Choi, T.-L. Sugar-Based Polymers from d-Xylose: Living Cascade Polymerization, Tunable Degradation, and Small Molecule Release. *Angew. Chem., Int. Ed.* **2021**, *60* (2), 849–855.
- (29) Debsharma, T.; Schmidt, B.; Laschewsky, A.; Schlaad, H. Ring-Opening Metathesis Polymerization of Unsaturated Carbohydrate Derivatives: Levoglucosanyl Alkyl Ethers. *Macromolecules* **2021**, *54* (6), 2720–2728.
- (30) Dong, Y.; Matson, J. B.; Edgar, K. J. Olefin Cross-Metathesis in Polymer and Polysaccharide Chemistry: A Review. *Biomacromolecules* **2017**, *18* (6), 1661–1676.
- (31) Montgomery, T. P.; Johns, A. M.; Grubbs, R. H. Recent Advancements in Stereoselective Olefin Metathesis Using Ruthenium Catalysts. *Catalysts* **2017**, *7* (3), 87.
- (32) Ogba, O. M.; Warner, N. C.; O'Leary, D. J.; Grubbs, R. H. Recent Advances in Ruthenium-Based Olefin Metathesis. *Chem. Soc. Rev.* **2018**, *47* (12), 4510–4544.
- (33) Vougioukalakis, G. C.; Grubbs, R. H. Ruthenium-Based Heterocyclic Carbene-Coordinated Olefin Metathesis Catalysts. *Chem. Rev.* **2010**, *110* (3), 1746–1787.
- (34) Fürstner, A. Teaching Metathesis “Simple” Stereochemistry. *Science* **2013**, *341* (6152), 1229713.
- (35) Müller, D. S.; Baslé, O.; Mauduit, M. A Tutorial Review of Stereoretentive Olefin Metathesis Based on Ruthenium Dithiolate Catalysts. *Beilstein J. Org. Chem.* **2018**, *14* (1), 2999–3010.
- (36) Dawood, K. M.; Nomura, K. Recent Developments in Z-Selective Olefin Metathesis Reactions by Molybdenum, Tungsten, Ruthenium, and Vanadium Catalysts. *Adv. Synth. Catal.* **2021**, *363* (8), 1970–1997.
- (37) Dang, Y.; Wang, Z.-X.; Wang, X. A Thorough DFT Study of the Mechanism of Homodimerization of Terminal Olefins through Metathesis with a Chelated Ruthenium Catalyst: From Initiation to Z Selectivity to Regeneration. *Organometallics* **2012**, *31* (20), 7222–7234.
- (38) Bronner, S. M.; Herbert, M. B.; Patel, P. R.; Marx, V. M.; Grubbs, R. H. Ru-Based Z-Selective Metathesis Catalysts with Modified Cyclometalated Carbene Ligands. *Chem. Sci.* **2014**, *5* (10), 4091–4098.
- (39) Herbert, M. B.; Suslick, B. A.; Liu, P.; Zou, L.; Dornan, P. K.; Houk, K. N.; Grubbs, R. H. Cyclometalated Z-Selective Ruthenium Metathesis Catalysts with Modified N-Chelating Groups. *Organometallics* **2015**, *34* (12), 2858–2869.
- (40) Dang, Y.; Wang, Z.-X.; Wang, X. Does the Ruthenium Nitrate Catalyst Work Differently in Z-Selective Olefin Metathesis? A DFT Study. *Organometallics* **2012**, *31* (24), 8654–8657.
- (41) Endo, K.; Grubbs, R. H. Chelated Ruthenium Catalysts for Z-Selective Olefin Metathesis. *J. Am. Chem. Soc.* **2011**, *133* (22), 8525–8527.
- (42) Dumas, A.; Tarrieu, R.; Vives, T.; Roisnel, T.; Dorcet, V.; Baslé, O.; Mauduit, M. A Versatile and Highly Z-Selective Olefin Metathesis Ruthenium Catalyst Based on a Readily Accessible N-Heterocyclic Carbene. *ACS Catal.* **2018**, *8* (4), 3257–3262.
- (43) Xu, Y.; Wong, J. J.; Samkian, A. E.; Ko, J. H.; Chen, S.; Houk, K. N.; Grubbs, R. H. Efficient Z-Selective Olefin-Acrylamide Cross-Metathesis Enabled by Sterically Demanding Cyclometalated Ruthenium Catalysts. *J. Am. Chem. Soc.* **2020**, *142* (50), 20987–20993.
- (44) Occhipinti, G.; Törnroos, K. W.; Jensen, V. R. Pyridine-Stabilized Fast-Initiating Ruthenium Monothiolate Catalysts for Z-Selective Olefin Metathesis. *Organometallics* **2017**, *36* (17), 3284–3292.
- (45) Occhipinti, G.; Hansen, F. R.; Törnroos, K. W.; Jensen, V. R. Simple and Highly Z-Selective Ruthenium-Based Olefin Metathesis Catalyst. *J. Am. Chem. Soc.* **2013**, *135* (9), 3331–3334.
- (46) Occhipinti, G.; Koudriavtsev, V.; Törnroos, K. W.; Jensen, V. R. Theory-Assisted Development of a Robust and Z-Selective Olefin Metathesis Catalyst. *Dalton Trans.* **2014**, *43* (29), 11106–11117.
- (47) Nelson, J. W.; Grundy, L. M.; Dang, Y.; Wang, Z.-X.; Wang, X. Mechanism of Z-Selective Olefin Metathesis Catalyzed by a Ruthenium Monothiolate Carbene Complex: A DFT Study. *Organometallics* **2014**, *33* (16), 4290–4294.
- (48) Smit, W.; Koudriavtsev, V.; Occhipinti, G.; Törnroos, K. W.; Jensen, V. R. Phosphine-Based Z-Selective Ruthenium Olefin Metathesis Catalysts. *Organometallics* **2016**, *35*, 1825–1837.
- (49) Smit, W.; Ekeli, J. B.; Occhipinti, G.; Woźniak, B.; Törnroos, K. W.; Jensen, V. R. Z-Selective Monothiolate Ruthenium Indenylidene Olefin Metathesis Catalysts. *Organometallics* **2020**, *39* (3), 397–407.
- (50) Renom-Carrasco, M.; Mania, P.; Sayah, R.; Veyre, L.; Occhipinti, G.; Jensen, V. R.; Thieuleux, C. Silica-Supported Z-Selective Ru Olefin Metathesis Catalysts. *Mol. Catal.* **2020**, *483*, No. 110743.
- (51) Khan, R. K.; Torker, S.; Hoveyda, A. H. Reactivity and Selectivity Differences between Catecholate and Catechthiolate Ru Complexes. Implications Regarding Design of Stereoselective Olefin Metathesis Catalysts. *J. Am. Chem. Soc.* **2014**, *136* (41), 14337–14340.
- (52) Koh, M. J.; Khan, R. K. M.; Torker, S.; Yu, M.; Mikus, M. S.; Hoveyda, A. H. High-Value Alcohols and Higher-Oxidation-State Compounds by Catalytic Z-Selective Cross Metathesis. *Nature* **2015**, *517* (7533), 181–186.
- (53) Xu, C.; Shen, X.; Hoveyda, A. H. In Situ Methylene Capping: A General Strategy for Efficient Stereoretentive Catalytic Olefin Metathesis. The Concept, Methodological Implications, and Applications to Synthesis of Biologically Active Compounds. *J. Am. Chem. Soc.* **2017**, *139* (31), 10919–10928.
- (54) Liu, Z.; Xu, C.; Del Pozo, J.; Torker, S.; Hoveyda, A. H. Ru-Based Catechthiolate Complexes Bearing an Unsaturated NHC Ligand: Effective Cross-Metathesis Catalysts for Synthesis of (Z)-Alpha,Beta-Unsaturated Esters, Carboxylic Acids, and Primary, Secondary, and Weinreb Amides. *J. Am. Chem. Soc.* **2019**, *141* (17), 7137–7146.
- (55) Reim, I.; Occhipinti, G.; Törnroos, K. W.; Fogg, D. E.; Jensen, V. R. Toward E-Selective Olefin Metathesis: Computational Design and Experimental Realization of Ruthenium Thio-Indolate Catalysts. *Top. Catal.* **2022**, *65* (1–4), 448–461.
- (56) Montgomery, T. P.; Grandner, J. M.; Houk, K. N.; Grubbs, R. H. Synthesis and Evaluation of Sterically Demanding Ruthenium Dithiolate Catalysts for Stereoretentive Olefin Metathesis. *Organometallics* **2017**, *36* (20), 3940–3953.
- (57) Chung, C. K.; Grubbs, R. H. Olefin Metathesis Catalyst: Stabilization Effect of Backbone Substitutions of N-Heterocyclic Carbene. *Org. Lett.* **2008**, *10* (13), 2693–2696.
- (58) Kuhn, K. M.; Bourg, J.-B.; Chung, C. K.; Virgil, S. C.; Grubbs, R. H. Effects of NHC-Backbone Substitution on Efficiency in Ruthenium-Based Olefin Metathesis. *J. Am. Chem. Soc.* **2009**, *131* (14), 5313–5320.
- (59) Fukata, Y.; Asano, K.; Matsubara, S. Facile Net Cycloaddition Approach to Optically Active 1,5-Benzothiazepines. *J. Am. Chem. Soc.* **2015**, *137* (16), 5320–5323.
- (60) Thiam, A.; Jojoiu, C.; Leprêtre, J. C.; Sanchez, J. Y. Lithium Salts Based on a Series of New Aniliny-Perfluorosulfonamide Salts and Their Polymer Electrolytes. *J. Power Sources* **2017**, *364*, 138–147.
- (61) Hirano, K.; Urban, S.; Wang, C.; Glorius, F. A Modular Synthesis of Highly Substituted Imidazolium Salts. *Org. Lett.* **2009**, *11* (4), 1019–1022.
- (62) Aidouni, A.; Demonceau, A.; Delaude, L. Microwave-Assisted Synthesis of N-Heterocyclic Carbene Precursors. *Synlett* **2006** (03), 0493–0495.
- (63) Rayner, P. J.; Norcott, P.; Appleby, K. M.; Iali, W.; John, R. O.; Hart, S. J.; Whitwood, A. C.; Duckett, S. B. Fine-Tuning the Efficiency

of Para-Hydrogen-Induced Hyperpolarization by Rational N-Heterocyclic Carbene Design. *Nat. Commun.* **2018**, *9* (1), 4251.

(64) Johns, A. M.; Ahmed, T. S.; Jackson, B. W.; Grubbs, R. H.; Pederson, R. L. High Trans Kinetic Selectivity in Ruthenium-Based Olefin Cross-Metathesis through Stereoretention. *Org. Lett.* **2016**, *18* (4), 772–775.

(65) Poater, A.; Cavallo, L. Mechanistic Insights into the Double C–H (de)Activation Route of a Ru-Based Olefin Metathesis Catalyst☆. *J. Mol. Catal. Chem.* **2010**, *324* (1–2), 75–79.

(66) Hong, S. H.; Chlenov, A.; Day, M. W.; Grubbs, R. H. Double C–H Activation of an N-Heterocyclic Carbene Ligand in a Ruthenium Olefin Metathesis Catalyst. *Angew. Chem., Int. Ed.* **2007**, *46* (27), 5148–5151.

(67) Grisi, F.; Mariconda, A.; Costabile, C.; Bertolasi, V.; Longo, P. Influence of Syn and Anti Configurations of NHC Backbone on Ru-Catalyzed Olefin Metathesis. *Organometallics* **2009**, *28* (17), 4988–4995.

(68) Ritter, T.; Day, M. W.; Grubbs, R. H. Rate Acceleration in Olefin Metathesis through a Fluorine-Ruthenium Interaction. *J. Am. Chem. Soc.* **2006**, *128* (36), 11768–11769.

(69) Mikus, M. S.; Torker, S.; Xu, C.; Li, B.; Hoveyda, A. H. Pentacoordinate Ruthenium(II) Catecholthiolate and Mercaptophenolate Catalysts for Olefin Metathesis: Anionic Ligand Exchange and Ease of Initiation. *Organometallics* **2016**, *35* (22), 3878–3892.

(70) Mikus, M. S.; Torker, S.; Hoveyda, A. H. Controllable ROMP Tacticity by Harnessing the Fluxionality of Stereogenic-at-Ruthenium Complexes. *Angew. Chem., Int. Ed.* **2016**, *55* (16), 4997–5002.

(71) Occhipinti, G.; Bjørsvik, H. R.; Jensen, V. R. Quantitative Structure–Activity Relationships of Ruthenium Catalysts for Olefin Metathesis. *J. Am. Chem. Soc.* **2006**, *128* (21), 6952–6964.

(72) Occhipinti, G.; Nascimento, D. L.; Foscatto, M.; Fogg, D. E.; Jensen, V. R. The Janus Face of High Trans-Effect Carbenes in Olefin Metathesis: Gateway to Both Productivity and Decomposition. *Chem. Sci.* **2022**, *13* (18), 5107–5117.

Supplementary Information for:

Pursuing *E*-Selective Olefin Metathesis: Tuning
Steric and Electronic Properties of S,N-Chelated
Ruthenium Alkylidenes

*Immanuel Reim, Giovanni Occhipinti, Karl W. Törnroos, Vidar R. Jensen**

Department of Chemistry, University of Bergen, Allégaten 41, N-5007 Bergen, Norway

Table of Contents

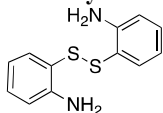
S1	Experimental Procedures and Additional Experimental Results	S3
S1.1	General Procedures	S3
S1.2	Synthesis of L4	S4
S1.3	Synthesis of L5	S4
S1.4	Synthesis of L2H₂	S4
S1.5	Synthesis of L6	S4
S1.6	Synthesis of Ru7	S5
S1.7	Synthesis of L9a	S5
S1.8	Synthesis of L9b	S6
S1.9	Synthesis of Ag1a	S6
S1.10	Synthesis of Ag1b	S7
S1.11	Synthesis of Ru8a	S7
S1.12	Synthesis of Ru8b	S7
S1.13	Synthesis of Ru8c	S8
S1.14	Synthesis of Ru8d	S8
S1.15	Synthesis of Ru9a	S9
S1.16	Synthesis of Ru9b	S9
S1.17	Synthesis of Ru9c	S10
S1.18	Synthesis of Ru9d	S10
S1.19	Synthesis of Ru12	S10
S1.20	Stability of Ru12 in Solution	S11
S1.21	Representative Procedure for Self-Metathesis of Propene	S12
S1.22	Representative Procedure for Self-Metathesis of 1-Octene	S12
S1.23	Representative Procedure for Self-Metathesis of Methyl Oleate	S12
S1.24	Representative Procedure for Self-Metathesis of Methyl Elaidate	S13
S1.25	Representative Procedure for Ring-Opening Metathesis Polymerization of 2-Norbornene	S13
S1.26	Representative Procedure for Ring-Opening Metathesis Polymerization of 1,5-Cyclooctadiene	S14
S2	Computational Methods	S15
S2.1	Geometry Optimization	S15
S2.2	Single-Point (SP) Energy Calculations	S15
S2.3	Calculations of Free Energies Including Standard-State Corrections	S16
S3	Computational Results	S17
S3.1	Comparison of the <i>E</i> -2-butene pathway of catalyst Ru5 , Ru12 and Ru12'	S17
S3.2	Computational Results of Ru12	S17
S4	NMR Spectra	S20
S5	X-ray Crystal Structures	S31
S5.1	X-ray Crystal Structure of L9a	S31
S5.2	X-ray Crystal Structure of Ag1b	S32
S5.3	X-ray Crystal Structure of Ru7	S33
S5.4	X-ray Crystal Structure of Ru9b	S34
S5.5	X-ray Crystal Structure of Ru10	S35
S5.6	X-ray Crystal Structure of Ru12	S36

S1 Experimental Procedures and Additional Experimental Results

S1.1 General Procedures

Reactions were carried out in an argon-filled glovebox at room temperature (25 ± 2 °C), unless otherwise indicated. Solvents were dried and degassed using a MBraun SPS-800 solvent purification system, then stored under argon in the glovebox over 4 Å molecular sieves for at least 16 h prior to use, unless otherwise indicated. Liquid reagents were degassed by five consecutive freeze/pump/thaw cycles, and then stored under argon in the glovebox freezer (-35 °C). Allylbenzene, methyl elaidate, methyl oleate, pyridine, potassium hydride, and propene were obtained from Sigma Aldrich. Potassium 7-sulfidoindol-1-ide **L10**¹, (1,3-Bis(2-fluoro-6-methylphenyl)-4,4-dimethyl-imidazolidinylidene)dichloro(phenylmethylene)(tricyclohexylphosphine) ruthenium **Ru8d**,² and 4,4,5,5-Tetramethyl-1,3-diphenylimidazolin-2-ylidene)dichloro(phenylmethylene)(tricyclohexylphosphine)ruthenium **Ru8c**³ were prepared according to literature procedures. NMR spectra were recorded on Bruker Biospin AV500 and 850 Ascend spectrometers at 298.0 K, and referenced against the residual proton signals of the deuterated solvents (¹H).⁴ The ¹³C{¹H} was referenced through the solvent ¹³C resonance.⁴ The ³¹P{¹H} spectra were referenced through the solvent lock (²H) signal according to IUPAC recommended method.⁵ HRMS ESI mass spectra were recorded by means of an orthogonal electron spray ionization ion source (ESI) interfaced to a 6546 LC/Q-TOF mass spectrometer from Agilent. The ions were transported into the orthogonal accelerating time-of-flight (TOF) single-stage reflectron mass analyzer by a high-frequency and high-voltage quadrupole ion guide. Detection was achieved with a dual microchannel plate detector. Elemental analyses were performed using an Elementar Vario EL III analyzer. GC quantification was performed on an Agilent 7890A series GC equipped with a flame ionization detector (FID), an Agilent 7683B series autosampler, and an Agilent HP-5 polysiloxane column (30 m length, 320 μm diameter). GC samples were quenched using ca. 10 equivalents of ethyl vinyl ether in THF prior to analysis. Suitable crystals for diffraction experiments were immersed in Paratone-N (Hampton Research) in a nylon loop. Data collection was done at the Swiss-Norwegian Beamlines at the ESRF synchrotron in Grenoble, France, using Si double-mirror monochromated radiation ($\lambda = 0.62379$ Å) in conjunction with a 360-degree phi-scan and a Pilatus2M detector.

S1.2 Synthesis of L4

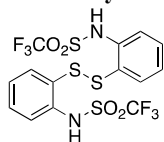


Procedure was modified from literature.⁶ 2-Aminothiophenol (1.25g, 10 mmol), KI (41 mg, 0.25 mmol), 1 mL 35% hydrogen peroxide in 30 mL EtOAc were placed in a reaction flask at 0 °C. 4 mL of EtOH was added to homogenize the solutions. After 2 h reaction time, it was allowed to warm up to room temperature and the organic layer was extracted three times with 1 M NaOH. The extracted aqueous fractions were acidified with 1 M HCl until pH 1. The precipitated product was filtered, washed with water and dried under reduced pressure to afford compound **2** as white solid. It was used without further purification.

Yield: 1.22 g (98%).

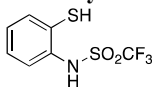
¹H NMR (850.13 MHz, CDCl₃): δ = 7.16 (m, 4 H), 6.71 (dd, *J* = 1.2, 7.5 Hz, 2H), 6.57 (td, *J* = 1.2, 7.5 Hz 2H), 4.32 (s, 4H).

S1.3 Synthesis of L5



Procedure was modified from literature.⁷ Under argon, **L4** (616 mg, 2.48 mmol) was dissolved in 10mL DCM and cooled to -78 °C. To this solution, Et₃N (1 mL, 7.44 mmol) was added, followed by trifluoromethanesulfonic anhydride (1 mL, 6.45 mmol). The reaction was stirred at -78 °C for 10 min before it was slowly warmed up to rt over 2h. The reaction was quenched with 4N aqueous HCl and extracted with DCM (10 mL x 2). The combined organic layers were washed with brine, dried over MgSO₄ and concentrated in vacuo. It was used without further purification. Yield: 1.5 g (122%).

S1.4 Synthesis of L2H₂

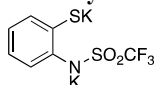


Procedure was taken from literature.⁶ Compound **L5** (640 mg, 1.25 mmol, 1.0 equiv.) was added to a solution obtained dissolving PPh₃ (721 mg, 2.75 mmol, 2.2 equiv.) in 4 mL THF/H₂O (1:1). The mixture was stirred for 30 min. The mixture was then extracted with DCM (15 ml x 3). The extract was first washed with water followed by brine, dried over MgSO₄ and concentrated in vacuo. The resulting solid was purified using flash chromatography (eluent: hexane/DCM (2:3), R_f = 0.35).

Yield: 95 mg (15%).

¹H NMR (850.13 MHz, CDCl₃): δ = 7.58 (d, *J* = 8.1 Hz, 1H), 7.55 (d, *J* = 8.1 Hz, 1H), 7.40 (b, 1H), 7.33 (t, *J* = 7.9 Hz, 1H), 7.19 (t, *J* = 7.9, 1H), 3.26 (s, 1H). ¹³C {¹H} NMR (213.77 MHz, CDCl₃): δ = 135.2, 129.6, 128.3, 122.8, 121.2, 119.1. HRMS (ESI⁻): calculated for C₇H₅F₃NO₂S₂ [M - H]⁻: m/z = 255.9719, found m/z = 255.9719.

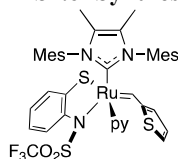
S1.5 Synthesis of L6



To 66.9 mg (0.26 mmol, 1.00 equiv.) of **L2H₂** in 8 mL THF was added 21.7 mg of KH (0.52 mmol, 2.05 equiv.) and the mixture was stirred for 14 h. The solvent was removed

under reduced pressure. The weight of the dried solid indicated a quantitative conversion to **L6**. The compound was used without further purification.

S1.6 Synthesis of Ru7

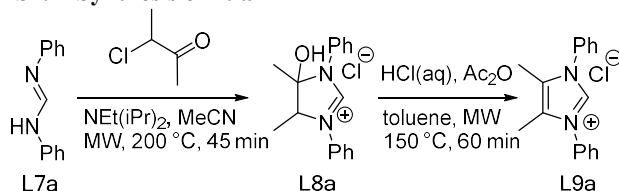


In a glovebox, a 20 mL vial was charged with 43.9 mg (0.06 mmol, 1.0 equiv.) of **Ru6**,¹ 1 mL THF, and 26.0 mg (0.08 mmol, 1.3 equiv.) of the dipotassium salt **L6**. A color change from green to yellow was observed immediately. After 15 min the reaction was completed, and the solvent was removed under reduced pressure. The crude reaction mixture was redissolved in toluene, filtered through celite, and concentrated to about 0.5 mL. To this solution 5 mL hexane was added and cooled to $-35\text{ }^{\circ}\text{C}$ for 15 h. The resulting solid was collected and washed with cold hexane ($2 \times 4\text{ mL}$) to yield the desired product as red microcrystalline solid. ^1H NMR of the complex showed broad signals for all protons making difficult the characterization of the complex by NMR.

Yield: 83 mg (96 %).

^1H NMR (850.13 MHz, C_6D_6): $\delta = 16.15$ (b, 1H), 8.35 (2H), 8.07 (1H), 7.91 (1H), 7.1 (1H), 7.0 (1H), 6.9-7.0 (4H), 6.9-7.0 (6H), 2.02 (b, 12H), 1.83 (b, 6H), 1.35 (s, 6H). $^{13}\text{C}\{^1\text{H}\}$ NMR (213.77 MHz, C_6D_6): $\delta = 150.26, 141.60, 139.21, 136.52, 135.58, 134.73, 129.66, 129.32, 123.10, 121.64, 20.68, 18.59, 17.78, 8.57$.

S1.7 Synthesis of L9a

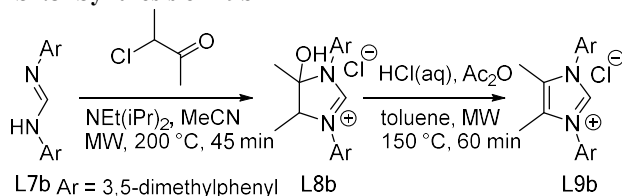


A microwave reactor was charged with *N,N'*-diphenylformamidine **L7a** (1177.4 mg, 6 mmol) and 12 ml MeCN. DIPEA (930.6 mg, 1.25 mL, 7.2 mmol) and 3-chloro-2-butanone (1278.0 mg, 1.21 mL, 12 mmol) was added subsequently. The reactor was capped and placed into the microwave reactor (adsorption = normal, time = 45 min, $T = 200\text{ }^{\circ}\text{C}$). The volatiles were slowly removed using the rotary evaporator. After the rotary evaporator reached its maximum power, the flask was transferred to a Schlenk line to remove the residual volatiles. Without further purification, the reactor was charged with 15 mL toluene, 2.4 mL Ac_2O and 1.2 mL HCl(aq) and placed into the microwave (adsorption = normal, time = 60 min, $T = 150\text{ }^{\circ}\text{C}$). The finished reaction mixture was poured into a separatory funnel filled with 200 mL H_2O and 100 ml DCM. The reactor vessel was then rinsed with an additional 50 mL of DCM, and the resulting solution was also transferred to the separatory funnel. The aqueous phase was extracted with DCM ($3 \times 150\text{ mL}$) and the combined organic phases dried over MgSO_4 . After removal of the volatiles, the oily residue was left. This residue was further purified by automatic flash chromatography (eluent: DCM: methanol $0 \rightarrow 10\%$). The resulting fractions were combined and recrystallized using EtOAc layered with hexane at $8\text{ }^{\circ}\text{C}$.

Yield: 515 mg (30.2 %).

^1H NMR (850.13 MHz, CDCl_3): δ = 9.61 (s, 1H), 7.81 (m, 4H), 7.52 (m, 6H), 2.20 (s, 6H). $^{13}\text{C}\{^1\text{H}\}$ NMR (213.77 MHz, C_6D_6): δ = 135.65, 133.2, 130.9, 130.2, 127.5, 126.5, 9.5. HRMS (ESI $^+$): calculated for $\text{C}_{17}\text{H}_{17}\text{N}_2$ $[\text{M} - \text{Cl}]^+$: m/z = 249.1383, found: m/z = 249.1394.

S1.8 Synthesis of L9b

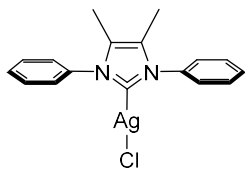


A microwave reactor was charged with *N,N'*-di(3,5-dimethylphenyl)formamidine **L7b** (1514.2 mg, 6 mmol) and 12 ml MeCN. DIPEA (930.6 mg, 1.25 mL, 7.2 mmol) and 3-chloro-2-butanone (1278.0 mg, 1.21 mL, 12 mmol) were added subsequently. The reactor was capped and placed into the microwave (adsorption = normal, time = 45 min, T = 200 °C). Afterwards, the reactor was connected to the rotary evaporator, and the volatiles were slowly removed. After the rotary evaporator reached its maximum power, the flask was transferred to a Schlenk line to remove the residual volatiles. Without further purification, the reactor was charged with toluene, Ac_2O and HCl and placed into the microwave (adsorption = normal, time = 60 min, T = 150 °C). The finished reaction mixture was poured into a separation funnel filled with 200 mL H_2O and 100 ml DCM. 50 mL DCM was used to rinse the reactor vessel. The aqueous phase was extracted with DCM (3×150 mL) and the combined organic phases dried over MgSO_4 . After removal of the volatiles, the oily residue was left. This residue was further purified using an automatic flash chromatography (eluent: DCM: methanol 0 \rightarrow 10%). The resulting fractions were combined and recrystallized using EtOAc layered with hexane at 8 °C.

Yield: 760 mg (44.5%).

^1H NMR (500.13 MHz, CDCl_3): δ = 9.79 (s, 1H), 7.37 (s, 4H), 7.16 (s, 2H), 2.40 (s, 12H), 2.23 (s, 6H). $^{13}\text{C}\{^1\text{H}\}$ NMR (213.77 MHz, C_6D_6): δ = 140.36, 135.6, 133.0, 132.4, 127.3, 123.8, 21.4, 9.5. HRMS (ESI $^+$): calculated for $\text{C}_{21}\text{H}_{25}\text{N}_2$ $[\text{M} - \text{Cl}]^+$: m/z = 305.2018, found m/z = 305.2020

S1.9 Synthesis of Ag1a



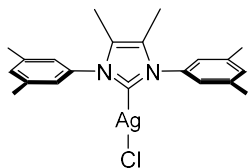
To a 5 mL suspension of Ag_2O (400.3 mg, 1.73 mmol) in DCM, **L9a** (101.2 mg, 0.36 mmol) was added. The solution was stirred in the dark at room temperature for 20 hours. The solution was then dried *in-vacuo*, and the product was extracted with toluene and filtered through a glass-fiber filter paper. The filtrate was dried, and a concentrated solution in DCM was made. Layering cold pentane over the solution resulted in

the formation of white needle-like crystals.

Yield: 32.5 mg (23.0%).

^1H NMR (500.13 MHz, C_6D_6): δ = 1.37 (s, 6H, $\text{NC}(\text{CH}_3)=\text{C}(\text{CH}_3)\text{N}$), 7.01 (s, 10H, N-Ph).

S1.10 Synthesis of Ag1b



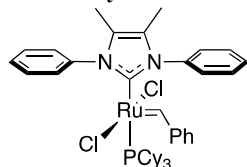
To a suspension of Ag₂O (209.5 mg, 0.9 mmol) in 5 mL DCM, **L9b** (101.2 mg, 0.30 mmol) was added. The solution was stirred in the dark at room temperature for 20 hours, before the solution was dried *in vacuo*, and the product was extracted with toluene and filtered through a glass-fiber filter paper. The filtrate was dried, and a concentrated DCM solution was made. Layering cold pentane over the solution

formed white needle-like crystals.

Yield: 31.4 mg (19.5%).

¹H NMR (500.13 MHz, C₆D₆): δ = 1.50 (s, 6H, NC(CH₃)=C(CH₃)N), 2.06 (d, J(H,H)=0.45 Hz, 12H, NAr-CH₃), 6.67 (t, J(H,H)=0.72, 2H, Ar-*p*-H), 6.78 (s 'br', 4H, Ar-*o*-H).

S1.11 Synthesis of Ru8a



In a glovebox, imidazolium salt **L9a** (48.12 mg, 0.17 mmol), KHMDS (35.59 mg, 0.18 mmol) and Grubbs first generation catalyst (139.9 mg, 0.17 mmol) were weighted into three separate 20 mL vials, each dissolved/suspended in THF (6 mL), equipped with a magnetic stir bar and the solution/suspension were chilled to -35 °C. The KHMDS solution was transferred into the vial containing **L9a** and stirred for five

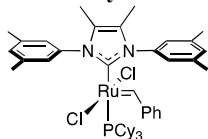
minutes to generate the free carbene **Me2IPh**. The carbene solution was then added to the vial containing the ruthenium catalyst at -35 °C and stirred for 5 min before allowing to warm up to room temperature over 1 h. The reaction was subsequently devolatilized under reduced pressure and triturated with hexane (2 × 5 mL). The remaining solid was washed three times with hexane, redissolved in toluene, filtered through celite, and finally dried in vacuum to yield a red solid.

Yield: 100 mg (74%). Replacing the in-situ generated carbene with the silver complex **Ag1a** did not improve the yield.

¹H NMR (500.13 MHz, C₆D₆): δ = 19.97 (d, 1H), 8.25 (b, 2H), 8.10 (d, 2H), 7.35 (m, 2H), 7.21 (m, 2H), 6.98 (m, 2H), 6.68 (m, 2H), 2.38 (m, 3H), 1.1-1.9 (m, 33H), 1.44 (d, 3H), 1.36 (d, 3H).

³¹P NMR (202.45 MHz, C₆D₆): δ = 22.76. HRMS (ESI⁺): calculated for C₄₂H₅₅ClN₂PRu [M - Cl]⁺: m/z = 755.2835, found m/z = 755.2854.

S1.12 Synthesis of Ru8b



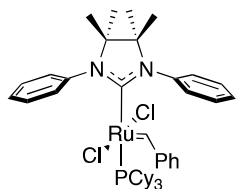
In a glovebox, imidazolium salt **L9b** (68.16 mg, 0.2 mmol), KHMDS (41.9 mg, 0.21 mmol) and Grubbs first generation catalyst (**G1**) (164.6 mg, 0.2 mmol) were weighted into three separate 20 mL vials, each dissolved/suspended in THF (6 mL), equipped with a magnetic stir bar and the solution/suspension were chilled to -35 °C. Then, the KHMDS solution was transferred into the vial containing **L9b** and stirred for five minutes to

generate the free carbene **Me2IXyl**. The carbene solution was then added to the vial containing the ruthenium catalyst at -35 °C and stirred for 5 min before allowing to warm up to room temperature over 1 h. The reaction was subsequently devolatilized under reduced pressure, triturated with hexane (2 × 5 mL), washed three times with hexane, redissolved in toluene, filtered through celite, and dried in vacuum to yield a red solid.

Yield: 100 mg (59%). Replacing the in-situ generated carbene with the silver complex **Ag1b** did not improve the yield.

^1H NMR (850.13 MHz, C_6D_6): δ = 20.03 (d, 1H), 7.84 (2H), 7.20 (3H), 6.97-7.14 (4H), 6.87 (1H), 6.31 (1H), 2.31 (s, 12H), 1.1-1.9 (m, 33H), 1.56 (s, 3H), 1.50 (s, 3H). ^{31}P NMR (202.45 MHz, C_6D_6): δ = 23.10. HRMS (ESI⁺): calculated for $\text{C}_{46}\text{H}_{63}\text{N}_2\text{ClN}_2\text{PRu}$ [$\text{M} - \text{Cl}$]⁺: m/z = 811.3461, found: m/z = 811.3475.

S1.13 Synthesis of Ru8c

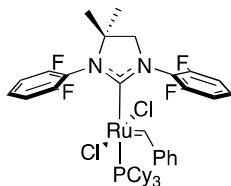


The synthesis was modified from a literature known procedure.³ In a glovebox, 4,4,5,5-tetramethyl-1,3-diphenyl-4,5-dihydro-1H-imidazol-3-ium chloride (94.4 mg, 0.30 mmol), KHMDS (71.8 mg, 0.36 mmol) and Grubbs first generation catalyst (**GI**) (206 mg, 0.25 mmol) were weighted into three separate 20 mL vials, each dissolved/suspended in THF (6 mL) and equipped with a magnetic stir bar. Afterwards, the solution/suspension were chilled to -35°C . Then, the KHMDS solution was added to the vial containing 4,4,5,5-tetramethyl-1,3-diphenyl-4,5-dihydro-1H-imidazol-3-ium chloride to generate the free carbene **MeIPh**. After the reaction was stirred for 30 min at -35°C , it was added to the cold suspension of **GI**. This reaction was allowed to slowly warm up to room temperature for 1 h. The conversion was monitored via ^1H NMR and an additional equivalent of **MeIPh** solution was added to the reaction mixture until the conversion reached more than 80%. The reaction was subsequently devolatilized, triturated with hexane (2×5 mL), washed three times with hexane, redissolved in toluene, filtered through celite, and dried in vacuum to yield a red solid.

Yield: 170 mg (83%).

The recorded ^1H NMR spectrum was consistent with literature data.³

S1.14 Synthesis of Ru8d



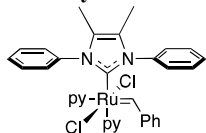
The synthesis was modified from a literature known procedure.² In a glovebox, 1,3-bis(2,6-difluorophenyl)-4,4-dimethyl-4,5-dihydro-1H-imidazol-3-ium tetrafluoroborate (216 mg, 0.53 mmol), sodium *tert*-butoxide (53.7 mg, 0.56 mmol) and Grubbs first generation catalyst (**GI**) (288 mg, 0.35 mmol) were weighted into three separate 20 mL vials, each dissolved/suspended in THF (6 mL) and equipped with a magnetic stir bar. Afterwards, the solution/suspension were chilled to -35°C . Then, the sodium *tert*-butoxide solution was added to the vial containing the imidazolium salt 1,3-bis(2,6-difluorophenyl)-4,4-dimethyl-4,5-dihydro-1H-imidazol-3-ium tetrafluoroborate. After the reaction had stirred for 30 minutes at -35°C , it was added to the cold suspension of **GI**. This reaction was allowed to slowly warm up to room temperature for 1 h. The conversion was monitored via ^1H NMR and an additional equivalent of NHC solution was added to the reaction mixture until the conversion reached more than 80%. The reaction was subsequently devolatilized, triturated with hexane (2×5 mL), washed three times with hexane, redissolved in toluene, filtered through celite and dried in vacuum to yield a red solid.

Yield: 180 mg (84%).

The recorded ^1H NMR spectrum was consistent with literature data.²

As previously reported,³ **Ru8d** is instable in solution. Our ^1H NMR data shows that the compound slowly converts into Grubbs first generation catalyst and another alkylidene complex, which presumably is the corresponding bis(NHC)-ruthenium benzylidene complex. The analysis suggests, thus, that **Ru8d** decomposes via a disproportionation reaction.

S1.15 Synthesis of Ru9a



In a glovebox, a 20 mL vial, equipped with a magnetic stirring bar and a screw cap, was charged with complex **Ru8a** (79.1 mg, 0.1 mmol) and pyridine (1 mL). The vial was closed, and the mixture stirred at room temperature for 5 min. Upon the addition of pentane (7mL), a green solid was formed which was isolated by filtration through a glass frit, washed

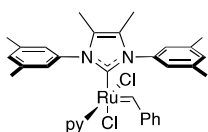
three times with 5 mL pentane and dried on the glass frit to give a green microcrystalline solid.

^1H NMR (850.13 MHz, CDCl_3): δ = 19.54 (s, 1H), 8.72 (d, 2H), 8.53 (m, 2H), 8.50 (d, 2H), 7.90 (d, 2H), 7.39 (t, 2H), 7.27 (m, 2H), 7.22 (m, 1H), 7.13 (d, 2H), 7.02 (m, 1H), 6.91 (t, 2H), 6.80 (m, 2H), 6.66 (m, 2H), 6.55 (m, 1H), 6.27 (m, 2H), 1.68 (s, 3H), 1.45 (s, 3H).

Yield: 3 mg (5% of yield).

A tiny amount of another alkylidene complex ($\delta_{\text{RuCHPh}} = 17.38$ ppm) was observed in the ^1H NMR spectrum of the reaction mixture. The compound is presumably the corresponding mono-pyridine complex, as the similarity of the alkylidene proton chemical shift with that of compound **Ru9b** ($\delta_{\text{RuCHPh}} = 17.53$ ppm) strongly suggests. This impurity disappeared, however, upon purification.

S1.16 Synthesis of Ru9b



In a glovebox, a 20 mL vial, equipped with a magnetic stirring bar and a screw cap, was charged with complex **Ru8b** (90.3 mg, 0.12 mmol) and pyridine (1 mL). The vial was closed, and the mixture stirred at room temperature for 5 min. Upon the addition of pentane (7mL), a green solid was formed which was isolated by filtration through a glass frit, washed

three times with 5 mL pentane and dried in the glovebox to give a green microcrystalline solid.

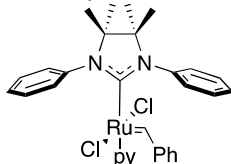
A tiny amount of another alkylidene complex ($\delta_{\text{RuCHPh}} = 19.62$ ppm) was observed in the ^1H NMR spectrum. The compound is presumably the corresponding bis-pyridine complex, as the similarity of the alkylidene proton chemical shift with that of compound **Ru9a** ($\delta_{\text{RuCHPh}} = 19.54$ ppm) strongly suggests. Crystals suitable for X-Ray analysis were grown by layering a concentrated DCM solution of **Ru9b** with pentane at -35 °C.

Yield: 15 mg (23% of yield).

^1H NMR (850.13 MHz, C_6D_6): δ = 17.52 (s, 1H), 9.51 (1H), 8.43 (m, 4H), 7.80 (s, 1H), 7.30 (dt, 1H), 7.06 (dt, 2H), 6.75 (d, 2H), 6.64 (m, 1H), 6.50 (tt, 1H), 6.05 (tt, 2H), 5.79 (1H), 2.81 (b, 3H), 2.19 (s, 3H), 1.73 (b, 3H), 1.68 (s, 3H), 1.52 (s, 3H), 1.45 (s, 3H). $^{13}\text{C}\{^1\text{H}\}$ NMR (213.77 MHz, C_6D_6): δ = 180.31, 158.83, 153.80, 152.15, 141.09, 139.41, 139.41, 137.5, 137.15, 133.50, 131.24, 130.60, 130.11, 139.72, 124.57, 123.42, 122.91, 20.85, 20.23, 9.78, 8.83.

HRMS (ESI $^+$): calculated for $\text{C}_{28}\text{H}_{31}\text{ClN}_2\text{ORu} [\text{M} - \text{C}_5\text{H}_5\text{N} - \text{HCl} + \text{H}_2\text{O}]^+$: $m/z = 548.1168$, found: $m/z = 548.1137$. The peak of the imidazolium cation indicating the loss of the carbene ligand is also detected. HRMS (ESI $^+$): calculated for $\text{C}_{21}\text{H}_{25}\text{N}_2 [\text{NHC} + \text{H}]^+$: $m/z = 305.2017$, found: $m/z = 305.2014$.

S1.17 Synthesis of Ru9c



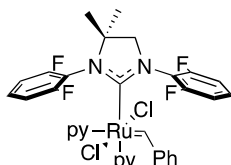
py = pyridine

In a glovebox, a 20 mL vial, equipped with a magnetic stirring bar and a screw cap, was charged with complex **Ru8c** (164.4 mg, 0.20 mmol) and with 1 mL of a pyridine/pentane (1:5) mixture and stirred at -35°C for 5 min. Pentane (7 mL) was then added to the mixture and the formed solid was isolated by vacuum filtration through a glass frit. The solid was washed three times with 5 mL pentane, and dried in the glovebox to give a green microcrystalline solid.

Yield: 32 mg (23% of yield).

^1H NMR (850.13 MHz, C_6D_6): δ = 19.3 (1H), 8.57 (dt J = 5.1, 1.2 Hz, 2H), 8.54 (dt, J = 7.4 Hz, 2H), 7.90 (dd, J = 7.4, 1.1 Hz, 2H), 7.36 (m, 2H), 7.30 (m, J = 7.4 Hz, 2H), 7.18 (m, 1H), 7.12 (m, 1H), 6.89 (m, 5H), 6.53 (tt, J = 1.5, 7.7 Hz, 1H), 6.25 (m, 2H), 1.1 (s, 6H), 0.89 (s, 6H). $^{13}\text{C}\{^1\text{H}\}$ NMR (213.77 MHz, C_6D_6): 314.2, 215.6, 153.1, 151.4, 139.7, 135.7, 131.3, 130.8, 129.61, 129.59, 129.3, 128.0, 123.0, 70.7, 69.6, 21.5. HRMS (ESI $^+$): calculated for $\text{C}_{28}\text{H}_{30}\text{N}_3\text{Ru} [\text{M} - \text{C}_5\text{H}_5\text{N} - \text{HCl} - \text{Cl} + \text{CH}_3\text{CN}]^+$: m/z = 510.1483, found: m/z = 510.1480.

S1.18 Synthesis of Ru9d



py = pyridine

In a glovebox, a 20 mL vial, equipped with a magnetic stirring bar and a screw cap, was charged with complex **Ru8d** (104 mg, 0.12 mmol) and pyridine (1 mL). The vial was closed, and the mixture stirred at room temperature for 1 hour. Then pentane (7 mL) was added to the reaction mixture causing the precipitation of a green solid. The solid was allowed to sediment (settle out) and then was isolated by vacuum filtration through a fritted glass funnel, washed three times with 5 mL of pentane and dried in the glovebox to give a green microcrystalline

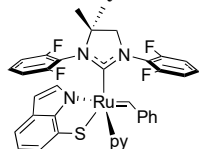
solid.

Yield: 84 mg (94 % of yield).

^1H NMR (850.13 MHz, C_6D_6) δ 20.0 (1H), 8.83 (2H), 8.66 (d, J = 5.6 Hz, 2H), 8.08 (d, J = 7.7 Hz, 2H), 7.17 (dt, J = 7.27, 1.2 Hz, 1H), 6.94 (t, J = 7.15 Hz, 1H), 6.86 (t, J = 7.7 Hz, 2H), 6.60 (t, J = 5.7 Hz, 2H), 6.46 (m, 4H), 6.34 (t, J = 6.8 Hz, 3H), 6.16 (t, J = 6.6 Hz, 2H), 3.55 (s, 2H), 1.14 (t, J = 2.2 Hz, 6H). $^{13}\text{C}\{^1\text{H}\}$ NMR (213.77 MHz, C_6D_6): 218.3, 161.8, 160.6, 153.2, 152.3, 150.5, 141.2, 135.3, 134.9, 129.1, 129.0, 122.9, 122.6, 111.6, 65.0, 34.0, 30.11. HRMS (ESI $^+$): calculated for $\text{C}_{28}\text{H}_{26}\text{ClF}_4\text{N}_4\text{Ru} [\text{M} - 2 \text{C}_5\text{H}_5\text{N} - \text{Cl} + 2 \text{CH}_3\text{CN}]^+$: m/z = 631.0826, found: m/z = 631.0822.

The peak of the imidazolium cation was also detected indicating the loss of the carbene ligand during HRMS. HRMS (ESI $^+$): calculated for $\text{C}_{17}\text{H}_{15}\text{F}_4\text{N}_2 [\text{NHC} + \text{H}]^+$: m/z = 323.1171, found: m/z = 323.1118.

S1.19 Synthesis of Ru12



In a glovebox, a 20 mL vial was charged with 44.5 mg (0.06 mmol, 1 eq) of **Ru9d** in 10 mL THF, and 15.5 mg (0.07 mmol, 1.15 equiv.) of dipotassium salt **L10**. A color change from green to red was observed immediately. After 15 min the reaction was completed, and the solvent was removed under reduced pressure. The crude reaction mixture was redissolved in toluene, filtered through celite, and concentrated to about 0.5 mL. To this solution 5 mL hexane was added and cooled to -35°C for 15 h. The resulting solid

was collected and washed with cold hexane (2 x 4 mL) to yield the desired product as red microcrystalline solid.

Yield: 28 mg (76 %).

NMR analysis shows the presence of the two isomers. DFT calculations suggest that they are the rotamers of the NHC ligand: rotamer 1 with the dimethyl-substituted backbone moiety on the same side of alkylidene ligand, while rotamer 2 owns this moiety pointing in the opposite direction.

Rotamer 1 (60%):

^1H NMR (850.13 MHz, C_6D_6): δ = 14.64 (1H), 8.56 (d, J = 4.9 Hz, 2H), 7.91 (d, J = 7.6 Hz, 1H), 7.74 (d, J = 7.1 Hz, 1H), 7.57 (s, 1H), 7.43 (t, J = 7.2 Hz, 1H), 7.06 (d, J = 2.2 Hz, 1H), 6.77 (m, 3H), 6.51 (m, 3H), 6.23-6.50 (m, 7H), 5.85 (t, J = 8.5 Hz, 1H), 3.41 (d, J = 10.2 Hz, 1H), 3.16 (d, J = 10.2 Hz, 1H), 0.9-1.0 (m, 6H).

Rotamer 2 (40%):

^1H NMR (850.13 MHz, C_6D_6): δ = 15.00 (1H), 8.69 (d, J = 4.9 Hz, 1H), 7.97 (d, J = 7.6 Hz, 1H), 7.76 (d, J = 7.1 Hz, 1H), 7.67 (s, 1H), 7.43 (t, J = 7.2 Hz, 1H), 7.13 (d, J = 2.2 Hz, 1H), 6.90 (m, 3H), 6.64 (m, 4H), 6.23-6.50 (m, 7H), 5.94 (t, J = 8.5 Hz, 1H), 3.27 (d, J = 10.2 Hz, 1H), 3.21 (d, J = 10.2 Hz, 1H), 0.9-1.0 (m, 6H).

Rotamers 1 and 2:

$^{13}\text{C}\{^1\text{H}\}$ NMR (213.77 MHz, C_6D_6): δ = 269.1, 267.9, 230.2, 229.0, 156.7, 153.0, 152.9, 152.7, 152.6, 139.7, 139.3, 135.7, 134.5, 134.3, 128.7, 128.3, 125.5, 123.3, 118.8, 117.2, 117.1, 114.7, 114.5, 113.4, 111.5, 111.4, 101.7, 101.5, 67.8, 66.5, 65.5, 64.1, 34.0, 30.1, 25.3, 25.2. HRMS (ESI⁺): calculated for $\text{C}_{32}\text{H}_{25}\text{F}_4\text{N}_3\text{NaRuS}$ [$\text{M} - \text{C}_5\text{H}_5\text{N} + \text{Na}$]⁺: m/z = 684.0646, found: m/z = 684.0653

S1.20 Stability of Ru12 in Solution

In a glovebox, a 4 mL vial was charged with **Ru12** (5.2 mg, 0.007 mmol), 600 μL of C_6D_6 , and 15 μL of a stock solution obtained by dissolving 1.46 mg (0.009 mmol) of hexamethylbenzene in 180 μL of C_6D_6 . The solution was filtered through a glass-fiber filter paper to remove undissolved complex, transferred to an NMR tube, and a ^1H NMR spectrum was immediately acquired to determine the initial integration of the alkylidene signals of **Ru12** (14.64 and 15.00 ppm) vs hexamethylbenzene (internal standard). Following this, other ^1H NMR spectra were periodically recorded. The decomposition of **Ru12**, determined by the decrease of the alkylidene signals, was monitored over a period of 72 h (see Figure S1). After 24h, 75% of the complex had decomposed. The disappearance of the alkylidene signals, indicating the complete decomposition of the complex, was observed after 72 h.

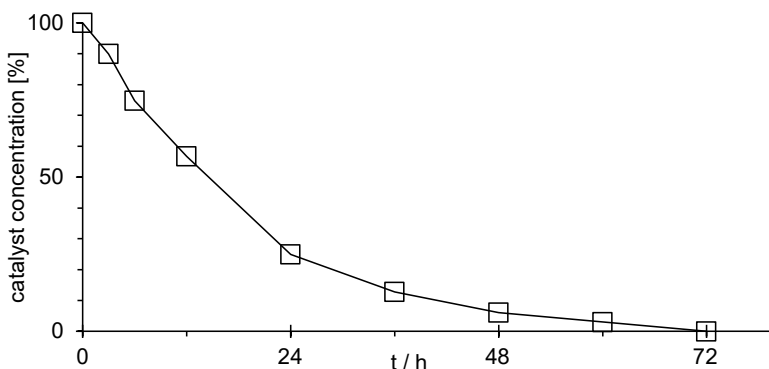


Figure S1. Decomposition of **Ru12** in C_6D_6 at 25 °C monitored by 1H NMR analysis.

S1.21 Representative Procedure for Self-Metathesis of Propene

In a 4 mL vial, catalyst **Ru12** (4.3 mg, 0.007 mmol) and hexamethylbenzene (I.S., 0.06 mg, 0.004 mmol, 0.05 eq) were dissolved in 0.7 mL C_6D_6 (10 mM Ru). The resulting solution was filtered through a pipette filter stuffed with a Kimwipe to remove any undissolved solid. 600 μ L of this solution was then transferred to a J-Young NMR tube. An initial 1H NMR spectrum was recorded to establish the initial ratio between the alkylidene and hexamethylbenzene. The NMR tube was connected to a Schlenk line and degassed (4 freeze-pump-thaw cycles), and then pressured with 1 bar of propene. The tube was sealed, shaken, and the timer started. A 1H NMR spectrum was immediately recorded to confirm the presence of propene ($\delta = 5.72, 4.97$ and 1.54 ppm). Additional spectra were recorded periodically to track the disappearing of the starting material and the appearing of products over time (ethylene (δ , ppm = 5.25 (s, 4H), *E*-butene (δ , ppm = 5.38 (m, 2H), 1.56 (m, 6H) and *Z*-butene ($\delta = 5.46$ (m, 2H), 1.51 (d, $J = 4.6$ Hz, 6H). After 24 hours, the equivalents vs **Ru12** of the following products were determined: styrene (0.23), ethylene (0.02), and 2-butene (0.09, *E*:*Z* 54:46).

S1.22 Representative Procedure for Self-Metathesis of 1-Octene

In a glovebox, an oven-dried vial equipped with a stir bar was charged with **Ru12** (3.7 mg, 0.005 mmol, 5 mol%), hexamethylbenzene (I.S., 0.06 mg, 0.003 mmol, 0.05 eq), and benzene- d_6 (200 μ L). To the resulting solution, 1-octene (0.12 mmol, 15.8 μ L, 20 equiv) was added and the mixture was stirred at room temperature. After 1 and 24 hours, aliquots were taken out and quenched with ethyl vinyl ether, and the product distribution was analyzed using 1H NMR. This reaction was repeated at 40 °C. In both experiments, no self-metathesis products were detected, but only isomerization products of 1-octene.

S1.23 Representative Procedure for Self-Metathesis of Methyl Oleate

In a glovebox, an oven-dried vial equipped with a stir bar was charged with methyl oleate (0.04 mmol, 14.5 μ L, 25 equiv) and dodecane (0.043 mmol, 5.37 μ L, 1.4 equiv). From a freshly prepared 0.02 M stock solution in THF, catalyst **Ru12** (0.0017 mmol, 4 mol %, 1 equiv., 100 μ L), was added to the alkene substrate and the vial was capped. After 2, 4 and 24 hours, aliquots were taken out and quenched with ethyl vinyl ether, and the product distribution was analyzed using gas chromatography. No self-metathesis product was observed.

S1.24 Representative Procedure for Self-Metathesis of Methyl Elaidate

In a glovebox, an oven-dried vial equipped with a stir bar was charged with methyl elaidate (0.04 mmol, 14.5 μ L, 25 equiv) and dodecane (0.043 mmol, 5.37 μ L, 1.4 equiv). From a freshly prepared 0.02 M stock solution in THF, catalyst **Ru12** (0.0017 mmol, 4 mol %, 1 equiv., 100 μ L), was added to the olefin and the vial was capped. After 2, 4 and 24 hours, aliquots were taken out and quenched with ethyl vinyl ether, and the product distribution was analyzed using gas chromatography. No self-metathesis product was observed.

S1.25 Representative Procedure for Ring-Opening Metathesis Polymerization of 2-Norbornene

In a glovebox, an oven-dried vial equipped with a stir bar was charged with 2-norbornene (0.171 mmol, 16.1 mg, 100 equiv) and hexamethylbenzene (0.009 mmol, 1.5 mg, 5.5 equiv.). **Ru12** (0.0017 mmol, 1 mol%, 1 equiv.) in 85 μ L C_6D_6 was added to the monomer and the vial was capped. After 1h, an aliquot (about 15 μ L) was taken, while the residual polymer was precipitated by addition of MeOH (4.0 mL). The polymer was washed with MeOH (2.0 mL) and dried under vacuum to yield 20% polymer (3.2 mg). 1H NMR of the aliquot showed the 20% conversion with 47% *Z*-selectivity (Figure S2a).

This reaction was repeated with **Ru5**: 1H NMR of the aliquot showed no residual starting material and the resulting polynorbornene showed 89% *Z*-selectivity (Figure S2b).

Furthermore, a catalytic test was performed using one tenth of catalyst loading to check if lower catalyst loading would improve the catalyst productivity: **Ru12** (0.0017 mmol, 0.1 mol %, 1 equiv.) in 853 μ L C_6D_6 , 2-norbornene (1.71 mmol, 161 mg, 1000 equiv) and hexamethylbenzene (0.095 mmol, 15.4 mg, 55.5 equiv), yielding 3 mg of polynorbornene (2%). 1H NMR analysis of the purified polynorbornene showed a *Z*-selectivity of 63%. The result showed no improved activity with lower catalyst loading.

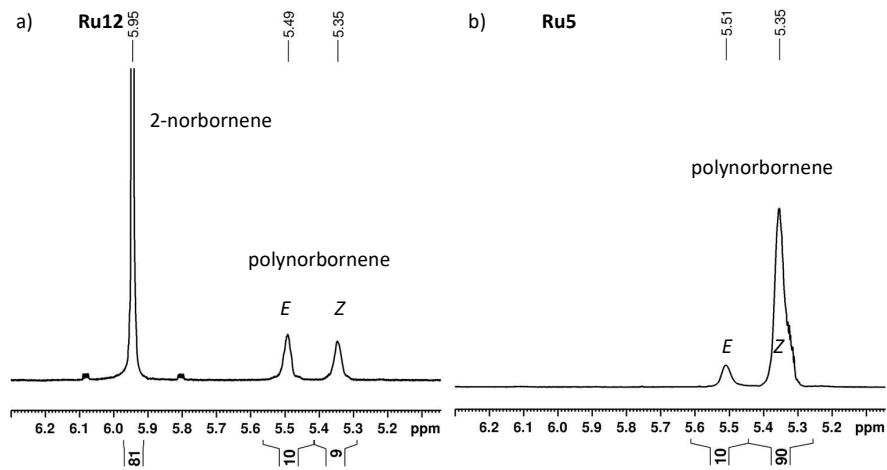


Figure S2. 1H NMR spectrum (from 5.0 to 6.3 ppm) of the reaction mixture used to determine the *E*:*Z* ratio and yield of resulting polynorbornene by (a) **Ru12** or (b) **Ru5**.⁸

S1.26 Representative Procedure for Ring-Opening Metathesis Polymerization of 1,5-Cyclooctadiene

In a glovebox, an oven-dried vial equipped with a stir bar was charged with 1,5-cyclooctadiene (COD) (0.171 mmol, 18.44 mg, 100 equiv.) and hexamethylbenzene (0.009 mmol, 1.54 mg, 5.5 equiv.). Catalyst **Ru12** (0.0017 mmol, 1 mol%, 1 equiv.) in 85 μ L THF was added to the monomer and the vial was capped. After 2h, ^1H NMR analysis of the reaction mixture showed 5% conversion of the starting material to poly(cyclooctadiene).

The reaction was repeated for **Ru5**, and the ^1H NMR analysis showed 20% conversion of the starting material to poly(cyclooctadiene).

S2 Computational Methods

Density functional theory (DFT) calculations were performed using revision C.01 of the Gaussian 16 suite of programs.⁹ The Gaussian 16 “ultrafine” grid (a pruned grid consisting of 99 radial shells and 590 angular points per shell) was explicitly specified for numerical integration (keyword `int=ultrafine`), which implies that the “ultrafine” grid was used also for analytical Hessian calculations.

S2.1 Geometry Optimization

Based on a brief validation against an experimentally determined stereoselectivity,¹ ω B97XD was selected as the functional for geometry optimization.¹⁰ The Stuttgart/Cologne 28-electron relativistic effective core potential (ECP28MDF)¹¹ was used for Ru atoms, in conjunction with the corresponding correlation-consistent valence double- ζ plus polarization basis set augmented by diffuse functions (aug-cc-pVDZ-PP),¹¹ as obtained from the Stuttgart/Cologne basis set repository.¹² Correlation-consistent, valence double- ζ plus polarization basis sets (cc-pVDZ¹³ from the EMSL basis set exchange website)¹⁴ were used for all other atoms.

Geometries were optimized using tight convergence criteria (max. force $1.5 \cdot 10^{-5}$ a.u., RMS force $1.0 \cdot 10^{-5}$ a.u., max. displacement $6.0 \cdot 10^{-5}$ a.u., RMS displacement $4.0 \cdot 10^{-5}$ a.u.), without symmetry constraints, using tighter convergence criteria for the self-consistent field (SCF) optimization procedure (RMS change in density matrix $< 1.0 \cdot 10^{-9}$, max. change in density matrix $= 1.0 \cdot 10^{-7}$), and with a spin multiplicity of 1. All stationary points were confirmed to be either minima (all-positive Hessian eigenvalues) or transition states (a single negative Hessian eigenvalue) by analytical calculation of the second derivatives, i.e., the Hessian matrix. In addition, each transition state was connected to its elementary-step reactant and product via intrinsic reaction coordinate calculations using the local quadratic approximation (LQA, `stepsize = 15`)^{15,16} for the predictor step. Textbook procedures were used to calculate the translational, rotational, and vibrational components of the thermal corrections to enthalpies and Gibbs free energies within the ideal-gas, rigid-rotor, and harmonic oscillator approximations, with one exception: All frequencies below 100 cm^{-1} were shifted to 100 cm^{-1} when calculating the vibrational component of the entropy, a strategy often referred to as the quasi-harmonic oscillator approximation.^{17,18} This approach is aimed at preventing breakdown of the harmonic approximation for low-frequency modes.¹⁹

S2.2 Single-Point (SP) Energy Calculations

The geometries obtained as described above were adopted in SP energy calculations using the PBE²⁰ functional in conjunction with the PCM polarizable continuum solvent model, with default parameters for benzene as solvent. All PBE calculations included Grimme’s empirical D3 dispersion corrections,¹⁹ with revised Becke–Johnson damping parameters (labelled D3M(BJ) for brevity).²¹ In all SP calculations, the above basis sets were extended to the valence quadruple- ζ level. Specifically, Ru was described by combining the 28-electron relativistic effective core potential (ECP28MDF)¹¹ with the corresponding correlation-consistent valence quadruple- ζ plus polarization basis set augmented by diffuse functions (aug-cc-pVQZ-PP)¹¹ from the Stuttgart/Cologne basis set repository.¹⁴ The other atoms were described by correlation-consistent, valence quadruple- ζ plus polarization basis sets (cc-pVQZ [19] from the EMSL repository).¹⁴ The SCF convergence criteria were relaxed compared to those of the geometry optimizations (RMS change in density matrix $< 1.0 \cdot 10^{-5}$, max. change in density matrix $< 1.0 \cdot 10^{-3}$).

S2.3 Calculations of Free Energies Including Standard-State Corrections

Free energies in solution were calculated according to equation 1.

$$G_{\text{PBE-D3M(BJ)}}^{\text{benzene, 298.15 K, c}} = E_{\text{PBE-D3M(BJ)}}^{\text{benzene}} + G_{\omega\text{B97Xd, qh}}^{298.15 \text{ K}} + G_{1 \text{ atm} \rightarrow c}^{298.15 \text{ K}} \quad (1)$$

where $E_{\text{PBE-D3M(BJ)}}^{\text{benzene}}$ is the SP energy calculated with the computational model and $G_{\omega\text{B97Xd, qh}}^{298.15 \text{ K}}$ is the thermal correction to the Gibbs free energy calculated at the geometry-optimization level with the quasi-harmonic oscillator approximation as described above. $G_{1 \text{ atm} \rightarrow c}^{298.15 \text{ K}}$ corrects from a 1 atm ideal-gas standard state to a solution of concentration c (but exhibiting infinite-dilution, ideal-gas-like behavior), as defined by equation 2.²²

$$G_{1 \text{ atm} \rightarrow c}^{298.15 \text{ K}} = RT \cdot \ln \left(\frac{RT}{p^0} \cdot c \right) \quad (2)$$

With $T = 298.15 \text{ K}$, $p^0 = 101325 \text{ N}\cdot\text{m}^{-2}$, and $R = 8.314 \text{ Nm}\cdot\text{mol}^{-1}\cdot\text{K}^{-1}$, equation (2) becomes:

$$G_{1 \text{ atm} \rightarrow c}^{298.15 \text{ K}} = 0.592 \frac{\text{kcal}}{\text{mol}} \cdot \ln \left(24.464 \frac{\text{L}}{\text{mol}} \cdot c \right) \quad (3)$$

In the present work, a standard state corresponding to an ideal solution of concentration $c = 1 \text{ M}$ has been used ($G_{1 \text{ atm} \rightarrow 1 \text{ M}}^{298.15 \text{ K}} = 1.89 \text{ kcal mol}^{-1}$ for all species) in the calculation of all tabulated (Table S1) and graphically illustrated free energies. This is also the standard-state correction used for relative free energies given in the text, except for a brief discussion, in the main part of the manuscript, of reaction barriers calculated at concentrations mimicking those of the propene self-metathesis experiment using **Ru12** (precatalyst: 0.0077 M; pyridine: 0.0023 M, styrene: 0.0023 M, catalytic intermediates and transition states: 0.0023 M; propene: 0.95 M). With the latter concentrations, the $G_{1 \text{ atm} \rightarrow c}^{298.15 \text{ K}}$ corrections are as follows: precatalyst: $-0.98 \text{ kcal mol}^{-1}$; pyridine: $-1.70 \text{ kcal mol}^{-1}$, styrene: $-1.70 \text{ kcal mol}^{-1}$, catalytic intermediates and transition states: $-1.70 \text{ kcal mol}^{-1}$; propene: $1.83 \text{ kcal mol}^{-1}$.

S3 Computational Results

S3.1 Comparison of the *E*-2-butene pathway of catalyst Ru5, Ru12 and Ru12'

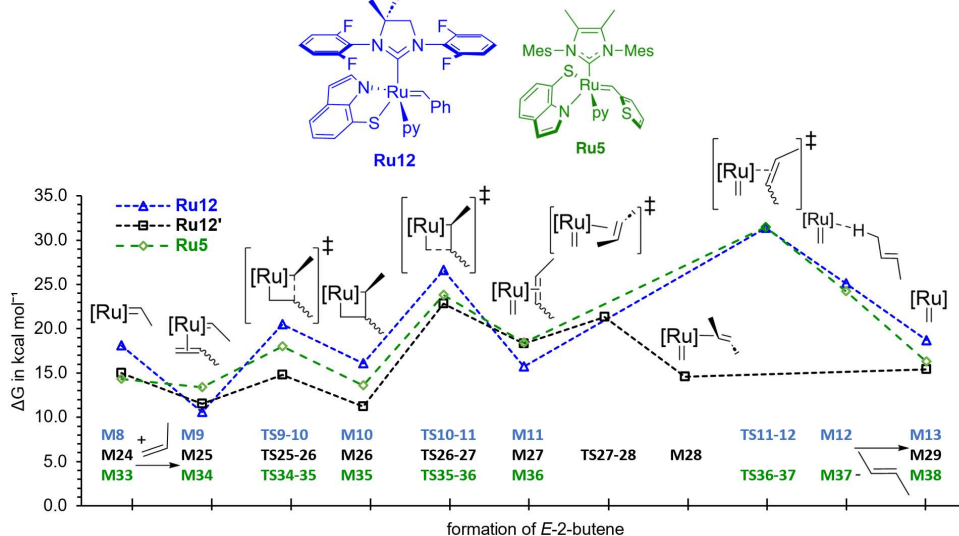


Figure S3. Gibbs free energies calculated for intermediates and transition states of propene self-metathesis to *E*-2-butene for the catalysts **Ru5** (green circles), **Ru12** (blue triangles) and **Ru12'** (black squares). Energies are relative to the most stable precursor, respectively. No transition state for product release for complex **Ru12'** after the formation of the more stable π -complex **M28** was identified, suggesting a diffusion-limited dissociation of *E*-2-butene. Computational data for **Ru5** was taken from literature.¹

S3.2 Computational Results of Ru12

Table S1. Gibbs Free Energies of Catalyst Ru12 and Ru12' in Olefin Metathesis

Model ID	$E_{\omega 97XD}$ [a.u.]	$G_{\omega 97XD, qh}^{298.15, K}$ [a.u.]	$E_{PBE-D3M(BJ)}^{benzene}$ [a.u.]	$\Delta G_{PBE-D3M(BJ)}^{benzene, 298.15, K, 1 \text{ mol } L^{-1}}$ [kcal/mol]
Pyridine	-248.211971	0.062066	-248.088722	-
Styrene	-309.557280	0.103658	-309.382524	-
Propene	-117.870108	0.054855	-117.790929	-
M1	-2538.780357	0.530653	-2537.715606	0.0
M1b	-2538.779541	0.530767	-2537.715369	0.6

TS1-2	-2538.750479	0.528029	-2537.670528	26.6
M2	-2538.748670	0.528503	-2537.676584	23.1
M3	-2290.509199	0.442283	-2289.576296	17.1
M3b	-2290.507824	0.442319	-2289.575915	17.4
M4	-2408.410533	0.524733	-2407.398862	12.7
TS4-5	-2408.397800	0.523795	-2407.381927	22.7
M5	-2408.409208	0.525987	-2407.390936	18.5
TS5-6	-2408.390635	0.522864	-2407.378429	24.4
M6	-2408.399709	0.522427	-2407.392476	15.3
TS6-7	-2408.391832	0.519337	-2407.374540	24.6
M7	-2408.391878	0.519291	-2407.375213	24.1
M8	-2098.813694	0.389460	-2097.984055	15.0
M9	-2216.720068	0.471703	-2215.806413	10.6
TS9-10	-2216.705730	0.471847	-2215.790727	20.5
M10	-2216.719919	0.475327	-2215.801181	16.1
TS10-11	-2216.693289	0.472350	-2215.781500	26.6
M11	-2216.708342	0.471798	-2215.798290	15.7
TS11-12	-2216.688747	0.466824	-2215.767807	31.4
M12	-2216.696946	0.468302	-2215.780145	25.1
M13	-2059.498122	0.363189	-2058.692457	18.7
M14	-2216.721719	0.470910	-2215.808563	8.7
TS14-15	-2216.708149	0.471422	-2215.791739	19.6
M15	-2216.716864	0.475560	-2215.799883	17.1
TS15-16	-2216.694325	0.471772	-2215.780479	26.9
M16	-2216.716251	0.472204	-2215.804181	12.3
TS16-17	-2216.688747	0.466824	-2215.767807	31.7
M17	-2216.696946	0.468302	-2215.780145	24.9
M13	-2059.498122	0.363189	-2058.692457	19.4
M18	-2538.770295	0.530121	-2537.711983	6.0
M18b	-2538.770519	0.530267	-2537.710962	6.8
M19	-2290.509199	0.441893	-2289.580902	13.7
M19b	-2290.509199	0.441893	-2289.580589	14.2
M20	-2408.405237	0.524026	-2407.397317	13.2
TS20-21	-2408.403038	0.524592	-2407.391459	17.3
M21	-2408.415105	0.525020	-2407.398222	13.3
TS21-22	-2408.396589	0.522519	-2407.385559	19.7
M22	-2408.399265	0.521888	-2407.392213	15.1
TS22-23	-2408.383310	0.520802	-2407.376391	24.3
M23	-2408.386246	0.518317	-2407.372164	25.4
M24	-2098.813694	0.389460	-2097.984055	15.0
M25	-2216.710519	0.470083	-2215.803311	11.5
TS25-26	-2216.708987	0.471255	-2215.799181	14.8
M26	-2216.724240	0.474696	-2215.808416	11.2
TS26-27	-2216.695262	0.470935	-2215.786122	22.8
M27	-2216.699962	0.471906	-2215.794326	18.3

TS27-28	-2216.697011	0.473047	-2215.790743	21.3
M28	-2216.712212	0.472227	-2215.800496	14.6
M29	-2059.499098	0.362630	-2058.697102	15.4
M30	-2216.709841	0.470940	-2215.802511	12.6
TS30-31	-2216.705299	0.471731	-2215.794633	18.0
M31	-2216.716799	0.475367	-2215.803111	15.0
TS31-32	-2216.688449	0.470416	-2215.778996	27.0
M32	-2216.702421	0.471677	-2215.791873	19.7
M29	-2059.499098	0.362630	-2058.697102	16.2
TS3-19	-2290.486791	0.440969	-2289.557293	28.2
TS8-24	-2098.790481	0.390402	-2097.958587	31.6

^a Gibbs free energies are relative to the most stable rotamer of the catalyst precursor **Ru12 (M1)**.

S4 NMR Spectra

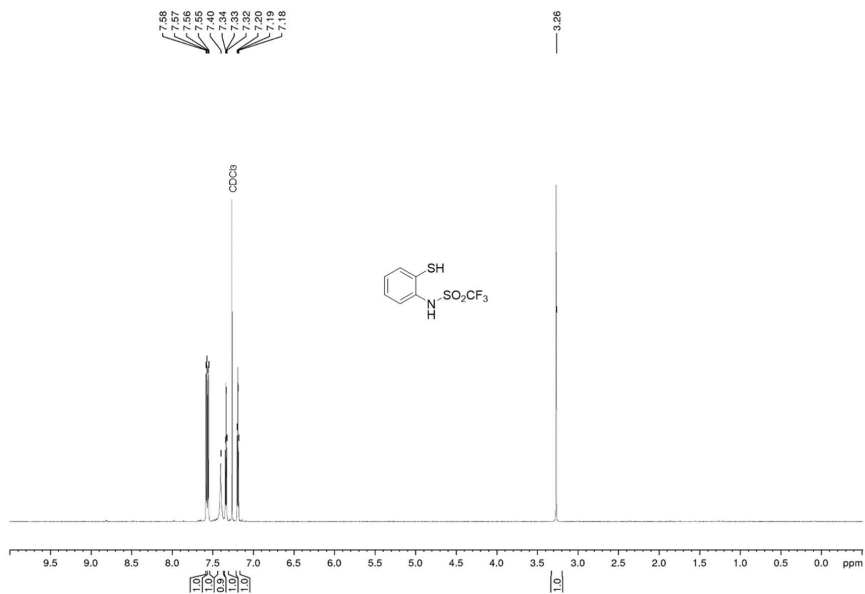


Figure S4. ¹H NMR spectrum of **L2H₂** (CDCl₃, 850.13 MHz).

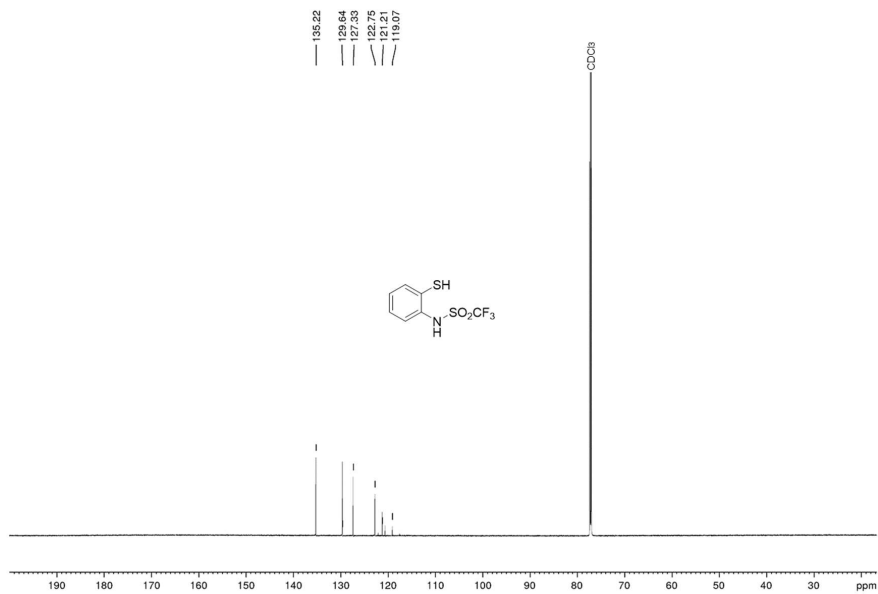


Figure S5. ¹³C{¹H} NMR spectrum of **L2H₂** (CDCl₃, 221.77 MHz).

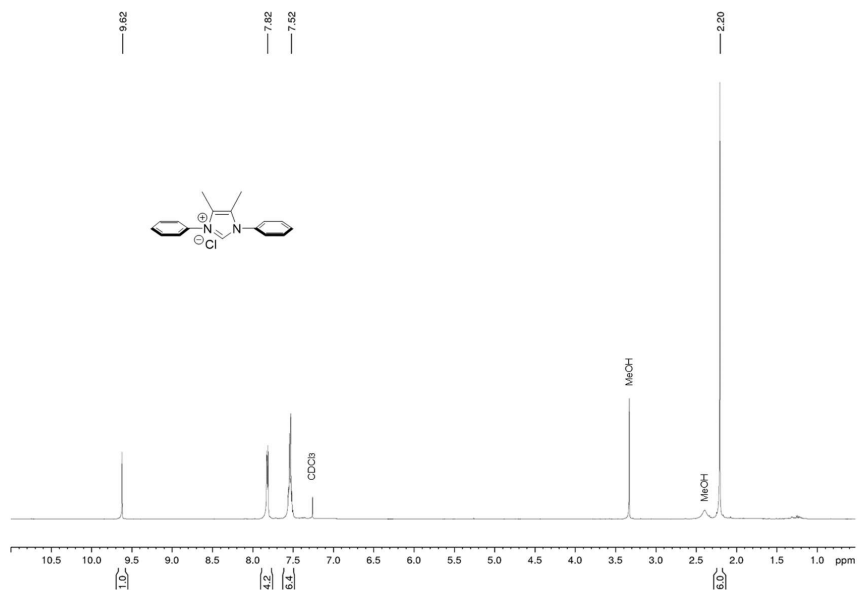


Figure S6. ^1H NMR spectrum of L9a (CDCl_3 , 500.13 MHz).

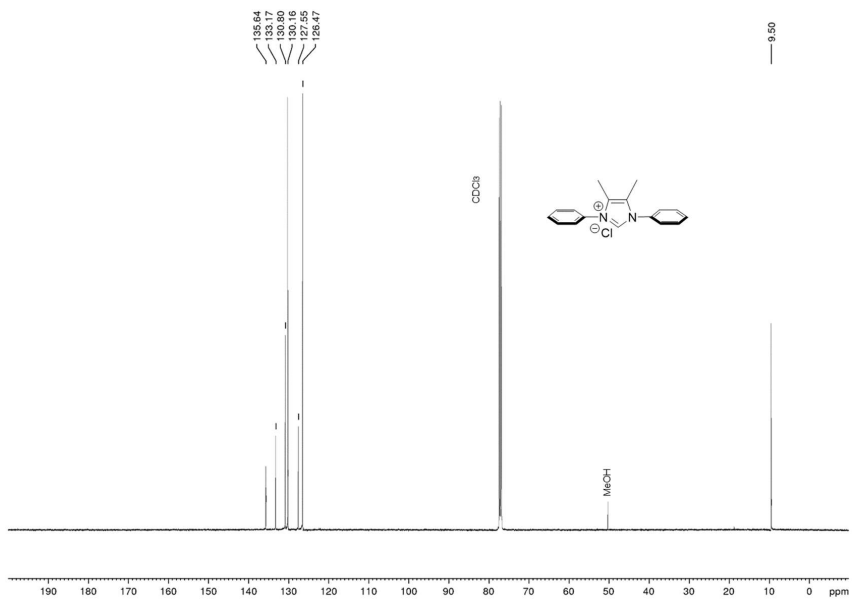


Figure S7. $^{13}\text{C}\{^1\text{H}\}$ NMR spectrum of L9a (CDCl_3 , 213.77 MHz).

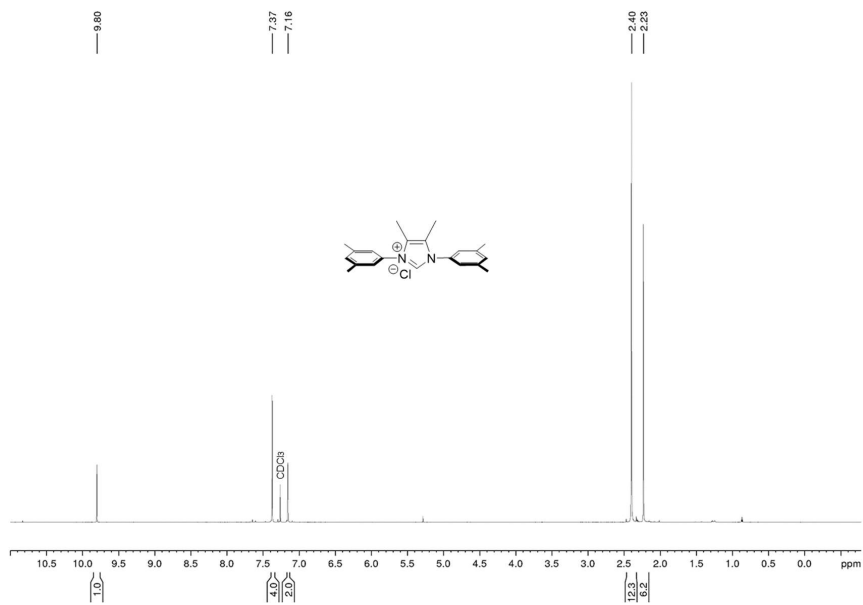


Figure S8. ^1H NMR spectrum of **L9b** (CDCl_3 , 500.13 MHz).

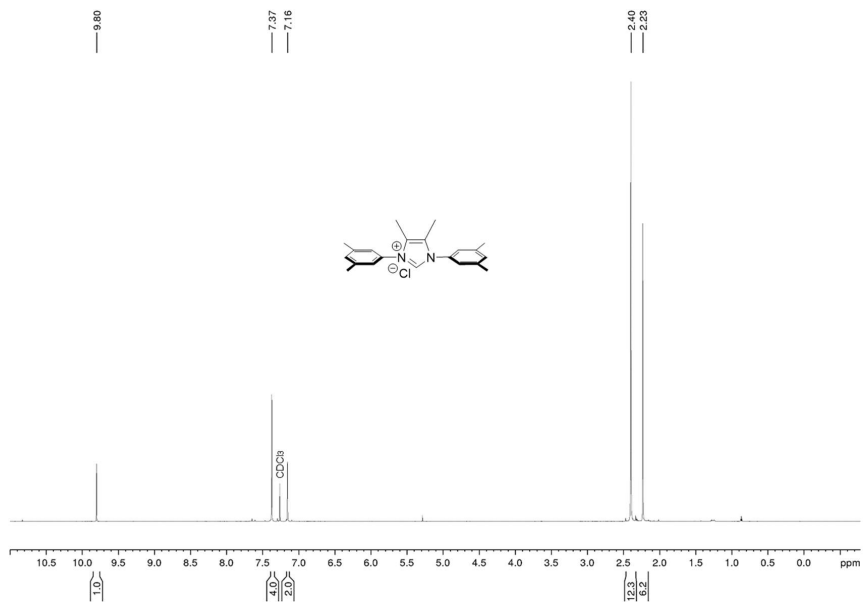
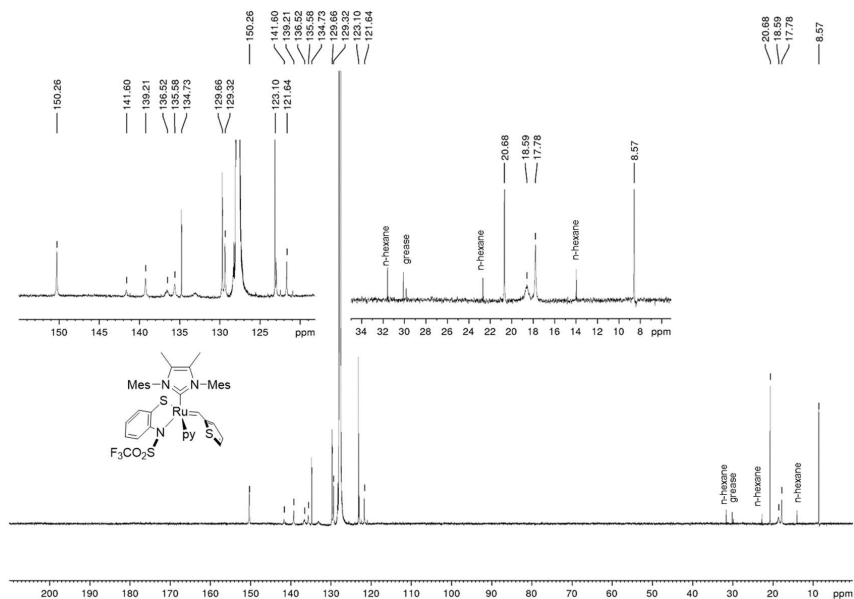
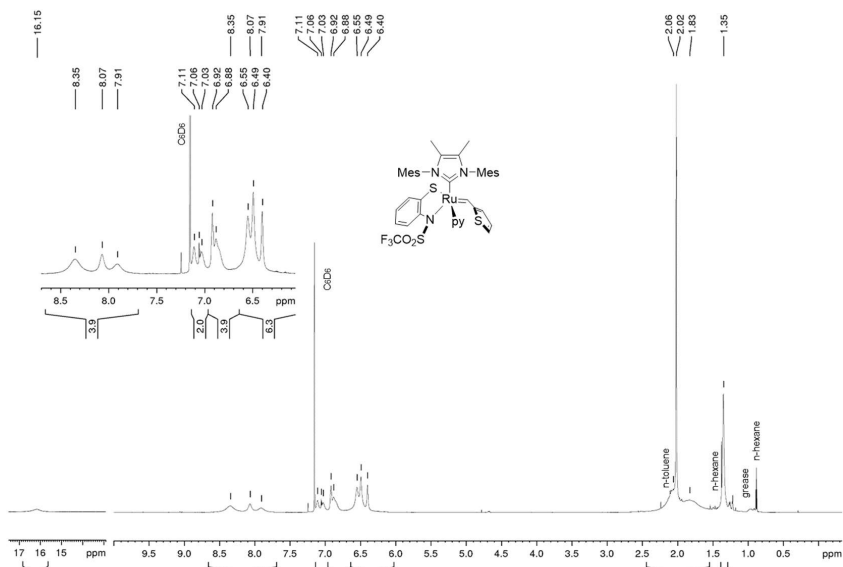


Figure S9. $^{13}\text{C}\{^1\text{H}\}$ NMR spectrum of **L9b** (CDCl_3 , 213.77 MHz).



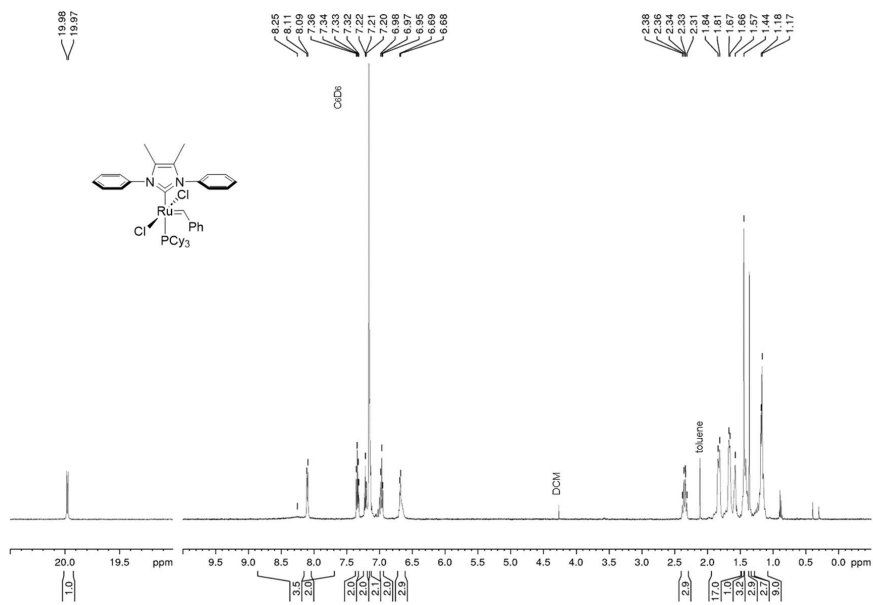


Figure S12. ¹H NMR spectrum of **Ru8a** (C₆D₆, 850.13 MHz).

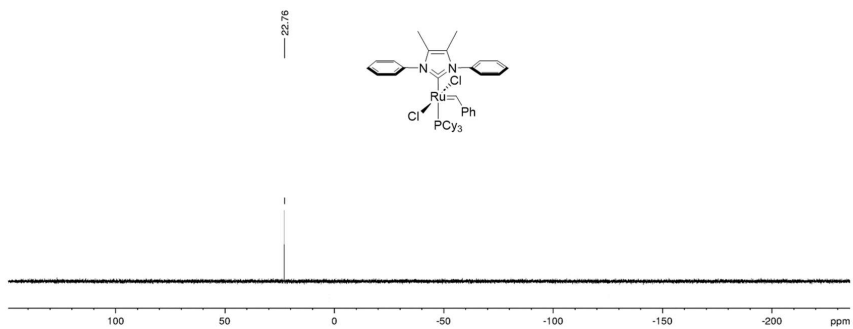


Figure S13. ³¹P{¹H} NMR spectrum of **Ru8a** (C₆D₆, 202.45 MHz).

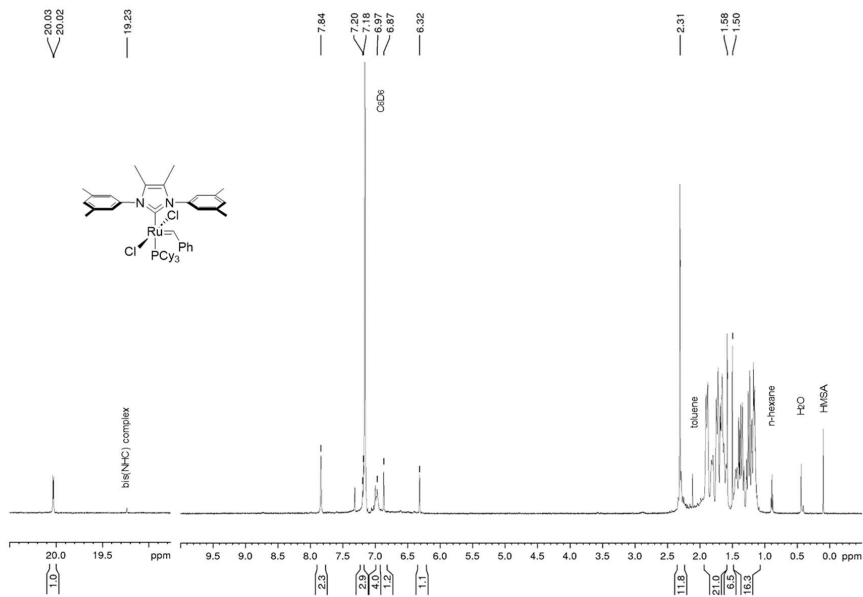


Figure S14. ¹H NMR spectrum of **Ru8b** including small amount of presumably bis(NHC) complex as impurity, identified through spiking with excess amount of NHC ligand (C₆D₆, 850.13 MHz).

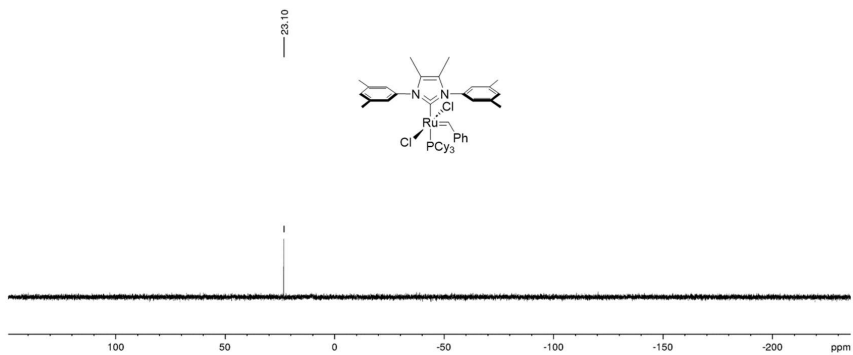


Figure S15. ³¹P{¹H} NMR spectrum of **Ru8b** (C₆D₆, 202.45 MHz).

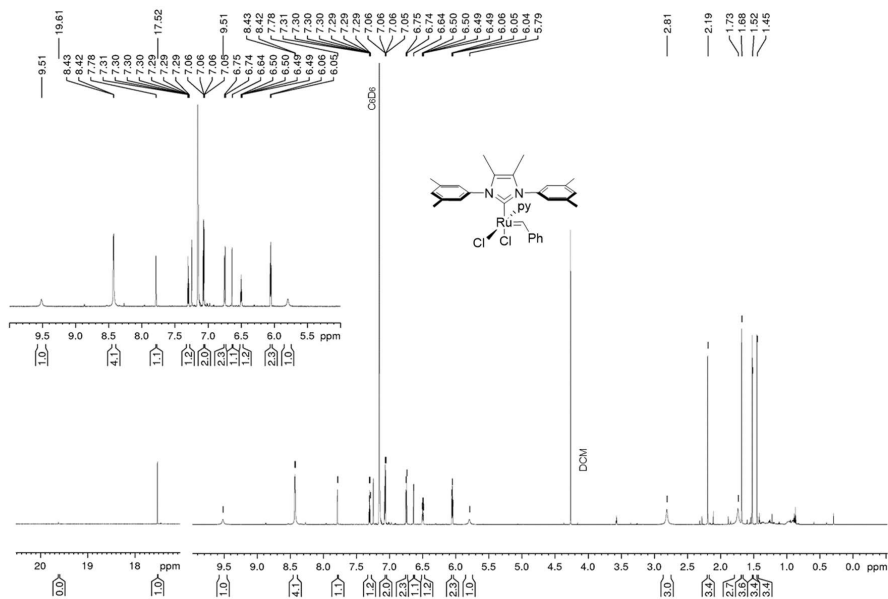


Figure S17. ¹H NMR spectrum of Ru9b (C₆D₆, 850.13 MHz)

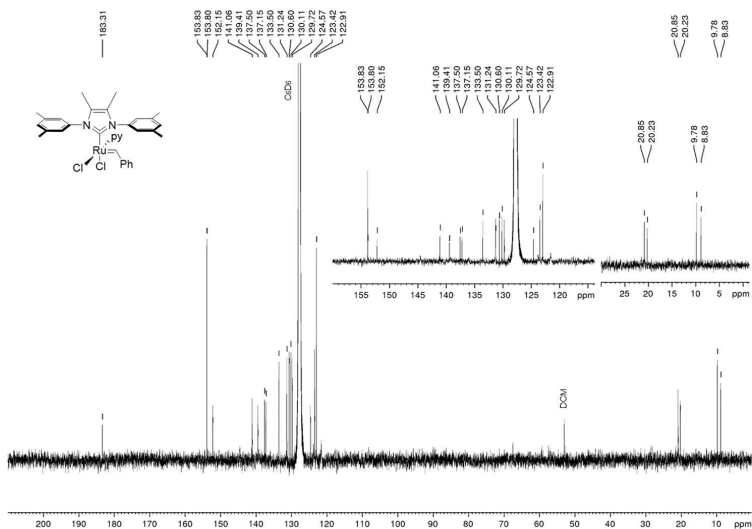


Figure S18. ¹³C{¹H} NMR spectrum of Ru9b (C₆D₆, 213.77 MHz). The alkylidene signal resonance was not visible due to the low concentration of the sample.

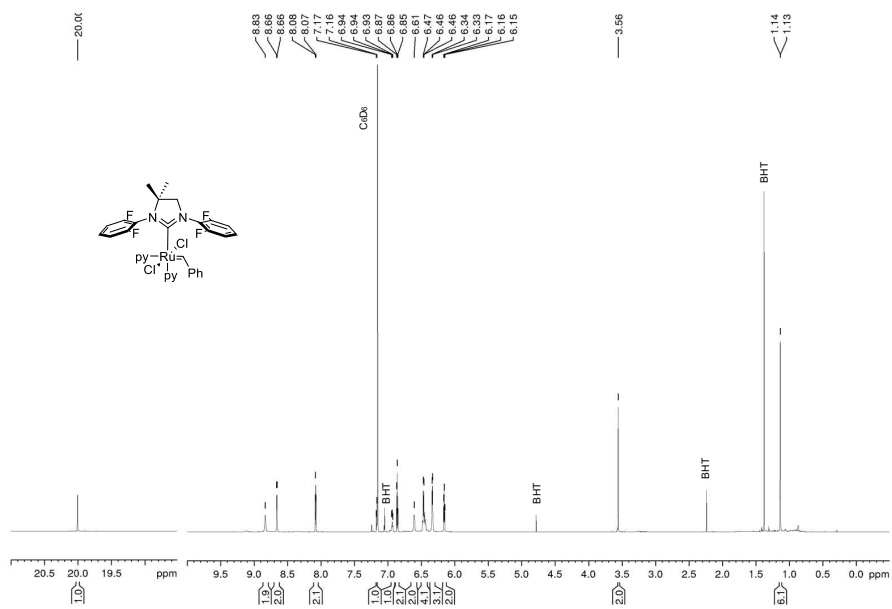


Figure S21. $^1\text{H NMR}$ spectrum of Ru9d (C_6D_6 , 850.13 MHz). BHT = 2,6-dimethyl-4-*tert*-butylphenol.²³

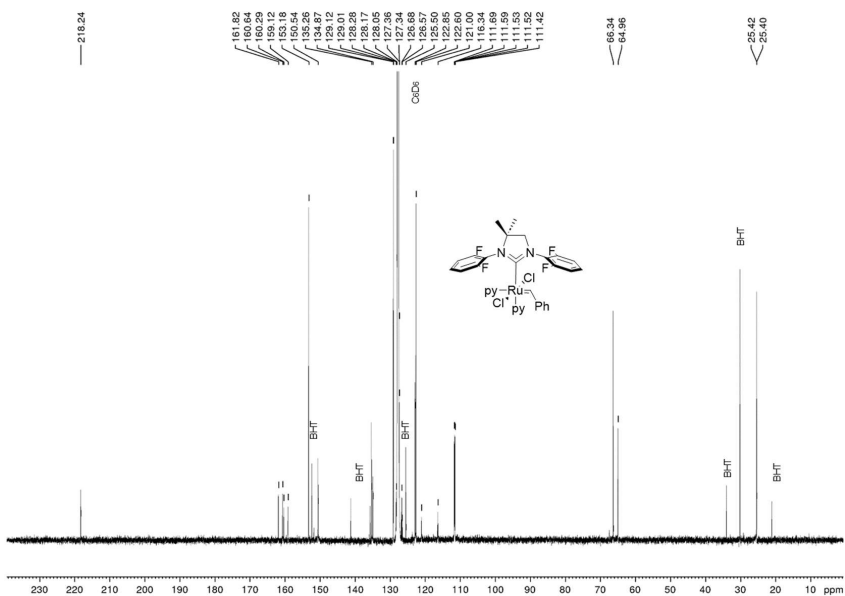


Figure S22. $^{13}\text{C NMR}$ spectrum of Ru9d (C_6D_6 , 213.77 MHz)

S5 X-ray Crystal Structures

Diffraction experiments were performed using beamline BM01 of the Swiss-Norwegian Beamlines at the ESRF synchrotron in Grenoble, France, using Si double-mirror monochromated radiation ($\lambda = 0.62379 \text{ \AA}$) in conjunction with a 360-degree phi-scan and a Pilatus2M detector.

S5.1 X-ray Crystal Structure of L9a

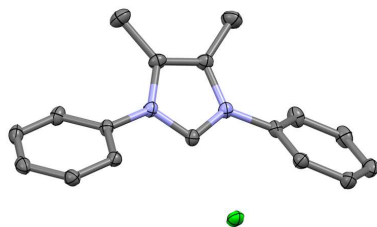


Figure S25. X-ray crystal structure of **L9a**, with displacement ellipsoids drawn at 50% probability. Nitrogen in blue, chloride in green and carbon in gray. Hydrogen atoms have been omitted for clarity.

Table S2 Crystal data and structure refinement for **L9a**.

Identification code	L9a
Empirical formula	C17 H17 Cl N2
Formula weight	284.77
Temperature	123(2) K
Wavelength	0.71073 \AA
Crystal system	Orthorhombic
Space group	P212121
Unit cell dimensions	$a = 7.1841(5) \text{ \AA}$, $\alpha = 90^\circ$. $b = 13.8406(10) \text{ \AA}$, $\beta = 90^\circ$. $c = 14.4706(10) \text{ \AA}$, $\gamma = 90^\circ$.
Volume	1438.84(18) \AA^3
Z	4
Density (calculated)	1.315 Mg m^{-3}
Absorption coefficient	0.257 mm^{-1}
F(000)	600
Crystal size	0.210 x 0.180 x 0.120 mm^3
Theta range for data collection	Yellow/Flat prism
Index ranges	2.036 to 30.082 $^\circ$.
Reflections collected	$-10 \leq h \leq 10$, $-19 \leq k \leq 19$, $-20 \leq l \leq 20$
Independent reflections	24148
Completeness to theta = 23.341 $^\circ$	4215 [R(int) = 0.0484]
Absorption correction	100.00%
Refinement method	Semi-empirical from equivalents
Data / restraints / parameters	Full-matrix least-squares on F2
Goodness-of-fit on F2	4215 / 0 / 188
Final R indices [$I > 2\sigma(I)$]	1.06
R indices (all data)	R1 = 0.0349, wR2 = 0.0922

Extinction coefficient	R1 = 0.0358, wR2 = 0.0930
Largest diff. peak and hole	0.38(7)
Extinction coefficient	n/a
Largest diff. peak and hole	0.492 and -0.202 e.Å ⁻³

S5.2 X-ray Crystal Structure of Ag1b

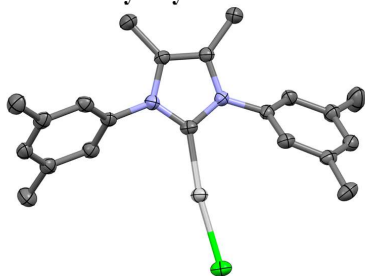


Figure S26. X-ray crystal structure of **Ag1b**, with displacement ellipsoids drawn at 50% probability. Silver in light grey, nitrogen in blue, chloride in green and carbon in gray. Hydrogen atoms have been omitted for clarity.

Table S3 Crystal data and structure refinement for **Ag1b**.

Identification code	Ag1b
Empirical formula	C ₂₁ H ₂₄ Ag Cl N ₂
Formula weight	447.74
Temperature	123(2) K
Wavelength	0.71073 Å
Crystal system	Orthorhombic
Space group	P212121
Unit cell dimensions	a = 8.646(2) Å, α = 90°. b = 12.697(3) Å, β = 90°. c = 18.705(5) Å, γ = 90°.
Volume	2053.4(9) Å ³
Z	4
Density (calculated)	1.448 Mg/m ³
Absorption coefficient	1.117 mm ⁻¹
F(000)	912
Crystal size	0.170 x 0.080 x 0.040 mm ³
Theta range for data collection	Colourless/Needle
Index ranges	1.939 to 28.970°.
Reflections collected	-11<=h<=11, -17<=k<=17, -25<=l<=25
Independent reflections	24686
Completeness to theta = 23.341°	5408 [R(int) = 0.0650]
Absorption correction	100.00%
Refinement method	Semi-empirical from equivalents
Data / restraints / parameters	Full-matrix least-squares on F ²

Goodness-of-fit on F2	5408 / 0 / 232
Final R indices [$I > 2\sigma(I)$]	1.094
R indices (all data)	R1 = 0.0312, wR2 = 0.0695
Extinction coefficient	R1 = 0.0403, wR2 = 0.0733
Largest diff. peak and hole	-0.009(17)
Extinction coefficient	n/a
Largest diff. peak and hole	0.590 and -0.383 e.Å ⁻³

S5.3 X-ray Crystal Structure of Ru7

Crystals suitable for single-crystal X-ray diffraction experiments were obtained by layering a concentrated DCM solution of **Ru7** with pentane at -30 °C. The CF₃-group and the thiophene ring are rotationally disordered.

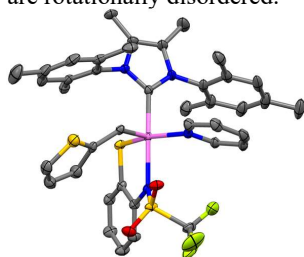


Figure S27. X-ray crystal structure of **Ru7**, with displacement ellipsoids drawn at 50% probability. Ruthenium is shown in violet, sulfur in yellow, oxygen in red, nitrogen in blue, fluorine in light green, and carbon in gray. Hydrogen atoms have been omitted for clarity.

Table S4 Crystal data and structure refinement for **Ru9b**.

Identification code	Ru7
Empirical formula	C45 H53 F3 N4 O2 Ru S3
Formula weight	936.16
Temperature	103(2) K
Wavelength	0.71073 Å
Crystal system	Monoclinic
Space group	P21/n
Unit cell dimensions	a = 12.211(4) Å, α = 90° b = 12.012(4) Å, β = 91.277(4)° c = 33.376(10) Å, γ = 90°
Volume	4894(3) Å ³
Z	4
Density (calculated)	1.270 Mg/m ³
Absorption coefficient	0.497 mm ⁻¹
F(000)	1944
Crystal size	0.195 x 0.100 x 0.033 mm ³
Crystal colour/habit	Red/Rod
Theta range for data collection	1.763 to 27.103°

Index ranges	-15<=h<=15, -15<=k<=15, -42<=l<=42
Reflections collected	65552
Independent reflections	10802 [R(int) = 0.0503]
Completeness to theta = 25.242°	100.00%
Absorption correction	Numerical
Max. and min. transmission	1.0000 and 0.7008
Refinement method	Full-matrix least-squares on F2
Data / restraints / parameters	10802 / 84 / 565
Goodness-of-fit on F2	1.047
Final R indices [I>2sigma(I)]	R1 = 0.0397, wR2 = 0.1030
R indices (all data)	R1 = 0.0443, wR2 = 0.1067
Extinction coefficient	n/a
Largest diff. peak and hole	1.216 and -0.671 e.Å ⁻³

S5.4 X-ray Crystal Structure of Ru9b

Crystals suitable for single-crystal X-ray diffraction experiments were obtained by layering a concentrated DCM solution of **Ru9b** with pentane at -30 °C.

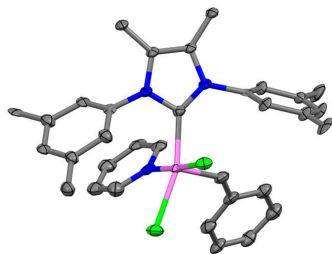


Figure S28. X-ray crystal structure of **Ru9b**, with displacement ellipsoids drawn at 50% probability. Ruthenium is shown in violet, chloride in green, nitrogen in blue, and carbon in gray. Hydrogen atoms have been omitted for clarity.

Table S5 Crystal data and structure refinement for Ru9b

Identification code	Ru9b (Pseudomerohedral twin)
Empirical formula	C33 H35 Cl2 N3 Ru
Formula weight	645.61
Temperature	123(2) K
Wavelength	0.71073 Å
Crystal system	Monoclinic
Space group	P2 ₁ /n
Unit cell dimensions	a = 8.514(5) Å, α = 90°. b = 17.194(9) Å, β = 92.089(11)°. c = 20.087(11) Å, γ = 90°.
Volume	2938(3) Å ³
Z	4

Density (calculated)	1.459 Mg/m ³
Absorption coefficient	0.743 mm ⁻¹
F(000)	1328
Crystal size	0.110 x 0.060 x 0.030 mm ³
Crystal colour/habit	Green/Lath
Theta range for data collection	2.029 to 23.341°
Index ranges	-9<=h<=9, 0<=k<=18, 0<=l<=22
Reflections collected	2828
Independent reflections	2828 [R(int) = ?]
Completeness to theta = 23.341°	66.10%
Absorption correction	Semi-empirical from equivalents
Refinement method	Full-matrix least-squares on F ²
Data / restraints / parameters	2828 / 545 / 358
Goodness-of-fit on F ²	1.153
Final R indices [I>2sigma(I)]	R1 = 0.1282, wR2 = 0.3447
R indices (all data)	R1 = 0.1453, wR2 = 0.3514
Extinction coefficient	n/a
Largest diff. peak and hole	1.731 and -0.938 e.Å ⁻³

S5.5 X-ray Crystal Structure of Ru10

Crystals suitable for single-crystal X-ray diffraction experiments were obtained by layering a concentrated DCM solution of **Ru9c** with pentane at -30 °C leading to a decomposition product.

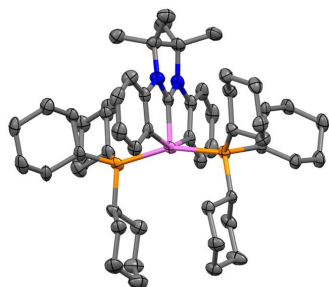


Figure S29. X-ray crystal structure of **Ru10**, with displacement ellipsoids drawn at 50% probability. Ruthenium is shown in violet, phosphor in orange, nitrogen in blue, and carbon in gray. Hydrogen atoms have been omitted for clarity.

Table S6 Crystal data and structure refinement for **Ru10**.

Identification code	Ru10
Empirical formula	C ₆₂ H ₉₄ N ₂ P ₂ Ru
Formula weight	1030.4
Temperature	100(2) K
Wavelength	0.69127 Å
Crystal system	Triclinic

Space group	P-1
Unit cell dimensions	a = 10.8524(6) Å, α = 79.203(4)° b = 13.6808(8) Å, β = 75.720(4)° c = 21.9803(9) Å, γ = 68.344(6)°
Volume	2922.5(3) Å ³
Z	2
Density (calculated)	1.171 Mg/m ³
Absorption coefficient	0.331 mm ⁻¹
F(000)	1108
Crystal size	0.080 x 0.050 x 0.030 mm ³
Crystal colour	Red
Theta range for data collection	1.870 to 26.061°
Index ranges	-13<=h<=13, -10<=k<=10, -26<=l<=26
Reflections collected	13002
Independent reflections	6848 [R(int) = 0.0527]
Completeness to theta = 24.504°	60.80%
Absorption correction	Semi-empirical from equivalents
Max. and min. transmission	1.00000 and 0.58667
Refinement method	Full-matrix least-squares on F2
Data / restraints / parameters	6848 / 547 / 609
Goodness-of-fit on F2	1.072
Final R indices [I>2sigma(I)]	R1 = 0.0629, wR2 = 0.1617
R indices (all data)	R1 = 0.0689, wR2 = 0.1675
Extinction coefficient	n/a
Largest diff. peak and hole	2.855 and -0.749 e.Å ⁻³

S5.6 X-ray Crystal Structure of Ru12

Crystals suitable for single-crystal X-ray diffraction experiments were obtained by layering a concentrated DCM solution of **Ru12** with pentane at -30 °C. The dimethyl-moiety of the imidazolidine ring is disordered around a 2-fold rotation axis through the 5-ring, refined to an occupancy of 0.560(8) vs 0.439(8).

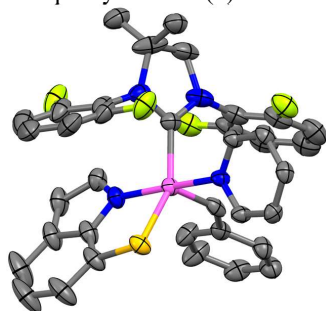


Figure S30. X-ray crystal structure of **Ru12**, with displacement ellipsoids drawn at 30% probability. Ruthenium is shown in violet, sulfur in yellow, fluorine in light green, nitrogen in blue, and carbon in gray. Hydrogen atoms have been omitted for clarity.

Table S7 Crystal data and structure refinement for Ru12

Identification code	Ru12
Empirical formula	C44 H38 F4 N4 Ru S
Formula weight	831.91
Temperature	100(2) K
Wavelength	0.69127 Å
Crystal system	Triclinic
Space group	P-1
Unit cell dimensions	a = 9.9255(5) Å, α = 74.938(7)°. b = 11.4727(13) Å, β = 87.54(5)°. c = 17.6279(12) Å, γ = 78.935(7)°.
Volume	1902.3(3) Å ³
Z	2
Density (calculated)	1.452 Mg/m ³
Absorption coefficient	0.481 mm ⁻¹
F(000)	852
Crystal size	0.120 x 0.080 x 0.050 mm ³
Crystal colour	Red
Theta range for data collection	1.820 to 26.032°.
Index ranges	-9<=h<=9, -14<=k<=14, -21<=l<=21
Reflections collected	8426
Independent reflections	4407 [R(int) = 0.0159]
Completeness to theta = 24.504°	60.00%
Absorption correction	Semi-empirical from equivalents
Max. and min. transmission	1.00000 and 0.99415
Refinement method	Full-matrix least-squares on F2
Data / restraints / parameters	4407 / 525 / 517
Goodness-of-fit on F2	1.048
Final R indices [I>2sigma(I)]	R1 = 0.0432, wR2 = 0.1036
R indices (all data)	R1 = 0.0521, wR2 = 0.1085
Extinction coefficient	n/a
Largest diff. peak and hole	0.622 and -0.439 e.Å ⁻³

S6 References

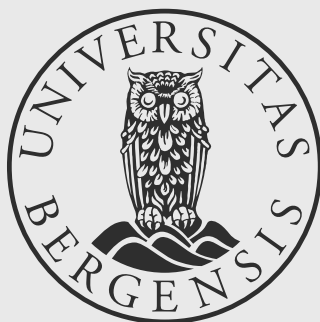
- (1) Reim, I.; Occhipinti, G.; Törnroos, K. W.; Fogg, D. E.; Jensen, V. R. Toward E-Selective Olefin Metathesis: Computational Design and Experimental Realization of Ruthenium Thio-Indolate Catalysts. *Top. Catal.* **2022**, *65* (1–4), 448–461. <https://doi.org/10.1007/s11244-021-01468-3>.
- (2) Johns, A. M.; Ahmed, T. S.; Jackson, B. W.; Grubbs, R. H.; Pederson, R. L. High Trans Kinetic Selectivity in Ruthenium-Based Olefin Cross-Metathesis through Stereoretention. *Org. Lett.* **2016**, *18* (4), 772–775. <https://doi.org/10.1021/acs.orglett.6b00031>.
- (3) Chung, C. K.; Grubbs, R. H. Olefin Metathesis Catalyst: Stabilization Effect of Backbone Substitutions of N-Heterocyclic Carbene. *Org. Lett.* **2008**, *10* (13), 2693–2696. <https://doi.org/10.1021/ol800824h>.

- (4) Fulmer, G. R.; Miller, A. J. M.; Sherden, N. H.; Gottlieb, H. E.; Nudelman, A.; Stoltz, B. M.; Bercaw, J. E.; Goldberg, K. I. NMR Chemical Shifts of Trace Impurities: Common Laboratory Solvents, Organics, and Gases in Deuterated Solvents Relevant to the Organometallic Chemist. *Organometallics* **2010**, *29* (9), 2176–2179. <https://doi.org/10.1021/om100106e>.
- (5) Harris, R. K.; Becker, E. D.; Cabral De Menezes, S. M.; Granger, P.; Hoffman, R. E.; Zilm, K. W. Further Conventions for NMR Shielding and Chemical Shifts (IUPAC Recommendations 2008). *Pure Appl. Chem.* **2008**, *80* (1), 59–84. <https://doi.org/10.1351/pac200880010059>.
- (6) Fukata, Y.; Asano, K.; Matsubara, S. Facile Net Cycloaddition Approach to Optically Active 1,5-Benzothiazepines. *J. Am. Chem. Soc.* **2015**, *137* (16), 5320–5323. <https://doi.org/10.1021/jacs.5b02537>.
- (7) Thiam, A.; Iojoiu, C.; Leprêtre, J. C.; Sanchez, J. Y. Lithium Salts Based on a Series of New Aniliny-Perfluorosulfonamide Salts and Their Polymer Electrolytes. *J. Power Sources* **2017**, *364*, 138–147. <https://doi.org/10.1016/j.jpowsour.2017.07.104>.
- (8) Dumas, A.; Tarrieu, R.; Vives, T.; Roisnel, T.; Dorcet, V.; Baslé, O.; Mauduit, M. A Versatile and Highly Z-Selective Olefin Metathesis Ruthenium Catalyst Based on a Readily Accessible N-Heterocyclic Carbene. *ACS Catal.* **2018**, *8* (4), 3257–3262. <https://doi.org/10.1021/acscatal.8b00151>.
- (9) Frisch, M. J.; Trucks, G. W.; Schlegel, H. B.; Scuseria, G. E.; Robb, M. A.; Cheeseman, J. R.; Scalmani, G.; Barone, V.; Petersson, G. A.; Nakatsuji, H.; Li, X.; Caricato, M.; Marenich, A. V.; Bloino, J.; Janesko, B. G.; Gomperts, R.; Mennucci, B.; Hratchian, H. P.; Ortiz, J. V.; Izmaylov, A. F.; Sonnenberg, J. L.; Williams-Young, D.; Ding, F.; Lipparini, F.; Egidi, F.; Goings, J.; Peng, B.; Petrone, A.; Henderson, T.; Ranasinghe, D.; Zakrzewski, V. G.; Gao, J.; Rega, N.; Zheng, G.; Liang, W.; Hada, M.; Ehara, M.; Toyota, K.; Fukuda, R.; Hasegawa, J.; Ishida, M.; Nakajima, T.; Honda, Y.; Kitao, O.; Nakai, H.; Vreven, T.; Throssell, K.; Montgomery, J. A. Jr.; Peralta, J. E.; Ogliaro, F.; Bearpark, M. J.; Heyd, J. J.; Brothers, E. N.; Kudin, K. N.; Staroverov, V. N.; Keith, T. A.; Kobayashi, R.; Normand, J.; Raghavachari, K.; Rendell, A. P.; Burant, J. C.; Iyengar, S. S.; Tomasi, J.; Cossi, M.; Millam, J. M.; Klene, M.; Adamo, C.; Cammi, R.; Ochterski, J. W.; Martin, R. L.; Morokuma, K.; Farkas, O.; Foresman, J. B.; Fox, D. J. Gaussian 16 Revision C.01, 2016.
- (10) Chai, J.-D.; Head-Gordon, M. Long-Range Corrected Hybrid Density Functionals with Damped Atom–Atom Dispersion Corrections. *Phys. Chem. Chem. Phys.* **2008**, *10* (44), 6615–6620. <https://doi.org/10.1039/B810189B>.
- (11) Peterson, K. A.; Figgen, D.; Dolg, M.; Stoll, H. Energy-Consistent Relativistic Pseudopotentials and Correlation Consistent Basis Sets for the 4d Elements Y–Pd. *J. Chem. Phys.* **2007**, *126* (12), 124101. <https://doi.org/10.1063/1.2647019>.
- (12) *Energy-consistent Pseudopotentials of the Stuttgart/Cologne Group*. <http://www.tc.uni-koeln.de/PP/clickpse.en.html>.
- (13) Dunning, T. H. Gaussian Basis Sets for Use in Correlated Molecular Calculations. I. The Atoms Boron through Neon and Hydrogen. *J. Chem. Phys.* **1989**, *90* (2), 1007–1023. <https://doi.org/10.1063/1.456153>.
- (14) Schuchardt, K. L.; Didier, B. T.; Elsethagen, T.; Sun, L. S.; Gurumoorthi, V.; Chase, J.; Li, J.; Windus, T. L. Basis Set Exchange: A Community Database for Computational Sciences. *J. Chem. Inf. Model.* **2007**, *47* (3), 1045–1052. <https://doi.org/10.1021/ci600510j>.
- (15) Page, M.; McIver, J. W. On Evaluating the Reaction Path Hamiltonian. *J. Chem. Phys.* **1988**, *88* (2), 922–935. <https://doi.org/10.1063/1.454172>.

- (16) Page, M.; Doubleday, C.; McIver, J. W. Following Steepest Descent Reaction Paths. The Use of Higher Energy Derivatives with *ab initio* Electronic Structure Methods. *J. Chem. Phys.* **1990**, *93* (8), 5634–5642. <https://doi.org/10.1063/1.459634>.
- (17) Ribeiro, R. F.; Marenich, A. V.; Cramer, C. J.; Truhlar, D. G. Use of Solution-Phase Vibrational Frequencies in Continuum Models for the Free Energy of Solvation. *J. Phys. Chem. B* **2011**, *115* (49), 14556–14562. <https://doi.org/10.1021/jp205508z>.
- (18) Zhao, Y.; Truhlar, D. G. Computational Characterization and Modeling of Buckyball Tweezers: Density Functional Study of Concave–Convex $\Pi\cdots\pi$ Interactions. *Phys Chem Chem Phys* **2008**, *10*, 2813–2818. <https://doi.org/10.1039/B717744E>.
- (19) Grimme, S. Supramolecular Binding Thermodynamics by Dispersion-Corrected Density Functional Theory. *Chem.-Eur. J.* **2012**, *18* (32), 9955–9964. <https://doi.org/10.1002/chem.201200497>.
- (20) Perdew, J.; Burke, K.; Ernzerhof, M. Generalized Gradient Approximation Made Simple [Phys. Rev. Lett. *77*, 3865 (1996)]. *Phys. Rev. Lett.* **1997**, *78* (7), 1396. <https://doi.org/10.1103/PhysRevLett.78.1396>.
- (21) Smith, D. G. A.; Burns, L. A.; Patkowski, K.; Sherrill, C. D. Revised Damping Parameters for the D3 Dispersion Correction to Density Functional Theory. *J. Phys. Chem. Lett.* **2016**, *7* (12), 2197–2203. <https://doi.org/10.1021/acs.jpcclett.6b00780>.
- (22) Minenkov, Y.; Occhipinti, G.; Jensen, V. R. Complete Reaction Pathway of Ruthenium-Catalyzed Olefin Metathesis of Ethyl Vinyl Ether: Kinetics and Mechanistic Insight from DFT. *Organometallics* **2013**, *32* (7), 2099–2111. <https://doi.org/10.1021/om301192a>.
- (23) Gottlieb, H. E.; Kotlyar, V.; Nudelman, A. NMR Chemical Shifts of Common Laboratory Solvents as Trace Impurities. *J. Org. Chem.* **1997**, *62* (21), 7512–7515. <https://doi.org/10.1021/jo971176v>.



Graphic design: Communication Division, UIB / Print: Skjipes Kommunikasjon AS



uib.no

ISBN: 9788230858363 (print)
9788230865231 (PDF)